Universidade de Brasília – Instituto de Geociências (UnB/IG)
Programa de Pós-graduação em Geologia

O MANTO LITOSFÉRICO SUBCONTINENTAL METASSOMATIZADO ABAIXO DE COYHAIQUE, PATAGÔNIA CHILENA: GEOQUÍMICA DE ROCHA TOTAL, QUÍMICA MINERAL E ISÓTOPOS DE GASES NOBRES E Sr-Nd

EDUARDO NOVAIS RODRIGUES

Dissertação de Mestrado n° 464

Orientador: Prof. Dr. Tiago Luís Reis Jalowitzki

Coorientadora: Profª. Drª. Fernanda Gervasoni

BRASÍLIA/DF
2020

Universidade de Brasília – Instituto de Geociências (UnB/IG)
Programa de Pós-graduação em Geologia

O MANTO LITOSFÉRICO SUBCONTINENTAL METASSOMATIZADO ABAIXO DE COYHAIQUE, PATAGÔNIA CHILENA: GEOQUÍMICA DE ROCHA TOTAL, QUÍMICA MINERAL E ISÓTOPOS DE GASES NOBRES E Sr-Nd

EDUARDO NOVAIS RODRIGUES

Dissertação apresentada ao Programa de Pós-graduação em Geologia do Instituto de Geociências da Universidade de Brasília – UnB para obtenção do título de Mestre em Geologia

Área de concentração: Geoquímica

Aprovada por:

_____

Prof. Dr. Tiago Luís Reis Jalowitziki

(Orientador)

_____

Prof. Dr. Guilherme de Oliveira Gonçalves

(Examinador Interno)

_____

Drª. María Isabel Varas-Reus

(Examinadora Externo)

Brasília-DF, julho de 2020.

Universidade de Brasília – Instituto de Geociências (UnB/IG)
Programa de Pós-graduação em Geologia

O MANTO LITOSFÉRICO SUBCONTINENTAL METASSOMATIZADO ABAIXO DE COYHAIQUE, PATAGÔNIA CHILENA: GEOQUÍMICA DE ROCHA TOTAL, QUÍMICA MINERAL E ISÓTOPOS DE GASES NOBRES E Sr-Nd

EDUARDO NOVAIS RODRIGUES

Dissertação apresentada ao Programa de Pós-graduação em Geologia Instituto de Geociências da Universidade de Brasília – UnB para obtenção do título de Mestre em Geologia

Área de concentração: Geoquímica

Orientador: Prof. Dr. Tiago Luís Reis Jalowitzki

Instituto de Geociências (IG)

Universidade de Brasília (UnB)

Coorientadora: Profª. Drª. Fernanda Gervasoni

Faculdade de Ciências e Tecnologia (FCT)

Universidade Federal de Goiás (UFG)

BRASÍLIA/DF

2020

FICHA CATALOGRÁFICA

CESSÃO DE DIREITOS

NOME DO AUTOR: Eduardo Novais Rodrigues

TÍTULO DA DISSERTAÇÃO: O MANTO LITOSFÉRICO SUBCONTINENTAL METASSOMATIZADO ABAIXO DE COYHAIQUE, PATAGÔNIA CHILENA: GEOQUÍMICA DE ROCHA TOTAL, QUÍMICA MINERAL E ISÓTOPOS DE GASES NOBRES E Sr-Nd

GRAU: Mestre   ANO: 2020

_____

Eduardo Novais Rodrigues

enrmesmo@gmail.com

AGRADECIMENTOS

Agradecimentos de cunho pessoal

Agradeço primeiramente às pessoas que estiveram ao meu lado nas maiores crises e nas melhores comemorações, meu namorado Dan e a minha família! Vocês me deram chão nas horas que eu mesmo não sabia onde pisar. Obrigado por todo apoio!

Principalmente aos meus amigos e orientadores Tiago e Fernanda por me guiarem por essa jornada mantélica de desafios, superações e satisfações acadêmicas. Com vocês eu aprendi, e sigo aprendendo muito mais do que geologia. Obrigado por essa honra e oportunidade.

Aos meus amigos de longa data (Ariel, Dandara, Luiza, Pedro, Saulo e Barbara). Aos amigos que fiz nessa nova caminhada (Brendha, Pedro, Carol, Frank, Debora, Marina). Agradeço as conversas, desabafos, risos e alegrias compartilhadas. Mesmo distantes puderam me trazer felicidade nos nossos encontros. Por grande sorte não me faltaram pontos de apoio!

Obrigado a todos que me ajudaram e me incentivaram a seguir com o sonho do mestrado mesmo durante esses tempos sombrios da humanidade e de nosso país. É preciso estar atento e forte!

RESUMO

Xenólitos mantélicos são comumente hospedados por lavas alcalinas na região de retro-arco patagônico. Os espinélio-lherzolitos de Coyhaique, região de Aysén, Chile (~46°S), estão entre as amostras mais próximas (~320 km) a Fossa do Chile e, portanto, sua composição geoquímica e isotópica podem registrar heterogeneidades do manto litosférico subcontinental (SCLM) causadas pela interação de componentes oriundos da zona de subducção atual e pretéritas. Neste trabalho apresentamos novos e detalhados dados de elementos maiores e traço de minerais (olivina, ortopiroxênio, clinopiroxênio e espinélio) e de rocha total juntamente com dados isotópicos de gases nobres (He, Ne, Ar) e de Sr-Nd de 16 espinélio-lherzolitos anidros. O processo de fusão parcial é evidenciado em rocha total e em minerais por correlações negativas de elementos basálticos (e.g., CaO, Al_2O_3, TiO_2 e Na_2O) vs. MgO. Todos os minerais silicáticos possuem padrão depletado de elementos terras raras leves (ETRL) com relação aos ETR-pesados (ETRP) (La/Yb_N <1), exceto por clinopiroxênios de quatro amostras (clinopiroxênio Tipo-2; La/Yb_N = 1,35–3,48). Além disso, ETRP de rocha total e clinopiroxênios registram variados graus de fusão parcial (2–15% e 1-9%, respectivamente). Razões de Sr-Nd de rocha total e clinopiroxênios ($^{87}Sr/^{86}Sr$ = 0,702347–0,703198; $^{143}Nd/^{144}Nd$ = 0,512940–0,513632; εNd = 5,89–19,39) atestam o caráter depletado dos lherzolitos de Coyhaique. Dados geoquímicos sugerem metassomatismo críptico evidenciado por: 1) padrões enriquecidos de ETRL em rocha total e em clinopiroxênios do Tipo-2; 2) assinatura de elementos traço típica de arco caracterizada por pronunciadas anomalias negativas de elementos de alto potencial iônico (HFSE; Nb, Ta e Ti) somado ao enriquecimento de elementos litófilos de grande raio iônico (LILE) e de elementos calcófilos com relação a HFSE e ETRP em rocha total; 3) correlações positivas de Pb e U vs. La, e correlações negativas de Nb/Nb* e Ti/Ti* vs. La em clinopiroxênios; e 4) anomalias positivas de Li observadas em todos os silicatos. As diferenças entre as composições geoquímicas observadas entre rocha total e os minerais constituintes indicam enriquecimento seletivo da rocha total devido a componentes intergranulares ricos em LILE e ETRL. As razões radiogênicas de $^3He/^4He$ observadas nos lherzolitos de Coyhaique representam a primeira ocorrência para o SCLM patagônico (0,20–2,52 R_A). A maioria das razões isotópicas de Ne analisadas não diferem da composição do ar, com exceção de algumas amostras que evidenciam um componente nucleogênico caracterizado pelo excesso de ^{21}Ne ($^{21}Ne/^{22}Ne$ = 0,0286–0,0308). As razões de $^{40}Ar/^{36}Ar$ (325–551) evidenciam forte contribuição de um componente atmosférico. Com base nos novos dados geoquímicos e isotópicos dos espinélio-lherzolitos de Coyhaique, identificamos um SCLM heterogêneo gerado a partir de

variados e baixos graus de fusão parcial subsequentemente metassomatizado em decorrência da reciclagem de materiais derivados da subducção (*melts* e/ou fluidos provenientes de sedimentos e crosta oceânica subductados) no campo de estabilidade do espinélio (1,06–1,90 GPa e 886–1150 °C).

Palavras chave: reciclagem de gases nobres; zona de subducção andina; manto litosférico subcontinental; espinélio-lherzolitos anidros.

ABSTRACT

Mantle xenoliths are commonly hosted by alkali lavas in the Patagonian back-arc region. The spinel-lherzolites from Coyhaique, Aysén Region, Chile (~46°S), are among the closest mantle samples (~320 km) to the Chile Trench and, therefore, their geochemical and isotopic compositions may record subcontinental lithospheric mantle (SCLM) heterogeneities caused by slab-derived components from current and/or ancient subduction zones. We present new detailed mineral (olivine, orthopyroxene, clinopyroxene and spinel) and whole-rock major and trace element analyses that are discussed together with noble gas (He, Ne, Ar) and Sr-Nd isotopic ratios from 16 selected anhydrous spinel-lherzolites. The xenoliths have experienced partial melting as evidenced by whole-rock and mineral negative correlations of basaltic elements (e.g., CaO, Al_2O_3, TiO_2 and Na_2O) vs. MgO. All silicate minerals show low light-rare earth element (LREE) over heavy-REE ratios (La/Yb_N <1), except four clinopyroxene samples that show some LREE enrichment (Type-2 clinopyroxene; La/Yb_N = 1.35–3.48). Additionally, whole-rock and clinopyroxenes HREE compositions record variables degrees of partial melting (2–15% and 1-9%, respectively). Whole-rock and clinopyroxene Sr-Nd ($^{87}Sr/^{86}Sr$ = 0.702347–0.703198; $^{143}Nd/^{144}Nd$ = 0.512940–0.513632; εNd = 5.89–19.39) data support the depleted character of Coyhaique lherzolite xenoliths. Our geochemical data suggest cryptic metasomatism that is evidenced by: 1) enriched LREE patterns in whole-rock and type-2 clinopyroxenes; 2) typical arc trace element signature characterized by pronounced negative anomalies of high field strength elements (HFSE; Nb, Ta and Ti) coupled with enrichment of large ion lithophile elements (LILE) and chalcophile elements in whole-rock samples; and 3) positive correlations of Pb and U vs. La, and negative correlations of Nb/Nb* and Ti/Ti* vs. La in clinopyroxene; and 4) Li positive anomalies observed in all silicates. The differences between whole-rock and mineral chemical compositions indicate a selective enrichment of the whole-rock samples due to LILE- and LREE-rich grain-boundary components. The $^3He/^4He$ ratios reported here are the first strongly radiogenic noble gas data for the Patagonian subcontinental lithospheric mantle (0.20–2.52 R_A). Most measured Ne isotopic ratios are undistinguishable from air composition with few samples showing a nucleogenic component ($^{21}Ne/^{22}Ne$ = 0.0286–0.0308). All $^{40}Ar/^{36}Ar$ ratios (325–551) were extensively affected by an atmospheric component. Based on the new geochemical and isotopic data of the Coyhaique spinel-lherzolite xenoliths, we identified a heterogeneous subcontinental lithospheric mantle affected by low but variable degrees of partial melting and subsequent enrichment by melts or fluids from recycled

subduction-related materials (sediments and oceanic crust) in the spinel stability field (1.06–1.90 GPa and 886–1150 °C).

LISTA DE FIGURAS

Corpo da dissertação

Artigo

Material suplementar (SUPPLEMENTARY MATERIAL)

ANEXO I

LISTA DE TABELAS

Corpo da dissertação

Artigo

Material suplementar (SUPPLEMENTARY MATERIAL)

SUMÁRIO

TEXTO EXPLICATIVO DA ESTRUTURA DA DISSERTAÇÃO

Esta dissertação possui como objetivo identificar e caracterizar as heterogeneidades presentes no manto litosférico subcontinental sob a região de Coyhaique, Patagônia chilena, através de dados petrográficos, geoquímica de elementos maiores e traços em rocha total e em minerais (olivina, ortopiroxênio, clinopiroxênio e espinélio), isótopos de Sr-Nd em rocha total e em separados de clinopiroxênio, e isótopos de gases nobres em rocha total. A dissertação de mestrado possui a seguinte estrutura:

Capítulo 1. INTRODUÇÃO: contém os objetivos da dissertação, a área de estudo e a caracterização do problema. Aqui também é apresentada uma síntese sobre a composição do manto terrestre e uma revisão teórica acerca dos sistemas isotópicos aplicados ao estudo de heterogeneidades mantélicas.

Capítulo 2. METODOLOGIA: apresenta as principais técnicas analíticas empregadas na obtenção dos dados químicos e isotópicos, tanto em rocha total quanto em minerais, de maneira mais detalhada que aquela apresentada no artigo científico.

Capítulo 3. CONTEXTO GEOLÓGICO E AMOSTRAGEM: apresenta a revisão bibliográfica sobre as rochas aflorantes na área de estudo e dos principais eventos geotectônicos atuantes na evolução da área, assim como indica o local de coleta das amostras.

Capítulo 4. ARTIGO CIENTÍFICO: intitulado "Partial melting and subduction-related metasomatism recorded by geochemical and isotope (He-Ne-Ar-Sr-Nd) compositions of spinel-lherzolites from Coyhaique, Chilean Patagonia". Constitui o corpo principal da dissertação, caracterizando as heterogeneidades do manto litosférico subcontinental sob a região de Coyhaique, Patagônia chilena. O artigo é apresentado na formatação exigida pela revista, porém a numeração das páginas e títulos foi adaptada ao corpo da dissertação. O comprovante da submissão do artigo para a revista Gowndwana Research e o material suplementar (figuras e tabelas) também estão inclusos neste capítulo

Capítulo 5. CONSIDERAÇÕES FINAIS: apresenta as considerações acerca das heterogeneidades presentes no manto litosférico subcontinental sob a região de Coyhaique.

1 INTRODUÇÃO

Ao longo da região de retro-arco continental da Patagônia, a interação do manto litosférico com componentes enriquecidos é possível através da interação com subducções pretéritas e da configuração atual da margem oeste da América do Sul, caracterizada pela subducção das placas oceânicas de Nazca e Antártica sob a placa continental Sul-americana (e.g., Boutonnet et al., 2010; Oliveros et al., 2020). A atual subdução que define o limite convergente andino favorece à fertilização da cunha do manto através da introdução de sedimentos e crosta oceânica (e.g., D'Orazio et al., 2004; Jacques et al., 2013; Jalowitzki et al., 2017; Lucassen et al., 2010). Outro processo tectônico com importante participação na evolução geoquímica do manto patagônico durante o Cenozoico é a colisão de dorsais meso-oceânicas, tais como a de Farallón-Aluk durante o Paleoceno-Eoceno e atualmente a do Chile (Cande e Leslie, 1986; Eagles et al., 2009; Espinoza et al., 2005; Gorring e Kay, 2001; Somoza e Ghidella, 2012).

Suítes de xenólitos mantélicos de natureza ultramáfica são comumente hospedadas por lavas alcalinas na região de retro-arco patagônico. Essas amostras representam fragmentos intrínsecos do manto litosférico subcontinental (SCLM) e fornecem valiosas informações sobre a heterogeneidade mineralógica e química dessa região do planeta. Diversas localidades da Patagônia têm sido objeto de estudos geoquímicos e isotópicos (e.g., Bertotto et al., 2013; Bjerg et al., 2005, 2009; Conceição et al., 2005; Dantas et al., 2009; Faccini et al., 2013; Gervasoni et al., 2012; Gorring and Kay, 2000; Jalowitzki et al., 2010, 2016, 2017; Laurora et al., 2001; Melchiorre et al., 2020; Mundl et al., 2015; Ntaflos et al., 2007; Rivalenti et al., 2004, 2007; Schilling et al., 2005, 2008, 2017; Stern et al., 1999; Zaffarana et al., 2014). Entretanto, a natureza e a evolução dos domínios mantélicos, assim como a influência de componentes relacionados à zona de subducção ou de líquidos de origem astenosférica permanecem em debate.

1.1 Caracterização do problema

Os dados geoquímicos e isotópicos de rocha total de 17 xenólitos mantélicos de Coyhaique foram discutidos por Jalowitzki et al. (2017), que identificaram metassomatismo caracterizado por forte assinatura de arco. Esse evento é caracterizado por pronunciadas anomalias negativas de Nb, Ta e Ti associadas ao enriquecimento de elementos litófilos de raio

17

iônico grande (LILE) e de elementos calcófilos (W, Pb e Sn). Com base nos elementos traço e isótopos de Sr-Nd-Pb, os autores propuseram mistura de um manto depletado com até 10% de componente de subducção com afinidade de manto enriquecido (EM2) para explicar a variedade composicional observada nas amostras. Estudos em detalhe integrando dados de elementos maiores e traço de rocha total e química mineral com isótopos são escassos para xenólitos mantélicos localizados próximos a zona de subducção andina. Além disso, apesar da importância de isótopos de gases nobres como traçadores de fonte e processos registrados pelo SCLM (e.g., Gautheron et al., 2005; Jalowitzki et al., 2016), assim como da reciclagem de voláteis em zonas de subducção (e.g., Kobayashi et al., 2017), dados na Patagônia são limitados ao Campo Vulcânico de Pali-Aike (PAVF) e Gobernador Gregores (Jalowitzki et al., 2016).

1.2   Objetivos

O objetivo do presente estudo é obter evidências e contribuir para o melhor entendimento dos processos de fusão parcial e de metassomatismo registrados pelos peridotitos de Coyhaique, Patagônia chilena. Para tanto, 16 amostras de espinélio-lherzolitos anidros foram investigadas. Os eventos de depleção e enriquecimento evidenciados por essas amostras são discutidos através de:

i.   Caracterização petrográfica e determinação das condições de equilíbrio das fases minerais;
ii. Caracterização química detalhada de amostras de rocha total e de minerais;
iii. Determinação de razões isotópicas de Sr-Nd em rocha total e em separados de clinopiroxênio;
iv. Determinação dos isótopos de He-Ne-Ar em rocha total.

1.3   O manto terrestre

Em termos composicionais, a Terra pode ser dividia em três grandes reservatórios: crosta, manto e núcleo. O manto terrestre tem início no limite crosta-manto (descontinuidade de Mohorovicic), com profundidades superiores a ~5-10 km abaixo dos oceanos e a ~40-70 km dos continentes; e se estende até o limite manto-núcleo a aproximadamente 2900 km (Anderson, 1989). O manto corresponde a 82% do volume e 65% da massa do planeta (Anderson, 1989) e sua composição química pode ser estimada a partir de modelos com base na abundância dos elementos no Sistema Solar e/ou com base na análise direta de rochas do manto superior (Tab.

1). Ambas as abordagens indicam que O, Mg, Si, Fe, Ca e Al são os principais elementos químicos que constituem esta porção do planeta, representando, assim, o maior reservatório silicático terrestre (Palme e O'Neill, 2014). As rochas ultramáficas ricas em olivina magnesiana (Mg_2SiO_4) e piroxênios [enstatita ($MgSiO_3$) e diopsídio ($CaMgSi_2O_6$)] são as mais estáveis em condições de pressão e temperaturas mantélicas. A composição modal do manto primitivo é dividida em: 1) espinélio-peridotitos com 56% de olivina, 22% de enstatita, 9% de diopsídio e 3% de espinélio; e 2) granada-peridotitos compostos 57% de olivina, 17% de enstatita e 10% de diopsídio e 14% de granada. (McDonough, 1990). A fase aluminosa estável presente no manto superior pode fornecer uma aproximação das condições de pressão de equilíbrio da paragênese mineral com base no sistema $CaO + MgO + Al_2O_3 + SiO_2$ (CMAS): peridotitos com plagioclásio (estável até ~35 km de profundidade) gradam para espinélio (~35 a ~80 km), até granada (~80 a ~300 km de profundidade) (O'Hara, 1968). Quando a composição peridotítica atual é comparada a dos meteoritos condríticos, são observadas depleções pronunciadas de Fe, Ni, S, W, Pt, Au e Pb, o que é interpretado como resultado do processo de segregação do núcleo terrestre nos estágios iniciais de formação do planeta (McDonough e Sun, 1995).

Tabela 1. Composição do manto terrestre assumindo a abundância média dos elementos do Sistema Solar para todo o planeta. Retirado de Palme e O'Neill (2014).

Óxido	Modelo Solar (%)	Baseado na composição de rochas do manto superior (%)
MgO	35.34	36.77
SiO_2	50.93	45.40
FeO	7.29	8.10
Al_2O_3	3.60	4.52
CaO	2.90	3.62
Total	100	98.41

1.3.1   Manto litosférico subcontinental (SCLM)

O SCLM possui espessuras variáveis, com início a ~30 km de profundidade (limite crosta-manto) e normalmente atingindo ~100 km (limite litosfera-astenosfera), chegando a 250 km abaixo de alguns crátons arqueanos (Pearson e Nowell, 2002). O estudo de xenólitos mantélicos em rochas vulcânicas tem mostrado que a composição do SCLM está relacionada com a idade da crosta sobrejacente, sendo fortemente empobrecido abaixo de zonas cratônicas enquanto abaixo de crosta fanerozóica é moderado a levemente empobrecido em relação à astenosfera subjacente (Griffin et al., 2009; O'Reilly et al., 2001; Pearson et al., 2003).

Dados de elementos maiores evidenciam o empobrecimento de óxidos como Na_2O, CaO, Al_2O_3, K_2O acompanhando o enriquecimento de MgO, mostrando a natureza empobrecida e residual do SCLM em regiões mais antigas ligada a processos de fusão parcial (Frey e Green, 1974). Entretanto, estudos envolvendo elementos terras raras (ETR) e outros elementos incompatíveis evidenciam enriquecimento em relação aos condritos e ao manto primitivo (Menzies, 1990; Pearson et al., 2003; Pearson e Nowell, 2002; Sun e McDonough, 1989). Tais dados sugerem uma evolução em múltiplos estágios para o manto litosférico, na qual os peridotitos são inicialmente depletados devido à extração de material para a formação da crosta e, posteriormente, são enriquecidos pela interação com pequenas quantidades de líquidos (*melts*) e/ou fluidos ricos em elementos incompatíveis (Frey e Green, 1974).

1.4 Xenólitos mantélicos

As únicas fontes diretas de informação acerca do manto terreste são maciços peridotíticos, exumados tectonicamente, assim como fragmentos de rocha transportados à superfície por rochas vulcânicas. O termo xenólito mantélico é utilizado para designar qualquer fragmento de rocha oriundo do manto transportado para a superfície e hospedado por rochas vulcânicas alcalinas e ultrapotássicas (e.g., basaltos alcalinos, lamproítos e kimberlitos) (Pearson et al., 2003). Apesar do estudo de xenólitos mantélicos apresentar a desvantagem de que os mesmos não preservam relações de campo devido ao pequeno tamanho das amostras (geralmente são menores que 30 cm), eles preservam as características geoquímicas e isotópicas da fonte, uma vez que o tempo de transporte é suficientemente rápido para que não haja reequilíbrio total com o magma hospedeiro (Pearson et al., 2003). No caso dos maciços peridotíticos, estas amostras comumente estão tectonizadas e/ou alteradas por processos superficiais (e.g., serpentinização), modificando as características químicas originais do manto.

1.4.1 Ocorrência de xenólitos mantélicos

Xenólitos mantélicos predominantemente têm composição peridotitica, porém piroxenitos também são identificados (Dawson, 1980; Menzies, 1990; Pearson et al., 2003). Peridotitos são rochas ultramáficas com mais de 40% de olivina (Streckeisen, 1976) e, dentro desse grupo, os lherzolitos são os mais abundantes, seguidos dos harzburgitos e dunitos (Pearson et al., 2003). Comumente, esses litotipos representam uma tendência de fusão parcial, partindo de um manto mais fértil (lherzolitos) até membros mais refratários (harzbugitos e

dunitos) (Bodinier e Godard, 2014). Wehrlitos, devido sua alta proporção de clinopiroxênios, têm sua origem relacionada a processos metassomáticos. Já os piroxenitos (<40% de olivina), são subdivididos em websteritos, orto e clinopiroxenitos, e ocorrem geralmente na forma de diques e veios de origem metassomática (Downes, 2001).

Segundo Pearson et al. (2003), o tipo litológico dos xenólitos juntamente com a natureza da rocha vulcânica hospedeira variam de acordo com o ambiente geológico em que ocorreu a erupção. Desta forma, as ocorrências de xenólitos podem ser classificadas em oceânicas e continentais, sendo a última mais abundante. A litosfera oceânica representa o produto de fusão parcial para a geração de basaltos de dorsais meso-oceânicas (MORBs; altas taxas de fusão) e basaltos de ilhas oceânicas (OIBs; baixas taxas de fusão), enquanto que a litosfera continental registra a influência de regiões cratônicas, faixas móveis, limites intraplaca associados ou não à anomalias térmicas, e limites convergentes.

1.5   Heterogeneidades mantélicas e a geologia isotópica

Em virtude da raridade de amostras diretas do manto (e.g., maciços peridotíticos e xenólitos), a composição do manto é estudada principalmente por meio de basaltos oceânicos. Tais rochas são o produto da fusão parcial do manto e indiretamente carregam consigo assinaturas químicas de suas fontes (Stracke, 2012). Diversos estudos demonstram que basaltos oceânicos apresentam diferenças isotópicas significantes de acordo com o ambiente tectônico em que são gerados, com OIBs caracterizados pelo enriquecimento e heterogeneidade isotópica quando comparados aos MORBs (Anderson, 2006; Hart, 1988; Hart et al., 1992; Hofmann, 1997, 2007; Stracke, 2012, 2018).

A geração de heterogeneidades no manto está ligada a uma combinação de processos relacionados a geodinâmica terrestre (Anderson, 2006; Carlson, 1995). A extração de material por meio de fusão parcial é o principal processo causador da depleção mantélica, enquanto o enriquecimento está ligado a diversos processos de introdução de material rico em elementos incompatíveis e isotopicamente diversos no manto. O processo de reciclagem da litosfera oceânica por meio de subducção e, consequentemente, de sedimentos depositados sobre a mesma, acompanhada da erosão tectônica da crosta continental inferior do arco sobrejacente, é capaz de introduzir grandes volumes de material no manto (Carlson, 1995, 2003; Stracke, 2018; Weaver, 1991). A destruição das heterogeneidades, ou seja homogeneização, é relacionada a

processos de convecção que distribuem o material reciclado no manto, em maior ou menor escala (Carlson, 1995; Hofmann, 1997, 2007). Há um consenso de que as heterogeneidades mantélicas ocorrem em escalas, desde micro a macroescala (e.g., desde inclusões dentro em um mesmo cristal até dezenas de quilômetros) (Anderson, 2006; Carlson, 2003; Hart, 1984; Hofmann, 2007; Stracke, 2018).

1.5.1 Sistemas isotópicos Rb-Sr, Sm-Nd e Pb-Pb e os reservatórios mantélicos

A variação observada nas razões isotópicas de basaltos oceânicos ocorre de uma maneira sistemática, mostrando padrões aproximadamente lineares/planares em diagramas de razões isotópicas 2D e 3D que relacionam Sr, Nd e/ou Pb. Tais arranjos demonstram: 1) uma forte correlação entre os sistemas Sr-Nd (Fig. 1A), conhecida como "*mantle array*"; 2) uma dissociação dos sistemas Sr e Nd com razões Pb-Pb (Fig. 1B-C) em diagramas 2D; e 3) formação de vetores e/ou tendências lineares ao menos em uma escala local (e.g., dentro de uma mesma ilha oceânica) no diagrama 3D que correlaciona as razões isotópicas de Sr-Nd-Pb (Fig. 1D) (Stracke, 2012, 2018; Workman et al., 2004; Zindler et al., 1982; Zindler e Hart, 1986).

Em decorrência do comportamento isotópico dos basaltos oceânicos, principalmente dos OIBs, foram propostos modelos petrogenéticos de membros finais de reservatórios mantélicos (i.e., DMM, EM1, EM2, HIMU e PREMA) (Hanyu et al., 2011; Hart et al., 1992; Stracke, 2012; Stracke et al., 2005; Workman et al., 2004; Workman e Hart, 2005; Zindler e Hart, 1986).
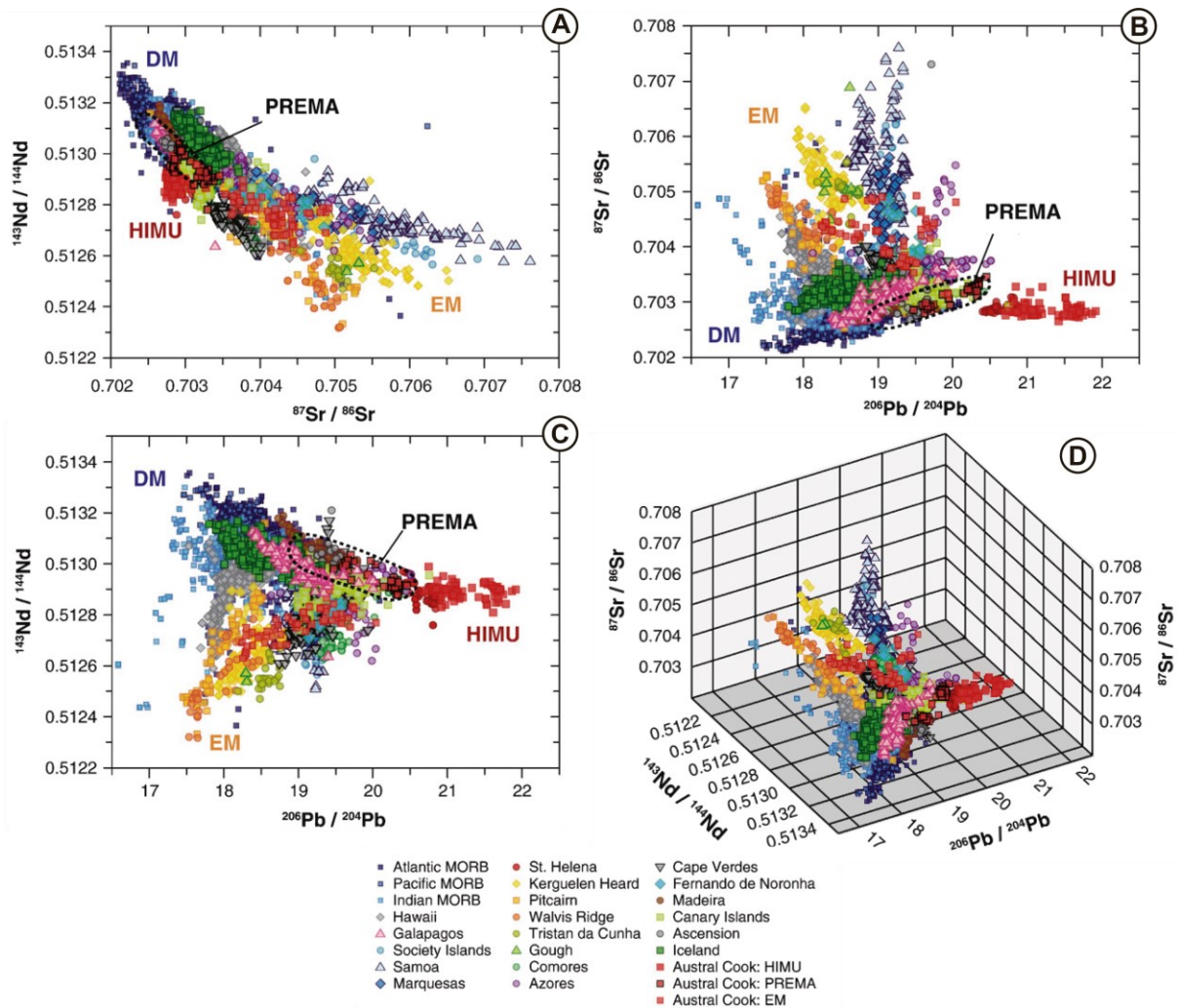
Figura 1. Diagramas mostrando a variação isotópicas de basaltos oceânicos (MORB e OIB) retirados de Stracke (2012). A) $^{87}Sr/^{86}Sr$ versus $^{143}Nd/^{144}Nd$ mostrando o padrão de distribuição aproximadamente linear, evidenciando uma correlação entre os sistemas isotópicos (*mantle array*); B) $^{206}Pb/^{204}Pb$ versus $^{87}Sr/^{86}Sr$ mostra que em muitos casos a razão $^{206}Pb/^{204}Pb$ permanece constante com o aumento da razão $^{87}Sr/^{86}Sr$; C) $^{206}Pb/^{204}Pb$ versus $^{143}Nd/^{144}Nd$ mostra que em muitos casos a razão $^{206}Pb/^{204}Pb$ permanece constante com o aumento da razão $^{143}Nd/^{144}Nd$; e D) $^{206}Pb/^{204}Pb$ versus $^{143}Nd/^{144}Nd$ e $^{87}Sr/^{86}Sr$ mostra que dentro de um mesmo grupo de amostras a distribuição segue um vetor ou uma tendência linear.

1.5.1.1   Manto empobrecido (DMM – *Depleted MORB Mantle*)

O DMM representa a porção residual de um ou mais eventos de fusão parcial envolvendo extração de magmas basálticos para formação de crosta, sendo muito bem caracterizado ao longo das dorsais meso-oceânicas. Possui baixas concentrações de LILE, baixas razões de

^{87}Sr/^{86}Sr e de ^{206}Pb/^{204}Pb e elevadas razões de ^{143}Nd/^{144}Nd , o que lhe confere um caráter empobrecido (Stracke, 2012; Workman e Hart, 2005; Zindler e Hart, 1986).

1.5.1.2   Manto enriquecido (EM1 e EM2 – *Enriched Mantle* 1 e 2)

Os componentes mantélicos enriquecidos são reservatórios ricos em elementos incompatíveis (e.g., Rb, Ba, Th, U, K, Sr, Pb) e isotopicamente distintos. Pelo menos dois componentes enriquecidos são necessários para explicar a variação isotópica nas fontes de basaltos oceânicos (Zindler e Hart, 1986): manto enriquecido 1 (EM1), que apresenta moderadas razões ^{87}Sr/^{86}Sr e baixas razões ^{206}Pb/^{204}Pb; e manto enriquecido 2 (EM2), que tem elevadas razões ^{87}Sr/^{86}Sr e moderadas razões ^{206}Pb/^{204}Pb. Ambos reservatórios têm baixas razões ^{143}Nd/^{144}Nd.

As propostas mais aceitas para a origem destes reservatórios enriquecidos são: 1) a introdução de elementos incompatíveis por meio da subducção de litosfera oceânica, possivelmente alterada, e de sedimentos pelágicos e terrígenos de origem crustal; 2) delaminação/erosão subcontinental; 3) manto inferior metassomatizado. Sendo que EM1 apresenta similaridades com a crosta continental inferior reciclada e sedimentos pelágicos, enquanto o EM2 apresenta razões isotópicas próximas à média da crosta continental superior ou a sedimentos continentais (Stracke, 2012; Stracke et al., 2005; Willbold e Stracke, 2010; Workman et al., 2004; Zindler e Hart, 1986).

1.5.1.3   HIMU (High-µ ou elevada razão U/Pb)

HIMU significa "*high*-µ", sendo µ= (^{238}U/^{204}Pb)$_{t=0}$ (Zindler e Hart, 1986). Este reservatório é caracterizado pelo extremo enriquecimento no isótopo radiogênico de ^{206}Pb observado em basaltos de algumas ilhas oceânicas (OIB) (e.g., Santa Helena e Austral Cook; símbolos vermelhos na Fig. 1). Para que o enriquecimento em ^{206}Pb ocorra é necessário que ^{238}U decaia em um sistema fechado por pelo menos 1,5 Ga. Este reservatório exige a existência de uma fonte mantélica enriquecida em U e Th com relação ao Pb, sem enriquecimento de Rb-Sr, geralmente ligado a reciclagem de crosta oceânica (Hanyu et al., 2011; Jackson e Dasgupta, 2008; Zindler e Hart, 1986). O reservatório tem razões ^{87}Sr/^{86}Sr similares às definidas para N-MORB, mas ele representa a crosta oceânica subductada em que a razão (U + Th)/Pb foi

aumentada pela perda preferencial de Pb junto com os voláteis durante o processo de desidratação da placa subductante.

1.5.2 Gases nobres (He, Ne e Ar)

Os gases nobres ocorrem em uma concentração muito baixa em rochas terrestres devido a sua natureza atmófila. No entanto, lavas oceânicas são passíveis de estudo em decorrência da formação de vidro vulcânico que aprisiona voláteis. Além disso, inclusões de líquidos ou fluidos aprisionados em feno ou xenocristais de basaltos alcalinos ou de peridotitos (e.g., olivina, ortopiroxênio e clinopiroxênio) também podem ser analisadas com precisão (Hilton e Porcelli, 2014). Esses elementos possuem três características que os fazem marcadores sensíveis em processos mantélicos: i) assinaturas geoquímicas características e diagnósticas entre os diferentes gases; ii) são elementos incompatíveis; iii) quimicamente inertes (Hilton e Porcelli, 2003). As razões isotópicas de He, Ne e Ar no manto terrestre são diretamente ligadas a relação entre os conteúdos primordiais desses gases e geração de isótopos radiogênico/nucleogênico. O ^{4}He é o isótopo produzido em maior quantidade, uma vez que é produto da radiação alfa (α) a partir do decaimento de ^{238}U, ^{235}U e ^{232}Th, o ^{21}Ne pode ser produzido por diferentes de reações de nucleogênicas induzidas pelo decaimento de U e Th, e Ar é produzido a partir da captura de elétrons pelo ^{40}K (Hilton e Porcelli, 2003).

1.5.2.1 Isótopos de hélio

Existem dois isótopos de He de ocorrência natural ^{3}He e ^{4}He, sendo o segundo muito mais abundante. Praticamente toda a quantidade de ^{4}He produzida é de origem radiogênica e a desgaseificação do interior do planeta, promovida pelo processo de fusão parcial, é a maior fonte de ^{3}He da atmosfera. A presença de ^{3}He, que é o isótopo primordial, em rochas derivadas do manto sugere que a Terra ainda retém voláteis dos estágios iniciais da formação planetária (Graham, 2002). Devido a sua baixa concentração na atmosfera e baixa densidade, o He atmosférico não é reciclado para o interior do planeta pela tectônica de placas, tornando a razão ^{3}He/^{4}He um excelente traçador de processos mantélicos e o menos suscetível a contaminação (Lupton, 1983). Costumeiramente as razões isotópicas de He são normalizadas com base na razão atmosférica [R_A, onde (^{3}He/^{4}He)$_{ar}$ = 1,4 x 10^{-6}].

MORBs apresentam razões ^{3}He/^{4}He bastante homogêneas (8 ± 1 R_A; Moreira, 1998; Sarda et al., 1988). OIBs, por sua vez, são caracterizados por razões ^{3}He/^{4}He entre 4 - 42 R_A (Fig. 2), sendo características as razões elevadas (>10 R_A). Neste caso, as razões inferiores a 10 R_A são observadas em reservatórios altamente radioativos (HIMU) (Farley e Neroda, 1998; Honda et al., 1991; Stuart et al., 2003; Sumino et al., 2006; Trieloff et al., 2000; Zindler e Hart, 1986). O SCLM apresenta uma distribuição de razões relativamente homogênea e mais radiogênica (6 ± 1 R_A) comparativamente ao MORB (Gautheron et al., 2005; Gautheron e Moreira, 2002; Jalowitzki et al., 2016). Os maiores valores de ^{3}He/^{4}He em OIBs conhecidos estão relacionados à pluma mantélica da Islândia nas localidades de Baffin Island (Stuart et al., 2003) e West Greenland (Starkey et al., 2009) que chegam a apresentar aproximados de 50 R_A, enquanto as mais baixas razões são encontradas em vários vulcões de pequeno porte relacionados a plumas mantélicas (e.g., St. Helena = 6 R_A; Guadalupe = 4 R_A; e Açores = 4 R_A) (Farley e Neroda, 1998). Com base nessas informações, razões ^{3}He/^{4}He medidas em basaltos oceânicos superiores a 10 R_A podem ser inferidas como presença de plumas mantélicas de raízes profundas no manto. Consequentemente, elevadas razões ^{3}He/^{4}He indicam a presença de um reservatório do manto inferior não desgaseificado (Farley e Neroda, 1998).
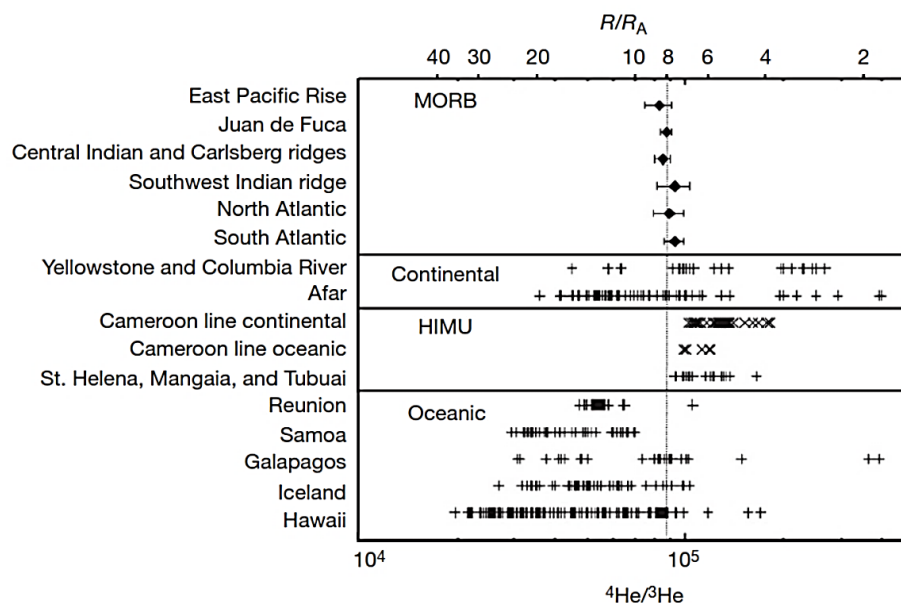
Figura 2. Diagrama mostrando a compilação de isótopos de He obtidos a partir de amostras de MORBs, *hotspots* continentais, OIBs e HIMU. Retirado de c.

1.5.2.2 Isótopos de neônio

O Ne possui três isótopos: ^{20}Ne, ^{21}Ne e ^{22}Ne, com 90,48%, 0,27% e 9,25% de abundância, respectivamente (Ozima e Podosek, 2002). A geração dos isótopos ^{21}Ne e ^{22}Ne é consequência de reações nucleogênicas, comumente chamadas de reações de Wetheril (Wetherill, 1954), em que partículas α e nêutrons interagem com ^{17}O, ^{24}Mg e ^{25}Mg, sendo a última interação ligada a geração de ^{22}Ne e as outras duas referentes ao ^{21}Ne . Modelagens matemáticas demonstram que a produção de ^{22}Ne é <2% da produção de ^{21}Ne (Leya e Wieler, 1999; Yatsevich e Honda, 1997), o que implica na diminuição da razão ^{20}Ne/^{22}Ne e aumento da razão ^{21}Ne/^{22}Ne (Moreira, 2018).

Diferentemente do He, o Ne possui concentrações mais elevadas na atmosfera, o que acarreta em uma contaminação quase inevitável com o ar (Hilton e Porcelli, 2003). Análises de alta precisão em diamantes e em vidros vulcânicos de MORBs (Honda et al., 1987; Ozima e Zashu, 1988; Sarda et al., 1988) evidenciaram que as razões ^{20}Ne/^{22}Ne e ^{21}Ne/^{22}Ne de rochas mantélicas são enriquecidas em relação a atmosfera. Quando plotadas em um diagrama ^{20}Ne/^{22}Ne vs. ^{21}Ne/^{22}Ne (Fig. 3), as análises mostram um arranjo que define uma reta entre o membro final analisado e a composição do ar, de modo que as medidas devem ser tomadas como estimativas mínimas para composição da fonte mantélica (Graham, 2002).

Mesmo que as tendências dos dados representem um produto de contaminação, as pequenas variações no conteúdo de ^{21}Ne/^{22}Ne costumam ser suficientes para que as retas tenham mudanças na inclinação quando comparados OIBs, MORBs, HIMU e SCLM (Fig.3 e 4). MORBs possuem uma tendência bem definida no diagrama ^{20}Ne/^{22}Ne versus ^{21}Ne/^{22}Ne, plotanto em uma reta que liga valores ^{20}Ne/^{22}Ne ≥ 12,5 e ^{21}Ne/^{22}Ne ≥ 0,07 com a composição do ar (Graham, 2002). Por sua vez, OIBs mostram inclinação mais acentuada em decorrência da menor quantidade de Ne nucleogênico, o que se traduz em razões ^{21}Ne/^{22}Ne mais baixas (Honda et al., 1991; Moreira e Allègre, 1998; Sarda et al., 1988) (e.g., Fig. 3 – Loihi, Islândia e Réunion). Reservatórios HIMU e SCLM apresentam razões de Ne mais nucleogências que MORB (Barfod et al., 1999; Hanyu et al., 2011; Jalowitzki et al., 2016; Parai et al., 2009) (Fig. 4).
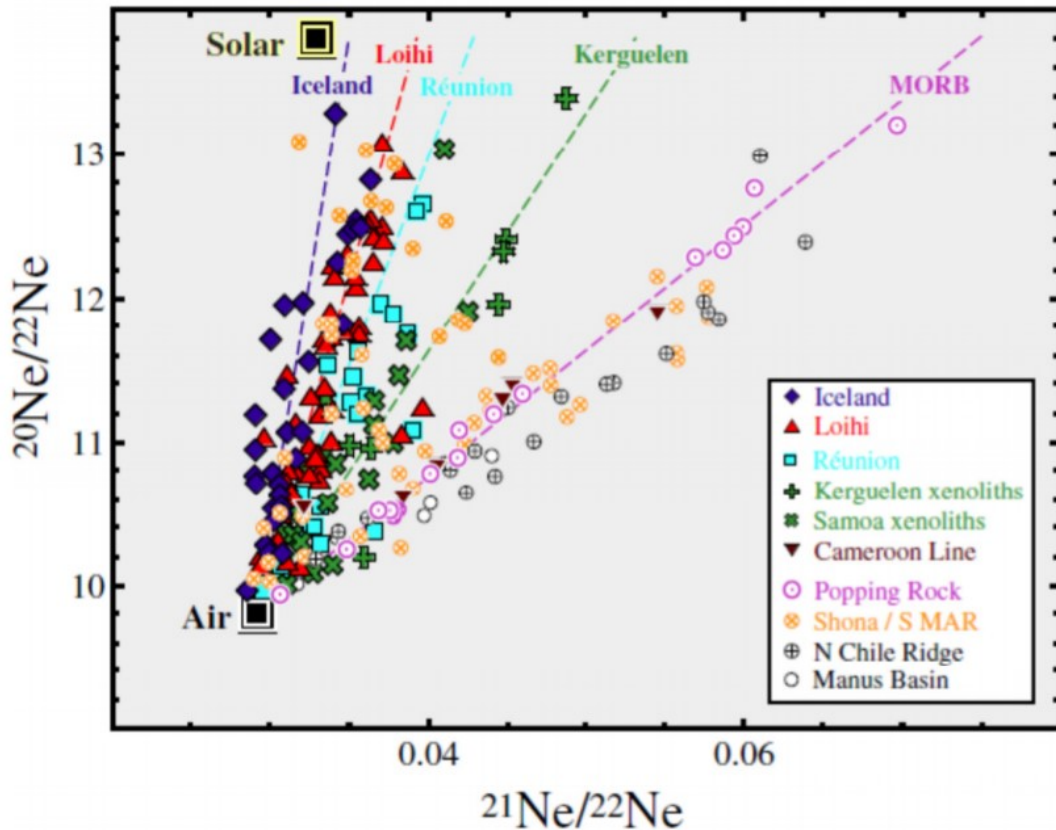
Figura 3. Diagrama que relaciona as razões $^{20}Ne/^{22}Ne$ versus $^{21}Ne/^{22}Ne$. Os círculos amarelos com "x" representam os dados do Mid-Atlantic Ridge (MAR) sul, que grosseiramente formam um *trend* entre a composição solar e a linha definida para MORBs, estas lavas (Shona e Discovery) mostram a influência de *hotspots* em cadeias meso-oceânicas, onde as razões de $^{3}He/^{4}He$ apresentam valores de até 15 R_A. As linhas tracejadas representam a mistura entre a composição do ar e a concentração de Ne no manto para a Islândia, Loihi, Réunion, Kerguelen e MORB (MAR). As razões extrapoladas de $^{21}Ne/^{22}Ne$ correspondem a razão solar de $^{20}Ne/^{22}Ne$ para cada localidade, que é de 0,035 para a Islândia; 0,039 para Loihi; 0,043 para Réunion; 0,053 para Kerguelen e 0,075 para MORB. Retirado de Graham (2002).

A produção de ^{21}Ne está intimamente ligada a produção de ^{4}He (partícula α) e, consequentemente, ao conteúdo de U e Th. Portanto, espera-se que as razões $^{21}Ne/^{22}Ne$ e $^{3}He/^{4}He$ sejam diretamente proporcionais (Graham, 2002; Hilton e Porcelli, 2014). Entretanto, evidências da dissociação entre os sistemas He-Ne foram reportadas por Shaw et al. (2001), que observou altos valores na razão $^{3}He/^{4}He$ (~15 R_A) acompanhado de razões $^{21}Ne/^{22}Ne$ enriquecidas em relação ao MORB. Matsumoto et al. (1997), em outro exemplo de dissociação entre He-Ne, analisaram apatitas ricas em voláteis em espinélio lherzolitos e observaram altas

concentrações de U e Th, baixas razões ^{3}He/^{4}He (<0,3 R$_A$) e assinaturas de Ne similares a de localidades como Havaí, Réunion e Samoa, o que implica na presença de uma pluma profunda, demonstrando que a análise dos isótopos de Ne fornece informações significativas de uma forma que não é possível através somente dos isótopos de He.
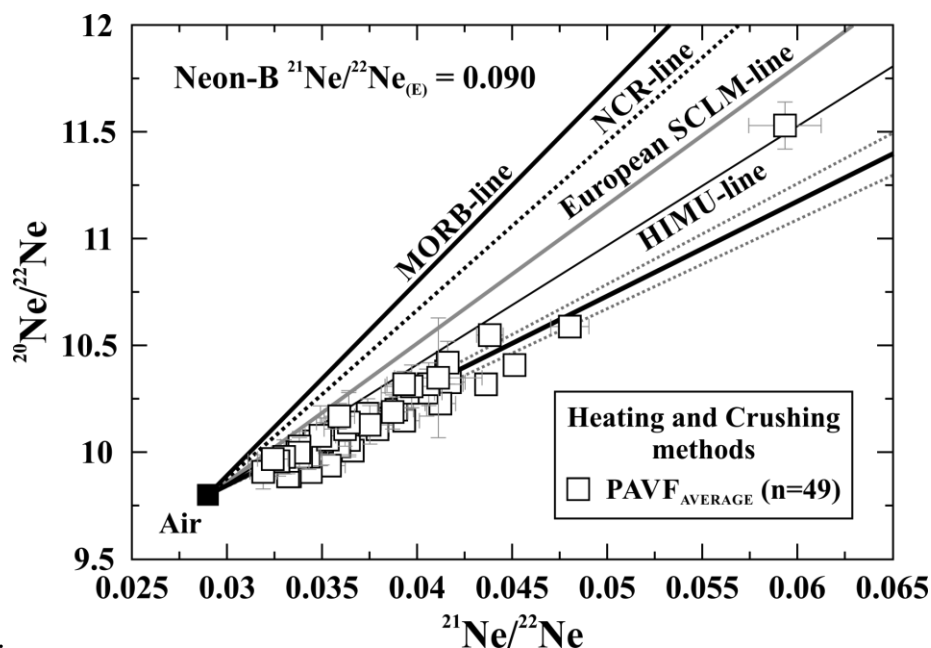
Figura 4. Diagrama que relaciona as razões ^{20}Ne/^{22}Ne versus ^{21}Ne/^{22}Ne com as linhas de misturas calculadas entre o ar e as médias extrapoladas (^{21}Ne/^{22}Ne$_{(E)}$) dos reservatórios MORB, HIMU e SCLM retirado de Jalowitzki et al. (2016). Notar as tendências mais nucleogênicas (maiores razões ^{21}Ne/^{22}Ne) do SCLM e HIMU com relação ao MORB. Os quadrados brancos representam o SCLM da região do Campo Vulcânico de Pali-Aiki (PAVF; Jalowitzki et al., 2016). Para comparação são mostradas as linhas de tendência de MORB (Moreira et al., 1998; Sarda et al., 1988), Dorsal do Chile (NCR; Niedermann e Bach, 1998), SCLM Europeu (Buikin et al., 2005) e Mangaia HIMU (Hanyu et al., 2011).

1.5.2.3 Isótopos de argônio

O argônio possui três isótopos: ^{36}Ar, ^{38}Ar e ^{40}Ar. Dentre os três apenas o último é radiogênico. O isótopo ^{40}Ar é produzido a partir do ^{40}K. O potássio possui três isótopos com massas 39, 40, e 41. Apenas o ^{40}K é radioativo com uma meia-vida do ^{40}K é de 1,25 Ga, e a particularidade de que pode decair de duas formas: emitindo uma partícula β$^-$ produzindo ^{40}Ca ou por uma captura de elétron produzindo ^{40}Ar. Diferentemente do He, o Ar foi acumulado na

atmosfera ao longo da evolução do planeta (Hilton e Porcelli, 2014). Pela grande abundância de Ar na atmosfera, a contaminação de amostras mantélicas é praticamente inevitável, de forma que as razões $^{40}Ar/^{36}Ar$ devem ser consideradas como uma estimativa mínima para a fonte mantélica analisada (Graham, 2002). Não é observado nenhum comportamento sistemático entre as razões $^{40}Ar/^{36}Ar$ e $^{3}He/^{4}He$ baseado nas análises de MORB. Razões $^{40}Ar/^{36}Ar$ são bastante variáveis para MORBs, entre 28000 a 42000 (Burnard et al., 1997; Moreira e Allègre, 1998; Tucker et al., 2012). O SCLM possui razões $^{40}Ar/^{36}Ar$ com valores estimados de 31100 a 54000 (Buikin et al., 2005; Jalowitzki et al., 2016).

2 CONTEXTO GEOLÓGICO E AMOSTRAGEM

Na costa oeste da América do Sul, a crosta oceânica do Pacífico tem sido consumida desde o Carbonífero, e há indícios de subducções Cambrianas (Oliveros et al., 2020). A Cordilheira dos Andes é dividida em quatro zonas com base na presença de vulcanismo recente relacionado à subducção das placas oceânicas de Nazca e Antártica abaixo da placa Sul-americana: Zona Vulcânica Norte (ZVN; 5° N e 2° S), Zona Vulcânica Central (ZVC; 14°S e 27°S), Zona Vulcânica Sul (ZVS – 33° S e 46° S) e Zona Vulcânica Austral (ZVA; 49° S e 55° S). As zonas de vulcanismo ativo são formadas devido ao alto ângulo de mergulho (>25°) da placa oceânica sob a placa Sul-americana. As regiões onde a placa oceânica possui ângulos de mergulhos mais baixo e horizontalizado (<10°) formam as regiões de vulcanismo inativo (*gap* vulcânico) que separam as zonas vulcânicas (Stern, 2004 e referências nele contidas). Entre as ZVS e ZVA a ausência de vulcanismo (*gap*) (Fig. 5A) é atribuída a Junção Tríplice do Chile (CTJ), uma intersecção do tipo fossa-dorsal meso-oceânica-fossa formada durante a colisão da Dorsal do Chile com placa continental Sul-americana, formando a abertura de uma janela astenosférica na região. A continuidade do esforço distensivo durante a subdução de dorsais meso-oceânicas, associada à sua alta densidade, favorece a divergência (quebra) da dorsal junto com a placa oceânica, gerando uma abertura que possibilita a ascensão da astenosfera a partir de uma "janela" (Thorkelson, 1996). A ascensão da astenosfera através desta janela é possível pela fusão por descompressão, produzindo anomalias térmicas e modificações químicas e físicas no manto litosférico sobrejacente (D'Orazio et al., 2004; Gorring e Kay, 2001; Thorkelson, 1996). A subducção da Dorsal do Chile está atualmente localizada na Península de Taitao (46°12′S) (Cande e Leslie, 1986).

A região de Aysén (44–47°S) é composta por três domínios dispostos paralelamente a margem continental: ante-arco, arco e retro-arco com idades que variam de Mesozóicas ao recente, respectivamente, nos domínios mais à leste para oeste (Pankhurst et al., 1999; Parada et al., 2001). A evolução magmática da região de Aysén é registrada majoritariamente no domínio de arco (Fig. 5B) pelo Batólito Norte Patagônico (NPB), composto por rochas plutônicas metaluminosas e calci-alcalinas formadas pela subducção desde o Jurássico Superior até o Cretáceo Inferior (Pankhurst et al., 1999; Parada et al., 2001). A Zona de Falha Liquiñe-Ofqui (LOFZ; Fig. 5B) localiza-se ao longo do eixo do complexo plutônico e é ativa desde o Mioceno (Parada et al., 2001). A oeste, o complexo plutônico intrude as rochas de baixo grau metamórfico do complexo acrecionário Chonos (Demant et al., 1996 e referências nele

contidas; Pankhurst et al., 1999). Este complexo metamórfico é composto à leste por meta-turbiditos preservados, que se encontram intercalados à oeste por xistos psamo-pelíticos de fácies xisto verde (Hervé et al., 1994). A idade do complexo é desconhecida, no entanto, é mais jovem que o contato intrusivo cretáceo com o NPB (Pankhurst et al., 1999). No domínio de retro-arco estão presentes intercalações vulcano-sedimentares geradas durante o Jurássico Tardio-Plioceno das formações Ibañez e Divisadero intrudidas pelas rochas do NPB (e.g., Morata et al., 2005 e referências nele contidas; Pankhurst et al., 1998, 1999, 2000). As formações Ibañez e Divisadero são ambas unidades vulcânicas bimodais extensas, sendo principalmente compostas por rochas andesíticas e riolíticas, incluindo unidades ignimbríticas maciças com afinidade calci-alcalinas (Pankhurst et al., 1999).

Dados geoquímicos das províncias vulcânicas basálticas continentais e intraplaca, bem como as reconstruções paleocinemáticas, indicam que a região de Aysén foi submetida a duas colisões de dorsais meso-oceânicas desde o início do Paleoceno (Aragón et al., 2013; Breitsprecher e Thorkelson, 2009; Cande e Leslie, 1986; D'Orazio et al., 2004; Eagles e Scott, 2014; Espinoza et al., 2005; Jalowitzki et al., 2017; Ramos e Kay, 1992). Modelos paleocinemáticos do Paleoceno no sudeste do Oceano Pacífico indicam que a subducção dorsal que separava as placas Farallón e Aluk (ou Phoenix) sob a Sul-americana ocorreu durante o Cretáceo Tardio até o Paleógeno. O ponto tríplice gerado nessa colisão entre três placas teria se deslocado mais para o sul de 52 até 42 Ma (Breitsprecher e Thorkelson, 2009; Cande e Leslie, 1986; Eagles e Scott, 2014; Gianni et al., 2018; Somoza e Ghidella, 2012). Dados de tomografia sísmica na Patagônia indicam uma lacuna na anomalia de alta velocidade, a qual dá suporte ao modelo de janela astenosférica (Aragón et al., 2011). Tais autores interpretaram a descontinuidade tomográfica como sendo a janela astenosférica gerada no Paleógeno durante a subducção da dorsal meso-oceânica Farallón-Aluk/Phoenix. A colisão com dorsal meso-oceânica culminou na abertura de uma janela astenosférica, registrada por extensos derrames de basaltos alcalinos com assinatura do tipo OIB, frequentemente hospedando xenólitos peridotíticos, como Posadas (57-45 Ma; Kay et al, 2004; Ramos e Kay, 1992), Balmaceda (51-44 Ma; Baker et al., 1981; Demant et al., 1996; Parada et al., 2001), e sequência basáltica inferior da Meseta Chile Chico (60-34 Ma; Baker et al., 1981; Espinoza et al., 2005). De acordo com Gianni et al. (2018), os produtos vulcânicos de Posadas, Balmaceda e Meseta de Chile Chico podem ser a consequência do fluxo lateral do manto resultante que ascende de uma janela astenosférica localizada a 100-150 km ao sul.

A colisão mais recente e mais bem estudada se refere a colisão entre a Dorsal do Chile (dorsal meso-oceânica que divide as placas de Nazca e Antártica) e a placa Sul-americana, representada pela CTJ. Reconstruções paleogeográficas indicam que ~14 Ma atrás a CTJ estava próxima das latitudes da região da Tierra del Fuego e de lá migrou para o norte até a localização atual (Breitsprecher e Thorkelson, 2009; Cande e Leslie, 1986). A migração em direção ao norte da CTJ durante o Neógeno foi responsável pela abertura de uma janela astenosférica sob a Patagônia. Este evento é registrado na região de retro-arco andina por extensos platôs basálticos do Mioceno ao recente (e.g., Meseta del Lago Buenos Aires), seguido por um vulcanismo menos volumoso pós-platô de natureza alcalina, que frequentemente hospeda xenólitos do manto (Boutonnet et al., 2010; D'Orazio et al., 2004; Gorring e Kay, 2001).

Os xenólitos mantélicos deste estudo foram coletados nos derrames basálticos de Balmaceda (59-54 Ma), durante campanha de campo do Projeto Manto da Universidade Federal do Rio Grande do Sul (UFRGS) em março de 2010. O ponto de amostragem está localizado a cerca de 30 km SE da cidade de Coyhaique e a ~320 km da Fossa do Chile (45°46′S; 71°47′W; Fig. 5B) (Jalowitzki et al., 2017). Esta localidade, está entre as mais próximas da margem continental andina. O afloramento é de ~4m de espessura e basaltos alcalinos datados do Eoceno (~54 ± 3 Ma) com assinatura tipo HIMU caracterizada por anomalias positivas de Nb-Ta, anomalias negativas em LILEs (Rb, K, Pb e Sr), $^{87}Sr/^{86}Sr_i$ (0,703039-0,703058), $^{143}Nd/^{144}Nd_i$ (0,512874-0,512880) e $^{206}Pb/^{204}Pb$ (19,333-19,389) (Jalowitzki et al., 2017). Estes autores relataram xenólitos do manto com razões de ETR variando de depletadas a enriquecidas [Ce/Yb_N = 0,6-1,8, onde N = valores normalizados para o manto primitivo de Sun e McDonough (1989)], elementos traço característicos de subducção (pronunciadas anomalias negativas de Nb, Ta e Ti), associadas a um enriquecimento de LILE e elementos calcófilos. Além disso, as razões isotópicas Sr-Nd-Pb indicam mistura com material reciclado (até 10% de material subductado, i.e., 50% de sedimentos de trincheiras do Chile e 50% de crosta oceânica modificada).
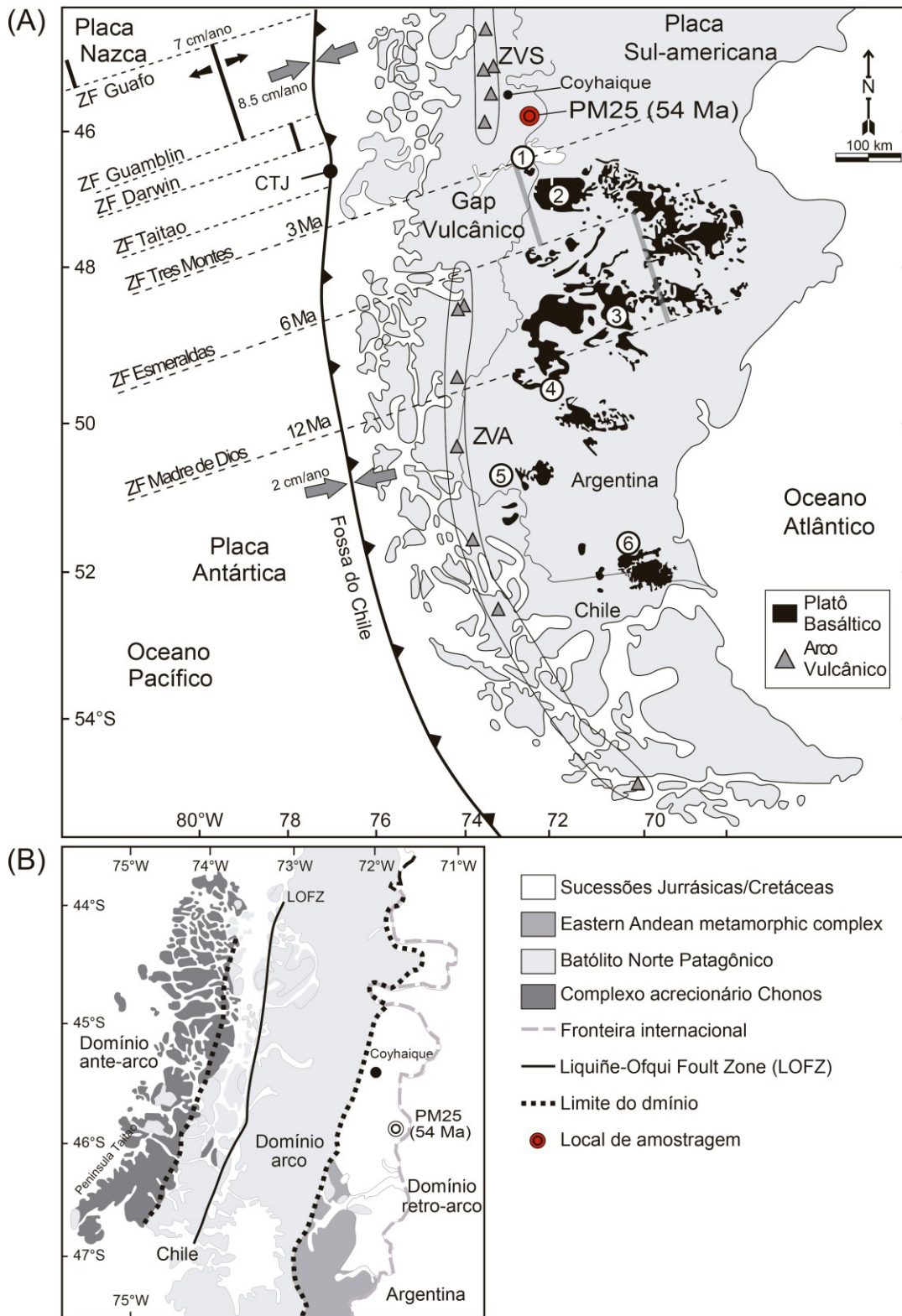
Figura 5. Configuração tectônia atual da porção sul da América do Sul, modificado de Jalowitzki et al. (2017). Posições esperadas para os segmentos da Dorsal do Chile estimadas por Cande e Leslie (1986). ZF = Zona de falha; ZVS = Zona Vulcância Sul; ZVA = Zona

Vulcânica Austral; CTJ = Junção Tríplice do Chile; 1= Meseta de Chile Chico, 2 = Meseta del Lago Buenos Aires, 3 = Gobernador Gregores, 4 = Tres Lagos, 5 = Cerro del Fraile, e 6 = Campo Vulcânico Pali-Aike. (B) Mapa geológico simplificado da região de Aysén entre 43°30′S e 47°30′S (modificado de Pankhurst et al., 1999). Círculos vermelhos indicam o local da amostragem (PM25).

3 METODOLOGIA

3.1 Preparação de amostras

A confecção das 16 lâminas petrográficas polidas (24 x 40 mm cada) utilizadas nesse trabalho foi realizada na Universidad Nacional de La Pampa, Santa Rosa, Argentina. Após rigorosa seleção das amostras, 13 delas foram fragmentadas através do SELFRAG®, no Laboratório de Geocronologia e Geoquímica Isotópica, Instituto de Geociências (IG) da Universidade de Brasília (UnB). A separação das fases minerais para as análises dos isótopos de gases nobres e de Sr-Nd foi realizada a com auxílio de uma lupa estereoscópica binocular de bancada para inspeção visual das amostras desagregadas e seleção dos cristais mais preservados (sem indícios de alteração intempérica). Estes cristais foram submetidos a dois sucessivos ataques "a frio" com HCl em um ultrassom: o primeiro a 0,1 mol/L por 30 min e, em seguida, um novo ataque a 1 mol/L por 10 min foi realizado. Em seguida, as amostras foram lavadas três vezes em água Milli-Q®. A pulverização das amostras selecionadas para as análises geoquímicas e isotópicas foi realizada com o auxílio de cadinho e pistilo de ágata até que a fração "talco" (< 200 mesh) fosse atingida.

3.2 Petrografia

A descrição petrográfica teve como objetivo identificar a paragênese mineral e as principais texturas dos peridotitos com o auxílio de um microscópio óptico petrográfico. A análise petrográfica destinou-se à observação e discussão dos processos de deformação em estado sólido presentes nas amostras, tais como *kink-bands*, extinções ondulantes e orientação de fluxo de certos minerais. O detalhamento da determinação das fases minerais, assim como das feições texturais foram realizadas no Laboratório de Microscopia, localizado nas dependências do IG-UnB. A quantificação das fases foi determinada por meio digital a partir da contagem de pontos com uso do software JMicroVision (Roduit, 2007), tendo no mínimo 2000 pontos por lâmina.

3.3 Geoquímica de rocha-total

A geoquímica de rocha total (elementos maiores e traço) dos xenólitos de Coyhaique foi executada seguindo a mesma metodologia descrita por Jalowitzki et al. (2017). Foram analisados elementos maiores e traço no The Earth Resources Research and Analysis (TERRA)

facility, Department of Earth Sciences, Memorial University of Newfoundland, Canadá, por fluorescência de raios-X (XRF; Bruker S8 Tiger sequential wavelength-dispersive) e por espectrometria de massa por plasma indutivamente acoplado (ICP-MS; PerkinElmer ELAN DRCII), respectivamente. Para os dados de XRF foram utilizadas pastilhas fundidas, produzidas pela mistura de 1,5 g de pó de rocha com 6,0 g de metaborato de lítio, 1,5 g de tetraborato de lítio junto com algumas gotas de brometo de lítio como agente umedecedor, em um cadinho de platina. Em seguida os cadinhos foram levados ao *Leco Fluxer* e aquecidos a ~850 °C durante 8,5 minutos e depois a ~1050 °C para a fusão durante 11,5 minutos. Para a perda ao fogo utilizou-se 2 g de pó de rocha que foram aquecidos a 1050 ºC por 7 horas, sendo a massa da amostra aferida novamente logo após o aquecimento.

Elementos traço foram obtidos por análise de solução em ICP-MS onde 0,1 g de pó de amostra foi digerida através da técnica de digestão de alta pressão desenvolvida por Diegor et al. (2001). Neste método, utilizam-se frascos de politetrafluoretileno, o que aumenta a velocidade de digestão total das amostras (4 dias), além de grande eficiência em dissolver minerais resistatos (e.g., granada e espinélio). Cada amostra (0,1 g), somada a 3 ml de HNO_3 8 M e 2 ml HF 30%, foram acopladas às bombas de politetrafluoretileno, que foram então aquecidas a 200 ºC por 24 horas. Em seguida, as bombas foram abertas para a evaporação das soluções sobre uma chapa quente (70 ºC). Após a evaporação dos primeiros reagentes, foram realizados mais dois ciclos de ataque químico com HNO_3, um sobre chapa quente e outro com bomba aberta. No fim do ataque, foram adicionados 1,35 ml de ácido oxálico (0,22 M) à solução para complexar o Fe e outros elementos traços em solução, 0,665 ml de mistura de HF-HBr (0,1 M HF / 0,45 M HBr) para estabilizar os metais Nb e Ta, e ácido bórico para complexar o excesso de íons F^-. Amostras dissolvidas (0,5 ml) foram então condicionadas em tubos de ensaio junto de 4,5 ml de 0,2 N HNO_3 e mais 5 ml da solução de padrão interno, atuando como *spike*. Adicionalmente, 0,5 ml de amostra dissolvida com 9,5 ml de 0,2 N HNO_3 também foram analisados. Três padrões externos foram utilizados parar calibrar diferentes elementos e com concentrações distintas para cada um deles. Os elementos Sc, Na, Re e U foram aplicados como padrões internos, também com diferentes concentrações. Para correção do *drift*, o sinal do In foi utilizado como padrão interno. A sensibilidade das massas foi determinada por calibrações externas. Utilizou-se calibrações por substituição (*surrogate calibration*) usando os elementos Zr e Hf para as determinações das massas de Nb, Ta e Mo (Jenner et al., 1990). Para as análises, o tempo de contagem total por massa foi de 10 s e o tempo de permanência por massa foi de

0,05 s. A aplicação de múltiplos padrões e calibração por substituição visam lidar com os efeitos da matriz, interferências e o *drift* durante as análises. Mais informações sobre o método aplicado podem ser encontradas em Jenner et al. (1990). Os dados foram reduzidos em uma planilha Excel pertencente ao laboratório.

3.4   Microssonda eletrônica

A composição química de elementos maiores das fases minerais e das reações observadas em 16 amostras foi determinada no Laboratório de Microssonda Eletrônica do IG-UnB, com uma microssonda eletrônica JEOL JXA 8900. As análises ocorreram em uma voltagem de aceleração de 15 kV, corrente de 10 nA e diâmetro do feixe de 1 μm. O período de contagem de cada elemento foi de 10 s para os picos e 5 s para o *background*. Todos os resultados foram reduzidos usando um programa interno de correção ZAF: Z (número atômico), A (probabilidade de absorção), F (fluorescência de raios-X secundária). Os seguintes padrões foram utilizados para clalibração dos dados: andradita (CaO e FeO), albita (Na_2O), forsterita (MgO), topázio (F), microclínio (K_2O, Al_2O_3 e SiO_2), vanadinita (Cl e V_2O_3) e pyrophanita (TiO_2 e MnO).

3.5   Elementos traço por LA-ICP-MS

Cristais selecionados de olivina, ortopiroxênio e clinopiroxênio tiveram seus conteúdos de elementos traço e terras raras determinados *in-situ* por ablação a laser (LA) acoplado com um ICP-MS no Institute for Mineralogy, University of Münster, Alemanha. Quatro amostras (PM25-02, PM25-04, PM25-06 e PM25-10) foram analisadas em Thermo Scientific Element 2 Single Collector ICP-MS acoplado a um 193 nm ArF excimer laser (Teledyne Photon Machines Analyte G2). O restante das amostras foi analisado com um Thermo Scientific Element XR ICP-MS equipado ao mesmo sistema de ablação. Ar foi utilizado para produzir o plasma e He foi usado como gás de transporte. As configurações do laser foram: *spot size* 85 μm, fluência de 4 J/cm², taxa de repetição 5 Hz, 200 *shots* por ponto. Antes de cada ablação, o *background* era lido por 30 s seguido de 20 s de *washout*. Durante as análises teve-se o cuidado de evitar fraturas e inclusões fluidas nos cristais. Os dados foram reduzidos com uso dos softwares GLITTER software (Griffin et al., 2008) e IOLITE (Paton et al., 2011). NIST SRM 612 foi usado para calibração do equipamento e [29]Si foi usada como padrão interno. Para monitorar precisão e acurácia outros materiais de referência (vidros silicáticos BIR-1G e BHVO-2G, e

olivina natural 355OL) foram analisados. A acurácia e precisão das análises dos padrões está disponível na Tabela S2, no material suplementar do artigo científico.

3.6   Isótopos de Sr-Nd

As análises isotópicas de Sr-Nd em rocha total foram executadas seguindo a mesma metodologia descrita por Jalowitzki et al. (2017). Os dados foram gerados no Laboratório de Geologia Isotópica (LGI) do Centro de Estudos em Petrologia e Geoquímica (CPGq) - IG da UFRGS com dois espectrômetros de massa multi-coletores por ionização termal TIMS (*Sector* 54; VG Scienta Holdings e Triton; Thermo Scientific). As amostras pulverizadas de rocha total (< 200 mesh) foram pesadas (0,1 g) em frascos de teflon (Savillex®) e foram adicionadas 15 gotas de HNO_3 concentrado. Após a dissolução em diferentes concentrações de HF, HNO_3 e HCl, as amostras foram diluídas em 3ml de HCl 2,5N e dispostas em tubos de ensaio. Colunas cromatográficas foram utilizadas para separar o Rb, Sr, Sm e Nd. Essas colunas são preenchidas por resina de troca catiônica AG-50W-X8 (200-400 mesh) e aniônica LN-B50-A (100-150 μm). As soluções individuais de Rb, Sr, Sm e Nd foram secas na chapa elétrica e transferidas com auxílio de 2 μ de H_3PO_4 com concentrações específicas para cada um dos elementos sobre filamentos simples de Ta (Rb, Sr e Sm) e triplo de Ta-Re-Ta (Nd) para o VG. No caso do Triton, foram usados filamentos duplos de Re para todos os elementos. As razões isotópicas foram determinadas no modo *static* multi-coletor, utilizando coletores Faraday. Para normalização, as razões de $^{86}Sr/^{88}Sr$ e $^{146}Nd/^{144}Nd$ consideradas foram 0,1194 e 0,7219, respectivamente. As replicadas dos padrões analíticos NBS-987 e JNd-1 resultaram em $^{87}Sr/^{86}Sr = 0.710254 \pm 19$ (n = 4, 2σ) e $^{143}Nd/^{144}Nd = 0,512101 \pm 8$ (n = 4, 2σ).

Para os separados de clinopiroxênios, as razões isotópicas de Nd foram determinadas no Laboratório de Geocronologia e Geoquímica Isotópica, IG/UnB, por TIMS (Finnigan Triton). De acordo com o volume de material disponível, foi possível preparar 13 separados de clinopiroxênio. Alíquotas individuais foram usadas para Sr (0,05 g; sem adição de *spike*) e Sm-Nd (0,2 g; com adição de ~9 mg de *spike* ^{149}Sm-^{150}Nd). A digestão da amostra para ambas as análises seguiu o procedimento descrito por Gioia and Pimentel (2000). O Sr foi separado usando resina Eichrom SR-B100-S (100–150 μm). Já Sm-Nd foi separado em colunas de Teflon em duas etapas: primeira coluna com resina catiônica AG-50W-X8 (200–400 mesh) para separar os elementos terras raras, seguido pela separação de Sm-Nd usando resina aniônica Eichrom LN Resin (100–150 μm). Amostras de Sr e Sm-Nd foram dispostas em um filamento

duplo de Re para análise isotópica. O fracionamento de massa foi corrigido normalizando-se a razão ^{88}Sr/^{86}Sr para 8,3752 e ^{146}Nd/^{144}Nd para 0,7219. A análise do BHVO-2 resultou em ^{143}Nd/^{144}Nd = 0,512981 ± 5. Valores do branco: Nd = 282,52 pg e Sm: 15,61 pg.

3.7   Isótopos de gases nobres (He, Ne e Ar)

As análises de isótopos de gases nobres (He, Ne, Ar) seguiram a mesma preparação dos isótopos radiogênicos. Cinco amostras de rocha total foram selecionadas e as análises foram realizadas no Graduate School of Arts and Sciences, Department of Basic Science, University of Tokyo. As razões isotópicas foram obtidas através da quebra (*crushing*) dos cristais em condições de alto vácuo em um espectrômetro de massa com linha de gás acoplada (MS-IV). Esse método é o mais adequado para este estudo, pois ele permite a liberação dos gases nobres aprisionados nas inclusões fluídas presentes nas fases minerais, evitando a extração de gases aprisionados nas bordas dos mesmos. Com o intuito de eliminar qualquer contribuição de assinaturas isotópicas que não representem aquelas contidas nas inclusões fluidas, foram aplicados a cada uma das amostras (> 1 g) diferentes números de golpes (*strockes*) (100x, 500x, 1000x e 2000x) com uso de um pistão de níquel movido externamente por um imã solenóide (Sumino et al., 2001). Os procedimentos empregados na obtenção dos resultados são descritos em detalhe por Jalowitzki et al. (2016).

Com base na reprodutibilidade das análises do padrão de hélio japonês (HESJ), as incertezas estimadas para a concentração de hélio e argônio é de <5% e <10% para o neônio. Durante a análise de neônio, correções de interferência de massa considerando-se ^{40}Ar^{++} sobre ^{20}Ne^{+} e CO_2^{++} sobre ^{22}Ne^{+} foram aplicadas seguindo o método de Osawa (2004) e foram determinados em <5%. As incertezas atribuídas às razões isotópicas observadas foram de um desvio padrão (1σ), incluindo correções de discriminação do branco e de massa. Os brancos analisados foram obtidos a partir do mesmo procedimento analítico das amostras. Os brancos são: ^{4}He = (2–5)×10^{-11} cm^3 STP; ^{20}Ne = (0,1–9)×10^{-13} cm^3 STP; e ^{40}Ar = (7–9)×10^{-10} cm^3 STP. Assumindo os mais altos valores dos brancos medidos para He, Ne e Ar, estimamos sua contribuição em nossos dados. Para as razões de He, a contribuição do branco é <1,5%. A contribuição do branco para as razões de Ne varia de 6 a 52% (a maioria com <15%). Para as razões de Ar, a contribuição do branco varia de 8 a 29% (a maioria com <18%). Portanto, os brancos de He confirmam contribuições insignificantes.

4 ARTIGO CIENTÍFICO

4.1 Comprovante de submissão

Eduardo Novais <enrmesmo@gmail.com>

Submission Confirmation
1 mensagem

Gondwana Research <eesserver@eesmail.elsevier.com>   14 de agosto de 2020 15:38
Responder a: Gondwana Research <santosh@cugb.edu.cn>
Para: enrmesmo@gmail.com, eduardonovaisrodrigues@gmail.com

*** Automated email sent by the system ***

Article Type: Research Paper

Dear Eduardo,

Your submission entitled "Partial melting and subduction-related metasomatism recorded by geochemical and isotope (He-Ne-Ar-Sr-Nd) compositions of spinel-lherzolites from Coyhaique, Chilean Patagonia" has been received by Gondwana Research

You may check on the progress of your paper by logging on to the Elsevier Editorial System as an author. The URL is https://ees.elsevier.com/gr/.

Your username is: enrmesmo@gmail.com
Your password is: *******

Your manuscript will be given a reference number once an Editor has been assigned.

Thank you for submitting your work to this journal.

Kind regards,

Elsevier Editorial System
Gondwana Research

4.2   Manuscrito

Partial melting and subduction-related metasomatism recorded by geochemical and isotope (He-Ne-Ar-Sr-Nd) compositions of spinel-lherzolites from Coyhaique, Chilean Patagonia

Eduardo NOVAIS-RODRIGUES[1], Tiago JALOWITZKI[1], Fernanda GERVASONI[2], Hirochika SUMINO[3], Yannick BUSSWEILER[4], Stephan KLEMME[4], Jasper BERNDT[4], Rommulo V. CONCEIÇÃO[5], Manuel E. SCHILLING[6], Gustavo W. BERTOTTO[7], Lucas TELES[1]

[1] Programa de Pós-graduação em Geologia, Universidade de Brasília (UnB), Brasília, Brazil.

[2] Faculdade de Ciências e Tecnologia, Universidade Federal de Goiás (UFG), Goiânia, Brazil.

[3] Department of Basic Science, Graduate School of Arts and Sciences, the University of Tokyo, Tokyo, Japan.

[4] Institut für Mineralogie, Universität Münster, Münster, Germany.

[5] Programa de Pós-Graduação em Geociências, Universidade Federal do Rio Grande do Sul (UFRGS), Porto Alegre, Brazil.

[6] Instituto de Ciencias de la Tierra, Facultad de Ciencias, Universidad Austral de Chile, Valdivia, Chile.

[7] INCITAP, CONICET - Universidad Nacional de La Pampa, La Pampa, Argentina.

Corresponding authors: eduardonovaisrodrigues@gmail.com, jalowitzki@unb.br.

Highlights

- We report the first subduction-related helium composition of Patagonian peridotites.

- Cryptic metasomatism is observed in anhydrous peridotites from Coyhaique, Patagonia.

- P-T estimates show that the lherzolites equilibrated in the spinel stability field.

Graphical Abstract
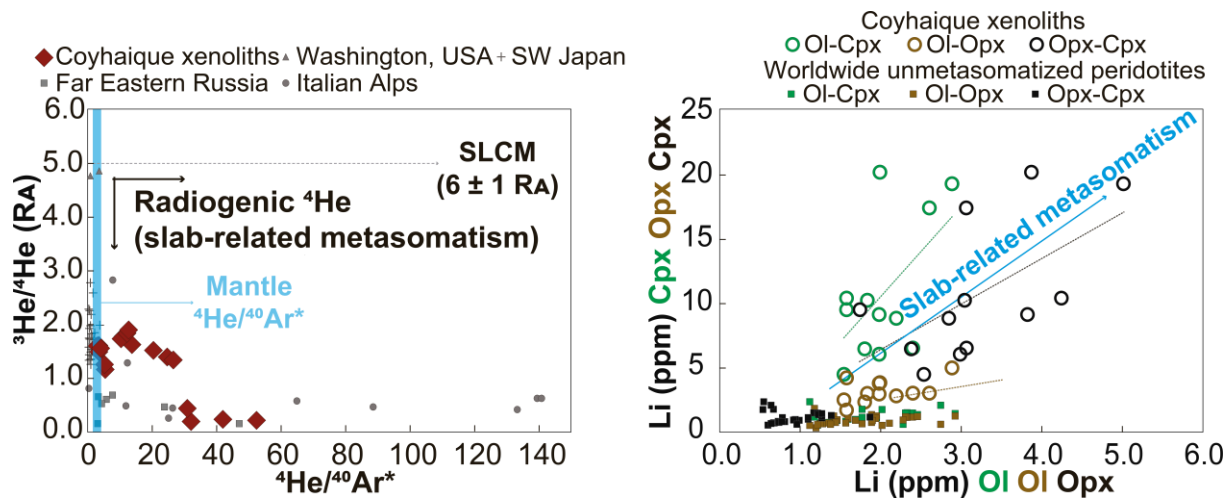
Abstract

Spinel-lherzolites from Coyhaique, Chilean Patagonia, are among the closest mantle samples (~320 km) to the Chile Trench and, therefore, their geochemical and isotopic compositions record slab-derived metasomatism from the current and/or ancient subduction zones. Here we present new mineral and whole-rock major and trace elements that are discussed together with noble gas (He, Ne, Ar) and Sr-Nd isotopic ratios. Partial melting process is evidenced by whole-rock and minerals negative correlations between basaltic elements vs. MgO. In general, silicate minerals show depleted light-rare earth element (LREE) over heavy-REE (HREE) patterns. Whole-rock and clinopyroxene record variable degrees of partial melting (2–15% and 1-9%, respectively), which is also corroborated by the Sr-Nd depleted character of lherzolites. Cryptic metasomatism is evidenced by: 1) enriched LREE patterns in whole-rock and type-2 clinopyroxenes; 2) negative anomalies of Nb-Ta-Ti coupled with enrichment of large ion lithophile elements (LILE) and chalcophile elements over high field strength elements (HFSE) and HREE in whole-rock samples; 3) clinopyroxene positive correlations of Pb and U vs. La and negative correlations of Nb/Nb* and Ti/Ti* vs. La, and 4) Li positive anomalies observed

in all silicate minerals. The geochemical differences between whole-rock and their mineral constituents indicate selective enrichment of the whole-rock samples due to the grain-boundary components. ^{3}He/^{4}He ratios reported here are the first strongly radiogenic for Patagonian SCLM (0.20–1.90 R_A). Most Ne isotopic ratios are undistinguishable from air composition with few samples showing nucleogenic component while Ar isotopic ratios are extensively affected by atmospheric component. The correlation between ^{3}He/^{4}He and ^{4}He/^{40}Ar* corroborate the metasomatism recorded by lithophile and chalcophile elements. Therefore, we identified a heterogeneous SCLM affected by low but variable degrees of partial melting and subsequent enrichment by melts or fluids from recycled subduction-related materials in the spinel stability field (1.06–1.90 GPa and 886–1150 °C).

4.2.1 Introduction

Mantle xenoliths brought to the surface by Cenozoic alkaline basalts from the Andean continental back-arc provide direct and valuable information about depletion and enrichment processes, allowing to better understand the chemical evolution of the subcontinental lithospheric mantle (SCLM) beneath Patagonia (e.g., Bertotto et al., 2013; Bjerg et al., 2009, 2005; Conceição et al., 2005; Dantas et al., 2009; Faccini et al., 2013; Gorring and Kay, 2000; Jalowitzki et al., 2017, 2016; Kilian and Stern, 2002; Laurora et al., 2001; Melchiorre et al., 2020; Ntaflos et al., 2007; Rivalenti et al., 2007, 2004; Schilling et al., 2017, 2008; Stern et al., 1999). Although there are important mineralogical, geochemical and isotopic studies of mantle

xenoliths from many regions in Patagonia (e.g., review of Melchiorre et al., 2020), information about the composition of the SCLM close to the Andean subduction zone is scarce. Mantle xenoliths from the mantle wedge with high proximity to the continental arc may be useful to constrain the chemical composition of melts and fluids released from the slab during subduction, and these samples may record the results of the metasomatic reactions between fluids and/or melts with the mantle rocks (e.g., Faccini et al., 2013; Gervasoni et al., 2017; Jalowitzki et al., 2017; Kilian and Stern, 2002; Rapp et al., 1999).

Therefore, mantle xenoliths from Coyhaique (Jalowitzki et al., 2017; Schilling et al., 2017), located approximately 320 km east from the Chile Trench are special samples as they are among the closest samples to the margin of the convergent plates, together with Cerro del Fraile (Faccini et al., 2013; Kilian and Stern, 2002) and Chile Chico (Schilling et al., 2017, 2008), which are located 280 to 300 km from the Chile Trench, respectively.

Kilian and Stern (2002) studied mantle xenoliths from Cerro del Fraile and discussed the role of adakitic slab-derived metasomatism in peridotites based on high Sr/Y, La/Yb, and La/Nb ratios. Thereafter, Faccini et al. (2013) also observed metasomatism by adakitic melts in clinopyroxene and orthopyroxene of peridotitic and pyroxenitic xenoliths from Cerro del Fraile. They also suggested that the enrichment of Zr, Th, and U in these pyroxenes were caused by subduction of Mn nodules and organic-rich sediments.

Mantle xenoliths from Chile Chico (2 samples) and Coyhaique (2 samples) were studied by Schilling et al. (2017, 2008), who analyzed mineral chemistry, whole-rock major elements, platinum group elements (PGEs) concentrations, and determined Re-Os ages ($T_{RD} = 0.57$-0.88, 1.31-1.70 Ga, respectively). However, these authors did not discuss mantle metasomatism.

Whole-rock geochemical and isotope data from Coyhaique mantle xenoliths were presented by Jalowitzki et al. (2017), who identified evidence of cryptic metasomatism in these rocks,

45

characterized by strong slab-derived trace element signature, such as pronounced negative Nb, Ta and Ti anomalies coupled with significant enrichment of large ion lithophile elements (LILEs) and chalcophile elements (e.g., W, Pb and Sn). Based on trace elements and Sr-Nd-Pb isotopes, they proposed a mixing between depleted mantle and up to 10% of a slab-derived component with enriched mantle (EM2) affinity to explain the compositional variability of these samples. Although there is an important contribution given by Jalowitzki et al. (2017), mantle xenoliths from Coyhaique remain far from settled with respect to the absence of any textural and mineralogical evidence of any kind of modal metasomatism in their petrography. Usually, mantle xenoliths near to the continental arc that were metasomatized by slab melts (adakite) record the presence of secondary amphibole [e.g., Cerro del Fraile in Patagonia (Faccini et al., 2013; Kilian and Stern, 2002), Luzon Arc in the Philippines (Gregoire et al., 2008), and Kamchatka Arc (Arai et al., 2003)].

In order to obtain additional information of the subduction-related components in the Patagonian SCLM, we studied 16 mantle xenoliths from Coyhaique using a different approach than that of Jalowitzki et al. (2017). We aim to investigate the depletion and metasomatic enrichment processes of the peridotites with detailed mineral chemistry, whole-rock geochemistry, whole-rock and clinopyroxene Sr-Nd isotopes, and whole-rock He-Ne-Ar isotopes of four mineral phases (olivine, orthopyroxene, clinopyroxene and spinel). Although noble gas isotopes are powerful tracers of mantle sources in the SCLM (e.g., Gautheron et al., 2005; Jalowitzki et al., 2016), as well as of volatile recycling in subduction zones (e.g., Kobayashi et al., 2017; Sumino et al., 2010), this type of studies in mantle xenoliths from Patagonia are limited to the Pali-Aike Volcanic Field (PAVF) and Gobernador Gregores (Jalowitzki et al., 2016). The new data presented here are hence discussed together with reported data from Jalowitzki et al. (2017), who studied 17 mantle xenoliths from Coyhaique.

Eight of these samples were chosen for further detailed investigation and they were aggregated to new eight samples.

4.2.2   Geologic setting and samples

The subduction in the western margin of South America has been periodically active since the Early Paleozoic, as early as the Cambrian, but certainly since the Early Carboniferous (Oliveros et al., 2020 and references therein). In the in Aysén region (44–47°S), the Gondwana fragmentation generated an active continental margin that lead to the eruption of Upper Jurassic-Lower Cretaceous volcanic rocks of the Ibañez and Divisadero formations and the intrusion of plutonic rocks (the Patagonian Batholith; e.g., Morata et al., 2005 and references therein; Pankhurst et al., 2000, 1999, 1998). The Patagonian Batholith is a subduction-related igneous body composed of metaluminous calc-alkaline plutonic rocks from the Late Jurassic–Late Cretaceous (Pankhurst et al., 1999). The Ibañez and Divisadero formations are both extensive bimodal volcanic units formed during the same interval. They are mainly composed of andesitic and rhyolitic rocks, including massive ignimbrite units, cropping out east of the North Patagonian Batholith (Pankhurst et al., 1999). This batholithic complex intruded Paleozoic and Mesozoic volcanic and sedimentary units to the east, and intruded the Chonos Late Paleozoic metamorphic complex to the west (Demant et al., 1996 and references therein; Pankhurst et al., 1999). Geochemical data of continental back-arc and within-plate basaltic volcanic provinces, as well as paleokinematic reconstructions, indicate that the Aysén region was submitted to two spreading ridge collisions since early Paleocene (Aragón et al., 2013; Breitsprecher and Thorkelson, 2009; Cande and Leslie, 1986; D'Orazio et al., 2004; Eagles and Scott, 2014; Espinoza et al., 2005; Jalowitzki et al., 2017, Ramos and Kay, 1992, Gianni et al., 2018).

Currently, the subduction of the Nazca-Antarctic spreading ridge beneath South America plate at the Taitao Peninsula (46°12′S) forms the Chile Triple Junction (CTJ), a trench-ridge-trench triple junction (Cande and Leslie, 1986). Paleokinematic reconstructions indicate that by ~14 Ma ago the CTJ was near latitudes of the Tierra del Fuego and migrated northward until it reached its present location (Breitsprecher and Thorkelson, 2009; Cande and Leslie, 1986). The Neogene northward trench-ridge-trench junction migration opened a slab-window beneath Patagonia and this caused voluminous tholeiitic volcanism from the Miocene to nearly the present (e.g., Meseta del Lago Buenos Aires), followed by less-voluminous post-plateau alkali basalts that often host mantle xenoliths (e.g., Mio-Pliocene Upper Basaltic Sequence from Meseta Chile Chico Formation) (Gorring and Kay, 2001).

Plate tectonic reconstructions in southeast Pacific Ocean indicate that Farallón-Aluk (or Phoenix) spreading ridge subduction beneath South America occurred during Late Cretaceous to Paleogene times (Breitsprecher and Thorkelson, 2009; Cande and Leslie, 1986; Eagles and Scott, 2014; Gianni et al., 2018; Somoza and Ghidella, 2012). Gianni et al. (2018) proposed a model for the Paleogene (62–40 Ma) tectonic evolution of Central Patagonia (Fig. 1) in which a southward oblique collision of a segmented Farallón-Aluk/Phoenix spreading ridge could explain the existence of two discrete areas with simultaneous slab window-related magmatism (black areas in Figure 1) separated by a sector with plate-wide contraction (red symbols in Figure 1). Seismic tomography in Patagonia also indicates a subduction gap manifested in an absence of fast anomaly continuity in the tomographic model, which supports the slab window model (Aragón et al., 2011). These authors interpreted the tomography discontinuity in the imaged slab as being the Paleogene detachment of the previous Aluk/Phoenix slab. The collision of the Farallón-Aluk/Phoenix ridge and the opening of an asthenospheric slab-window coincide with extensive alkaline flood basalts (often xenolith-bearing) with a typical OIB-like

signatures, i.e., from Posadas (57–45 Ma; Kay et al., 2004; Ramos and Kay, 1992), Balmaceda (59–44 Ma; Baker et al., 1981; Demant et al., 1996; Jalowitzki et al., 2017; Morata et al., 2000; Parada et al., 2001), and the Lower Basaltic Sequence of Meseta Chile Chico (60–34 Ma; Baker et al., 1981; Espinoza et al., 2005). According to Gianni et al. (2018), the volcanic products of the Posadas, Balmaceda and Meseta de Chile Chico may be a consequence of lateral mantle flow resulting from the upwelling caused by a slab-window located 100–150 km to the south (Fig. 1).

The mantle xenoliths present in this study were collected from the Balmaceda flood basalts (59-54 Ma; Jalowitzki et al., 2017; Morata et al., 2000), located approximately 30 km SE from the city of Coyhaique and ~320 km from the Chile Trench (45°46′S; 71°47′W) (Jalowitzki et al., 2017). This locality, together with Cerro del Fraile and Chile Chico, is among the closest to the Andean continental margin. The outcrop is ~4 m thick and comprises alkaline basalt with HIMU-like signature characterized by marked positive Nb–Ta anomalies, negative anomalies in highly incompatible and fluid-mobile elements (Rb, K, Pb, and Sr), $^{87}Sr/^{86}Sr_i$ (0.703039–0.703058), $^{143}Nd/^{144}Nd_i$ (0.512874–0.512880) and $^{206}Pb/^{204}Pb$ (19.333–19.389) (Jalowitzki et al., 2017). These authors reported mantle xenoliths with variable light rare earth elements (LREE) ratios [Ce/Yb$_N$ = 0.6–1.8, where N = primitive mantle (PM) normalized values from Sun and McDonough (1989)], trace element compositions characteristic of a subduction zone setting, such as pronounced negative Nb, Ta and Ti anomalies coupled with significant enrichment of LILEs and chalcophile elements. Furthermore, Sr–Nd–Pb isotopic ratios indicate mixing with slab-related material (up to 10% of subducted material, e.g., 50% Chile Trench sediments and 50% modified oceanic crust).
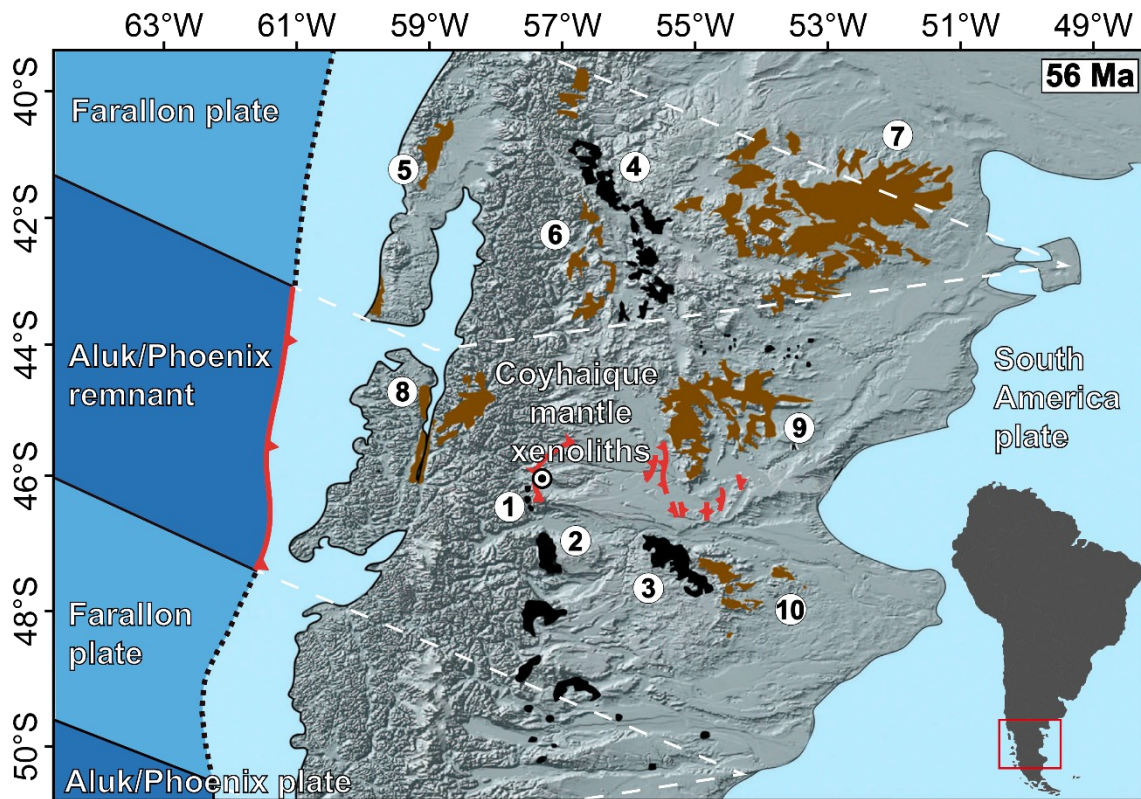
Figure 1. Geodynamic setting of the studied area at 56 Ma (modified from Gianni et al., 2018) showing the proposed locations of slab windows (dashed white lines), Farallón (blue), Aluk/Phoenix (dark blue) and South America (light blue) plates. Volcanic rocks from late Paleocene to Eocene (62–40 Ma) are shown as black areas (1-4) and late Eocene to early Miocene (37–17 Ma) volcanism are the brown areas (5-10). 1 = Balmaceda basalts; 2 = Posadas basalts; 3 = Meseta de Chile Chico; 4 = Pilcaniyeu magmatic belt; 5 = Coastal magmatic belt; 6 = El Maitén magmatic belt; 7 = Meseta de Somún Curá; 8 = Traiguen Basin; 9 = Meseta del

Canquel; 10 = Alma Gaucha basalts. Red symbols represent records of Paleogene contraction (62–40 Ma) (Gianni et al., 2018 and references therein).

4.2.3 Methodology

4.2.3.1 Whole-rock geochemistry

Major and trace elements of 8 new mantle xenoliths (PM25-02, PM25-04, PM25-06, PM25-08, PM25-10, PM25-13, PM25-16 and PM25-42) were determined by X-ray fluorescence analysis (Bruker S8 Tiger sequential wavelength-dispersive XRF) and by inductively coupled plasma mass spectrometry (ICP-MS; PerkinElmer ELAN DRCII) at the Earth Resources Research and Analysis (TERRA) facility, Department of Earth Sciences, Memorial University of Newfoundland, Canada. The detailed analytical procedures are described in Jalowitzki et al. (2017). Reference materials (BIR-1G and MRG-1) were used as the calibration materials and sample duplicates were also analyzed to monitor precision and accuracy (Tab. S1).

4.2.3.2 Electron microprobe analysis

Major element mineral compositions of olivine, orthopyroxene, clinopyroxene, and spinel were determined by wavelength-dispersive spectrometry (WDS) using a JEOL JXA-8900 Electron Probe Micro Analyzer (EPMA) at the Laboratório de Microssonda Eletrônica, Instituto de Geociências (IG), Universidade de Brasília (UnB), Brazil. The analytical conditions applied during the measurements were accelerating voltage of 15 kV, beam current of 10 nA, and beam diameter of 1 μm in the spot mode. Counting time per peak was 10 s and 5 s for the background. All results were reduced using an in-house ZAF correction program. The data were calibrated with the following standards: andradite (CaO and FeO), albite (Na_2O), forsterite (MgO),

microcline (K_2O, Al_2O_3 and SiO_2), pyrophanite (TiO_2 and MnO), chromium oxide (Cr_2O_3), and nickel oxide (NiO).

4.2.3.3 Laser ablation inductively coupled plasma mass spectrometry

Trace elements of selected grains of olivine, orthopyroxene and clinopyroxene were analyzed by laser ablation (LA) ICP-MS at the Institute for Mineralogy, University of Münster, Germany. Four samples (PM25-02, PM25-04, PM25-06 and PM25-10) were analyzed with a Thermo Scientific Element 2 Single Collector ICP-MS coupled to a 193 nm ArF excimer laser (Teledyne Photon Machines Analyte G2) ablation system. The other samples were analyzed with a Thermo Scientific Element XR ICP-MS and the same laser ablation system. The plasma gas was Ar, and the transport gas carrying the ablated aerosol into the plasma was He. Laser repetition rate was 5 Hz using an energy density of about 4 J/cm^2. Prior to sample analyses, the system was tuned with the NIST SRM 612 standard for maximum sensitivity, stability, and low oxide production rates ($^{232}Th^{16}O/^{232}Th$ < 0.1%). Ablation time was 40 s and the background was measured for 20 s prior to sample ablation. The gas blank was measured for 30 s before each ablation, and the washout time was 20 s. We used a laser spot size of 85 μm. Great care was taken during the measurements to avoid cracks and mineral/fluid inclusions. The resulting data were evaluated using the GLITTER software (PM25-02, PM25-04, PM25-06 and PM25-10; Griffin et al., 2008) and the IOLITE software (other samples; Paton et al., 2011). NIST SRM 612 was used as the calibration material and ^{29}Si as the internal standard. Further reference materials (silicate glasses BIR-1G and BHVO-2G, and natural olivine 355OL) were analyzed to monitor precision and accuracy (see Tab. S2). Reference values for the silicate glasses and natural olivine can be found respectively on the GeoRem database (Jochum et al., 2005) and in Bussweiler et al. (2019).

4.2.3.4 Isotopic geochemistry

4.2.3.4.1 Whole-rock Sr-Nd isotopes

Whole-rock Sr–Nd isotopic ratios of 8 mantle xenoliths were measured at the Laboratório de Geologia Isotópica, Universidade Federal do Rio Grande do Sul (UFRGS), Porto Alegre, Brazil. Radiogenic isotopes were analyzed using two different thermal ionization mass spectrometers (TIMS; Sector 54, VG Scienta Holdings AB for Sr; and Triton, Thermo Scientific for Nd). The data were corrected for mass fractionation by normalizing to $^{86}Sr/^{88}Sr = 0.1194$ and $^{146}Nd/^{144}Nd = 0.7219$. The replicate analyses of NBS-987 and JNd-1 standards gave $^{87}Sr/^{86}Sr = 0.710254 \pm 19$ (n = 4, 2σ) and $^{143}Nd/^{144}Nd = 0.512101 \pm 8$ (n = 4, 2σ). The analytical procedure applied for radiogenic isotopes were described in detail by Jalowitzki et al. (2017).

4.2.3.4.2 Clinopyroxene Sr-Nd isotopes

Clinopyroxene Sr–Nd isotopic ratios were determined at the Laboratório de Geocronologia e Geoquímica Isotópica, IG/UnB, Brasília, Brazil, using Triton (Thermo Scientific) TIMS. With the available material, we could prepare thirteen clinopyroxene separates. Samples were disaggregated by high voltage electric discharges (SELFRAG® Lab system) and then, to avoid contamination, crystals without inclusions and/or any signal of weathering/alteration were carefully handpicked under a binocular microscope. These selected crystals were leached twice ("cold chemical attack") with HCl to remove impurities, first with 0.1 mol/L in an ultrasonic bath for 30 min and then with 1 mol/L for 10 min. Subsequently, the samples were washed three times with Milli-Q® water. The mineral powders were produced manually using an agate mortar and pestle. Individual aliquots of the samples were used for Sr (0.05 g; without addition of spike) and Sm-Nd isotopic analysis (0.2 g; with addition of ca. 9 mg of mixed ^{149}Sm-^{150}Nd

spike). Sample digestion for both analyses followed the procedure described by Gioia and Pimentel (2000). Sr was separated using Eichrom SR-B100-S (100–150 μm) resin. Sm-Nd were separated in teflon columns in two steps: the first column procedure used cationic resin AG-50W-X8 (200–400 mesh) to separate the REEs, followed by Sm-Nd separation using anionic Eichrom LN resin (100–150 μm). Sm-Nd samples were loaded onto double Re filaments for the isotopic measurements. The data were corrected for mass fractionation by normalizing to $^{146}Nd/^{144}Nd = 0.7219$. The analyses of NBS-987 and BHVO-2 standards gave $^{87}Sr/^{86}Sr = 0.71032 \pm 2$ (n = 2, 2σ) and $^{143}Nd/^{144}Nd = 0.512981 \pm 5$ (n = 1, 2σ), respectively. Laboratory blanks values are Nd = 282.52 pg and Sm: 15.61 pg.

4.2.3.4.3 Noble gas isotopes (He, Ne and Ar)

The sample preparation for noble gas measurements included the disaggregation process by high voltage electric discharges (SELFRAG® Lab system) and the subsequent washing of samples with ultrapure acetone in an ultrasonic bath twice for 30 min at the University of Brasília. Five whole-rock samples were selected by careful handpicked under a binocular microscope to determine noble gas isotope ratios by using the crushing method at the Department of General Systems Studies, Graduate School of Arts and Sciences, the University of Tokyo. Samples with more than 1 g were crushed in a stainless-steel tube with a sequential number of strokes (100, 500, 1000, and 2000 times) using a nickel piston driven from outside the vacuum line by a solenoid magnet (Sumino et al., 2001). The analytical procedure for noble gas extraction by crushing was described in detail by Jalowitzki et al. (2016).

Based on the reproducibility of measurements of the Japanese helium standard (HESJ) and those of a calibrated air standard for other noble gases, the estimated experimental uncertainties for noble gas concentrations were <5% for He and Ar, and <10% for Ne. During Ne analysis,

corrections for $^{40}Ar^{++}$ on $^{20}Ne^{+}$ and CO_2^{++} on $^{22}Ne^{+}$ were applied following the method described by Osawa (2004) and were determined to be <5%. Uncertainties assigned to the observed isotopic ratios were one standard deviation (1σ), including blank and mass discrimination corrections. Blanks were run using the same procedure as the samples: $^{4}He =$ $(2–5)\times10^{-11}$ cm^3 STP; $^{20}Ne = (0.1–9)\times10^{-13}$ cm^3 STP; and $^{40}Ar = (7–9)\times10^{-10}$ cm^3 STP. Assuming the higher measured blank values obtained for He, Ne, and Ar, we estimated its contribution in our data. For ^{4}He, the blank contribution is <1.5%. The ^{20}Ne blank contribution ranges from 6 to 52% (most with <15%). For ^{40}Ar, the blank contribution is varying from 8 to 29% (most with <18%). Therefore, the He blanks confirm negligible atmospheric noble gas contribution.

4.2.4   Results

4.2.4.1   Petrography

Modal proportions of mineral phases from 16 Coyhaique mantle xenoliths were defined by point-counting and they were classified as anhydrous spinel-lherzolites (Fig. S1 and Tab. S2). The point-counting was carried out digitally by using the JMicroVision software (Roduit, 2007). For each sample were counted 2000-2800 points per thin section (each one with 24 x 40 mm). All xenoliths display protogranular texture (Fig. 2A-B), indicating low strain rates (Mercier and Nicolas, 1975). Fractures are identified in mineral boundaries and through them in all spinel-lherzolites. They are commonly associated with the formation of iddingsite, which mostly occurs in olivines and subordinately in pyroxenes. The contact between the xenolith and the host basalt is always sharp and well-defined, indicating negligible interaction among them (Fig. 2C).

Olivine (Ol) occurs as subhedral to anhedral grains and their size ranges from 0.8 to 4.8 mm in diameter. In all xenoliths, olivine grain boundaries are dominantly curvilinear. Many crystals present kink-bands, but no neoblasts were found (Fig. 2A-B). Locally, olivine contains spinel inclusions.

Orthopyroxene (Opx) grains are usually larger than olivine (2.0–11.0 mm in diameter), they are subhedral to anhedral. Most xenoliths display non-deformed orthopyroxene with curvilinear grain boundaries, with exception of samples PM25-08, PM25-09 and PM25-21 that present kink-bands. Several large orthopyroxene grains contain clinopyroxene exsolution lamellae and inclusions of olivine, clinopyroxene and spinel (Fig. 2D).

Clinopyroxene (Cpx) is emerald-green in color, and occurs as subhedral to anhedral grains with a diameter size between 0.2 to 3.0 mm. Usually, clinopyroxenes present spongy rims (Fig. 2E) and curvilinear grain boundaries in contact with other crystals (Fig. 2A and E).

Spinel (Sp) occurs randomly distributed as reddish brown to black crystals (Fig. 2A and C). They commonly occur interstitially and have elongated shapes with size varying from 0.1 to 1.6 mm. Locally, spinel contains olivine inclusions.

Fluid inclusions are observable in all silicate phases (Fig. 2A and F) but are mainly found in orthopyroxene and olivine, occurring as trails within larger crystals and near crystal boundaries, usually associated with fractures.
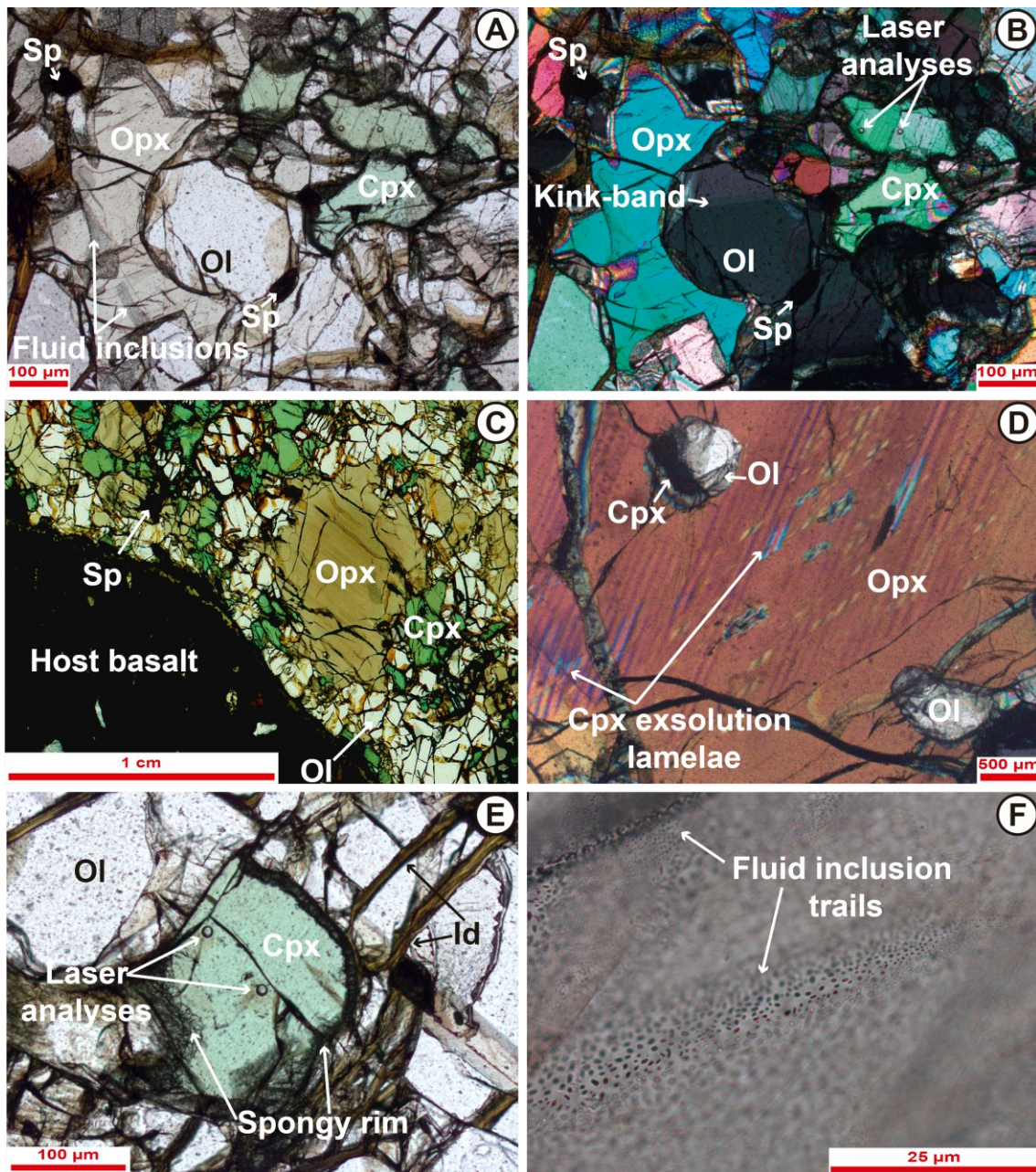
Figure 2. Photomicrographs of Coyhaique mantle xenoliths showing the main mineral assemblages and main textures. (A-B) Sample PM25-06 in plane- and crossed-polarized lights showing the protogranular texture with the representative mineralogy of spinel-lherzolites, with curvilinear grain boundaries and kink-bands in olivine; (C) Sharp contact between the xenolith (sample PM25-15) with the host basalt; scanned thin section with enhanced contrast; (D) Orthopyroxene with clinopyroxene exsolution lamellae and inclusions of olivine and clinopyroxene (extinct) (sample PM25-10). (E) Clinopyroxene spongy rims and iddingsite in

olivine fractures in sample PM25-06; (F) Fluid inclusion trails observed in orthopyroxene (sample PM25-04). Ol = olivine; Cpx = clinopyroxene; Opx = orthopyroxene; Sp = spinel; Id = iddingsite.

4.2.4.2 Whole-rock geochemistry

Major and trace element whole-rock contents and loss on ignition (LOI) data of 8 new spinel-lherzolite samples are presented in Table S4. For comparison, the previous results of 17 spinel-lherzolites from Coyhaique (Jalowitzki et al., 2017) are integrated into this work for a broader discussion. Our samples (8 selected from Jalowitzki et al., 2017 and 8 inedited) show lower SiO_2 content (43.39–44.58 wt.%), and higher MgO (38.01–45.14 wt.%) and magnesium number [Mg# = Mg/(Mg + Fe$_{Total}$×0.9)×100] (88.67–91.15) compared to the primitive mantle (PM; SiO_2 = 45.00 wt.%, MgO = 37.80 wt.%, and Mg# = 90.40; McDonough and Sun, 1995) and depleted MORB mantle (DMM; SiO_2 = 44.71 wt.%, MgO = 38.73 wt.%, and Mg# = 90.70; Workman and Hart, 2005). Furthermore, CaO, Al_2O_3, TiO_2, and Na_2O correlate negatively with MgO, defining linear trends (r² = 0.84–0.94) (Fig. S2, see details in the figure caption). Although Ni contents (in ppm) plot scattered (r^2 = 0.42), they display a positive correlation with MgO. These patterns indicate different degrees of partial melting. Comparatively, CaO (0.93–2.36 wt.%) and Al_2O_3 (1.19–3.09 wt.%) contents of our new samples are similar or lower than that reported by Jalowitzki et al. (2017) (2.43–3.29 wt.% and 2.69–3.86 wt.%, respectively), which could be related to the different modal proportion of clinopyroxene and spinel. Our samples show Cpx/Opx average ratios of 0.37 and spinel modal percent of 2.0% (Tab. S3), whereas the previous data show higher values (0.65 and 3.2%, respectively), which attest to the refractory character of these new samples.

In the primitive mantle (PM; Sun and McDonough, 1989) normalized multi-element diagram, all samples from Coyhaique display similar patterns with enrichment in LILE (e.g., Cs, U) and chalcophile elements (e.g., W, Pb, and Sn), and strong negative anomalies of Ba, Nb, Ta, and Ti (Fig. 3A). Cs, Rb, Sr and Zr vary from positive to negative anomalies. In the PM-normalized rare earth elements (REEs) diagram, three different patterns (Fig. 3B): 1) light-REE (LREE) enrichment ($La/Yb_N = 1.11–3.07$; n = 9); 2) flat REE distribution ($La/Yb_N = 0.93–1.08$; n = 4), and 3) LREE depletion ($La/Yb_N = 0.50–0.62$; n = 3). Samples reported by Jalowitzki et al. (2017) (gray field and black lines in Figure 3A-B) show heavy-REE (HREE) concentrations similar or slightly higher values when compared to the PM. Except for sample PM25-16, all new samples show depleted HREE concentrations compared to DMM (red lines in Figure 3B). Our new spinel-lherzolites have strong negative Nb anomalies [$Nb/Nb^* = 0.04–0.27$; $Nb/Nb^* = Nb_N/(Th_N \times La_N)^{1/2}$], and low Ce/Pb (5.18–12.88) and Nb/U (0.88–4.32) ratios, similar to the samples reported by Jalowitzki et al. (2017) ($Nb/Nb^* = 0.05–0.35$; Ce/Pb commonly <15; Nb/U <5). They show similar trace element ratios when compared to Chile Trench sediments (CTS; Lucassen et al., 2010), for example, Ba/Th (12.24–171.46; CTS = 96.62), U/Th (0.25–0.99; CTS = 0.46), Sr/Th (37.04–273.35; CTS = 76.80) and Pb/Th (0.28–2.62; CTS = 2.86).
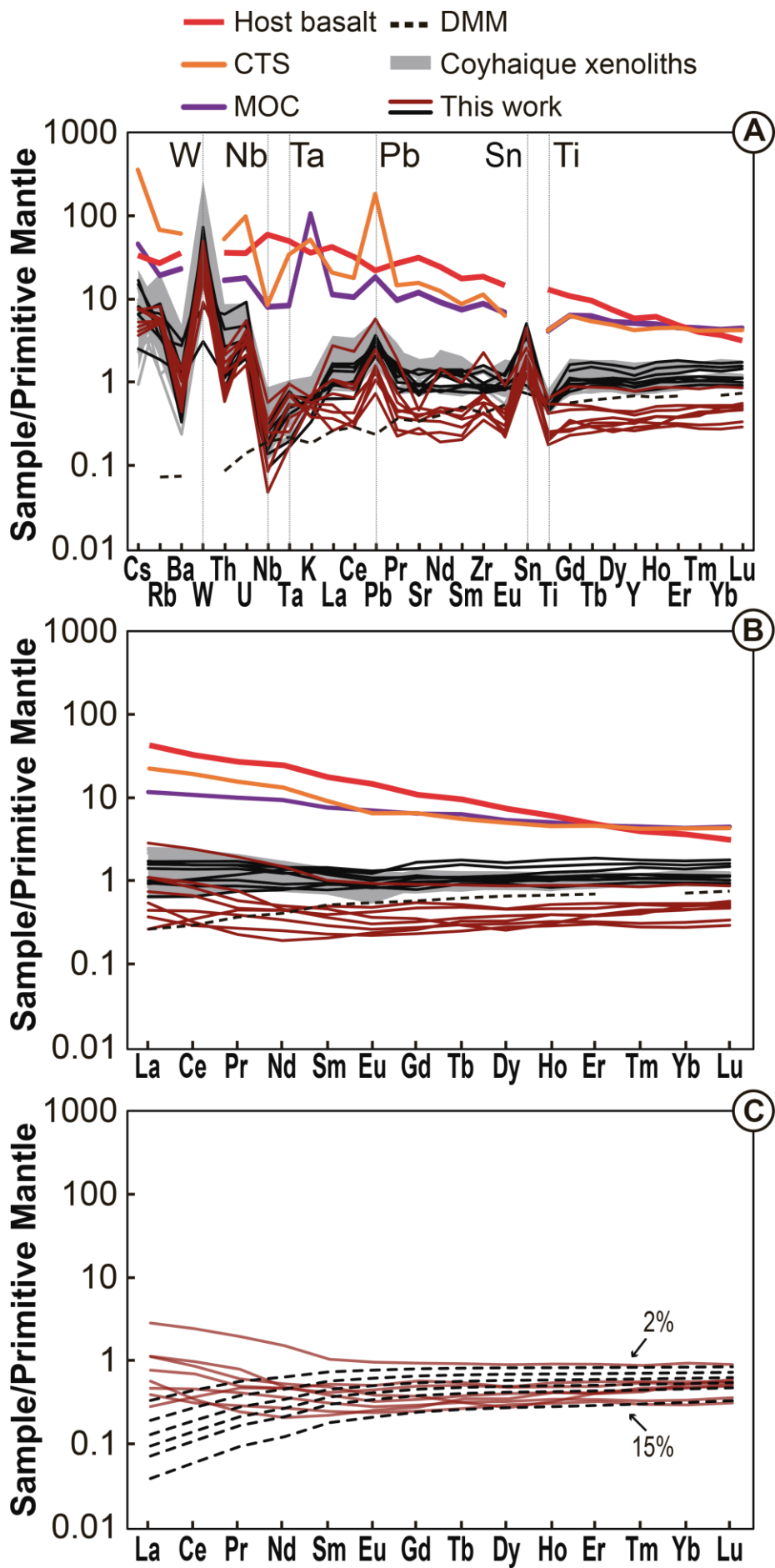
Figure 3. Whole-rock trace and REE elements of spinel-lherzolites normalized to the primitive mantle (Sun and McDonough, 1989). Multi-element diagram (A) and REE diagrams (B-C). This work samples are represented by red lines. For comparison, samples from Jalowitzki et al. (2017) that do not contain mineral chemistry data are plotted in the gray field, and black lines represent samples studied in detail in this work that were published by these authors. Host basalt (Jalowitzki et al., 2017), Chile Trench sediments average (CTS; Lucassen et al., 2010), modified oceanic crust (MOC; Chile Ridge Segment 3 metabasalt, sample D42-4; Klein and Karsten, 1995), and depleted MORB mantle (DMM; Workman and Hart, 2005) are also plotted for comparison. Whole-rock partial melting degree estimates (C) were obtained by applying the non-modal batch melting equation of Shaw (2006). Primitive mantle REE composition (Sun and McDonough, 1989) and mineralogy ($Ol_{0.56}$ + $Opx_{0.22}$ + $Cpx_{0.19}$ +$Sp_{0.03}$; McDonough, 1990) as source (starting material). Melt modes are those proposed by Johnson (1998) for spinel stability field ($Ol_{-0.06}$ + $Opx_{0.28}$ + $Cpx_{0.67}$ +$Sp_{0.11}$). Mineral/melt partition coefficients are from Ionov (2002). Each dashed line indicates the percentage of partial melting as follows: 2%, 4%, 6%, 8%, 10%, and 15%.

4.2.4.3   Mineral geochemistry

Mineral chemistry measurements were determined for olivine, orthopyroxene, clinopyroxene, and spinel crystals (Tab. 1, Fig. 4A-D and Fig. 5A-D). Major and trace elements mineral data are given in Table S5. No significant core-rim variations (<5%) were observed in any mineral phase in terms of major oxides (e.g., MgO, FeO), therefore, only core average compositions are shown in the major element diagrams. Moreover, no relevant core and rim variations were observed in terms of trace element contents and, therefore, we assumed the average value of laser analyses as representative of each sample. Data plotted for comparison include spinel-

peridotites related to continental arc tectonic setting from Patagonia [Agua Poca (Bertotto et al., 2013), Cerro del Fraile (Faccini et al., 2013; Kilian and Stern, 2002; Rivalenti et al., 2004), Cerro de los Chenques (Dantas et al., 2009; Rivalenti et al., 2007, 2004), Chile Chico (Schilling et al., 2017, 2008), and Tres Lagos (Ntaflos et al., 2007; Rivalenti et al., 2004)] and Western North America [south-central British Columbia, Canadian Cordillera (Greenfield et al., 2013), Mojave Desert, North American Cordillera (Luffi et al., 2009), southern Canadian Cordillera (Peslier et al., 2002), and northern Canadian Cordillera (Shi et al., 1998)] (Fig. 4A-D).

4.2.4.3.1 Olivine and spinel

Olivines are forsterite ($Fo_{86.6-91.2}$) and have average Mg# of 89.62 [Fig. 4A; Mg# = $Mg/Fe_{Total}+Mg)\times100$]. Sample PM25-42 shows anomalous low Mg# contents (Fo = 86.6–88.6; Mg# = 86.83–88.71). NiO and CaO average contents are 0.34–0.40 wt.% and 0.07–0.12 wt.%, respectively. In PM-normalized multi-element diagram, strongly positive anomalies of Pb and Li are observed in all olivines (Fig. 5A). Regarding the REE diagram, olivines show depleted pattern related to PM (<1) with LREE<HREE (Ce/Yb_N = 0.01–0.03) (Fig. 5B).

The aluminum phase of our samples is classified as **Al-spinel** due its low Cr# [8.96–24.66; where Cr# = $100\times(Cr/Cr+Al)$] and high Al_2O_3 contents (45.99–56.82 wt.%). Figure 4A shows that our samples resemble the Fo–Cr# (Arai, 1994) field composed by continental arc-related spinel peridotites from Patagonia and Western North America (i.e., Canadian and North American Cordillera). All analyzed crystals fall into the olivine-spinel mantle array (OSMA) in the Fo–Cr# diagram (Arai, 1994), with exception of sample PM25-42 that defines a metasomatic trend because of its low Mg# and Fo (Fig. 4A).

4.2.4.3.2 Orthopyroxene

Orthopyroxenes are enstatite ($En_{86.0-90.2}Fs_{8.5-12.0}Wo_{1.2-2.2}$) and display a narrow range of Mg# (87.74–91.71), which correlates positively and linearly ($r^2 = 0.86$) with the Mg# of coexisting clinopyroxene (Fig, 4B), indicating equilibrium between the two pyroxenes. The Al_2O_3 concentration is variable (3.14–5.15 wt.%) and decrease with progressive increase of Mg# (Fig. 4C). As observed in Figure 4A, our samples have strong affinity with peridotites from Patagonia, Canadian Cordillera, and North American Cordillera (Fig. 4C). Sample PM25-42 has A different pattern than the other orthopyroxenes from Coyhaique lherzolites (Fig. 4C), as observed in the olivine-spinel diagram (Fig. 4A). The compositional trend defined by this sample in Al_2O_3 vs. Mg# (Opx and Cpx, latter is not shown) is similar to that shown by metasomatized spinel-lherzolites from Rayfield River and Big Timothy Mountain, southern British Columbia, Canadian Cordillera (Greenfield et al., 2013). CaO and TiO_2 contents show narrow ranges (0.72–1.05 wt.% and 0.06–0.20 wt.%, respectively; Tab. S5). Orthopyroxene trace element compositions display positive anomalies of U, Pb, Zr, Hf, Ti, and Li coupled with Sr negative anomalies in the multi-element PM-normalized diagram (Fig. 5A). The negative Nb-Ta anomalies observed in whole-rock (Fig. 3A) and clinopyroxene (Fig. 5C) samples are not observed in orthopyroxenes due to their low concentrations of LREE (e.g., La and Ce) concentrations (Fig. 5A). Orthopyroxenes show a gradual decrease from HREE toward LREE in PM-normalized REE diagram for all samples, which implies depletion processes ($Ce/Yb_N <$ 0.08). Two clinopyroxene exsolutions within orthopyroxene were analyzed in PM25-16 sample. Clinopyroxene exsolutions differ from the crystals because they show Sr negative anomalies, Zr and Ti positive anomalies, and lower REE concentrations (see cyan lines in Fig. 5A-D).

4.2.4.3.3 Clinopyroxene

Clinopyroxenes are diopside ($En_{49.1-51.5}Wo_{42.9-46.4}Fs_{4.4-6.5}$) with Mg# ranging from 87.12 to 91.91. They show intermediate CaO contents (18.70–20.72 wt.%) and Ca/Al ratios (2.40–4.39), higher than chondritic values (1.1; McDonough and Sun, 1995), with moderate to high Cr_2O_3 (0.72–1.49 wt.%) and low TiO_2 (0.2–0.7 wt.%) contents. The high Al_2O_3 contents (4.29–7.26 wt. %) has negative correlation with clinopyroxene CaO (Fig. 4D), Mg#, and spinel Cr# (not shown), suggesting variable degrees of melt extraction. In the CaO vs. Al_2O_3 diagram, Coyhaique clinopyroxenes plot in the same trend defined for peridotites from Patagonia and Western North America (Fig. 4D). However, in general, our samples have lower CaO contents for a given Al_2O_3, showing higher affinity with Agua Poca, Cerro de los Chenques, Chile Chico, Tres Lagos, and with higher Al_2O_3 and lower CaO peridotites from Western North American (Fig. 4D). Samples from Cerro del Fraile contain higher CaO values than most Patagonian peridotites. As observed in orthopyroxene, clinopyroxenes of sample PM25-42 have lower Mg# with respect to similar Al_2O_3. In general, Coyhaique clinopyroxenes are strongly depleted in Ba, with negative anomalies of Pb, HFSE (Nb, Ta, Zr, Hf, and Ti), and positive U and Li anomalies in the PM-normalized multi-element diagram (Fig. 5C). Moreover, our peridotites show low $Nb/Nb^* = 0.02–1.00$, $Zr/Zr^* = 0.33–0.91$, and $Ti/Ti^* = 0.10–0.60$ [where $Nb/Nb^* = Nb_N/(U_N \times La_N)^{1/2}$), $Zr/Zr^* = Zr_N/(Sm_N \times Hf_N)^{1/2}$), and $Ti/Ti^* = Ti_N/(Eu_N \times Gd_N)$)] (Tab. 1 and Fig. 5C). As exceptions, sample PM25-16 displays positive Zr and Hf anomalies in the multi-element diagram while samples PM25-06, PM25-10, and PM25-13 show Nb/Nb* higher than 1 (1.11–1.24), and sample PM25-02 shows Zr/Zr* higher than 1 (1.10). Li (4.51–20.22 ppm) and B (0.36–0.68 ppm) concentrations are higher compared to clinopyroxenes of the MORB mantle source (1.6–1.8 and 0.07–0.10 ppm, respectively; Ottolini et al., 2004). According to REE patterns, two clinopyroxene groups were identified: Type-1 comprises most of the samples (n=12) with depleted REE patterns (LREE<HREE; La/Yb_N = 0.23–0.63; green lines in Figure 5D), and Type-2 comprises four samples (pink lines in Figure 5D) with enriched patterns

(LREE>HREE; La/Yb$_N$ = 1.35–3.48). The pattern of middle-REE (MREE) to HREE is flat (Ho/Yb$_N$ = 0.93–1.27).
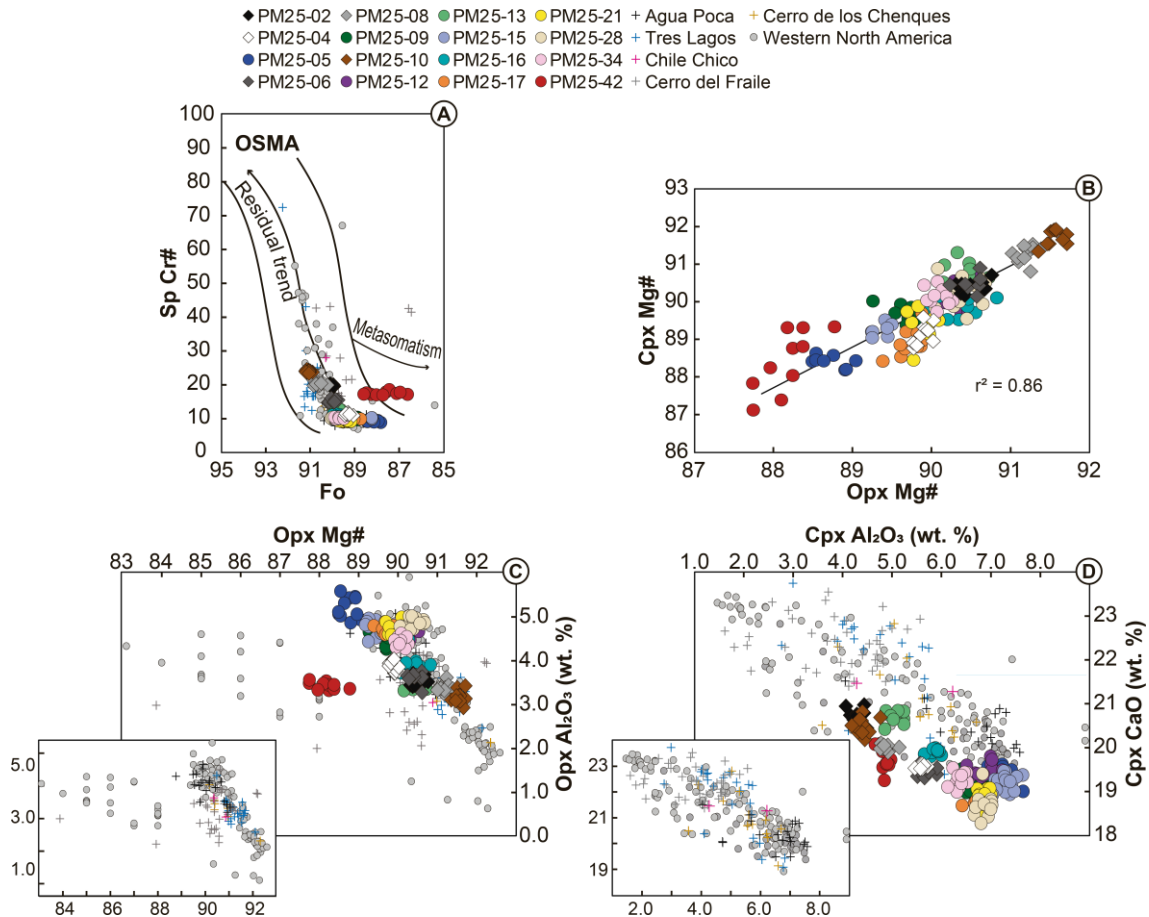
Figure 4. Major element trends (core averages) for silicates and spinel of Coyhaique xenoliths. (A) Spinel Cr# versus olivine Fo, samples are within the olivine spinel mantle array (OSMA), metasomatism and residual trend for spinel peridotites are from Arai (1994); (B) positive correlation between Mg# of Cpx and Opx; (C) negative correlation between Opx Al$_2$O$_3$ versus Mg#; (D) negative correlation between Cpx Al$_2$O$_3$ versus CaO. Reference data are for Patagonia localities [Agua Poca (Bertotto et al., 2013), Tres Lagos (Ntaflos et al., 2007; Rivalenti et al., 2004), Chile Chico (Schilling et al., 2017, 2008), Cerro del Fraile (Faccini et al., 2013; Kilian and Stern, 2002; Rivalenti et al., 2004), and Cerro de los Chenques (Rivalenti et al., 2007, 2004)]; and for Western North America (Greenfield et al., 2013; Luffi et al., 2009; Peslier et

al., 2002; Shi et al., 1998). Smaller diagrams in C and D present literature data without our samples plotted for better visualization. Samples represented by diamonds are those selected for noble gas isotopes measurements. Fo = forsterite; Cpx = clinopyroxene; Opx = orthopyroxene; Sp = spinel.
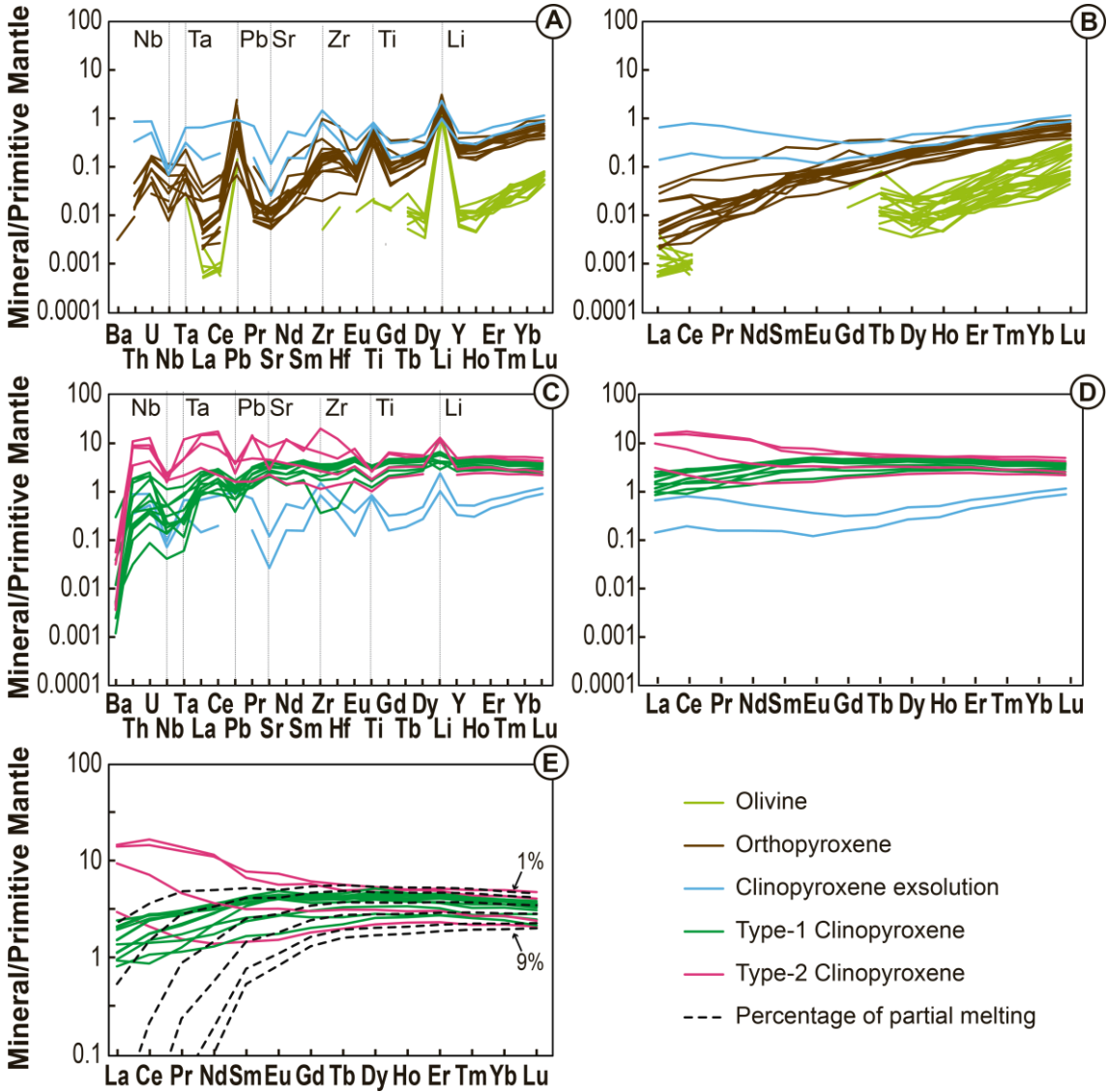
Figure 5. Primitive mantle (Sun and McDonough, 1989) normalized multi-element and REE diagrams for olivine and orthopyroxene (A-B), and clinopyroxene (C-D). Two clinopyroxene exsolutions in orthopyroxene (A-D) from sample PM25-16 are shown in cyan. Partial melting estimates (E) for clinopyroxene were obtained by applying the non-modal fractional melting

equation of Johnson et al. (1990). Coyhaique whole-rock spinel-lherzolite average composition and mineralogy ($Ol_{0.58}$ + $Opx_{0.26}$ + $Cpx_{0.13}$ + $Sp_{0.03}$) were assumed as the source composition (or starting material). Each dashed line indicates the percentage of partial melting as follows: 1%, 2%, 4%, 6%, 8%, and 9%. The melt modes and mineral/melt partition are the same as in Figure 3.

4.2.4.3.4   Geothermobarometry

Geothermobametry estimates were calculated only with mineral core data. The similar Mg# (ca. 90) for all silicate phases, positive correlation between two pyroxenes Mg# (Fig. 4B), as well as minimal clinopyroxene exsolution lamellae in orthopyroxene, attest equilibrium between all mineral phases. Although sample PM25-42 records lower values of Mg#, this lherzolite preserve the same consistency of equilibrium described above. The temperature estimates were calculated using the two-pyroxene (Brey and Köhler, 1990) and single-pyroxene (Ca in orthopyroxene from Köhler and Brey, 1990) geothermometers (Tab. 1). The temperature estimates were calculated with the PTEXL program developed by Thomas Köhler and updated by Thomas Stachel. For these calculations, a preset pressure of 15 kbar was assumed. In addition, the single-pyroxene (Mercier, 1980), and the two-pyroxene REE and Y geothermometers, (Liang et al., 2013) were applied (Tab. 1). Major element thermometers resulted in an interval between 886 and 1150 °C, which is consistent with results obtained from the REE and Y two-pyroxene thermometer (978–1135 °C; Liang et al., 2013). These temperatures are also compatible with those reported by Schilling et al. (2017) for samples PM25-08 and PM25-10 (1057 and 1040 °C, respectively). Pressure estimates were obtained using the barometer of Mercier (1980) that considers only clinopyroxene composition. Coyhaique spinel-lherzolites yield pressure estimates ranging from 1.06 to 1.90 GPa, corresponding to depths between 35 and 63 km. These estimations are situated close to the

lower crust and lithospheric mantle boundary. The present-day Mohorovičić discontinuity, based on geophysical data (Rodriguez and Russo, 2020), is situated at 35.6 ± 5.4 km under the Coyhaique area. The method employed for this approximation was the H-k Bootstrapping estimate, which considers integrated data from neighborhood stations. Crustal thicknesses were determined by the LAPO station (45°42'S–71°49'W) that is located approximately 8 km from the Coyhaique area. Although samples PM23-13 (37 km) and PM25-16 (35 km) show depth estimates lower than 40 km, they are consistent with the crustal thickness uncertainty for the studied area. Moreover, based on LAPO single station (H-k estimate), the crustal thickness under Coyhaique area is 33.9 km. It is important to consider that this station has a robust results due to the high quantity of seismic traces to generate the receiver function (RFs = 23; Rodriguez and Russo, 2020).

Sample	Olivine			Spinel		Orthopyroxene		Clinopyroxene						Geothermobarometers				
	Mg#	Li	$(Ce/Yb)_N$	Cr#	Mg#	Mg#	$(Ce/Yb)_N$	Mg#	Li	Nb/Nb*	Zr/Zr*	Ti/Ti*	$(La/Yb)_N$	T_{REE} (L_{13})	T_{2Px} (BK_{90})	T_{Cpx} (M_{80})	$T_{Ca-in-Opx}$ (BK_{90})	P_{Cpx} (M_{80})
PM25-02	90.23	-	-	19.91	73.18	90.57	0.05	90.23	-	0.27	1.10	0.68	1.35	1103 ± 43	1007	1125	1069	1.90
PM25-04	89.46	-	-	11.38	75.49	89.87	0.08	89.46	-	0.04	0.33	0.11	3.25	1135 ± 69	983	1123	1017	1.73
PM25-05	88.39	1.96	0.02	9.26	75.39	88.78	0.02	88.39	6.07	1.00	0.42	0.34	0.39	1095 ± 37	1075	1110	1027	1.39
PM25-06	90.04	-	-	15.31	76.34	90.47	-	90.04	-	1.11	0.44	0.20	0.62	-	1010	1111	1014	1.67
PM25-08	90.75	1.78	0.03	20.36	75.89	91.18	0.01	90.75	6.49	0.49	0.70	0.27	0.39	977 ± 50	926	1023	1000	1.27
PM25-09	89.16	1.82	0.02	10.11	77.31	89.72	0.02	89.16	10.26	0.11	0.49	0.39	0.59	1035 ± 27	1095	1108	1015	1.47
PM25-10	91.13	-	-	24.06	75.31	91.49	0.05	91.13	-	1.13	0.66	0.84	0.51	1001 ± 34	949	1031	1010	1.38

Table 1. Summary of mineral data of studied samples. Mineral data are based on average values. Li concentrations are in ppm. Temperatures estimates (°C) were calculated assuming a pressure of 15 kb. Geothermometers are: REE-in-two-pyroxene (T_{REE}; Liang et al., 2013); two-pyroxene (T_{2Px}; Köhler and Brey, 1990); Ca in orthopyroxene ($T_{Ca-in-Opx}$; Brey and Köhler, 1990); and single-pyroxene (T_{Cpx}; Mercier, 1980). Geobarometer (GPa) were determined by single-pyroxene (P_{Cpx}; Mercier, 1980). Sample PM25-06 lack orthopyroxene trace element data, therefore, do not have T_{REE} estimate.

Sample	Olivine			Spinel		Orthopyroxene		Clinopyroxene						Geothermobarometers				
	Mg#	Li	$(Ce/Yb)_N$	Cr#	Mg#	Mg#	$(Ce/Yb)_N$	Mg#	Li	Nb/Nb*	Zr/Zr*	Ti/Ti*	$(La/Yb)_N$	T_{REE} (L_{13})	T_{2Px} (BK_{90})	T_{Cpx} (M_{80})	$T_{Ca\text{-}in\text{-}Opx}$ (BK_{90})	P_{Cpx} (M_{80})
PM25-12	89.75	1.52	0.01	10.12	78.70	90.23	0.01	89.75	4.51	0.74	0.47	0.32	0.30	1021 ± 20	1067	1095	998	1.40
PM25-13	89.93	2.87	-	12.66	76.84	90.37	0.01	89.93	19.32	1.24	0.91	1.55	0.29	971 ± 39	887	995	976	1.13
PM25-15	88.39	2.17	0.02	10.18	76.29	89.49	0.02	88.39	8.86	0.06	0.44	0.32	0.51	1036 ± 27	1065	1095	992	1.35
PM25-16	89.92	1.97	0.02	11.01	77.73	90.40	0.08	89.92	20.22	0.02	0.48	0.02	2.93	992 ± 64	886	992	1017	1.06
PM25-17	89.34	1.96	-	10.27	76.55	89.73	0.02	89.34	9.17	0.53	0.40	0.49	0.29	1061 ± 16	1081	1150	1032	1.70
PM25-21	89.59	1.56	-	9.29	77.21	89.91	0.02	89.59	10.42	0.81	0.40	0.36	0.38	1052 ± 21	1079	1133	1014	1.60
PM25-28	90.04	2.38	0.01	10.18	78.64	90.40	0.02	90.04	6.55	0.43	0.48	0.27	0.63	1054 ± 33	1133	1140	1013	1.60
PM25-34	89.84	1.56	0.02	10.33	77.58	90.11	0.005	89.84	9.54	0.99	0.49	1.19	0.23	1023 ± 21	1067	1103	996	1.52
PM25-42	87.88	2.59	-	17.55	69.49	88.16	0.07	87.88	17.44	0.05	0.72	0.23	3.48	1011 ± 50	986	1129	1024	1.87

Table 1. Continued.

4.2.4.4 Sr-Nd isotopes

Measured Sr–Nd isotopic ratios of whole-rock (samples PM25-02, PM25-04, PM25-06, PM25-08, PM25-10, PM25-13, and PM25-16) and of separated clinopyroxenes (PM25-02, PM25-04, PM25-05, PM25-06, PM25-08, PM25-09, PM25-10, PM25-12, PM25-13, PM25-16, PM25-21, PM25-28, PM25-34) from Coyhaique spinel-lherzolites are given in Table S6. The new whole-rock $^{87}Sr/^{86}Sr$ (0.702347–0.703198) and $^{143}Nd/^{144}Nd$ (0.512940–0.513159; $\varepsilon Nd = 5.89$–10.17) isotopic ratios show a narrow range when compared to previous data ($^{87}Sr/^{86}Sr =$ 0.702422–0.704239 and $^{143}Nd/^{144}Nd =$ 0.512859–0.513242; Jalowitzki et al. 2017). Clinopyroxene separates (n = 13) display a narrow isotopic variation, with $^{87}Sr/^{86}Sr$ between 0.70200 and 0.70403, and $^{143}Nd/^{144}Nd$ between 0.513022 and 0.513632 ($\varepsilon Nd = +7.50$ to +19.39) (Tab. S6). All studied samples display a distribution trend from the depleted mantle (DM; Hart et al., 1992; Workman and Hart, 2005) field, or from an even more depleted composition, towards lower Nd and higher Sr ratios, close to HIMU reservoir (Hart et al., 1992). This trend is similar to that defined by depleted (LREE<HREE) and flat (LREE~HREE) samples reported by Jalowitzki et al. (2017). However, new whole-rock isotopic results reveal different distribution patterns, with the majority of samples being characterized by LREE enrichment (La/Yb$_N$ = 1.33–3.07; PM25-02, PM25-04, PM25-08, PM25-10, and PM25-16), or flat patterns (La/Yb$_N$ = 1.08; PM25-13). Although sample PM25-06 has depleted REE pattern (La/Yb$_N$ = 0.5), it notably contains one of the more enriched Sr isotopic ratio considering the new set of whole-rock Coyhaique spinel peridotites ($^{87}Sr/^{86}Sr$ = 0.703192).

Clinopyroxene Sr-Nd data from Patagonia were plotted for comparison (e.g., Mazzucchelli et al., 2016; Melchiorre et al., 2020; Rivalenti et al., 2007; Stern et al., 1999). Coyhaique samples show strong similarity with the depleted composition range of Tres Lagos group 1 clinopyroxenes (Mazzucchelli et al., 2016) and with Chile ridge basalts (Bach et al., 1996;

Sturm et al., 1999) (Fig. 6). Clinopyroxenes from Cerro de los Chenques (Melchiorre et al., 2020; Rivalenti et al., 2007) and Pali-Aike Volcanic Field display similar to enriched compositional range (Melchiorre et al., 2020; Stern et al., 1999) (Fig. 6). In general, clinopyroxenes from Cerro Clark, Cerro del Fraile, Estancia Sol de Mayo, Gobernador Gregores (Melchiorre et al., 2020); and Group 2 clinopyroxene samples from Tres Lagos (Mazzucchelli et al., 2016) have higher Sr coupled with lower Nd compared to our samples (Fig. 6).
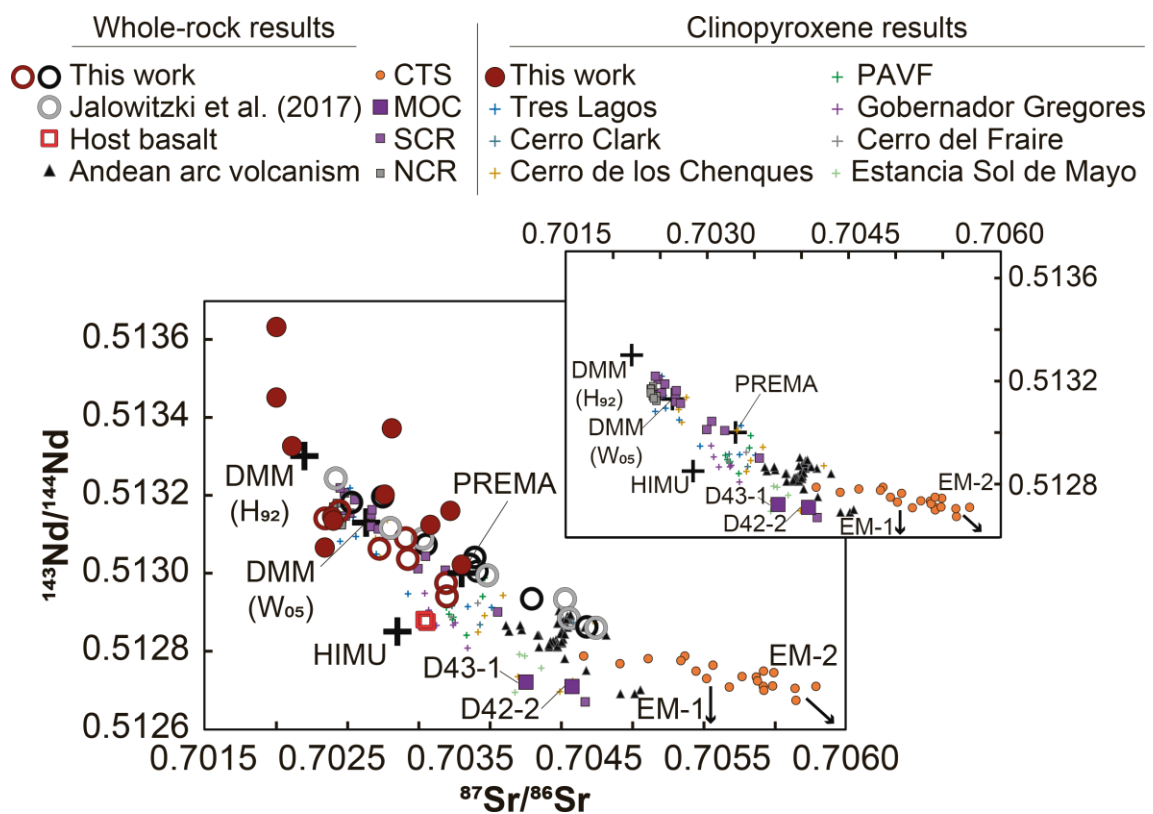
Figure 6. Whole-rock and clinopyroxene Sr-Nd data from Coyhaique spinel-lherzolites. This study new whole-rock samples are in red open circles and clinopyroxene data are represented by red circles. Whole-rock samples from Jalowitzki et al. (2017) that do not contain mineral

chemistry data are plotted in gray open circles, and black open circles represent whole-rock samples studied in detail in this work that were published by these authors. Clinopyroxene data from Patagonia were plotted for comparison [Cerro Clark (Melchiorre et al., 2020); Cerro de los Chenques (Melchiorre et al., 2020; Rivalenti et al., 2007); Cerro del Fraile (Melchiorre et al., 2020); Estancia Sol de Mayo (Melchiorre et al., 2020); Gobernador Gregores (Melchiorre et al., 2020); Pali-Aike Volcanic Field (PAVF; Melchiorre et al., 2020; Stern et al., 1999); Tres Lagos (Mazzucchelli et al., 2016)]. Host basalt (Jalowitzki et al., 2017); Chile Trench sediments (CTS; Lucassen et al., 2010); Southern Chile Ridge basaltic glasses [SCR; samples D42-2 and D43-1 represent modified oceanic crust (MOC) from Segment 3; Sturm et al., 1999]; Northern Chile Ridge (NCR; Bach et al., 1996); and mantle reservoirs (Hart et al., 1992; Workman and Hart, 2005).

4.2.4.5 Noble gas isotopes (He, Ne and Ar)

4.2.4.5.1 Helium

The ^{3}He/^{4}He isotope ratios and the ^{4}He concentrations are presented in Table 2. According to petrographic observations (see Fig. 2F), olivine and pyroxene crystals of Coyhaique lherzolites contain abundant fluid inclusions. It is well known that fluid inclusions retain noble gases, which are powerful tracers to investigate the mantle source of different geological processes (e.g., Gautheron et al., 2005).

Helium concentrations [^{4}He] show a range from 4.1 to 67.1 $\times$ 10^{-9} cm^3 STP/g, and ^{3}He/^{4}He ratios are strongly radiogenic (0.20–2.52 R$_A$, where 1 R$_A$ corresponds to atmospheric ratio of 1.4 $\times$ 10^{-6}; Ozima and Podosek, 1983). Although ^{3}He/^{4}He ratios display a negative correlation with the increase of ^{4}He concentration (Fig.7), our samples show consistent ^{3}He/^{4}He ratios, without significant variation with an increasing number of strokes during stepwise crushing.

Sample PM25-06 shows the extreme radiogenic ^{3}He/^{4}He ratios, varying from 0.20 ± 0.01 to 0.44 ± 0.02 R$_A$. The least radiogenic analyzed sample is PM25-08, with ^{3}He/^{4}He ratios varying from 1.52 ± 0.08 to 1.90 ± 0.12 R$_A$. Sample PM25-02 shows the highest ^{3}He/^{4}He ratio (2.52 R$_A$; not shown). However, this data was obtained by 100 times strokes and might reflect some cosmogenic contribution due to the slightly lower He concentration ([^{4}He] $= 4.4 \times 10^{-9}$ cm^3 STP/g) compared with the other measurements ([^{4}He] $= 5.0$–8.3×10^{-9} cm^3 STP/g). The narrow range of ^{3}He/^{4}He isotope ratios obtained in the next number of strokes for this sample (1.49–1.61 R$_A$) corroborate this interpretation. It is expected that ^{3}He/^{4}He ratios lower than the MORB (8 ± 1 R$_A$; Sarda et al., 1988; Moreira and Allègre, 1998) and SCLM (6 ± 1 R$_A$; Gautheron and Moreira, 2002; Jalowitzki et al., 2016) reservoirs imply in enrichment of ^{4}He due to U and Th radioactive decay. Therefore, ratios higher than 6.0 R$_A$ were not considered in this study because they likely do not represent an arc component. Comparing the noble gas signature of Coyhaique lherzolites with available noble gas data from Pali-Aike Volcanic Field (6.87 ± 0.03 R$_A$; Jalowitzki et al., 2016) and Gobernador Gregores (7.27 ± 0.10 R$_A$; Jalowitzki et al., 2016), these new results represent the lowest ^{3}He/^{4}He values found for Patagonia so far. The He isotope results presented here are significantly more radiogenic when compared with mantle xenoliths from the Cascades volcanic arc (Western North America) that have been associated with ^{4}He-rich melt or fluid interaction (^{3}He/^{4}He $= 4.14$–4.86 R$_A$, Dodson and Brandon, 1999) (Fig. 7). Our samples are also equivalent or slightly more radiogenic than basaltic andesite phenocrysts (olivine and clinopyroxene, ^{3}He/^{4}He $= 0.18$–5.39 R$_A$, average 3.40 R$_A$) (Fig. 7) and water/gas of hot springs (^{3}He/^{4}He $= 0.07$–5.19 R$_A$, average 2.33 R$_A$) (not shown due to the high ^{4}He concentration) from Andean Cordillera (Hilton et al., 1993). In the same way, the radiogenic Chile Ridge MORB glasses from Segment 3 show ^{3}He/^{4}He ratios ranging from 3.51 to 4.39 R$_A$ (Sturm et al., 1999) (Fig. 7). Sample PM25-06 has ^{3}He/^{4}He ratios (0.20–0.44 R$_A$) similar to the highly radiogenic exhumed mantle wedge peridotites from the Italian Alps reported by

Matsumoto et al. (2005) (0.15–0.69 R_A) (Fig. 7). However, Italian samples have much higher He concentrations (^{4}He = 0.18–2.89 × 10^{-6} cm^3 STP/g) than our samples. Except for sample PM25-06, the others have similar radiogenic ^{3}He/^{4}He ratios (1.17–1.90 R_A) when compared to those reported by Sumino et al. (2010) (1.26–2.78 R_A) for exhumed mantle wedge peridotites from Sanbagawa metamorphic belt, SW Japan (Fig. 7). Yamamoto et al. (2004) presented radiogenic ^{3}He/^{4}He isotopic ratios of olivine and pyroxene (Opx and Cpx) concentrates from Far Eastern Russia spinel-lherzolites. However, the available ^{3}He/^{4}He ratios obtained by the crushing extraction method have extremely high uncertainties (see Table 2 of Yamamoto et al., 2004) which makes these results less reliable. For this reason, we decided to compare our He data with selected spinel-lherzolite samples from Far Eastern Russia, analyzed by stepwise heating extraction considering their uncertainties and avoiding the cosmogenic contribution. Thus, data from two olivine separate samples (Sv-1 and Fev-1) and one clinopyroxene (En21) were plotted for comparison in Figure 7 (^{3}He/^{4}He = 0.26–2.83 R_A; Yamamoto et al., 2004). These results are in the same interval as the Coyhaique lherzolites (0.20–1.90 R_A). Moreover, ^{3}He/^{4}He ratios define negative correlation with whole-rock ^{87}Sr/^{86}Sr and positive correlation with ^{143}Nd/^{144}Nd (Fig. S3). Conversely, ^{3}He/^{4}He ratios correlate negatively with clinopyroxene ^{143}Nd/^{144}Nd and positively with ^{87}Sr/^{86}Sr (Fig. S3), except for the sample PM25-06, which display the more radiogenic ^{143}Nd/^{144}Nd and ^{3}He/^{4}He ratios. Sample PM25-06 shows the expected correlation between whole-rock Sr-Nd against He isotopes, which is inconsistent with their REE depleted pattern (La/Yb$_N$ = 0.5).

4.2.4.5.2 Neon and argon

The majority of Ne isotopic data do not differ from air composition (^{20}Ne/^{22}Ne$_{air}$ = 9.80; ^{21}Ne/^{22}Ne$_{air}$ = 0.029; Ozima and Podosek, 1983) within 1σ analytical uncertainties. However,

neon isotope compositions of some samples present lower $^{20}Ne/^{22}Ne$ ratios (9.45–9.72) and ^{21}Ne excess ($^{21}Ne/^{22}Ne$ = 0.0286–0.0308) compared to the global MORB source data (Moreira et al., 1998; Sarda et al., 1988) (Fig. S4). Considering that there is no evidence of a cosmogenic ^{3}He component in our samples except the first crushing step of PM25-02, we assume that the observed excess of ^{21}Ne in Coyhaique fluid inclusions is nucleogenic in origin, which is supported by applying the crushing method in order to minimize the contribution from nuclides in the mineral lattice.

The measured $^{40}Ar/^{36}Ar$ ratios range from 325 to 551, which are slightly higher than air value (296; Ozima and Podosek, 1983) but significantly lower than those found in MORBs (from 28000 to 42000; Burnard et al., 1997; Moreira and Allègre, 1998; Tucker et al., 2012). Assuming two-component mixing between atmospheric Ar ($^{40}Ar/^{36}Ar$ = 296) and MORB mantle Ar ($^{40}Ar/^{36}Ar$ >40000, Burnard et al., 1997; Tucker et al., 2012) this corresponds to >98% atmospheric Ar. These near-atmospheric values are similar to the lower $^{40}Ar/^{36}Ar$ ratios of Gobernador Gregores (380) and Pali-Aike (510) (Jalowitzki et al., 2016). All the $^{38}Ar/^{36}Ar$ ratios are indistinguishable from the atmospheric value within analytical uncertainties (0.188; Ozima and Podosek, 1983).
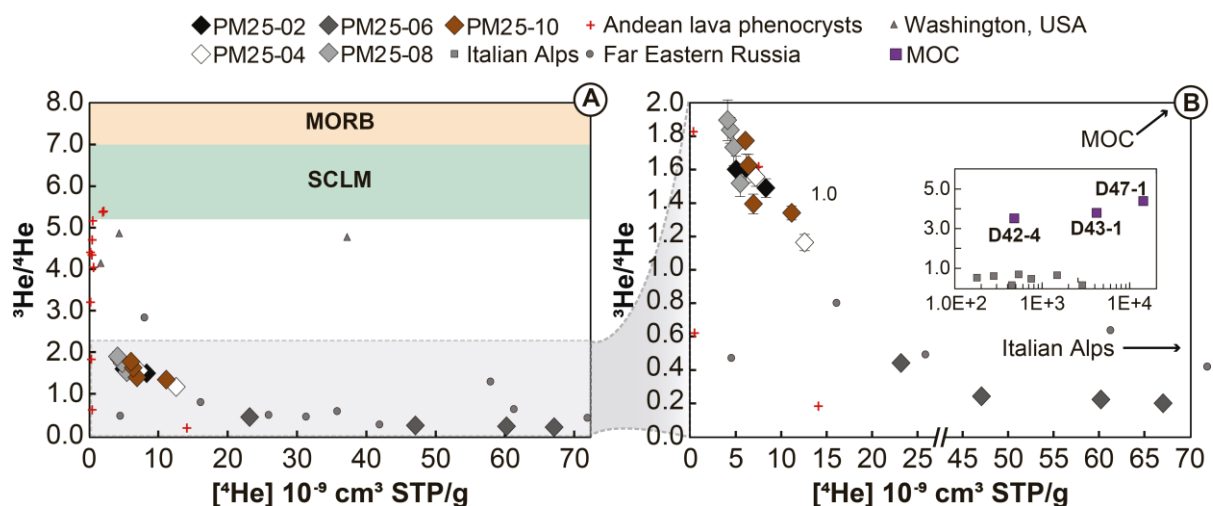
Figure 7. ^{3}He/^{4}He isotopic ratios vs. ^{4}He concentration (10^{-9} cm^3 STP/g) of Coyhaique spinel-lherzolites analyzed by the crushing extraction method with data from literature for comparison (A). Detailed plot of studied samples (B). Uncertainties are 1σ. Typical MORB (8 ± 1 R$_A$; Sarda et al., 1988; Moreira and Allègre, 1998) and SCLM (6 ± 1 R$_A$; Gautheron and Moreira, 2002; Jalowitzki et al., 2016) He compositions are represented by yellow and green fields, respectively in A. In some cases, the ^{3}He/^{4}He uncertainties are smaller than the symbol size. For comparison, He isotopic data from Andean lava phenocrysts (Hilton et al., 1993); Modified oceanic crust (MOC) from Southern Chile Ridge Segment 3 basaltic glasses (Sturm et al., 1999); radiogenic mantle xenoliths from Washington, USA (Dodson and Brandon, 1999), Far Eastern Russia (Yamamoto et al., 2004), and exhumed mantle wedge peridotites from Italian Alps (Matsumoto et al., 2005) and SW Japan (Sumino et al., 2010) are plotted.

Sample	Weight (g)	Number of strokes	[^{4}He] 10^{-9}	^{3}He/^{4}He (R/R$_A$)	[^{4}He]$_c$ 10^{-9}	(^{3}He/^{4}He)$_c$ (R/R$_A$)	[^{20}Ne] 10^{-12}	^{20}Ne/^{22}Ne	^{21}Ne/^{22}Ne	[^{40}Ar] 10^{-9}	^{38}Ar/^{36}Ar	^{40}Ar/^{36}Ar	^{4}He/^{20}Ne	^{4}He/^{40}Ar*	^{3}He/^{36}Ar
PM25-02		100	*4.40*	*2.52 ± 0.12*	*4.40*	*2.53*	2.48	9.72 ± 0.02	0.0295 ± 0.0020	3.99	0.1876 ± 0.0010	468.18 ± 0.77	1776	3.00	0.00180 ± 0.00009
Ol	0.7034	500	6.12	1.61 ± 0.09	6.12	1.61	2.84	9.63 ± 0.23	0.0305 ± 0.0017	5.04	0.1872 ± 0.0012	452.77 ± 1.28	2155	3.51	0.00120 ± 0.000066
Opx	0.3028	1000	5.01	1.60 ± 0.08	5.01	1.60	2.32	9.67 ± 0.20	0.0302 ± 0.0012	5.33	0.1879 ± 0.0010	430.05 ± 0.73	2156	3.02	0.00090 ± 0.000046
Cpx	0.1031	2000	8.31	1.49 ± 0.06	8.30	1.49	3.06	9.67 ± 0.23	0.0303 ± 0.0005	7.57	0.1884 ± 0.0008	430.65 ± 0.80	2717	3.51	0.00100 ± 0.000037
Total	**1.1093**		**19.44**	**1.56 ± 0.04**			**10.70**	**9.67 ± 0.05**	**0.0302 ± 0.0005**	**21.92**		**441.90 ± 0.76**			

Table 2. He, Ne and Ar concentrations (in cm^3 STP/g) and isotopic ratios measured in whole-rock Coyhaique spinel-lherzolites. All measurements were carried out by stepwise crushing extraction method. [^{4}He]$_c$ concentrations and (^{3}He/^{4}He)$_c$ ratios were corrected to the air (c). See the text for details. Values in italic were not considered in the sample total and discussion section because they represent anomalous results.

Sample	Weight (g)	Number of strokes	[^{4}He] 10^{-9}	^{3}He/^{4}He (R/R$_A$)	[^{4}He]$_c$ 10^{-9}	(^{3}He/^{4}He)$_c$ (R/R$_A$)	[^{20}Ne] 10^{-12}	^{20}Ne/^{22}Ne	^{21}Ne/^{22}Ne	[^{40}Ar] 10^{-9}	^{38}Ar/^{36}Ar	^{40}Ar/^{36}Ar	^{4}He/^{20}Ne	^{4}He/^{40}Ar*	^{3}He/^{36}Ar
PM25-04		100	7.21	1.56 ± 0.06	7.21	1.56	3.51	9.55 ± 0.17	0.0293 ± 0.0017	4.48	0.1887 ± 0.0007	489.91 ± 0.88	2056	4.07	0.00172 ± 0.00006
Ol	0.5997	500	12.58	1.17 ± 0.05	12.58	1.17	4.47	9.56 ± 0.09	0.0304 ± 0.0007	5.33	0.1876 ± 0.0013	519.64 ± 0.78	2817	5.49	0.00200 ± 0.00008
Opx	0.3571	1000	*34.22*	*0.62 ± 0.02*	*34.22*	*0.62*	4.96	9.58 ± 0.14	0.0291 ± 0.0012	6.45	0.1885 ± 0.0010	551.19 ± 0.63	6900	11.46	0.00252 ± 0.00007
Cpx	0.1287	2000	11.94	1.26 ± 0.04	11.93	1.26	3.54	9.59 ± 0.07	0.0299 ± 0.0006	5.92	0.1881 ± 0.0008	480.06 ± 0.66	3372	5.26	0.00170 ± 0.00006
Total	**1.0855**		**31.73**	**1.29 ± 0.03**			**16.47**	**9.57 ± 0.05**	**0.0297 ± 0.0005**	**22.17**		**510.65 ± 0.88**			

Table 2. Continued.

Sample	Weight (g)	Number of strokes	$[^4\text{He}]$ 10^{-9}	$^3\text{He}/^4\text{He}$ (R/R$_A$)	$[^4\text{He}]_c$ 10^{-9}	$(^3\text{He}/^4\text{He})_c$ (R/R$_A$)	$[^{20}\text{Ne}]$ 10^{-12}	$^{20}\text{Ne}/^{22}\text{Ne}$	$^{21}\text{Ne}/^{22}\text{Ne}$	$[^{40}\text{Ar}]$ 10^{-9}	$^{38}\text{Ar}/^{36}\text{Ar}$	$^{40}\text{Ar}/^{36}\text{Ar}$	$^4\text{He}/^{20}\text{Ne}$	$^4\text{He}/^{40}\text{Ar}^*$	$^3\text{He}/^{36}\text{Ar}$
PM25-06		100	60.23	0.22 ± 0.01	60.23	0.22	3.93	9.64 ± 0.14	0.0305 ± 0.0011	4.52	0.1879 ± 0.0014	396.88 ± 0.70	15329	52.39	0.00162 ± 0.00008
Ol	0.6506	500	67.10	0.20 ± 0.01	67.10	0.20	3.47	9.64 ± 0.09	0.0308 ± 0.0009	6.59	0.1891 ± 0.0010	433.45 ± 0.51	19322	32.10	0.00121 ± 0.00005
Opx	0.3385	1000	47.08	0.24 ± 0.01	47.08	0.24	2.42	9.57 ± 0.13	0.0307 ± 0.0013	6.22	0.1876 ± 0.0007	361.20 ± 0.67	19446	41.94	0.00091 ± 0.00004
Cpx	0.1100	2000	23.19	0.44 ± 0.02	23.18	0.44	2.82	9.67 ± 0.25	0.0294 ± 0.0019	5.97	0.1885 ± 0.0005	338.53 ± 0.56	8207	30.91	0.00081 ± 0.00003
Total	**1.0991**		**197.60**	**0.24 ± 0.01**			**12.65**	**9.63 ± 0.05**	**0.0304 ± 0.0005**	**23.30**		**379.19 ± 0.66**			

Table 2. Continued.

Sample	Weight (g)	Number of strokes	$[^4\text{He}]$ 10^{-9}	$^3\text{He}/^4\text{He}$ (R/R_A)	$[^4\text{He}]_c$ 10^{-9}	$(^3\text{He}/^4\text{He})_c$ (R/R_A)	$[^{20}\text{Ne}]$ 10^{-12}	$^{20}\text{Ne}/^{22}\text{Ne}$	$^{21}\text{Ne}/^{22}\text{Ne}$	$[^{40}\text{Ar}]$ 10^{-9}	$^{38}\text{Ar}/^{36}\text{Ar}$	$^{40}\text{Ar}/^{36}\text{Ar}$	$^4\text{He}/^{20}\text{Ne}$	$^4\text{He}/^{40}\text{Ar}^*$	$^3\text{He}/^{36}\text{Ar}$
PM25-08		100	5.46	1.52 ± 0.08	5.46	1.52	3.26	9.63 ± 0.14	0.0286 ± 0.0008	2.89	0.1883 ± 0.0014	326.20 ± 0.92	1677	20.42	0.00131 ± 0.00007
Ol	0.7149	500	4.38	1.84 ± 0.08	4.38	1.84	3.87	9.52 ± 0.11	0.0295 ± 0.0011	3.55	0.1877 ± 0.0007	329.25 ± 0.78	1131	12.23	0.00105 ± 0.00004
Opx	0.2499	1000	4.78	1.74 ± 0.11	4.78	1.74	2.09	9.45 ± 0.23	0.0302 ± 0.0016	3.69	0.1876 ± 0.0008	338.28 ± 0.88	2288	10.36	0.00107 ± 0.00007
Cpx	0.1016	2000	4.09	1.90 ± 0.12	4.09	1.90	2.09	9.65 ± 0.12	0.0291 ± 0.0014	3.64	0.1883 ± 0.0006	324.70 ± 0.55	1960	12.73	0.00097 ± 0.00006
Total	**1.0664**		**18.72**	**1.73 ± 0.05**			**11.31**	**9.56 ± 0.05**	**0.0293 ± 0.0005**	**13.77**		**329.74 ± 0.56**			

Table 2. Continued.

Sample	Weight (g)	Number of strokes	[^{4}He] 10^{-9}	^{3}He/^{4}He (R/R$_A$)	[^{4}He]$_c$ 10^{-9}	(^{3}He/^{4}He)$_c$ (R/R$_A$)	[^{20}Ne] 10^{-12}	^{20}Ne/^{22}Ne	^{21}Ne/^{22}Ne	[^{40}Ar] 10^{-9}	^{38}Ar/^{36}Ar	^{40}Ar/^{36}Ar	^{4}He/^{20}Ne	^{4}He/^{40}Ar*	^{3}He/^{36}Ar
PM25-10		100	6.92	1.40 ± 0.06	6.92	1.40	3.89	9.55 ± 0.17	0.0295 ± 0.0008	3.13	0.1882 ± 0.0010	325.16 ± 0.78	1779	24.68	0.00141 ± 0.00006
Ol	0.6337	500	11.14	1.34 ± 0.04	11.14	1.34	4.90	9.46 ± 0.07	0.0298 ± 0.0009	3.61	0.1880 ± 0.0008	334.80 ± 0.74	2272	26.60	0.00194 ± 0.00006
Opx	0.3777	1000	6.38	1.63 ± 0.07	6.38	1.63	3.34	9.63 ± 0.20	0.0289 ± 0.0017	3.21	0.1881 ± 0.0013	346.07 ± 0.91	1912	13.75	0.00157 ± 0.00006
Cpx	0.1186	2000	6.05	1.78 ± 0.02	6.05	1.78	3.24	9.57 ± 0.18	0.0295 ± 0.0011	3.60	0.1878 ± 0.0008	349.33 ± 1.00	1866	10.99	0.00146 ± 0.00002
Total	**1.1300**		**30.49**	**1.50 ± 0.03**			**15.38**	**9.54 ± 0.05**	**0.0295 ± 0.0005**	**13.55**		**338.84 ± 0.57**			

Table 2. Continued.

4.2.5 Discussion

4.2.5.1 Partial melting of Coyhaique spinel-lherzolite

Mineralogical and chemical features of Proterozoic Coyhaique spinel-lherzolites (Re-Os T_{RD} model ages between 1.3–1.7 Ga; Schilling et al., 2017) reveal a long history, involving depletion and further enrichment events related to slab-derived metasomatism (Jalowitzki et al., 2017). In terms of depletion, the restrict presence of lherzolites in the mantle xenolith suite of Coyhaique attests to lower degree of partial melting. Figure S2 shows well-defined negative correlations between MgO vs. selected basaltic elements (e.g., CaO, Al_2O_3, TiO_2 and Na_2O) (all major elements in wt. %), which is expected during partial melting processes of solid residue. These diagrams were constructed considering the major element compositions of 8 new samples together with the complete dataset from Jalowitzki et al. (2017) (17 samples). Our new set of data is characterized by similar to higher MgO coupled with lower CaO, Al_2O_3, TiO_2, and Na_2O when compared to the other Coyhaique lherzolites reported by Jalowitzki et al. (2017). With respect to the new whole-rock REE concentration, the majority of the lherzolite samples are depleted compared to the primitive mantle (Sun and McDonough, 1989). The exceptions are sample PM25-16, which demonstrates a strong chemical correlation with the samples from Jalowitzki et al. (2017) (see Fig. 3); and the La_N concentration of samples PM25-02 and PM25-42 (La_N = 1.13 and 1.14, respectively). The HREE values of the new samples (Yb_N = 0.29–0.56, with sample PM25-16 = 0.94) are considerably lower than previously reported for Coyhaique lherzolites (Yb_N = 0.98–1.77) (Fig. 3 and Tab. S4). Thus, whole-rock major and REE element compositions indicate that the new lherzolite samples represent higher degrees of partial melting compared to previous samples.

This evidence of depletion processes in the SCLM beneath Coyhaique is further corroborated by our new mineral chemistry data. Except for sample PM25-42, which defines a metasomatic

trend in the spinel Cr# and olivine Fo diagram (17.03–18.65 and 86.6–88.6, respectively), the other studied samples have low spinel Cr# (8.96–24.66) and Fo contents (87.9–91.2), plotting within the field of less depleted (i.e., fertile) xenoliths (Fig. 4A; Arai, 1994). Figures 4A-D show the well-defined Mg# positive correlation ($r^2 = 0.86$) of pyroxenes (Opx and Cpx), as well as the negative correlations established between Mg# (Opx) vs. Al_2O_3 (Opx), CaO (Cpx) vs. Al_2O_3 (Cpx). The patterns described above provide further evidence of partial melting.

It is well constrained that trace and REE elements of whole-rock and mineral phases are powerful tools to identify the partial melting and enrichment events of mantle peridotites. All REE patterns of olivine, orthopyroxene and clinopyroxene demonstrate depletion, except for 4 Type-2 clinopyroxenes (samples PM25-02, PM25-04, PM25-16 and PM25-42) and two clinopyroxene exsolutions analyzed within orthopyroxene from sample PM25-16 (Fig. 5).

Aiming to achieve partial melting degree estimates (Tab. S7), whole-rock and clinopyroxene HREE compositions were used in partial melting models (Fig. 3C and Fig. 5E, respectively). We selected the Yb and Lu values for the depletion models because they have similar bulk partition coefficients and, consequently, similar geochemical behavior during partial melting. Considering the complex history of depletion and/or enrichment revealed by HREE-enriched lherzolites from Coyhaique (HREE $>1 \times$ PM), less than 8% of partial melting was proposed assuming a mixture of 90% PM with the addition of 10% slab-derived component (sediments and modified oceanic crust) as a potential source (see Jalowitzki et al., 2017 for further details and references). For the new whole-rock data, the extent of partial melting (F) was calculated using the non-modal batch melting equation as follows:

$$C^S = ((D-P \times F) \times C)/((1-F) \times (D+F \times (1-P)))] \qquad \text{(Equation 1)}$$

where C^S is the concentration of the element in the solid, D_i is the distribution coefficient of the element between solid and liquid, F is the fraction of the liquid (melt), and P is the distribution coefficient of the element for the assemblage in equilibrium with the liquid (Shaw, 2006). As mantle source starting material, we used the primitive mantle REE values (Sun and McDonough, 1989) and the spinel peridotite modal composition of McDonough (1990). The melt mode for spinel facies (Ol = -0.06, Opx = 0.28, Cpx = 0.6, and Sp = 0.11) was from Johnson (1998) while the mineral/melt partition coefficients were taken from Ionov (2002). Sample PM25-16 displays a different HREE pattern compared to the other samples (similar to those reported by Jalowitzki et al., 2017) and, for this reason, yielded only ~2% of partial melting. Note that this estimate is unrealistic because we consider that this sample was affected by slab-derived metasomatism similar to other Coyhaique HREE-enriched lherzolites (Lu_N > PM; Jalowitzki et al., 2017). Regarding the strongly depleted Coyhaique lherzolites, they indicate ~6 to 15% of partial melting (Fig. 3C).

We applied the same principle assumed for the whole-rock partial melting model above for our measured clinopyroxene HREE patterns by using the non-modal fractional melting equation of Johnson et al. (1990):

$$\frac{C_i^{cpx}}{C_i^{o,cpx}} = \left[1 - \frac{PF}{D_i^o}\right]^{\left(\frac{1}{P}-1\right)} \qquad \text{(Equation 2)}$$

The parameters used in the modelling (Tab. S7; C, P, D, and F are the same as in Eq. 1) are the melt mode from Johnson (1998, and references therein), partition coefficients from Ionov

(2002); and spinel-lherzolite modal average of Coyhaique samples (Ol = 0.58, Opx = 0.26, Cpx = 0.13 and Sp = 0.03%) and whole-rock spinel-lherzolite average as the mantle source. The best fit for the Coyhaique clinopyroxenes requires between 1 and 9% of partial melting (Fig. 5E). Comparatively, our clinopyroxene estimates are similar to slightly lower than the partial melting degrees reported by Melchiorre et al. (2020, and references therein) for clinopyroxene of spinel-bearing samples from Patagonia (e.g., Tres Lagos = 1–14%, Cerro del Fraile = 4–21%, Las Cumbres = 5–12%, and Pali-Aike Volcanic Field = 2–24%).

4.2.5.2 Subduction-related metasomatism recorded by Coyhaique spinel-lherzolites

Mantle xenoliths derived from the mantle wedge close to the arc regions are believed to undergo metasomatic reactions caused by fluids and/or melts released from the subducted material. Coyhaique lherzolites represent Patagonian SCLM fragments among the closest already sampled with respect to the Chile trench (~320 km), which offer the valuable opportunity to observe mantle metasomatism in the Andean continental arc context.

4.2.5.2.1 Metasomatism recorded by trace elements and Sr-Nd isotopes

Possible scenarios of slab-derived metasomatism beneath Coyhaique were evaluated and discussed on the basis of whole-rock data for 17 spinel-lherzolite xenoliths by Jalowitzki et al. (2017). These authors identified typical arc-related enrichment in lherzolites, such as negative Nb-Ta-Ti anomalies coupled with a significant enrichment of LILE and chalcophile elements over HFSE and REE. Moreover, the depleted mantle toward enriched mantle-2 array observed in the Sr-Nd isotopic ratios supported the mantle metasomatism event. They attributed these chemical features to metasomatic components originating from a mixing of fluids/melts derived from subducted Chile Trench sediments and from modified oceanic crust, which interacted with

the Proterozoic depleted SCLM. The origin of these fluids and/or melts is probably related to the initial stages of the Farallón-Aluk ridge collision during Paleocene-Eocene time. However, the possibility that this metasomatic event is associated with an older subduction event cannot be refuted.

In hot subduction zones, it is well known that the slab can undergo partial melting thereby generating hydrated adakite melts that react with peridotites from the mantle wedge, forming a new metasomatic assemblage characterized by secondary orthopyroxene and amphibole (e.g., Corgne et al., 2018; Gervasoni et al., 2017; Rapp et al., 1999). In Patagonia, metasomatism by adakite melts is recorded only by xenoliths from Cerro del Fraile (Faccini et al., 2013; Kilian and Stern, 2002). The presence of new phases, such as secondary orthopyroxene, pargasite and phlogopite are absent in the studied samples and, therefore, there is no textural evidence of modal metasomatism. Instead, metasomatism recorded by Coyhaique lherzolites is cryptic as the original mineral paragenesis remains the same (olivine, orthopyroxene, clinopyroxene, and spinel), whereas changes in the mineral compositions can be identified.

The new whole-rock spinel-lherzolite data show similar trace element patterns when compared to the previous study of Jalowitzki et al. (2017) (see red and black lines in Figure 3), suggesting that our samples record the same metasomatic processes. However, it is important to note that the new samples contain lower REE concentrations, especially HREE, which imply residues with higher degrees of partial melting (see above). The depleted character of our new samples, evidenced by low HREE values, may facilitate the re-enrichment of LREE due to the slab-derived metasomatism (La/Sm$_N$ = 1.52–2.97). This character is suggested by the low $^{87}Sr/^{86}Sr$ ratios (0.702347–0.703198) coupled with high $^{143}Nd/^{144}Nd$ (0.512940–0.513159) and εNd (5.89–10.17) data. Sample PM25-06 shows a contrasting pattern with LREE<MREE (La/Sm$_N$

= 0.54) coupled with the highest radiogenic whole-rock Sr and He isotopic ratios (^{87}Sr/^{86}Sr = 0.703192; ^{3}He/^{4}He = 0.24 R$_A$).

Olivines, orthopyroxenes and clinopyroxenes from 16 selected Coyhaique lherzolites (Tab. 1) had their trace element and REE compositions determined. Among all analyzed mineral phases, the clear enrichment of LREE/HREE ratios usually observed in metasomatized samples is evident only in few Type-2 clinopyroxenes (samples PM25-02, PM25-04, PM25-16 and PM25-42). However, it is not conclusive that the other clinopyroxene samples were not affected by metasomatism, because the expected LREE pattern for partial melting requires lower concentrations from La to Pr (see Fig. 5E). On the other hand, there also is no REE evidence of slab-derived metasomatism in olivine and orthopyroxene samples as they show strong depletion in LREE (e.g., Ol La$_N$ = 4.5×10^{-4}–2.2×10^{-3}; Opx La$_N$ = 2.1×10^{-3}–1.2×10^{-1}).

In general, olivines, orthopyroxenes and clinopyroxenes show positive anomalies of Li in the PM-normalized multi-element diagram (Fig. 5A). Lithium is a mobile element usually enriched in sediments (pelagic and terrigenous) and continental crust in comparison to the mantle and mantle-derived melts (e.g., Bouman et al., 2004; Caciagli et al., 2011; Prelević et al., 2013). The upper continental crust on average has a significantly higher Li concentration (e.g., 24 ppm; Rudnick and Gao, 2003) compared to the primitive mantle (Li = 1.6 ppm; Sun and McDonough, 1989) and to worldwide spinel facies peridotites (Ol = 1.1–2.9 ppm, Opx = 0.3–1.9 ppm, Cpx = 0.5–2.4 ppm; e.g., Jeffcoate et al., 2007; Ottolini et al., 2004; Seitz and Woodland, 2000). It should be noted that Li$^+$ has similar ionic radius to Mg$^+$ and Fe^{2+}, which allows a coupled substitution in the octahedral sites of olivines and pyroxenes (Seitz and Woodland, 2000). Olivines from the Coyhaique lherzolites show higher Li concentration (1.5–2.9 ppm) than primitive mantle but similar with worldwide peridotites, whereas orthopyroxene (1.7–5.0 ppm) and clinopyroxene (4.5–20.2 ppm) are notably enriched. All mineral phases show a relatively

scattered distribution, but positive correlations are discernible among them (Fig. 8). The enrichment of Li in olivine and pyroxenes reinforce the contribution of fluids and/or melts derived from the slab that have reacted with the mantle wedge generating cryptic metasomatism, in agreement to what was proposed by Jalowitzki et al. (2017). Slab-derived enriched components are also highlighted in clinopyroxene by positive correlations of La vs. U and Pb (all in ppm) as well as by La (ppm) vs. Nb* and Ti* negative correlations (Fig. S5). Coyhaique spinel-lherzolites display significant differences between trace and REE element compositions (e.g., LILE/HFSE, LILE/HREE and LREE/HREE ratios) among whole-rock and mineral phases. This strongly suggests that the enrichment observed in whole-rock lherzolites with the absence of these geochemical features recorded by olivine, orthopyroxene and clinopyroxene, is a result of "grain-boundary components" that may contain high concentrations of incompatible trace elements when compared to the minerals (e.g., Ishimaru et al., 2007 and references therein). The role of the grain boundary component in concentrating LILE and LREE is emphasized in the Coyhaique lherzolites because of the extremely small concentration of incompatible elements in minerals such as clinopyroxene. Therefore, we suggest that most of the studied mineral phases display incipient metasomatism.
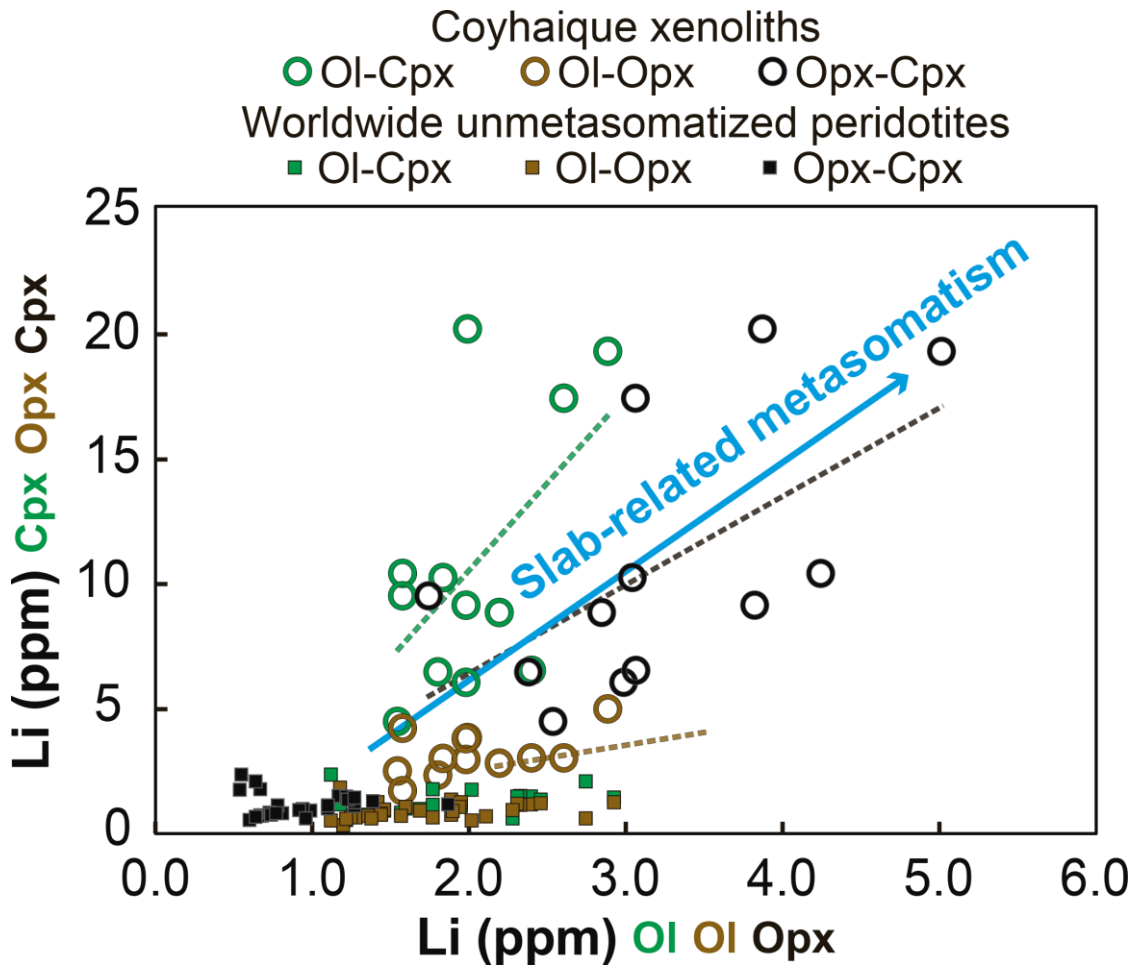
Figure 8. Lithium (ppm) concentrations of silicate phases from Coyhaique lherzolites showing variable extents of cryptic metasomatism through of correlation trends (dashed lines) that define positive correlations. Mineral trends represent olivine-clinopyroxene (green; Ol: x and Cpx: y), olivine-orthopyroxene (brown; Ol: x and Opx: y), and orthopyroxene-clinopyroxene (black; Opx: x and Cpx: y). Note higher pyroxenes Li contents compared to olivine composition. Worldwide spinel facies peridotites are shown for comparison (Jeffcoate et al., 2007; Ottolini et al., 2004; Seitz and Woodland, 2000).

4.2.5.2.2 Recycled noble gas component in the SCLM beneath Coyhaique

In order to verify the measured ^{3}He/^{4}He isotopic ratios of Coyhaique spinel-lherzolites represent the mantle component, we tested whether our results were affected by enrichment of post eruptive cosmogenic (^{3}He) or radiogenic ^{4}He components. Moreover, we tested the possibility of atmospheric contamination.

4.2.5.2.2.1 Atmospheric contamination and post-eruptive processes

All noble gas isotopic ratios (He, Ne and Ar) were obtained by the stepwise crushing extraction method under high vacuum conditions to release the noble gases trapped in fluid inclusions within the whole-rock, avoiding the matrix-sited components. Although we analyzed whole-rock samples (olivine, orthopyroxene, clinopyroxene; Tab. 2), the low and uniform ^{3}He/^{4}He isotopic ratios obtained by applying stepwise crushing with sequential number of strokes (100, 500, 1000 and 2000 times; see Tab. 2), show that all mineral phases share the same mantle component. This is important because olivine is a mineral poor in U and Th while pyroxenes retain these elements. Besides the crushing method, the low abundance of He in air (5.2 ppm) reduces the influence of atmospheric component in mantle-derived samples. In contrast, the low ^{40}Ar/^{36}Ar ratios of fluid inclusions from Coyhaique lherzolites (325–551, Tab. 2) probably represent air contamination that occurred at shallow depths or after the entrapment of fluid inclusions. Thus, the contribution of air in our samples was verified through ^{4}He/^{40}Ar* ratios [where ^{40}Ar* = ^{40}Ar$_{measured}$-(^{40}Ar/^{36}Ar$_{air}$ × ^{36}Ar$_{measured}$)] and by ^{4}He/^{20}Ne sensitive ratios. The ^{4}He/^{40}Ar* ratios (3.0–52.4) together with the ^{4}He/^{20}Ne ratios (1133–19446) (Tab. 2) exclude the contribution from the air in ^{3}He/^{4}He isotope ratios (< 0.2%) (Martelli et al., 2011; Sumino et al., 2004). Sample PM25-06 shows the highest ^{4}He/^{20}Ne ratios (8207–19446), which define this sample as unmodified by air contamination (<0.01%). The ^{3}He/^{4}He ratios and the ^{4}He

concentrations were corrected to the atmospheric contamination by applying the equations proposed by Giggenbach et al. (1993) (Eq. 3) and Harrison et al. (2004) (Eq. 4), respectively:

$$\left(\frac{^{3}\text{He}}{^{4}\text{He}}\right)_{c} = \frac{\left(\dfrac{\left(^{3}\text{He}/^{4}\text{He}\right)_{\text{measured}}}{1.4 \times 10^{-6}} \times \left(^{4}\text{He}/^{20}\text{Ne}\right)_{\text{measured}}\right) - 0.318}{\left(^{4}\text{He}/^{20}\text{Ne}\right)_{\text{measured}} - 0.318} \times 1.4 \times 10^{-6}$$

(Equation 3)

$$\left[^{4}\text{He}\right]_{c} = \left[^{4}\text{He}\right]_{\text{measured}} \times \left(\frac{\left(^{4}\text{He}/^{20}\text{Ne}\right)_{\text{measured}}}{0.318} - 1\right) \Big/ \frac{\left(^{4}\text{He}/^{20}\text{Ne}\right)_{\text{measured}}}{0.318}$$

(Equation 4)

The post-eruptive radiogenic production from U and Th can be calculated with the measured U and Th concentrations, as well as the eruption ages of the samples known from previous studies. For the calculations, the eruption age of 54 Ma (Jalowitzki et al., 2017) and U-Th concentrations (in ppm) for each whole-rock sample were used (Tab. S4), which resulted in a radiogenic ^{4}He production rate of 4.88–7.91×10^{-12} cm^{3} STP/g. These values represent less than 0.2% of radiogenic ^{4}He production from the decay of U and Th, implying insignificant contribution to the ^{3}He/^{4}He of Coyhaique lherzolites (see Graham, 2002 and Kim et al., 2005 for the mathematical formulas). Thus, we interpret that the measured ^{3}He/^{4}He ratios represent the originally trapped He during a subduction-derived metasomatic event.

4.2.5.2.2.2 Source of recycled components in the SCLM

The flux and recycling of noble gas isotopes back into the SCLM through subduction zones recorded by mantle xenoliths, especially in case of He, is still poorly constrained (e.g., Dodson and Brandon, 1999; Hilton et al., 1993; Matsumoto et al., 2005; Yamamoto et al., 2004). Coyhaique spinel-lherzolites show remarkably radiogenic He signature (0.20–1.90 R_A; Fig 7), which probably is the result of high time-integrated $(U+Th)/^3He$ ratios related to the addition of fluids/melts rich in ^4He due to dehydration of subducting materials. The subduction event in the Aysén Region (44–47°S) is characterized by the occurrence of a large and widely distributed calc-alkaline plutonic complex that defines the North Patagonian Batholith (NPB; e.g., Demant et al., 1996; Hervé et al., 2007; Pankhurst et al., 1999). To the west, this batholith intrudes the Chonos Late Paleozoic metamorphic complex, whereas to the east it intrudes Paleozoic and Mesozoic volcanic and sedimentary units (Demant et al., 1996 and references therein; Pankhurst et al., 1999). Additionally, $^{206}Pb/^{204}Pb$ isotopic data of the Coyhaique host basalt display HIMU-like signature (19.333–19.389), suggesting a prolonged period of recycling of subduction-derived material (Jalowitzki et al., 2017).

The recycling of oceanic crust and sediment-enriched components with high $(U-Th)/^3He$ ratios into the SCLM beneath Coyhaique could have lowered the He isotopic ratios since, at least, the Early Carboniferous subduction event (Oliveros et al., 2020 and references therein). We assume the oceanic crust and sediments as potential sources of recycled materials into the Patagonian mantle wedge. Sturm et al. (1999) presented radiogenic $^3He/^4He$ ratios (3.51–4.39 R_A) for MORB glasses from the Chile Ridge Segment 3 (samples D42-4, D43-1, D47-1), whereas Hilton et al. (1993) show radiogenic $^3He/^4He$ ratios (0.18–5.39 R_A) for basaltic andesite phenocrysts (olivine and clinopyroxene) and water/gas of hot springs (0.07–5.19 R_A) from the Andean Cordillera. Considering that Chilean trench sediments are mostly continentally-derived

turbidites eroded from the Southern Volcanic Zone (SVZ; e.g., Lucassen et al., 2010; Völker et al., 2008), we consider that these sediments represent the He composition of the Andean Cordillera. Lucassen et al. (2010) also suggested that the dominance of detritus from the SVZ rocks in the continental sedimentary input is likely a stable feature at a time scale longer than that calculated for the subduction of sediment from the trench down to the depth of fluid/melt generation and eclogite formation.

As proposed here, Sumino et al. (2010) associated the radiogenic ^{3}He/^{4}He ratios (1.26–2.78 R_A) of exhumed mantle wedge peridotites from Sanbagawa metamorphic belt, SW Japan, to the slab-derived fluids directly captured at just above the slab (~100 km depth) (Fig. 7). Comparatively, Coyhaique spinel-lherzolites also show similar or even more radiogenic ^{3}He/^{4}He isotopic ratios (0.20–1.90 R_A) compared to peridotites from the Cascades volcanic arc (^{3}He/^{4}He = 4.14–4.86 R_A, Dodson and Brandon, 1999), Italian Alps (^{3}He/^{4}He = 0.15–0.69 R_A; Matsumoto et al., 2005), and Far Eastern Russia (^{3}He/^{4}He = 0.26–2.83 R_A; Yamamoto et al., 2004) (Fig. 7). Our radiogenic results also show a strong affinity to those reported for volcanic gases and lava phenocrysts from Indonesia (^{3}He/^{4}He = 0.008–5.70 R_A; Hilton et al., 1992; Hilton and Craig, 1989) and Mount Vesuvius (^{3}He/^{4}He = 2.23–2.72 R_A; Graham and Lupton, 1999). It should be noted that we decided to only use ^{3}He/^{4}He values lower than 6.0 R_A for comparison.

Three Ne measurements of sample PM25-04 (500 strokes with ^{21}Ne/^{22}Ne = 0.0304) and one of PM25-06 (100, 500 and 1000 strokes with ^{21}Ne/^{22}Ne = 0.0305–0.0308) have isotopic ratios that differ from air with 1σ uncertainties. They show strongly nucleogenic patterns characterized by ^{21}Ne enrichment (Fig. S4), which probably is associated with the radiogenic ^{3}He/^{4}He ratios. Thus, Ne data also may indicate a mixing between air and subduction-related endmembers.

However, it is not possible to confirm this interpretation, due to the high blank contribution and the limited number of measurements.

Because of the low $^{40}Ar/^{36}Ar$ ratios of Coyhaique lherzolites (<600), we assume that all ^{36}Ar is atmospheric (e.g., Martelli et al., 2011; Matsumoto et al., 2001). Conversely, the extremely low abundance of ^{3}He in the atmosphere imply all ^{3}He observed can be assumed as a mantle component. Hence, the correlation between $^{40}Ar/^{36}Ar$ and $^{3}He/^{36}Ar$ ratios may reveal a mixing between the local SCLM and atmosphere components (e.g., Matsumoto et al., 2001). By extrapolating a regression line to the estimated $^{40}Ar/^{36}Ar_{MORB}$ ~40000 (Moreira et al., 1998; Tucker et al., 2012), we found a $^{3}He/^{36}Ar_{(E)}$ ratio of 0.45, whereas the $^{40}Ar/^{36}Ar_{(E)}$ ratio (extrapolated to the $^{3}He/^{36}Ar_{MORB}$ endmember of 0.7) is 63000 ($^{3}He/^{36}Ar$ = 0.45; Fig. S6) for local SCLM. This interval is in agreement with that proposed for Pali-Aike Volcanic Field SCLM ($^{40}Ar/^{36}Ar$ = 31100–54000; Jalowitzki et al., 2016) and European SCLM ($^{40}Ar/^{36}Ar$ = 34000–52000; Buikin et al., 2005). Due to its higher solubility compared to other noble gases (e.g., about 7–10 times than Ar), He is susceptible to fractionate between melt and solid residue phases during partial melting processes, favoring the low $^{4}He/^{40}Ar*$ ratios in the mantle peridotite residue as a result of preferential He loss (e.g., Hopp and Ionov, 2011 and references therein; Yamamoto et al., 2009). The SCLM beneath Coyhaique has experienced relatively low degrees of partial melting (see section 5.1) and shows similar to higher $^{4}He/^{40}Ar*$ ratios (3.0–52.4; Tab. 2) than mantle production ratio of 1.6–4.2 (Graham, 2002). In the diagram that correlate $^{3}He/^{4}He$ vs. $^{4}He/^{40}Ar*$ (Fig. 9), our samples show clear evidence of slab-derived metasomatism as evidenced by high ^{4}He radiogenic component that defines low $^{3}He/^{4}He$ and high $^{4}He/^{40}Ar*$. This pattern also is observed in subduction-related mantle xenoliths from Far Eastern Russia (Yamamoto et al., 2004), Italian Alps (Matsumoto et al., 2005), and Cascades volcanic arc (Dodson and Brandon, 1999) (Fig. 9). Moreover, based on $^{3}He/^{36}Ar$ and $^{4}He/^{40}Ar*$

ratios, our samples are the product of a mixing between atmospheric endmember and a subduction-related mantle component.
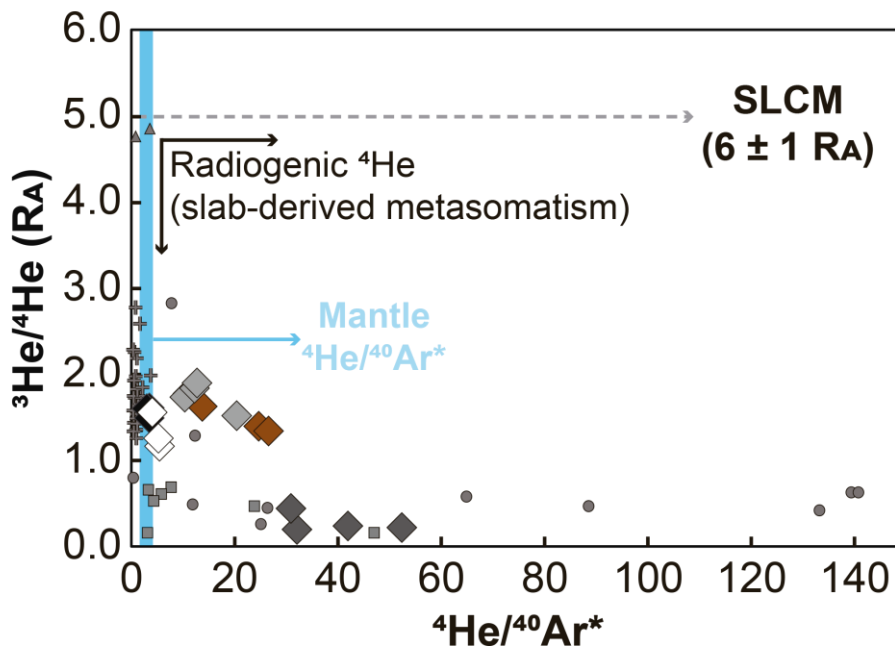
Figure 9. ^{3}He/^{4}He versus ^{4}He/^{40}Ar* ratios of fluid inclusions from Coyhaique spinel-lherzolites. Our samples show similar to higher ^{4}He/^{40}Ar* ratios (3.0–52.4) with respect to the mantle production (1.6–4.2; Graham, 2002), as well as lower ^{3}He/^{4}He ratios than MORB (8 ± 1 R$_A$; Moreira and Allègre, 1998; Sarda et al., 1988) and SCLM (6 ± 1 R$_A$; Gautheron and Moreira, 2002; Jalowitzki et al., 2016). Coyhaique lherzolites have strong affinity with subduction-related mantle xenoliths from Far Eastern Russia (Yamamoto et al., 2004), Cascades volcanic arc (Dodson and Brandon, 1999), and exhumed mantle wedge peridotites from Italian Alps (Matsumoto et al., 2005)and SW Japan (Sumino et al., 2010).

4.2.5.2.2.3 Correlation between lithophile (Sr-Nd) and volatile (He) isotopic ratios

The negative correlation defined by whole-rock He and Sr isotopic ratios of Coyhaique lherzolites (Fig. S3A) is expected for radiogenic enrichment related to slab-derived metasomatism. This pattern is corroborated by the positive correlation between less radiogenic He and more radiogenic Nd whole-rock samples (Fig. S3B). Conversely, whole-rock He ratios correlate negatively with clinopyroxene Nd and positively with clinopyroxene Sr, except for the sample PM25-06 that display both more radiogenic Nd and He ratios (Fig. S3C-D). Thus, we attributed the decoupling between whole-rock He and clinopyroxene Sr-Nd to the preservation of the depleted character of Coyhaique SCLM in terms of Sr-Nd isotopes with fluid inclusion composition replaced due to successive subduction events recorded in the western margin of South America at least since Paleozoic. Moreover, it should be noted that the absence of Sr-Nd enriched mantle component with high $^{87}Sr/^{86}Sr$ and low $^{143}Nd/^{144}Nd$ in acid-leached clinopyroxene when compared to whole-rock samples (Fig. 6) suggests that radiogenic Sr and unradiogenic Nd are related to the grain boundary components.

6. Conclusions

The SCLM beneath Coyhaique area is composed of anhydrous spinel-lherzolites with protogranular texture, showing low strain and abundant fluid inclusions observable in all silicate phases. The well-defined negative correlations between MgO and basaltic elements (CaO, Al_2O_3, TiO_2, Na_2O) coupled with REE depletion ($<1\times$ primitive mantle) observed in whole-rock and mineral phases attest a residual character of our samples. The unradiogenic Sr and radiogenic Nd isotopic ratios determined for whole-rock and clinopyroxene separates ($^{87}Sr/^{86}Sr$ = 0.702347–0.703198; $^{143}Nd/^{144}Nd$ = 0.512940–0.513632) corroborate the depleted character of Coyhaique lherzolites. Pressure estimates yielded values between 1.06 and 1.90

GPa, which represent a mantle column between 35 and 63 km (most lherzolites > 40 km) with temperatures ranging from 886 to 1150 °C. Whole-rock and clinopyroxene HREE compositions (e.g., Yb and Lu) suggest low degrees of partial melting (1–15%). Cryptic metasomatism is characterized by the absence of secondary pyroxene and hydrous minerals combined with high LREE/HREE in whole-rock and Type-2 clinopyroxenes, as well as by the LILE and chalcophile enrichment coupled with typical arc signature (e.g., negative anomalies of Nb, Ta and Ti) observed in whole-rock lherzolites. Additionally, olivines show similar to higher Li concentrations compared to the primitive mantle, whereas pyroxenes are strongly enriched, which support the cryptic metasomatism generated by melts and/or fluids released from subducted materials (i.e., oceanic crust and sediments). This assumption is supported by clinopyroxene positive correlations of Pb and U vs. La, and negative correlations of Nb/Nb* and Ti/Ti* vs. La. The geochemical differences between whole-rock and their mineral constituents indicate selective enrichment of the whole-rock samples due to LILE- and LREE-rich grain-boundary components. Spinel-lherzolites have strongly radiogenic $^{3}He/^{4}He$ (0.20–1.90 R_A), nucleogenic $^{21}Ne/^{22}Ne$ (0.0304–0.0308), and atmospheric-like $^{40}Ar/^{36}Ar$ (325–551) ratios. We propose that radiogenic (U-Th)/^{3}He ratios of Coyhaique lherzolites, attested by the correlation between $^{3}He/^{4}He$ vs. $^{4}He/^{40}Ar*$, are the consequence of recycling of terrigenous sediments and/or oceanic crust through subduction zone processes. Therefore, Coyhaique spinel-lherzolites record the effective recycling of crustal material and volatiles through the long-lived subduction system beneath Patagonia related to the Andean orogeny since the Early Carboniferous or to previous subduction.

Acknowledgments

References

Aragón, E., D'Eramo, F., Castro, A., Pinotti, L., Brunelli, D., Rabbia, O., Rivalenti, G., Varela, R., Spakman, W., Demartis, M., Cavarozzi, C.E., Aguilera, Y.E., Mazzucchelli, M., Ribot, A., 2011. Tectono-magmatic response to major convergence changes in the North Patagonian suprasubduction system; the Paleogene subduction-transcurrent plate margin transition. Tectonophysics 509, 218–237. https://doi.org/10.1016/j.tecto.2011.06.012

Aragón, E., Pinotti, L., D'eramo, F., Castro, A., Rabbia, O., Coniglio, J., Demartis, M., Hernando, I., Cavarozzi, C.E., Aguilera, Y.E., 2013. The Farallon-Aluk ridge collision with South America: Implications for the geochemical changes of slab window magmas from fore- to back-arc. Geosci. Front. 4, 377–388. https://doi.org/10.1016/j.gsf.2012.12.004

Arai, S., 1994. Characterization of spinel peridotites by olivine-spinel compositional relationships: Review and interpretation. Chem. Geol. 113, 191–204. https://doi.org/10.1016/0009-2541(94)90066-3

Arai, S., Ishimaru, S., Okrugin, V.M., 2003. Metasomatized hazburgite xenoliths from Avacha volcano as fragments of mantle wedge of the Kamchatka arc: Implication for the metasomatic agent. Isl. Arc 12, 233–246. https://doi.org/10.1046/j.1440-1738.2003.00392.x

Bach, W., Erzinger, J., Dosso, L., Bollinger, C., Bougault, H., Etoubleau, J., Sauerwein, J., 1996. Unusually large Nb-Ta depletions in North Chile ridge basalts at 36°50′ to 38°56′s: Major element, trace element, and isotopic data. Earth Planet. Sci. Lett. 142, 223–240. https://doi.org/10.1016/0012-821x(96)00095-7

Baker, P.E., Rea, W.J., Skarmeta, J., Caminos, R., Rex, D.C., 1981. Igneous history of the

Andean Cordillera and Patagonian plateau around latitude 46°S. Philos. Trans. R. Soc. London. Ser. A, Math. Phys. Sci. 303, 105–149. https://doi.org/10.1098/rsta.1981.0194

Bertotto, G.W., Mazzucchelli, M., Zanetti, A., Vannucci, R., 2013. Petrology and geochemistry of the back-arc lithospheric mantle beneath eastern Payunia (La Pampa, Argentina): Evidence from Agua Poca peridotite xenoliths. Geochem. J. 47, 219–234. https://doi.org/10.2343/geochemj.2.0256

Bjerg, E.A., Ntaflos, T., Kurat, G., Dobosi, G., Labudía, C.H., 2005. The upper mantle beneath Patagonia, Argentina, documented by xenoliths from alkali basalts. J. South Am. Earth Sci. 18, 125–145. https://doi.org/10.1016/j.jsames.2004.09.002

Bjerg, E.A., Ntaflos, T., Thöni, M., Aliani, P., Labudia, C.H., 2009. Heterogeneous lithospheric mantle beneath Northern Patagonia: Evidence from Prahuaniyeu garnet- and spinel-peridotites. J. Petrol. 50, 1267–1298. https://doi.org/10.1093/petrology/egp021

Bouman, C., Elliott, T., Vroon, P.Z., 2004. Lithium inputs to subduction zones. Chem. Geol. 212, 59–79. https://doi.org/10.1016/j.chemgeo.2004.08.004

Breitsprecher, K., Thorkelson, D.J., 2009. Neogene kinematic history of Nazca-Antarctic-Phoenix slab windows beneath Patagonia and the Antarctic Peninsula. Tectonophysics 464, 10–20. https://doi.org/10.1016/j.tecto.2008.02.013

Brey, G.P., Köhler, T., 1990. Geothermobarometry in Four-phase Lherzolites II. New Thermobarometers, and Practical Assessment of Existing Thermobarometers. J. Petrol. 31, 1353–1378. https://doi.org/10.1093/petrology/31.6.1353

Buikin, A., Trieloff, M., Hopp, J., Althaus, T., Korochantseva, E., Schwarz, W.H., Altherr, R., 2005. Noble gas isotopes suggest deep mantle plume source of late Cenozoic mafic alkaline volcanism in Europe. Earth Planet. Sci. Lett. 230, 143–162.

https://doi.org/10.1016/j.epsl.2004.11.001

Burnard, P., Graham, D., Turner, G., 1997. Vesicle-specific noble gas analyses of "popping rock": Implications for primordial noble gases in earth. Science (80-.). 276, 568–571. https://doi.org/10.1126/science.276.5312.568

Bussweiler, Y., Giuliani, A., Greig, A., Kjarsgaard, B.A., Petts, D., Jackson, S.E., Barrett, N., Luo, Y., Pearson, D.G., 2019. Trace element analysis of high-Mg olivine by LA-ICP-MS – Characterization of natural olivine standards for matrix-matched calibration and application to mantle peridotites. Chem. Geol. 524, 136–157. https://doi.org/10.1016/j.chemgeo.2019.06.019

Caciagli, N., Brenan, J.M., McDonough, W.F., Phinney, D., 2011. Mineral-fluid partitioning of lithium and implications for slab-mantle interaction. Chem. Geol. 280, 384–398. https://doi.org/10.1016/j.chemgeo.2010.11.025

Cande, S.C., Leslie, R.B., 1986. Late Cenozoic tectonics of the Southern Chile Trench. J. Geophys. Res. 91, 471. https://doi.org/10.1029/JB091iB01p00471

Conceição, R. V., Mallmann, G., Koester, E., Schilling, M., Bertotto, G.W., Rodriguez-Vargas, A., 2005. Andean subduction-related mantle xenoliths: Isotopic evidence of Sr-Nd decoupling during metasomatism. Lithos 82, 273–287. https://doi.org/10.1016/j.lithos.2004.09.022

Corgne, A., Schilling, M.E., Grégoire, M., Langlade, J., 2018. Experimental constraints on metasomatism of mantle wedge peridotites by hybridized adakitic melts. Lithos 308–309, 213–226. https://doi.org/10.1016/j.lithos.2018.03.006

D'Orazio, M., Innocenti, F., Piero, M., Haller, M., Orazio, M.D., Innocenti, F., Manetti, P., Miguel, P., 2004. Cenozoic back-arc magmatism of the southern extra-Andean Patagonia

(44° 30'-52° S): A review of geochemical data and geodynamic interpretations. Rev. la Asoc. Geol. Argentina 59, 525–538.

Dantas, C., Grégoire, M., Koester, E., Conceição, R.V., Rieck, N., 2009. The lherzolite–websterite xenolith suite from Northern Patagonia (Argentina): Evidence of mantle–melt reaction processes. Lithos 107, 107–120. https://doi.org/10.1016/j.lithos.2008.06.012

Demant, A., Hervé, F., Pankhurst, R.J., Suárez, M., 1996. Geochemistry of Early Tertiary back-arc basalts from Aysén, southern Chile (44-46 S): geodynamic implications.

Dodson, A., Brandon, A.D., 1999. Radiogenic helium in xenoliths from Simcoe, Washington, USA: Implications for metasomatic processes in the mantle wedge above subduction zones. Chem. Geol. 160, 371–385. https://doi.org/10.1016/S0009-2541(99)00108-4

Eagles, G., Scott, B.G.C., 2014. Plate convergence west of Patagonia and the Antarctic Peninsula since 61Ma. Glob. Planet. Change 123, 189–198. https://doi.org/10.1016/j.gloplacha.2014.08.002

Espinoza, F., Morata, D., Pelleter, E., Maury, R.C., Suárez, M., Lagabrielle, Y., Polvé, M., Bellon, H., Cotten, J., De la Cruz, R., Guivel, C., 2005. Petrogenesis of the Eocene and Mio-Pliocene alkaline basaltic magmatism in Meseta Chile Chico, southern Patagonia, Chile: Evidence for the participation of two slab windows. Lithos 82, 315–343. https://doi.org/10.1016/j.lithos.2004.09.024

Faccini, B., Bonadiman, C., Coltorti, M., Grégoire, M., Siena, F., 2013. Oceanic Material Recycled within the Sub-Patagonian Lithospheric Mantle (Cerro del Fraile, Argentina). J. Petrol. 54, 1211–1258. https://doi.org/10.1093/petrology/egt010

Gautheron, C., Moreira, M., 2002. Helium signature of the subcontinental lithospheric mantle. Earth Planet. Sci. Lett. 199, 39–47. https://doi.org/10.1016/S0012-821X(02)00563-0

Gautheron, C., Moreira, M., Allègre, C., 2005. He, Ne and Ar composition of the European lithospheric mantle. Chem. Geol. 217, 97–112. https://doi.org/10.1016/j.chemgeo.2004.12.009

Gervasoni, F., Klemme, S., Rohrbach, A., Grützner, T., Berndt, J., 2017. Experimental constraints on mantle metasomatism caused by silicate and carbonate melts. Lithos 282–283, 173–186. https://doi.org/10.1016/j.lithos.2017.03.004

Gianni, G.M., Pesce, A., Soler, S.R., 2018. Transient plate contraction between two simultaneous slab windows: Insights from Paleogene tectonics of the Patagonian Andes. J. Geodyn. 121, 64–75. https://doi.org/10.1016/j.jog.2018.07.008

Giggenbach, W.., Sano, Y., Wakita, H., 1993. Isotopic composition of helium, and CO2 and CH4 contents in gases produced along the New Zealand part of a convergent plate boundary. Geochim. Cosmochim. Acta 57, 3427–3455. https://doi.org/10.1016/0016-7037(93)90549-C

Gioia, S.M.C.L., Pimentel, M.M., 2000. The Sm-Nd isotopic method in the geochronology laboratory of the University of Brasília. An. Acad. Bras. Cienc. 72, 219–245. https://doi.org/10.1590/S0001-37652000000200009

Gorring, M.L., Kay, S.M., 2001. Mantle processes and sources of neogene slab window magmas from Southern Patagonia, Argentina. J. Petrol. 42, 1067–1094. https://doi.org/10.1093/petrology/42.6.1067

Gorring, M.L., Kay, S.M., 2000. Carbonatite metasomatized peridotite xenoliths from southern Patagonia: Implications for lithospheric processes and Neogene plateau magmatism. Contrib. to Mineral. Petrol. 140, 55–72. https://doi.org/10.1007/s004100000164

Graham, D.W., 2002. Noble Gas Isotope Geochemistry of Mid-Ocean Ridge and Ocean Island

Basalts: Characterization of Mantle Source Reservoirs. Rev. Mineral. Geochemistry 47, 247–317. https://doi.org/10.2138/rmg.2002.47.8

Graham, D.W., Lupton, J.E., 1999. Helium isotopes in historical lavas from Mount Vesuvius Comment on "Noble gas isotopic ratios from historical lavas and fumaroles at Mount Vesuvius" by D. Tedesco et al. Earth Planet. Sci. Lett. 174, 241–244. https://doi.org/10.1016/S0012-821X(99)00268-X

Greenfield, A.M.R., Ghent, E.D., Russell, J.K., 2013. Geothermobarometry of spinel peridotites from southern British Columbia: implications for the thermal conditions in the upper mantle. Can. J. Earth Sci. 50, 1019–1032. https://doi.org/10.1139/cjes-2013-0037

Gregoire, M., Jego, S., Maury, R.C., Polve, M., Payot, B., Tamayo, R.A., Yumul, G.P., 2008. Metasomatic interactions between slab-derived melts and depleted mantle: Insights from xenoliths within Monglo adakite (Luzon arc, Philippines). Lithos 103, 415–430. https://doi.org/10.1016/j.lithos.2007.10.013

Griffin, W., Powell, W., Pearson, N.J., O'Reilly, S., 2008. GLITTER: data reduction software for laser ablation ICP-MS. Short Course Ser. 40, 308–311.

Harrison, D., Barry, T., Turner, G., 2004. Possible diffusive fractionation of helium isotopes in olivine and clinopyroxene phenocrysts. Eur. J. Mineral. 16, 213–220. https://doi.org/10.1127/0935-1221/2004/0016-0213

Hart, S.R., Hauri, E.H., Oschmann, L.A., Whitehead, J.A., 1992. Mantle Plumes and Entrainment: Isotopic Evidence. Science (80-.). 256, 517–520. https://doi.org/10.1126/science.256.5056.517

Hervé, F., Pankhurst, R.J., Fanning, C.M., Calderón, M., Yaxley, G.M., 2007. The South Patagonian batholith: 150 my of granite magmatism on a plate margin. Lithos 97, 373–

394. https://doi.org/10.1016/j.lithos.2007.01.007

Hilton, D.R., Craig, H., 1989. A helium isotope transect along the Indonesian archipelago. Nature 342, 906–908. https://doi.org/10.1038/342906a0

Hilton, D.R., Hammerschmidt, K., Teufel, S., Friedrichsen, H., 1993. Helium isotope characteristics of Andean geothermal fluids and lavas. Earth Planet. Sci. Lett. 120, 265–282. https://doi.org/10.1016/0012-821X(93)90244-4

Hilton, D.R., Hoogewerff, J.A., Bergen, M.J.V.A.N., Merschmidt, K.H.A., 1992. Mapping magma sources in the east Sunda-Banda arcs , Indonesia : Constraints from helium isotopes 56, 851–859.

Hopp, J., Ionov, D.A., 2011. Tracing partial melting and subduction-related metasomatism in the Kamchatkan mantle wedge using noble gas compositions. Earth Planet. Sci. Lett. 302, 121–131. https://doi.org/10.1016/j.epsl.2010.12.001

Ionov, D.A., 2002. Mechanisms and Sources of Mantle Metasomatism: Major and Trace Element Compositions of Peridotite Xenoliths from Spitsbergen in the Context of Numerical Modelling. J. Petrol. 43, 2219–2259. https://doi.org/10.1093/petrology/43.12.2219

Ishimaru, S., Arai, S., Ishida, Y., Shirasaka, M., Okrugin, V.M., 2007. Melting and multi-stage metasomatism in the mantle wedge beneath a frontal arc inferred from highly depleted peridotite xenoliths from the avacha volcano, Southern Kamchatka. J. Petrol. 48, 395–433. https://doi.org/10.1093/petrology/egl065

Jalowitzki, T., Gervasoni, F., Conceição, R. V., Orihashi, Y., Bertotto, G.W., Sumino, H., Schilling, M.E., Nagao, K., Morata, D., Sylvester, P., 2017. Slab-derived components in the subcontinental lithospheric mantle beneath Chilean Patagonia: Geochemistry and Sr–

Nd–Pb isotopes of mantle xenoliths and host basalt. Lithos 292–293, 179–197. https://doi.org/10.1016/j.lithos.2017.09.008

Jalowitzki, T., Sumino, H., Conceição, R. V., Orihashi, Y., Nagao, K., Bertotto, G.W., Balbinot, E., Schilling, M.E., Gervasoni, F., 2016. Noble gas composition of subcontinental lithospheric mantle: An extensively degassed reservoir beneath Southern Patagonia. Earth Planet. Sci. Lett. 450, 263–273. https://doi.org/10.1016/j.epsl.2016.06.034

Jeffcoate, A.B., Elliott, T., Kasemann, S.A., Ionov, D., Cooper, K., Brooker, R., 2007. Li isotope fractionation in peridotites and mafic melts. Geochim. Cosmochim. Acta 71, 202–218. https://doi.org/10.1016/j.gca.2006.06.1611

Jochum, K.P., Nohl, U., Herwig, K., Lammel, E., Stoll, B., Hofmann, A.W., 2005. GeoReM: A New Geochemical Database for Reference Materials and Isotopic Standards. Geostand. Geoanalytical Res. 29, 333–338. https://doi.org/10.1111/j.1751-908X.2005.tb00904.x

Johnson, K.T.M., 1998. Experimental determination of partition coefficients for rare earth and high-field-strength elements between clinopyroxene, garnet, and basaltic melt at high pressures. Contrib. to Mineral. Petrol. 133, 60–68. https://doi.org/10.1007/s004100050437

Johnson, K.T.M., Dick, H.J.B., Shimizu, N., 1990. Melting in the oceanic upper mantle: An ion microprobe study of diopsides in abyssal peridotites. J. Geophys. Res. 95, 2661. https://doi.org/10.1029/JB095iB03p02661

Kay, S., Gorring, M., Ramos, V., 2004. Magmatic sources, setting and causes of Eocene to Recent Patagonian plateau magmatism (36°S to 52°S latitude). Rev. la Asoc. Geol. Argentina 59, 556–568.

Kilian, R., Stern, C.R., 2002. Constraints on the interaction between slab melts and the mantle wedge from adakitic glass in peridotite xenoliths. Eur. J. Mineral. 14, 25–36.

https://doi.org/10.1127/0935-1221/2002/0014-0025

Kim, K.H., Nagao, K., Tanaka, T., Sumino, H., Nakamura, T., Okuno, M., Lock, J.B., Youn, J.S., Song, J., 2005. He-Ar and Nd-Sr isotopic compositions of ultramafic xenoliths and host alkali basalts from the Korean peninsula. Geochem. J. 39, 341–356. https://doi.org/10.2343/geochemj.39.341

Klein, E.M., Karsten, J.L., 1995. Ocean-ridge basalts with convergent-margin geochemical affinities from the Chile Ridge. Nature 374, 52–57. https://doi.org/10.1038/374052a0

Kobayashi, M., Sumino, H., Nagao, K., Ishimaru, S., Arai, S., Yoshikawa, M., Kawamoto, T., Kumagai, Y., Kobayashi, T., Burgess, R., Ballentine, C.J., 2017. Slab-derived halogens and noble gases illuminate closed system processes controlling volatile element transport into the mantle wedge. Earth Planet. Sci. Lett. 457, 106–116. https://doi.org/10.1016/j.epsl.2016.10.012

Köhler, T.P., Brey, G.P., 1990. Calcium exchange between olivine and clinopyroxene calibrated as a geothermobarometer for natural peridotites from 2 to 60 kb with applications. Geochim. Cosmochim. Acta 54, 2375–2388. https://doi.org/10.1016/0016-7037(90)90226-B

Laurora, A., Mazzucchelli, M., Rivalenti, G., Vannucci, R., Zanetti, A., Barbieri, M.A., Cingolani, C.A., 2001. Metasomatism and Melting in Carbonated Peridotite Xenoliths from the Mantle Wedge: The Gobernador Gregores Case (Southern Patagonia). J. Petrol. 42, 69–87. https://doi.org/10.1093/petrology/42.1.69

Liang, Y., Sun, C., Yao, L., 2013. A REE-in-two-pyroxene thermometer for mafic and ultramafic rocks. Geochim. Cosmochim. Acta 102, 246–260. https://doi.org/10.1016/j.gca.2012.10.035

Lucassen, F., Wiedicke, M., Franz, G., 2010. Complete recycling of a magmatic arc: Evidence from chemical and isotopic composition of Quaternary trench sediments in Chile (36°-40°S). Int. J. Earth Sci. 99, 687–701. https://doi.org/10.1007/s00531-008-0410-4

Luffi, P., Saleeby, J.B., Lee, C.-T.A., Ducea, M.N., 2009. Lithospheric mantle duplex beneath the central Mojave Desert revealed by xenoliths from Dish Hill, California. J. Geophys. Res. 114. https://doi.org/10.1029/2008jb005906

Martelli, M., Bianchini, G., Beccaluva, L., Rizzo, A., 2011. Helium and argon isotopic compositions of mantle xenoliths from Tallante and Calatrava, Spain. J. Volcanol. Geotherm. Res. 200, 18–26. https://doi.org/10.1016/j.jvolgeores.2010.11.015

Matsumoto, T., Chen, Y., Matsuda, J., 2001. Concomitant occurrence of primordial and recycled noble gases in the Earth's mantle. Earth Planet. Sci. Lett. 185, 35–47. https://doi.org/10.1016/S0012-821X(00)00375-7

Matsumoto, T., Morishita, T., Matsuda, J.I., Fujioka, T., Takebe, M., Yamamoto, K., Arai, S., 2005. Noble gases in the Finero phlogopite-peridotites, western Italian Alps. Earth Planet. Sci. Lett. 238, 130–145. https://doi.org/10.1016/j.epsl.2005.07.005

Mazzucchelli, M., Cipriani, A., Hémond, C., Zanetti, A., Bertotto, G.W., Cingolani, C.A., 2016. Origin of the DUPAL anomaly in mantle xenoliths of Patagonia (Argentina) and geodynamic consequences. Lithos 248–251, 257–271. https://doi.org/10.1016/j.lithos.2016.01.010

McDonough, W.F., 1990. Constraints on the composition of the continental lithospheric mantle. Earth Planet. Sci. Lett. 101, 1–18. https://doi.org/10.1016/0012-821X(90)90119-I

McDonough, W.F., Sun, S. -s., 1995. The composition of the Earth. Chem. Geol. 120, 223–253. https://doi.org/10.1016/0009-2541(94)00140-4

Melchiorre, M., Faccini, B., Grégoire, M., Benoit, M., Casetta, F., Coltorti, M., 2020. Melting and metasomatism/refertilisation processes in the Patagonian sub-continental lithospheric mantle: A review. Lithos 354–355, 1–16. https://doi.org/10.1016/j.lithos.2019.105324

Mercier, J.C.C., 1980. Single-pyroxene thermobarometry. Tectonophysics 70, 1–37. https://doi.org/10.1016/0040-1951(80)90019-0

Mercier, J.C.C., Nicolas, A., 1975. Textures and fabrics of upper-mantle peridotites as illustrated by xenoliths from basalts. J. Petrol. 16, 454–487. https://doi.org/10.1093/petrology/16.1.454

Morata, D., De La Cruz, R., Suárez, M., Demant, A., 2000. Mantle xenoliths and xenocrysts in the late Paleocene Patagonian continental flood basalts from Aysen, southern Chile, in: IX Congreso Geologico Chileno (Puerto Varas). Actas. pp. 226–229.

Morata, D., Oliva, C., de la Cruz, R., Suárez, M., 2005. The Bandurrias gabbro: Late Oligocene alkaline magmatism in the Patagonian Cordillera. J. South Am. Earth Sci. 18, 147–162. https://doi.org/10.1016/j.jsames.2004.09.001

Moreira, M., Allègre, C.J., 1998. Helium–neon systematics and the structure of the mantle. Chem. Geol. 147, 53–59. https://doi.org/10.1016/S0009-2541(97)00171-X

Moreira, M., Kunz, J., Allègre, C., 1998. Rare gas systematics in popping rock: Isotopic and elemental compositions in the upper mantle. Science (80-.). 279, 1178–1181. https://doi.org/10.1126/science.279.5354.1178

Ntaflos, T., Bjerg, E.A., Labudia, C.H., Kurat, G., 2007. Depleted lithosphere from the mantle wedge beneath Tres Lagos, southern Patagonia, Argentina. Lithos 94, 46–65. https://doi.org/10.1016/j.lithos.2006.06.011

Oliveros, V., Vásquez, P., Creixell, C., Lucassen, F., Ducea, M.N., Ciocca, I., González, J., Espinoza, M., Salazar, E., Coloma, F., Kasemann, S.A., 2020. Lithospheric evolution of the Pre- and Early Andean convergent margin, Chile. Gondwana Res. 80, 202–227. https://doi.org/10.1016/j.gr.2019.11.002

Osawa, T., 2004. A New Correction Technique for Mass Interferences by 40Ar++ and CO2++ during Isotope Analysis of a Small Amount of Ne. J. Mass Spectrom. Soc. Jpn. 52, 230–232. https://doi.org/10.5702/massspec.52.230

Ottolini, L., Le Fèvre, B., Vannucci, R., 2004. Direct assessment of mantle boron and lithium contents and distribution by SIMS analyses of peridotite minerals. Earth Planet. Sci. Lett. 228, 19–36. https://doi.org/10.1016/j.epsl.2004.09.027

Ozima, M., Podosek, F.A., 1983. Noble Gas Geochemistry, 1st ed. Cambridge University Press.

Pankhurst, R.., Leat, P.., Sruoga, P., Rapela, C.., Márquez, M., Storey, B.., Riley, T.., 1998. The Chon Aike province of Patagonia and related rocks in West Antarctica: A silicic large igneous province. J. Volcanol. Geotherm. Res. 81, 113–136. https://doi.org/10.1016/S0377-0273(97)00070-X

Pankhurst, R.J., Riley, T.R., Fanning, C.M., Kelley, S.P., 2000. Episodic Silicic Volcanism in Patagonia and the Antarctic Peninsula: Chronology of Magmatism Associated with the Break-up of Gondwana. J. Petrol. 41, 605–625. https://doi.org/10.1093/petrology/41.5.605

Pankhurst, R.J., Weaver, S.D., Hervé, F., Larrondo, P., 1999. Mesozoic-Cenozoic evolution of the North Patagonian Batholith in Aysen, southern Chile. J. Geol. Soc. London. 156, 673–694. https://doi.org/10.1144/gsjgs.156.4.0673

Parada, M.A., Lahsen, A., Palacios, C., 2001. Ages and geochemistry of Mesozoic-Eocene back-arc volcanic rocks in the Aysén region of the Patagonian Andes, Chile. Rev.

geológica Chile.

Paton, C., Hellstrom, J., Paul, B., Woodhead, J., Hergt, J., 2011. Iolite: Freeware for the visualisation and processing of mass spectrometric data. J. Anal. At. Spectrom. 26, 2508. https://doi.org/10.1039/c1ja10172b

Peslier, A.H., Francis, D., Ludden, J., 2002. The Lithospheric Mantle beneath Continental Margins: Melting and Melt-Rock Reaction in Canadian Cordillera Xenoliths. J. Petrol. 43, 2013–2047. https://doi.org/10.1093/petrology/43.11.2013

Prelević, D., Jacob, D.E., Foley, S.F., 2013. Recycling plus: A new recipe for the formation of Alpine-Himalayan orogenic mantle lithosphere. Earth Planet. Sci. Lett. 362, 187–197. https://doi.org/10.1016/j.epsl.2012.11.035

Ramos, V.A., Kay, S.M., 1992. Southern Patagonian plateau basalts and deformation: Backarc testimony of ridge collisions. Tectonophysics 205, 261–282. https://doi.org/10.1016/0040-1951(92)90430-E

Rapp, R.P., Shimizu, N., Norman, M.D., Applegate, G.S., 1999. Reaction between slab-derived melts and peridotite in the mantle wedge: Experimental constraints at 3.8 GPa. Chem. Geol. 160, 335–356. https://doi.org/10.1016/S0009-2541(99)00106-0

Rivalenti, G., Mazzucchelli, M., Laurora, A., Ciuffi, S.I.A., Zanetti, A., Vannucci, R., Cingolani, C.A., 2004. The backarc mantle lithosphere in Patagonia, South America. J. South Am. Earth Sci. 17, 121–152. https://doi.org/10.1016/j.jsames.2004.05.009

Rivalenti, G., Mazzucchelli, M., Zanetti, A., Vannucci, R., Bollinger, C., Hémond, C., Bertotto, G.W., 2007. Xenoliths from Cerro de los Chenques (Patagonia): An example of slab-related metasomatism in the backarc lithospheric mantle. Lithos 99, 45–67. https://doi.org/10.1016/j.lithos.2007.05.012

Rodriguez, E.E., Russo, R.M., 2020. Southern Chile crustal structure from teleseismic receiver functions: Responses to ridge subduction and terrane assembly of Patagonia. Geosphere 16, 378–391. https://doi.org/10.1130/GES01692.1

Roduit, N., 2007. JMicroVision: un logiciel d'analyse d'images pétrographiques polyvalent. Terre Environ.

Rudnick, R.L., Gao, S., 2003. Composition of the Continental Crust, in: Treatise on Geochemistry. Elsevier, pp. 1–64. https://doi.org/10.1016/B0-08-043751-6/03016-4

Sarda, P., Staudacher, T., Allègre, C.J., 1988. Neon isotopes in submarine basalts. Earth Planet. Sci. Lett. 91, 73–88. https://doi.org/10.1016/0012-821X(88)90152-5

Schilling, M.E., Carlson, R.W., Conceição, R.V., Dantas, C., Bertotto, G.W., Koester, E., 2008. Re–Os isotope constraints on subcontinental lithospheric mantle evolution of southern South America. Earth Planet. Sci. Lett. 268, 89–101. https://doi.org/10.1016/j.epsl.2008.01.005

Schilling, M.E., Carlson, R.W., Tassara, A., Conceição, R.V., Bertotto, G.W., Vásquez, M., Muñoz, D., Jalowitzki, T., Gervasoni, F., Morata, D., 2017. The origin of Patagonia revealed by Re-Os systematics of mantle xenoliths. Precambrian Res. 294, 15–32. https://doi.org/10.1016/j.precamres.2017.03.008

Seitz, H.-M., Woodland, A.B., 2000. The distribution of lithium in peridotitic and pyroxenitic mantle lithologies — an indicator of magmatic and metasomatic processes. Chem. Geol. 166, 47–64. https://doi.org/10.1016/S0009-2541(99)00184-9

Shaw, D.M., 2006. Trace Elements in Magmas: A Theoretical Treatment. Cambridge University Press.

Shi, L., Francis, D., Ludden, J., Frederiksen, A., Bostock, M., 1998. Xenolith evidence for lithospheric melting above anomalously hot mantle under the northern Canadian Cordillera. Contrib. to Mineral. Petrol. 131, 39–53. https://doi.org/10.1007/s004100050377

Somoza, R., Ghidella, M.E., 2012. Late Cretaceous to recent plate motions in western South America revisited. Earth Planet. Sci. Lett. 331–332, 152–163. https://doi.org/10.1016/j.epsl.2012.03.003

Stern, C.R., Kilian, R., Olker, B., Hauri, E.H., Kurtis Kyser, T., 1999. Evidence from mantle xenoliths for relatively thin (<100 km) continental lithosphere below the Phanerozoic crust of southernmost South America, in: Developments in Geotectonics. pp. 217–235. https://doi.org/10.1016/S0419-0254(99)80013-5

Sturm, M.E., Klein, E.M., Graham, D.W., Karsten, J., 1999. Age constraints on crustal recycling to the mantle beneath the southern Chile Ridge: He-Pb-Sr-Nd isotope systematics. J. Geophys. Res. Solid Earth 104, 5097–5114. https://doi.org/10.1029/1998JB900107

Sumino, H., Nagao, K., Notsu, K., 2001. Highly Sensitive and Precise Measurement of Helium Isotopes Using a Mass Spectrometer with Double Collector System. J. Mass Spectrom. Soc. Jpn. 49, 61–68. https://doi.org/10.5702/massspec.49.61

Sumino, H., Notsu, K., Nakai, S., Sato, M., Nagao, K., Hosoe, M., Wakita, H., 2004. Noble gas and carbon isotopes of fumarolic gas from Iwojima volcano, Izu-Ogasawara arc, Japan: Implications for the origin of unusual arc magmatism. Chem. Geol. 209, 153–173. https://doi.org/10.1016/j.chemgeo.2004.05.002

Sun, S. -s., McDonough, W.F., 1989. Chemical and isotopic systematics of oceanic basalts:

implications for mantle composition and processes. Geol. Soc. London, Spec. Publ. 42, 313–345. https://doi.org/10.1144/GSL.SP.1989.042.01.19

Tucker, J.M., Mukhopadhyay, S., Schilling, J.G., 2012. The heavy noble gas composition of the depleted MORB mantle (DMM) and its implications for the preservation of heterogeneities in the mantle. Earth Planet. Sci. Lett. 355–356, 244–254. https://doi.org/10.1016/j.epsl.2012.08.025

Völker, D., Reichel, T., Wiedicke, M., Heubeck, C., 2008. Turbidites deposited on Southern Central Chilean seamounts: Evidence for energetic turbidity currents. Mar. Geol. 251, 15–31. https://doi.org/10.1016/j.margeo.2008.01.008

Workman, R.K., Hart, S.R., 2005. Major and trace element composition of the depleted MORB mantle (DMM). Earth Planet. Sci. Lett. 231, 53–72. https://doi.org/10.1016/j.epsl.2004.12.005

Yamamoto, J., Kaneoka, I., Nakai, S., Kagi, H., Prikhod'ko, V.S., Arai, S., 2004. Evidence for subduction-related components in the subcontinental mantle from low 3He/4He and 40Ar/36Ar ratio in mantle xenoliths from Far Eastern Russia. Chem. Geol. 207, 237–259. https://doi.org/10.1016/j.chemgeo.2004.03.007

Yamamoto, J., Nishimura, K., Sugimoto, T., Takemura, K., Takahata, N., Sano, Y., 2009. Diffusive fractionation of noble gases in mantle with magma channels: Origin of low He/Ar in mantle-derived rocks. Earth Planet. Sci. Lett. 280, 167–174. https://doi.org/10.1016/j.epsl.2009.01.029
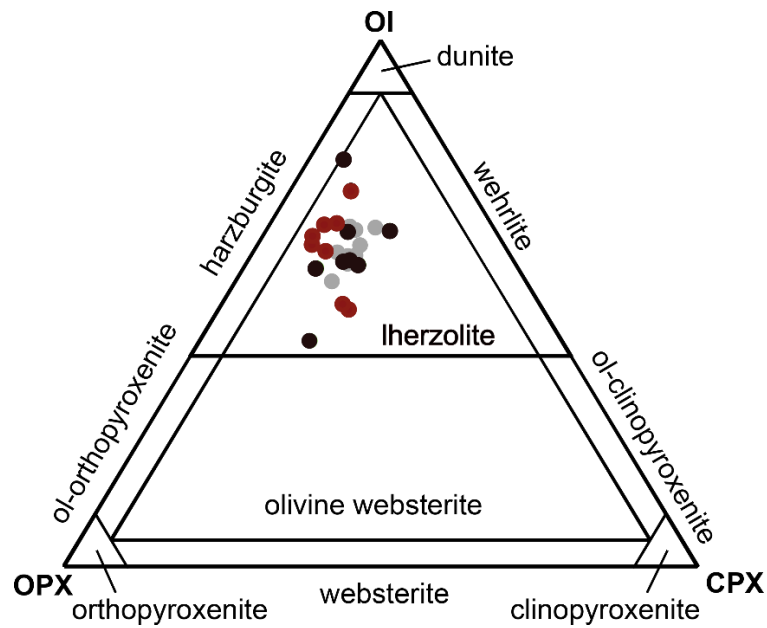
Figure S1. Ternary diagram (Ol–Cpx–Opx) (Streckeisen, 1976) containing Coyhaique xenoliths mineral abundances. Samples with inedited whole-rock results are indicated in red. For comparison, samples from Jalowitzki et al. (2017) are displayed in black and gray circles. The prior represents samples that were detailed investigated in this work.
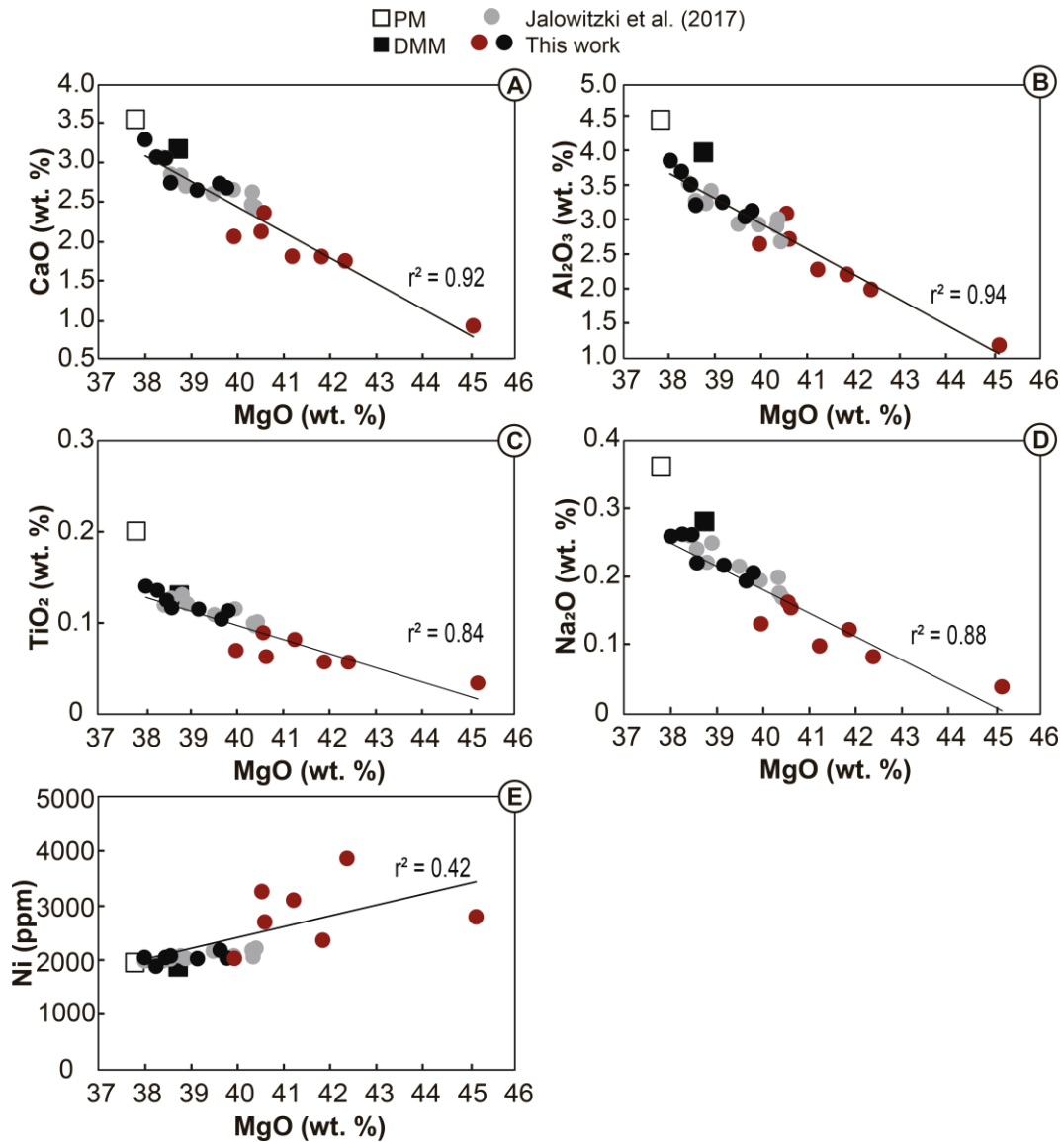
Figure S2. Whole-rock MgO variation diagrams with well-defined correlation coefficients (r^2 = 0.84–0.94) for selected major elements (wt.%) and Ni (ppm) (r^2 = 0.42) for Coyhaique xenoliths. Samples with inedited whole-rock results are indicated in red. For comparison, Coyhaique xenoliths from Jalowitzki et al. (2017) are plotted in black and gray circles. The prior represents samples that were detailed investigated in this work. Primitive mantle (PM; McDonough and Sun, 1995) and Depleted MORB mantle (DMM; Workman and Hart, 2005) compositions are plotted for comparison.
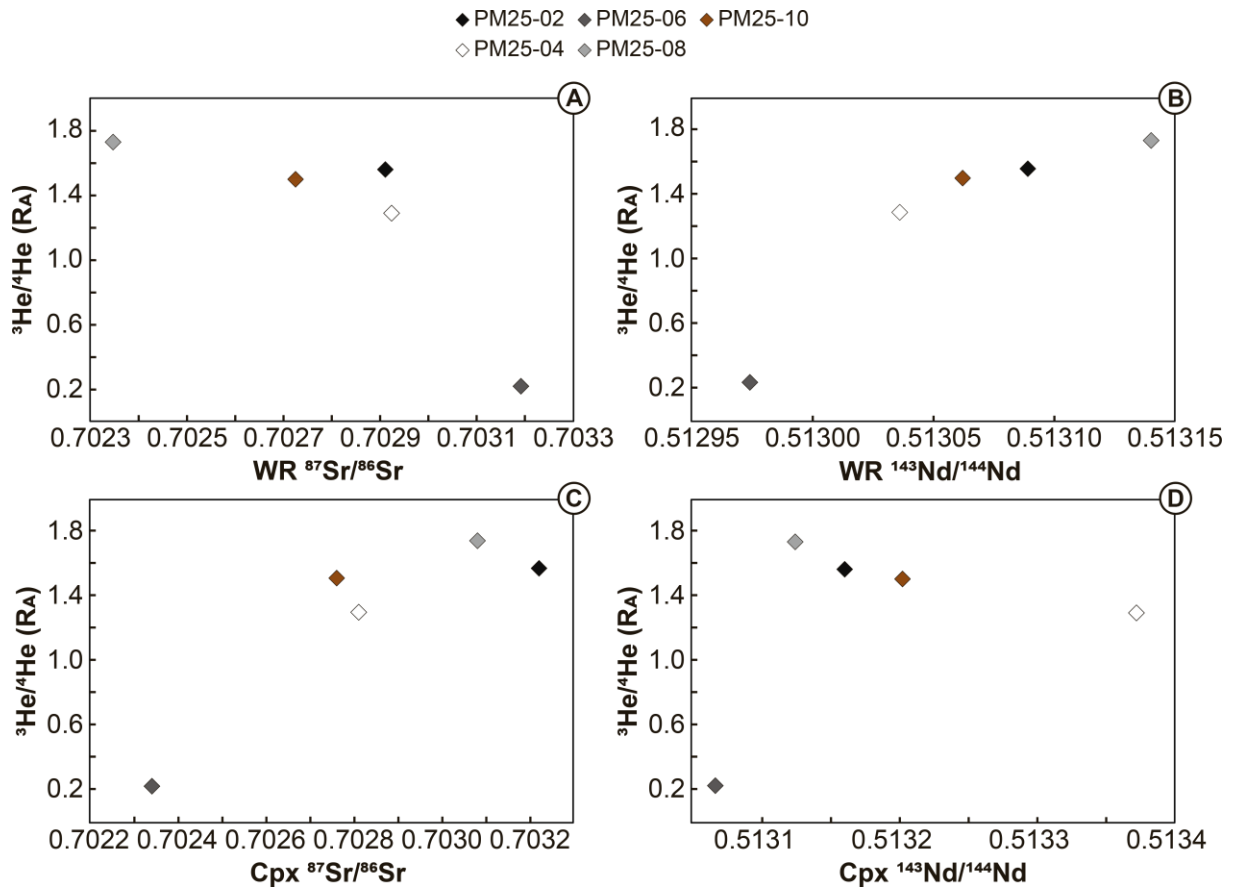
Figure S3. Total ^{3}He/^{4}He versus whole-rock ^{87}Sr/^{86}Sr (A) and ^{144}Nd/^{143}Nd (B), and clinopyroxene ^{87}Sr/^{86}Sr (C) and ^{144}Nd/^{143}Nd (D) ratios. Samples define a negative correlation in A and B, and a positive correlation in B and C. WR = whole-rock; Cpx = clinopyroxene. See details in sections 4.2. 4.5.1 and 4.2.5.2.2.3.
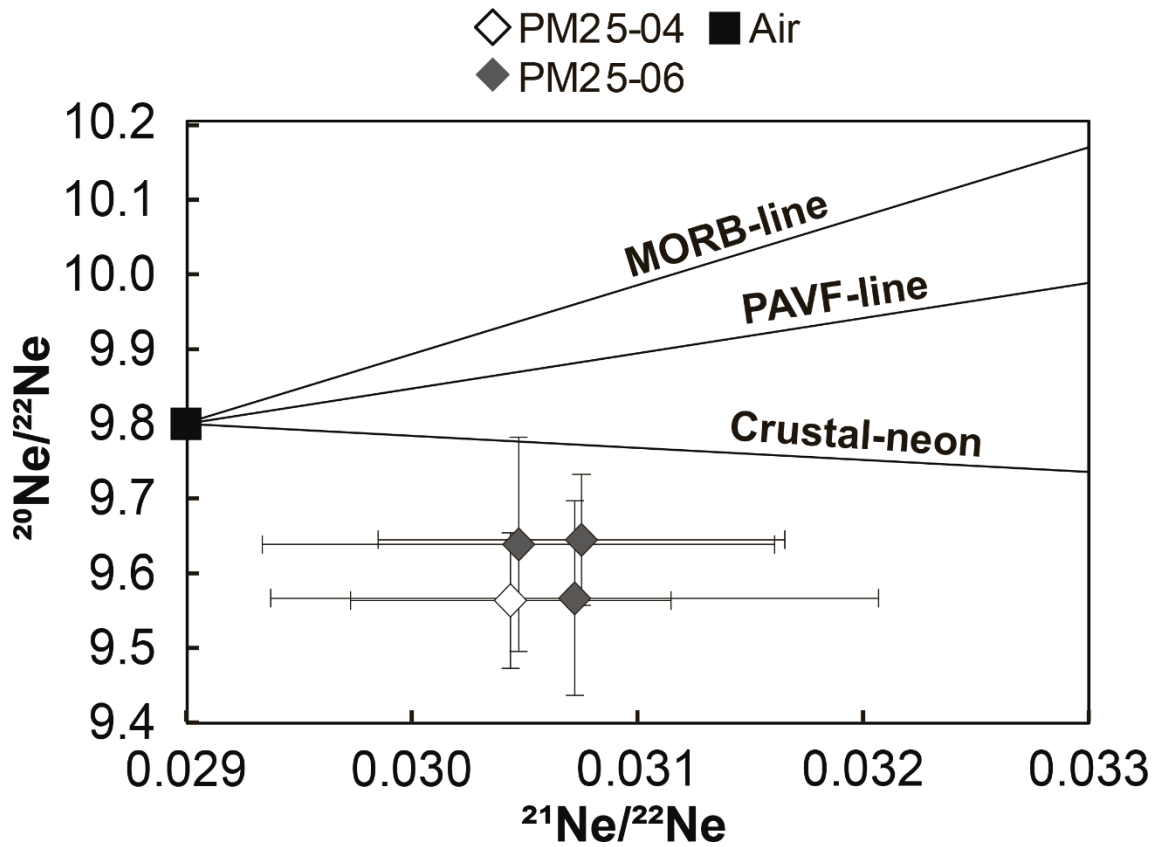
Figure S4. Three-isotopes Ne diagram showing the distribution of studied samples, showing strongly nucleogenic behavior (^{21}Ne excess) with respect to MORB (Moreira and Allègre, 1998; Sarda et al., 1988) and Pali-Aike Volcanic Field (PAVF) SCLM (Jalowitzki et al., 2016) endmembers. Note that our samples show even more nucleogenic component than Crustal-neon trend (Kennedy et al., 1990). Only data that differ from air within 1σ uncertainty are shown.
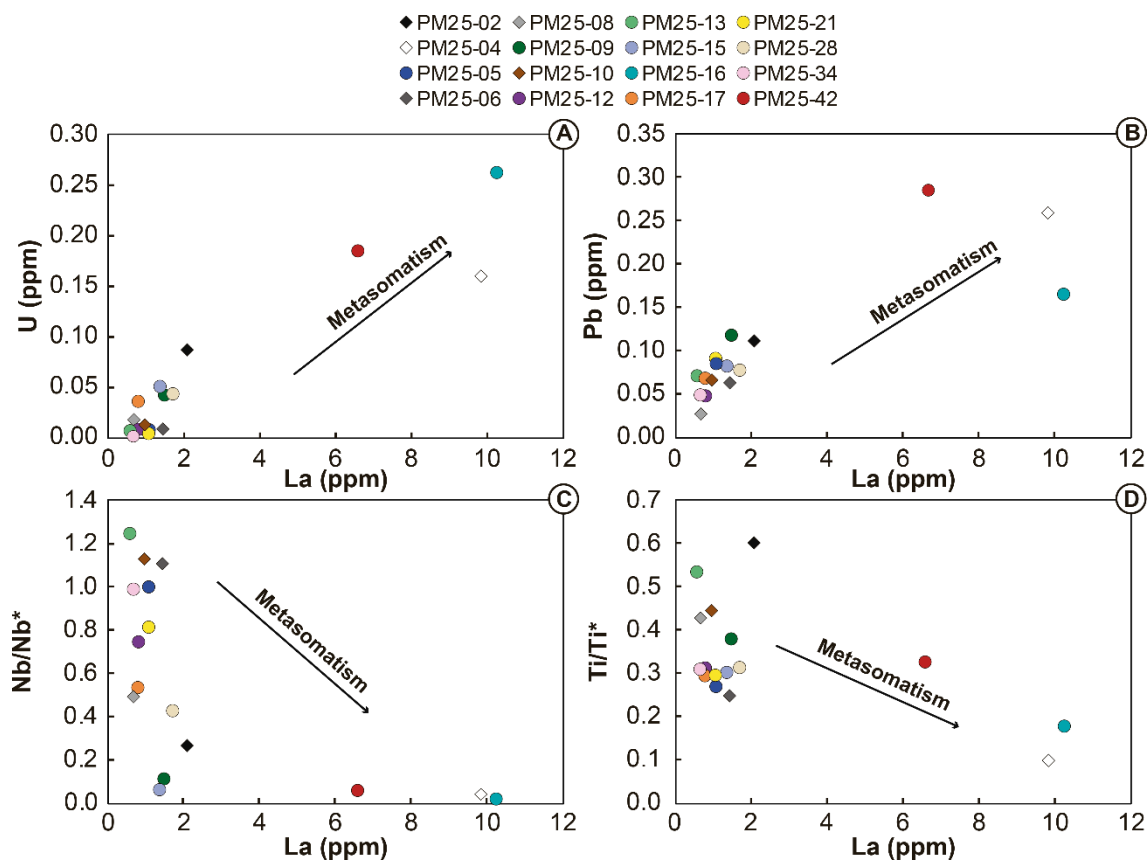
Figure S5. La versus U (A) and Pb (B) (all in ppm) displaying positive correlations while negative correlations are observed when La is compared to Nb/Nb* (C) and Ti/Ti* (D). These patterns indicate enrichment in incompatible elements and suggest slab-derived metasomatism.
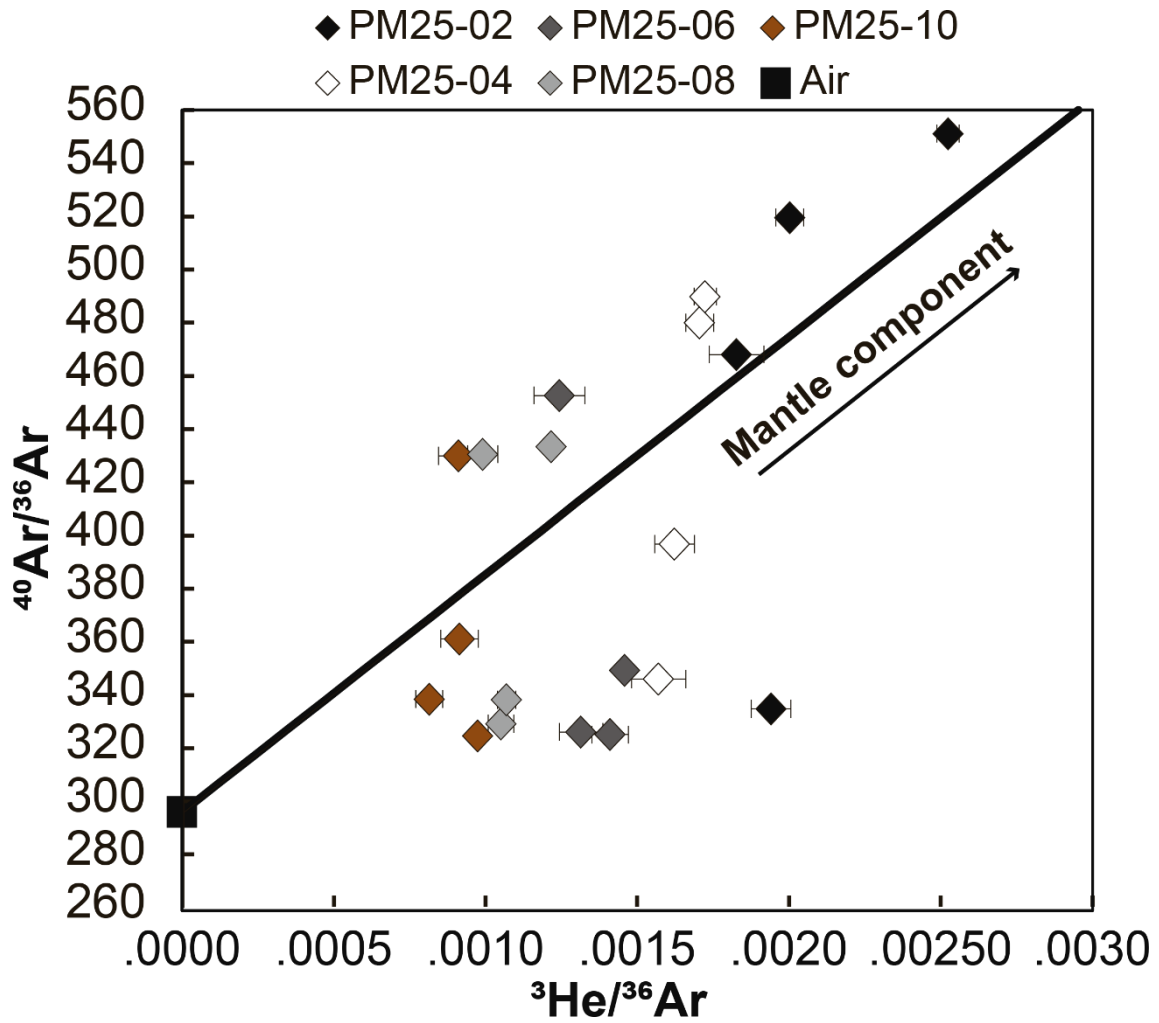
Figure S6. $^{40}Ar/^{36}Ar$ vs. $^{3}He/^{36}Ar$ ratios of Coyhaique lherzolites. Individual stepwise crushing analyses (100, 500, 1000, 2000 times strokes) defining a mixing between atmospheric and the local mantle source component with a $^{3}He/^{36}Ar_{(E)}$ ratio of 0.45 assuming a $^{40}Ar/^{36}Ar$ ratio of 40000 (Moreira et al., 1998; Tucker et al., 2012). Extrapolating the mixing line between air and $^{3}He/^{36}Ar$ MORB ratio at 0.7, the Coyhaique SCLM shows $^{40}Ar/^{36}Ar_{(E)}$ = 63000. All errors are shown to 1σ.

Supplementary material

Major element obtained by X-ray fluorescenc (XRF)

(wt. %)	Reference material		Reference material preferred values (PV)	Precision (run1/run2)	Accuracy (run1/PV)
	BIR-1-G		BIR-1-G (GeoRem)		
	(run 1)	(run 2)			
SiO_2	47.82	48.02	47.50	1.00	1.01
TiO_2	0.95	0.95	1.04	1.00	0.91
Al_2O_3	15.59	15.65	15.50	1.00	1.01
Fe_2O_3	11.56	11.65	10.40	0.99	1.11
MnO	0.17	0.17	0.19	1.03	0.91
MgO	9.45	9.45	9.40	1.00	1.01
CaO	13.39	13.43	13.30	1.00	1.01
Na_2O	2.13	2.14	1.85	0.99	1.15
K_2O	0.06	0.05	0.03	1.17	2.01
P_2O_5	0.07	0.07	0.03	1.02	2.52
Total	101.31	101.70	99.24	1.00	1.02

Trace element obtained by inductively- coupled plasmamass spectrometer (ICP-MS)

(ppm)		Sample		Reference material	Reference material preferred values (PV)	Precision	Accuracy
	Limit of detection	PM25-34 (run)	PM25-34 (duplicate)	MRG-1 (run)	MRG-1 (MUN 495-633)	PM25-34 (run/duplicate)	MRG-1 (run/PV)
Cs	0.01	0.05	0.05	0.65	0.60	0.98	1.08
Rb	1.67	2.28	1.89	15.59	7.65	1.20	2.04
Ba	0.19	9.24	7.84	53.35	47.50	1.18	1.12
W	0.003	0.53	0.06	1.02	0.30	9.55	3.41
Th	0.02	0.38	0.13	1.07	0.78	3.06	1.37
U	0.01	0.11	0.11	0.28	0.25	0.96	1.12
Nb	0.02	0.11	0.16	19.76	22.30	0.66	0.89
Ta	0.004	0.01	0.01	0.83	0.83	0.75	1.00
La	0.01	1.20	0.97	9.66	9.07	1.23	1.07
Ce	0.01	3.11	3.33	25.59	26.20	0.93	0.98
Pb	0.05	0.20	0.11	4.22	5.20	1.87	0.81
Pr	0.01	0.49	0.45	4.02	3.79	1.07	1.06
Sr	0.20	20.12	22.03	260.65	274.00	0.91	0.95
Nd	0.07	2.08	1.83	19.35	18.30	1.14	1.06
Sm	0.08	0.55	0.40	4.56	4.51	1.36	1.01
Zr	0.02	16.09	18.61	100.87	93.70	0.86	1.08
Hf	0.08	0.44	0.43	4.39	3.76	1.02	1.17
Eu	0.02	0.17	0.14	1.45	1.46	1.22	1.00
Sn	0.24	0.21	0.11	2.84	3.60	1.91	0.79
Ti	2.51	833.91	711.12	22.07	22.60	1.17	0.98
Gd	0.04	0.71	0.68	4.34	4.11	1.04	1.06
Tb	0.01	0.12	0.11	0.60	0.55	1.11	1.09
Dy	0.05	0.82	0.82	3.27	3.01	1.00	1.09
Y	0.01	4.74	4.47	13.20	11.60	1.06	1.14
Ho	0.01	0.18	0.18	0.57	0.51	0.99	1.12
Er	0.03	0.57	0.57	1.48	1.21	1.01	1.22
Tm	0.01	0.09	0.10	0.25	0.15	0.89	1.69
Yb	0.06	0.57	0.50	1.17	0.81	1.14	1.45
Lu	0.01	0.09	0.08	0.17	0.11	1.06	1.51

Table S1. Whole-rock major (XRF) and trace (ICP-MS) reference material and sample duplicates data used for analyses calibration.

	Limit of detection	Reference Material				Reference material preferred values (PV)				Precision and accuracy			
		NIST612 (run)	BIR-1G (run)	BHVO-2G (run)	355OL (run)	NIST612 (GeoRem 5211)	BIR-1G (GeoRem 492)	BHVO-2G (GeoRem 492)	355OL (Bussweiler et al., 2019)	NIST612 (run/PV)	BIR-1G (run/PV)	BHVO-2G (run/PV)	355OL (run/PV)
B	0.350	-	-	-	-	-	-	-	-	-	-	-	-
Cs	0.012	42.03	-	0.10	-	42.70	0.01	0.10	-	0.98	-	1.00	-
Rb	0.027	31.42	0.19	8.99	-	31.40	0.20	9.20	-	1.00	0.99	0.98	-
Ba	0.005	39.74	6.51	134.64	-	39.30	6.50	131.00	-	1.01	1.00	1.03	-
W	0.044	38.27	0.01	0.53	-	38.00	-	0.23	-	1.01	-	2.31	-
Th	0.0005	37.93	0.03	1.17	-	37.79	0.03	1.22	-	1.00	0.92	0.96	-
U	0.012	37.49	0.04	0.42	-	37.38	0.02	0.40	-	1.00	1.56	1.05	-
Nb	0.001	40.03	0.52	17.85	0.34	38.90	0.52	18.30	0.39	1.03	1.01	0.98	0.87
Ta	0.001	39.96	0.03	1.12	0.03	37.60	0.04	1.15	-	1.06	0.97	0.98	-
La	0.0003	35.81	0.56	14.68	-	36.00	0.61	15.20	-	0.99	0.93	0.97	-
Ce	0.001	38.77	1.92	37.51	-	38.40	1.89	37.60	0.02	1.01	1.01	1.00	-
Pb	0.005	38.70	3.50	1.62	-	38.57	3.70	1.70	-	1.00	0.95	0.95	-
Pr	0.001	37.27	0.35	4.97	-	37.90	0.37	5.35	-	0.98	0.93	0.93	-
Sr	0.016	78.47	107.80	393.29	-	78.40	109.00	396.00	0.09	1.00	0.99	0.99	-
Nd	0.003	35.93	2.29	23.61	-	35.50	2.37	24.50	-	1.01	0.97	0.96	-
Sm	0.004	38.14	1.02	5.87	-	37.70	1.09	6.10	-	1.01	0.94	0.96	-
Zr	0.036	38.04	12.55	153.51	0.10	37.90	14.00	170.00	0.12	1.00	0.90	0.90	0.83
Hf	0.002	35.03	0.49	3.96	0.004	36.70	0.57	4.32	-	0.95	0.86	0.92	-
Eu	0.001	35.04	0.49	1.99	0.001	35.60	0.52	2.07	-	0.98	0.95	0.96	-
Sn	0.121	38.82	0.80	2.03	-	38.60	2.30	2.60	-	1.01	0.35	0.78	-
Sb	0.088	34.91	0.51	0.29	-	34.70	0.56	0.30	-	1.01	0.90	0.96	-
Ti	11.260	44.08	6239	18260	10.34	44.00	5400	16300	-	1.00	1.16	1.12	-
Gd	0.003	36.73	1.62	5.70	-	37.30	1.85	6.16	-	0.98	0.88	0.93	-
Tb	0.001	36.01	0.31	0.82	-	37.60	0.35	0.92	-	0.96	0.88	0.89	-
Dy	0.002	36.05	2.33	4.93	0.003	35.50	2.55	5.28	-	1.02	0.91	0.93	-
Li	0.350	42.10	3.05	4.37	0.80	40.20	3.00	4.40	0.90	1.05	1.02	0.99	0.89
Y	0.001	38.06	13.14	22.44	0.002	38.30	14.30	26.00	0.002	0.99	0.92	0.86	0.90
Ho	0.001	38.01	0.51	0.90	0.001	38.30	0.56	0.98	-	0.99	0.92	0.91	-
Er	0.002	38.00	1.52	2.29	-	38.00	1.70	2.56	-	1.00	0.90	0.90	-
Tm	0.001	38.08	0.22	0.30	-	36.80	0.24	0.34	-	1.03	0.91	0.87	-
Yb	0.002	39.28	1.48	1.87	-	39.20	1.64	2.01	-	1.00	0.90	0.93	-
Lu	0.001	36.94	0.22	0.25	0.001	37.00	0.25	0.28	-	1.00	0.88	0.89	-

Table S2. LA-ICP-MS trace element data of calibration reference materials (BIR-1G, BHVO-2G and NIST 612 and 355OL).

Sample	Texture (Mercier and Nicolas, 1975)	Modes (%)				Cpx/Opx	Classification
		Ol	Opx	Cpx	Sp		
PM25-02	Protogranular	64.0	26.0	8.5	1.5	0.3	Spinel lherzolite
PM25-04	Protogranular	58.0	27.7	11.0	3.3	0.4	Spinel lherzolite
PM25-05*	Protogranular	47.2	29.6	19.9	3.3	0.7	Spinel lherzolite
PM25-06	Protogranular	60.4	29.8	8.5	1.3	0.3	Spinel lherzolite
PM25-08	Protogranular	71.1	18.9	9.6	0.3	0.5	Spinel lherzolite
PM25-09*	Protogranular	62.6	23.3	10.1	4.0	0.4	Spinel lherzolite
PM25-10	Protogranular	62.0	29.0	7.8	1.2	0.3	Spinel lherzolite
PM25-12*	Protogranular	48.5	30.2	18.6	2.7	0.6	Spinel lherzolite
PM25-13	Protogranular	62.1	22.8	12.7	2.4	0.6	Spinel lherzolite
PM25-15	Protogranular	55.2	24.0	17.2	3.6	0.7	Spinel lherzolite
PM25-16	Protogranular	53.9	30.4	11.0	4.8	0.4	Spinel lherzolite
PM25-17*	Protogranular	56.8	25.1	15.7	2.4	0.6	Spinel lherzolite
PM25-21*	Protogranular	62.1	16.2	19.1	2.6	1.2	Spinel lherzolite
PM25-28*	Protogranular	41.7	38.7	16.9	2.7	0.4	Spinel lherzolite
PM25-34*	Protogranular	56.2	26.1	14.7	3.0	0.6	Spinel lherzolite
PM25-42	Protogranular	75.6	17.1	5.0	2.4	0.3	Spinel lherzolite

Table S3. Modal mineralogy of studied samples. The modal proportions of the minerals were determined by point-counting with 2000–2800 points covering the entire thin section. All samples were classified as spinel-lherzolites with protogranular texture. *Samples published by Jalowitzki et al. (2017). Ol: olivine. Opx: orthopyroxene. Cpx: clinopyroxene. Sp: spinel.

	PM25-02	PM25-04	PM25-05*	PM25-06	PM25-08	PM25-09*	PM25-10	PM25-12*	PM25-13	PM25-15*	PM25-16	PM25-17*	PM25-21*	PM25-28*	PM25-34*	PM25-42
SiO_2	-	44.26	44.23	44.38	44.43	43.81	43.39	43.65	44.58	43.79	44.20	44.11	-	44.48	43.86	44.53
TiO_2	-	0.06	0.14	0.08	0.06	0.10	0.03	0.11	0.06	0.11	0.09	0.12	-	0.14	0.12	0.07
Al_2O_3	-	2.00	3.70	2.28	2.21	3.05	1.19	3.26	2.73	3.13	3.09	3.51	-	3.86	3.22	2.65
Fe_2O_3	-	8.95	9.68	9.27	8.96	9.92	8.68	8.93	9.26	8.65	9.30	9.56	-	8.94	9.23	9.52
MnO	-	0.12	0.14	0.13	0.12	0.14	0.12	0.13	0.13	0.12	0.13	0.13	-	0.13	0.13	0.14
MgO	-	42.36	38.26	41.21	41.85	39.63	45.14	39.15	40.59	39.79	40.53	38.46	-	38.01	38.57	39.95
CaO	-	1.75	3.07	1.81	1.80	2.73	0.93	2.65	2.36	2.68	2.12	3.05	-	3.29	2.74	2.06
Na_2O	-	0.08	0.26	0.10	0.12	0.19	0.04	0.22	0.15	0.21	0.16	0.26	-	0.26	0.22	0.13
K_2O	-	0.02	0.02	0.02	0.02	0.02	0.01	0.02	0.02	0.02	0.02	0.01	-	0.01	0.02	0.02
P_2O_5	-	0.03	0.02	0.02	0.02	0.02	0.02	0.02	0.01	0.02	0.03	0.02	-	0.02	0.01	0.02
Total	-	99.64	99.50	99.30	99.58	99.62	99.55	98.14	99.90	98.52	99.68	99.23	-	99.14	98.11	99.08
Mg#[a]	-	90.4	88.7	89.8	90.2	88.8	91.1	89.7	89.7	90.1	89.6	88.8	-	89.4	89.2	89.3
LOI%	-	1.32	0.69	1.02	1.27	0.91	0.92	0.75	0.51	8.76	0.50	0.41	-	0.60	0.59	0.91
V	64	83	89	75	56	64	37	66	78	74	86	75	78	82	65	55
Cr	2541	3848	3088	2806	3152	2830	2253	2994	2777	3002	3275	2909	2982	2982	2802	3128
Ni	2974	3863	1893	3101	2370	2184	2795	2033	2702	2041	3261	2050	2199	2050	2083	2038
Co	146	181	176	151	113	104	127	118	132	114	157	119	126	111	135	108
Cu	20	18	24	186	16	21	14	19	23	28	33	28	21	32	25	8
Zn	83	80	22	133	56	32	61	32	117	27	75	35	25	21	20	108
Rb	3.57	3.85	3.29	3.38	3.57	2.23	3.62	1.25	3.79	3.09	5.38	5.76	4.40	3.74	2.28	3.55
Sr	8.72	9.18	31.94	10.98	7.84	21.33	5.41	15.57	6.32	20.81	10.37	16.68	27.48	17.25	20.12	7.71
Y	1.39	1.96	7.03	2.15	1.63	4.14	1.27	5.16	1.56	4.25	3.75	3.75	5.76	4.61	4.74	1.70
Zr	8.52	8.01	18.77	6.76	5.13	9.80	6.49	8.99	4.21	11.09	26.73	8.75	11.56	10.25	16.09	5.00
Nb	0.26	0.20	0.26	0.07	0.13	0.12	0.20	0.13	0.04	0.20	0.43	0.07	0.15	0.24	0.11	0.19
Sn	0.80	0.37	0.62	0.23	0.32	0.21	0.22	0.16	0.28	0.27	0.46	0.90	0.66	0.13	0.21	0.37
Cs	0.03	0.06	0.07	0.03	0.04	0.14	0.06	0.02	0.04	0.12	0.06	0.05	0.06	0.06	0.05	0.06
Ba	10.49	4.04	2.79	4.31	5.32	20.12	3.31	9.23	7.53	2.47	3.85	10.53	23.01	8.05	9.24	8.11
La	0.78	0.53	0.65	0.19	0.32	0.71	0.27	0.99	0.39	0.46	1.98	0.67	1.21	1.11	1.20	0.78
Ce	1.53	1.23	1.92	0.65	0.81	1.86	0.55	2.51	0.60	1.20	4.36	1.59	2.81	2.83	3.11	1.74
Pr	0.17	0.14	0.34	0.13	0.11	0.29	0.08	0.40	0.07	0.21	0.55	0.25	0.44	0.43	0.49	0.22
Nd	0.71	0.63	1.90	0.63	0.49	1.28	0.36	1.71	0.28	1.10	2.07	1.15	2.02	1.77	2.08	0.65
Sm	0.22	0.18	0.62	0.23	0.14	0.43	0.11	0.58	0.10	0.42	0.47	0.36	0.66	0.46	0.54	0.17
Eu	0.06	0.08	0.21	0.08	0.05	0.14	0.04	0.19	0.04	0.16	0.16	0.15	0.23	0.16	0.17	0.05
Gd	0.22	0.30	1.02	0.34	0.17	0.54	0.15	0.68	0.16	0.60	0.56	0.49	0.86	0.66	0.71	0.20
Tb	0.03	0.05	0.20	0.06	0.03	0.11	0.03	0.12	0.04	0.11	0.10	0.10	0.17	0.12	0.12	0.04
Dy	0.20	0.35	1.25	0.36	0.24	0.79	0.22	0.88	0.26	0.75	0.66	0.70	1.09	0.87	0.82	0.30
Ho	0.05	0.08	0.30	0.09	0.06	0.17	0.05	0.21	0.07	0.17	0.15	0.14	0.25	0.19	0.18	0.07
Er	0.20	0.24	0.92	0.27	0.16	0.56	0.15	0.65	0.19	0.51	0.44	0.45	0.78	0.58	0.57	0.20
Tm	0.03	0.04	0.13	0.04	0.02	0.08	0.02	0.11	0.03	0.08	0.07	0.07	0.12	0.09	0.09	0.03
Yb	0.24	0.26	0.87	0.28	0.17	0.55	0.14	0.70	0.26	0.53	0.46	0.48	0.78	0.60	0.57	0.23
Lu	0.04	0.04	0.14	0.04	0.03	0.09	0.02	0.11	0.04	0.08	0.07	0.07	0.12	0.09	0.09	0.04
Hf	0.43	1.08	1.03	0.49	0.39	0.52	1.37	0.55	0.63	0.60	0.72	0.73	0.55	0.61	0.39	0.34
Ta	0.04	0.03	0.03	0.02	0.02	0.02	0.03	0.02	0.01	0.02	0.04	0.01	0.02	0.03	0.01	0.01
W	0.35	1.01	1.48	0.36	0.86	0.40	0.59	1.12	0.78	0.71	0.19	0.98	0.16	0.06	0.53	0.46
Pb	0.18	0.10	0.27	0.08	0.12	0.23	0.11	0.25	0.06	0.20	0.43	0.15	0.19	0.17	0.20	0.18
Th	0.12	0.12	0.10	0.05	0.06	0.12	0.15	0.24	0.08	0.08	0.21	0.10	0.58	0.11	0.38	0.19
U	0.09	0.05	0.06	0.07	0.07	0.08	0.07	0.07	0.04	0.08	0.12	0.04	0.20	0.09	0.10	0.08

Table S4. Whole-rock major (wt.%) and trace (ppm) element compositions, and loss on ignition (LOI) data for the Coyhaique mantle xenoliths. The total iron is reported as Fe_2O_3. *Samples published by Jalowitzki et al. (2017). [a]Mg# = 100 × Mg/(Mg + Fe)

Ol	PM25-02		PM25-04		PM25-05		PM25-06		PM25-08		PM25-09		PM25-10		PM25-12		PM25-13		PM25-15		PM25-16		PM25-17		PM25-21		PM25-28		PM25-34		PM25-42	
Major (n=)	20	2σ	20	2σ	28	2σ	19	2σ	18	2σ	19	2σ	20	2σ	19	2σ	20	2σ	30	2σ	20	2σ	19	2σ	19	2σ	24	2σ	23	2σ	20	2σ
SiO$_2$	39.94	0.99	39.69	0.56	41.09	0.81	39.67	0.69	39.29	0.53	40.48	0.44	39.80	0.60	40.99	0.75	39.79	0.60	41.33	0.45	38.92	0.69	40.20	0.35	40.25	0.31	40.53	0.48	40.39	0.41	39.11	0.74
TiO$_2$	0.04	0.08	0.05	0.14	0.01	0.03	0.05	0.15	0.04	0.10	0.02	0.10	0.05	0.12	0.02	0.09	0.04	0.12	0.01	0.04	0.04	0.10	0.03	0.07	0.02	0.08	0.04	0.13	0.05	0.14	0.04	0.13
Al$_2$O$_3$	0.03	0.09	0.02	0.06	0.03	0.05	0.01	0.02	0.01	0.02	0.02	0.04	0.03	0.04	0.03	0.04	0.03	0.04	0.02	0.03	0.04	0.19	0.02	0.04	0.03	0.05	0.04	0.06	0.02	0.04	0.01	0.02
Cr$_2$O$_3$	0.05	0.09	0.03	0.08	0.01	0.04	0.05	0.09	0.04	0.07	0.02	0.05	0.03	0.07	0.05	0.09	0.02	0.05	0.02	0.05	0.02	0.05	0.01	0.03	0.04	0.07	0.01	0.04	0.01	0.04	0.02	0.06
MgO	49.70	0.99	49.06	0.57	47.45	0.80	50.07	0.43	50.80	0.95	48.48	0.50	51.02	0.70	48.70	0.62	50.23	0.51	47.64	0.56	50.63	1.16	49.26	0.53	49.33	0.52	48.58	0.57	49.23	0.48	48.47	1.13
CaO	0.12	0.06	0.10	0.07	0.10	0.07	0.09	0.06	0.07	0.04	0.07	0.05	0.09	0.06	0.08	0.04	0.07	0.05	0.09	0.06	0.07	0.05	0.10	0.08	0.10	0.08	0.08	0.03	0.08	0.06	0.09	0.06
MnO	0.12	0.12	0.14	0.11	0.16	0.09	0.13	0.11	0.13	0.08	0.12	0.11	0.11	0.12	0.14	0.08	0.17	0.10	0.16	0.06	0.14	0.11	0.13	0.09	0.15	0.13	0.15	0.14	0.13	0.10	0.21	0.12
FeO$_T$	9.59	0.36	10.30	0.23	11.11	0.26	9.88	0.31	9.23	0.27	10.50	0.32	8.85	0.21	9.91	0.31	10.02	0.22	10.52	0.39	10.11	0.30	10.47	0.31	10.21	0.20	9.57	0.26	9.92	0.22	11.91	1.21
NiO	0.37	0.12	0.37	0.11	0.34	0.08	0.37	0.10	0.40	0.08	0.37	0.09	0.38	0.12	0.37	0.08	0.37	0.08	0.35	0.10	0.38	0.06	0.38	0.10	0.36	0.10	0.36	0.09	0.39	0.11	0.35	0.08
Na$_2$O	0.02	0.04	0.01	0.05	0.02	0.03	0.02	0.04	0.01	0.03	0.02	0.04	0.02	0.03	0.01	0.03	0.01	0.03	0.03	0.07	0.02	0.04	0.02	0.02	0.02	0.04	0.02	0.06	0.01	0.03	0.01	0.03
K$_2$O	0.01	0.02	0.01	0.02	0.01	0.02	0.01	0.02	0.01	0.02	0.01	0.02	0.01	0.02	0.01	0.02	0.00	0.01	0.01	0.02	0.01	0.03	0.01	0.02	0.00	0.02	0.01	0.02	0.01	0.02	0.01	0.02
Total	100.00	1.54	99.79	0.88	100.35	0.56	100.36	0.98	100.05	1.04	100.12	0.72	100.39	1.13	100.32	1.16	100.75	0.95	100.36	0.02	100.37	1.18	100.65	0.41	100.54	0.45	99.42	0.88	100.23	0.52	100.23	0.98
Fo	90.12	0.31	89.33	0.30	88.24	0.33	89.91	0.28	90.63	0.34	89.05	0.34	91.03	0.23	89.62	0.30	89.78	0.18	88.25	0.02	89.79	0.36	89.22	0.36	89.46	0.30	89.90	0.29	89.72	0.20	87.69	1.30
Mg#^{a}	90.23	0.32	89.46	0.27	88.39	0.31	90.04	0.30	90.75	0.30	89.16	0.29	91.13	0.22	89.75	0.30	89.93	0.20	88.39	0.02	89.92	0.34	89.34	0.33	89.59	0.23	90.04	0.29	89.84	0.21	87.88	1.31
Ol Trace (n=)	-		-		8	2σ	-		8	2σ	8	2σ	-		8	2σ	8	2σ	8	2σ	8	2σ	8	2σ	8	2σ	8	2σ	8	2σ	8	2σ
B	-		-		0.50	0.04	-		0.65	0.14	0.56	0.06	-		0.67	0.000	0.63	0.000	0.50	0.000	0.49	0.21	-		0.47	0.000	0.45	0.000	-		0.43	0.000
Cs	-		-		-		-		-		-		-		-		-		-		-		-		-		-		-		-	
Rb	-		-		-		-		-		-		-		-		-		-		-		-		-		-		-		-	
Ba	-		-		0.01	0.004	-		-		-		-		-		0.02	0.000	0.01	0.000	0.01	0.00	-		0.01	0.000	0.01	0.000	-		-	
W	-		-		-		-		-		-		-		-		-		-		-		-		-		-		-		-	
Th	-		-		-		-		-		-		-		-		-		-		-		-		-		-		-		-	
U	-		-		-		-		-		-		-		-		0.001	0.000	-		-		-		-		-		-		-	
Nb	-		-		-		-		-		-		-		-		-		-		0.002	0.000	-		-		-		-		0.002	0.001
Ta	-		-		-		-		-		-		-		-		-		-		-		-		-		-		-		-	
La	-		-		-		-		0.001	0.000	0.002	0.000	-		-		-		-		0.001	0.000	-		-		-		-		-	
Ce	-		-		0.002	0.002	-		0.001	0.000	0.001	0.000	-		0.001	0.001	-		0.001	0.000	0.002	0.002	-		-		0.001	0.001	0.002	0.000	0.01	0.000
Pb	-		-		-		-		-		-		-		0.01	0.000	-		0.01	0.01	0.02	0.01	0.01	0.000	0.01	0.000	-		-		0.01	0.000
Pr	-		-		-		-		-		-		-		-		-		-		-		-		-		-		-		-	
Sr	-		-		-		-		-		-		-		-		-		0.02	0.000	-		-		-		0.02	0.000	0.01	0.000	-	
Nd	-		-		-		-		-		-		-		-		-		-		-		-		-		-		-		-	
Sm	-		-		-		-		-		-		-		-		-		-		-		-		-		-		-		-	
Zr	-		-		0.06	0.01	-		-		-		-		-		-		-		0.11	0.04	-		0.06	0.01	0.06	0.000	-		0.04	0.000
Hf	-		-		-		-		-		-		-		-		-		-		0.004	0.002	-		0.005	0.000	-		-		-	
Eu	-		-		-		-		-		-		-		-		-		-		-		0.002	0.000	-		-		-		-	
Sn	-		-		-		-		-		-		-		-		-		-		-		-		-		-		-		-	
Sb	-		-		-		-		-		-		-		-		-		-		-		-		-		-		-		-	
Gd	-		-		-		-		-		-		-		0.01	0.000	-		-		0.005	0.000	-		-		-		0.01	0.000	-	
Tb	-		-		-		-		-		0.001	0.000	-		-		0.001	0.000	0.001	0.000	-		0.001	0.000	0.002	0.001	0.001	0.000	0.001	0.000	-	
Dy	-		-		0.01	0.003	-		0.003	0.000	0.003	0.001	-		0.01	0.001	0.01	0.000	0.01	0.003	0.004	0.002	0.01	0.01	0.01	0.01	0.01	0.003	0.01	0.01	0.003	0.000
Li	-		-		1.96	0.87	-		1.78	0.52	1.82	0.64	-		1.52	0.81	2.87	2.19	2.17	1.05	1.97	0.35	1.96	0.71	1.56	0.43	2.38	0.52	1.56	0.29	2.59	0.40
Y	-		-		0.06	0.02	-		0.03	0.008	0.04	0.01	-		0.05	0.01	0.03	0.02	0.05	0.02	0.05	0.01	0.05	0.01	0.07	0.02	0.05	0.02	0.05	0.05	0.03	0.02
Ho	-		-		0.002	0.001	-		0.001	0.000	0.002	0.001	-		0.001	0.001	0.001	0.000	0.002	0.002	0.001	0.001	0.002	0.001	0.003	0.002	0.002	0.002	0.001	0.001	0.002	0.000
Er	-		-		0.01	0.008	-		0.01	0.006	0.01	0.003	-		0.01	0.01	0.01	0.01	0.01	0.01	0.01	0.008	0.01	0.003	0.01	0.01	0.01	0.004	0.01	0.01	0.01	0.004
Tm	-		-		0.003	0.002	-		0.002	0.002	0.002	0.001	-		0.001	0.001	0.001	0.001	0.002	0.001	0.002	0.001	0.002	0.001	0.003	0.002	0.003	0.003	0.003	0.004	0.001	0.001
Yb	-		-		0.03	0.02	-		0.01	0.01	0.02	0.01	-		0.02	0.01	0.01	0.01	0.02	0.01	0.03	0.01	0.03	0.01	0.02	0.01	0.03	0.02	0.02	0.02	0.02	0.01
Lu	-		-		0.01	0.004	-		0.004	0.001	0.005	0.003	-		0.01	0.004	0.003	0.003	0.004	0.003	0.01	0.003	0.01	0.003	0.01	0.002	0.01	0.005	0.01	0.003	0.004	0.003

Opx	PM25-02		PM25-04		PM25-05		PM25-06		PM25-08		PM25-09		PM25-10		PM25-12		PM25-13		PM25-15		PM25-16		PM25-17		PM25-21		PM25-28		PM25-34		PM25-42	
Major (n=)	20	2σ	20	2σ	22	2σ	20	2σ	23	2σ	22	2σ	20	2σ	20	2σ	16	2σ	25	2σ	19	2σ	21	2σ	18	2σ	24	2σ	19	2σ	19	2σ
SiO_2	53.92	0.45	53.89	0.57	54.59	0.52	53.89	0.53	53.49	0.39	54.43	0.49	54.21	0.74	55.40	1.32	53.98	0.52	54.66	0.75	53.11	0.82	53.99	1.03	54.63	0.45	54.55	0.49	55.44	0.55	53.41	0.36
TiO_2	0.06	0.16	0.14	0.20	0.16	0.05	0.14	0.20	0.13	0.19	0.13	0.22	0.09	0.19	0.15	0.23	0.09	0.21	0.13	0.06	0.15	0.22	0.16	0.23	0.20	0.22	0.14	0.23	0.13	0.21	0.14	0.21
Al_2O_3	3.57	0.18	3.84	0.23	5.15	0.46	3.57	0.34	3.34	0.18	4.48	0.25	3.14	0.25	4.65	0.23	3.47	0.28	4.73	0.26	3.90	0.36	4.68	0.17	4.67	0.28	4.84	0.22	4.40	0.22	3.44	0.14
Cr_2O_3	0.51	0.15	0.36	0.18	0.38	0.08	0.48	0.17	0.56	0.17	0.37	0.19	0.65	0.22	0.36	0.20	0.35	0.17	0.34	0.09	0.36	0.18	0.40	0.19	0.35	0.19	0.37	0.20	0.36	0.12	0.45	0.18
MgO	33.21	0.48	32.75	0.38	31.63	0.53	33.51	0.89	34.17	0.39	32.43	0.43	34.24	0.46	32.45	0.49	33.88	0.49	32.13	0.60	33.80	0.78	32.86	0.50	32.45	0.45	32.36	0.63	32.52	0.53	32.55	0.37
CaO	1.05	0.08	0.85	0.08	0.90	0.07	0.84	0.07	0.84	0.09	0.79	0.09	0.84	0.07	0.82	0.07	0.72	0.09	0.77	0.09	0.81	0.07	0.93	0.10	0.86	0.11	0.84	0.05	0.80	0.07	0.87	0.11
MnO	0.10	0.10	0.14	0.10	0.15	0.07	0.14	0.09	0.14	0.11	0.14	0.11	0.11	0.11	0.15	0.10	0.16	0.09	0.15	0.06	0.14	0.08	0.13	0.09	0.14	0.08	0.14	0.13	0.15	0.07	0.18	0.14
FeO_T	6.16	0.19	6.58	0.18	7.12	0.25	6.29	0.27	5.89	0.16	6.62	0.24	5.67	0.20	6.26	0.23	6.43	0.27	6.73	0.29	6.40	0.20	6.70	0.26	6.49	0.20	6.13	0.30	6.36	0.17	7.79	0.35
NiO	0.10	0.09	0.11	0.08	0.10	0.08	0.12	0.07	0.11	0.06	0.09	0.07	0.11	0.07	0.10	0.06	0.10	0.06	0.08	0.07	0.10	0.08	0.11	0.08	0.10	0.06	0.10	0.07	0.10	0.07	0.11	0.06
Na_2O	0.09	0.06	0.15	0.07	0.12	0.07	0.14	0.07	0.13	0.05	0.10	0.08	0.13	0.12	0.13	0.04	0.09	0.05	0.13	0.07	0.14	0.07	0.17	0.06	0.16	0.07	0.10	0.07	0.15	0.04	0.13	0.05
K_2O	0.01	0.02	0.01	0.02	0.01	0.02	0.01	0.02	0.01	0.02	0.01	0.02	0.01	0.02	0.01	0.03	0.01	0.02	0.00	0.02	0.02	0.02	0.01	0.02	0.01	0.02	0.01	0.02	0.01	0.02	0.01	0.01
Total	98.79	0.88	98.82	0.78	100.31	0.76	99.13	0.98	98.83	0.44	99.60	0.81	99.21	0.82	100.48	1.41	99.28	0.77	99.87	0.86	98.93	0.61	100.15	1.24	100.07	0.86	99.60	0.97	100.42	0.47	99.08	0.46
Ens	88.60	0.38	88.20	0.18	86.99	0.37	88.84	0.55	89.54	0.30	88.13	0.44	89.89	0.31	88.58	0.35	88.92	0.28	87.92	0.55	88.82	0.48	87.95	0.53	88.21	0.32	88.70	0.24	88.48	0.28	86.45	0.61
Fs	9.22	0.29	9.94	0.24	10.99	0.35	9.36	0.53	8.66	0.22	10.10	0.33	8.36	0.28	9.59	0.30	9.47	0.35	10.33	0.47	9.44	0.40	10.07	0.42	9.90	0.31	9.42	0.42	9.72	0.26	11.61	0.49
Wo	2.02	0.16	1.65	0.15	1.78	0.15	1.60	0.14	1.58	0.17	1.55	0.18	1.58	0.15	1.60	0.14	1.36	0.18	1.51	0.17	1.53	0.14	1.79	0.20	1.68	0.22	1.65	0.11	1.57	0.14	1.66	0.20
Mg#[a]	90.57	0.30	89.87	0.25	88.78	0.35	90.47	0.54	91.18	0.22	89.72	0.35	91.49	0.28	90.23	0.31	90.37	0.34	89.49	0.48	90.40	0.41	89.73	0.44	89.91	0.31	90.40	0.43	90.11	0.26	88.16	0.51
Opx Trace (n=)	3	2σ	3	2σ	8	2σ	-		8	2σ	8	2σ	5	2σ	8	2σ	8	2σ	8	2σ	6	2σ	8	2σ	8	2σ	8	2σ	8	2σ	8	2σ
B	-		-		0.66	0.000	-		0.70	0.09	-		-		-		-		-		0.71	0.09	-		0.52	0.000	-		0.52	0.000	0.51	0.000
Cs	0.06	0.000	-		-		-		-		-		-		-		-		-		-		-		-		-		-		-	
Rb	0.14	0.000	-		0.04	0.000	-		-		-		0.21	0.001	-		-		-		-		-		-		-		-		-	
Ba	-		-		0.03	0.000	-		-		0.02	0.02	-		-		-		-		-		-		-		0.03	0.000	0.01	0.000	-	
W	0.03	0.000	-		-		-		-		-		-		-		-		-		-		-		-		-		-		-	
Th	0.001	0.000	0.004	0.003	-		-		-		0.001	0.001	0.002	0.001	-		0.001	0.000	0.001	0.001	0.01	0.000	-		-		0.001	0.000	-		0.004	0.002
U	0.01	0.005	0.003	0.004	0.001	0.000	-		-		-		0.001	0.001	-		-		0.001	0.000	0.004	0.005	0.001	0.000	-		-		-		0.003	0.001
Nb	0.08	0.02	0.05	0.01	0.01	0.005	-		0.01	0.01	0.01	0.01	0.03	0.004	0.01	0.003	0.01	0.005	0.01	0.003	0.02	0.01	0.01	0.01	0.01	0.003	0.03	0.01	0.004	0.002	0.05	0.01
Ta	0.004	0.004	0.01	0.000	0.003	0.000	-		-		0.001	0.000	-		-		-		0.002	0.000	0.00	0.003	-		-		0.002	0.002	-		0.003	0.002
La	-		0.03	0.01	0.003	0.001	-		0.002	0.001	0.01	0.004	0.01	0.000	0.001	0.001	0.002	0.003	0.01	0.01	0.02	0.006	0.003	0.003	0.003	0.001	0.004	0.002	0.002	0.001	0.01	0.003
Ce	0.04	0.001	0.12	0.05	0.02	0.004	-		0.01	0.01	0.02	0.01	0.05	0.01	0.01	0.003	0.01	0.02	0.02	0.03	0.10	0.01	0.02	0.01	0.02	0.002	0.02	0.01	0.005	0.003	0.05	0.013
Pb	0.17	0.21	-		0.02	0.02	-		-		0.07	0.10	0.08	0.14	-		-		0.03	0.03	0.04	0.03	0.01	0.000	0.04	0.000	0.04	0.04	-		0.005	0.000
Pr	-		0.03	0.02	0.01	0.003	-		0.002	0.001	0.004	0.004	-		0.003	0.003	0.003	0.002	0.01	0.01	0.01	0.004	0.003	0.003	0.004	0.002	0.01	0.003	0.002	0.001	0.01	0.004
Sr	0.29	0.01	0.62	0.13	0.24	0.03	-		0.13	0.03	0.17	0.02	0.42	0.35	0.18	0.02	0.16	0.30	0.31	0.54	0.15	0.02	0.23	0.03	0.22	0.03	0.27	0.04	0.11	0.02	0.22	0.04
Nd	-		0.19	0.13	0.04	0.03	-		0.02	0.01	0.04	0.02	0.05	0.03	0.03	0.01	0.02	0.02	0.03	0.04	0.09	0.04	0.03	0.02	0.04	0.02	0.03	0.02	0.02	0.02	0.04	0.03
Sm	0.03	0.000	0.12	0.13	0.02	0.02	-		0.02	0.02	0.02	0.02	-		0.02	0.02	0.01	0.00	0.03	0.02	0.03	0.02	0.03	0.03	0.03	0.01	0.03	0.01	0.02	0.01	0.02	0.01
Zr	0.92	0.44	4.28	2.15	2.13	0.20	-		0.94	0.13	1.62	0.10	1.23	0.50	1.79	0.16	0.23	0.11	1.82	0.53	11.11	1.72	1.74	0.16	1.98	0.18	2.69	0.27	1.47	0.20	1.65	0.81
Hf	0.03	0.03	0.06	0.05	0.07	0.02	-		0.02	0.02	0.05	0.02	0.05	0.03	0.05	0.02	0.01	0.01	0.06	0.03	0.22	0.05	0.06	0.03	0.07	0.03	0.04	0.02	0.04	0.02	0.04	0.02
Eu	0.02	0.000	0.04	0.05	0.01	0.01	-		0.01	0.003	0.01	0.01	0.02	0.002	0.01	0.01	0.01	0.01	0.005	0.003	0.01	0.01	0.01	0.01	0.01	0.005	0.01	0.01	0.01	0.01	0.01	0.01
Sn	0.31	0.26	0.12	0.04	-		-		-		-		0.17	0.74	-		-		-		-		-		-		-		-		-	
Sb	-		0.02	0.000	-		-		-		-		-		-		-		-		-		-		-		-		-		-	
Gd	0.13	0.000	0.21	0.12	0.07	0.03	-		0.03	0.01	0.05	0.01	-		0.05	0.01	0.02	0.01	0.05	0.04	0.07	0.02	0.07	0.02	0.08	0.03	0.06	0.02	0.05	0.01	0.04	0.01
Tb	0.02	0.01	0.04	0.01	0.02	0.004	-		0.01	0.002	0.01	0.003	0.02	0.02	0.01	0.003	0.01	0.004	0.01	0.004	0.02	0.00	0.02	0.005	0.02	0.005	0.02	0.003	0.01	0.01	0.01	0.002
Dy	0.12	0.02	0.24	0.04	0.16	0.04	-		0.09	0.04	0.14	0.04	0.15	0.02	0.15	0.04	0.15	0.03	0.14	0.03	0.16	0.03	0.18	0.03	0.16	0.03	0.17	0.02	0.14	0.04	0.11	0.03
Li	-		-		2.97	2.78	-		2.36	3.52	3.02	2.56	-		2.52	2.15	5.00	6.43	2.83	4.84	4.26	4.39	3.81	3.51	4.23	4.29	3.05	2.35	1.72	2.19	3.05	4.57
Y	0.88	0.06	1.80	0.23	1.24	0.09	-		0.72	0.04	1.10	0.11	1.01	0.17	1.16	0.07	0.76	0.13	1.12	0.18	1.28	0.06	1.23	0.11	1.19	0.12	1.25	0.11	1.25	0.11	0.85	0.05
Ho	0.04	0.01	0.07	0.02	0.05	0.01	-		0.03	0.01	0.04	0.01	0.03	0.01	0.04	0.01	0.02	0.01	0.04	0.01	0.05	0.01	0.04	0.003	0.05	0.01	0.05	0.01	0.04	0.01	0.03	0.01
Er	0.16	0.07	0.21	0.03	0.18	0.02	-		0.11	0.02	0.16	0.03	0.16	0.02	0.17	0.03	0.11	0.03	0.17	0.03	0.18	0.03	0.17	0.03	0.18	0.04	0.18	0.04	0.17	0.03	0.11	0.03
Tm	0.02	0.01	0.04	0.01	0.04	0.01	-		0.02	0.003	0.03	0.01	0.02	0.01	0.03	0.01	0.02	0.003	0.03	0.01	0.04	0.01	0.04	0.003	0.03	0.01	0.04	0.01	0.03	0.00	0.02	0.01
Yb	0.21	0.03	0.44	0.10	0.30	0.05	-		0.18	0.04	0.27	0.04	0.24	0.06	0.27	0.04	0.22	0.04	0.27	0.07	0.34	0.05	0.27	0.07	0.26	0.06	0.30	0.05	0.29	0.03	0.20	0.03
Lu	0.04	0.01	0.07	0.03	0.05	0.01	-		0.03	0.01	0.05	0.01	0.04	0.02	0.05	0.01	0.04	0.01	0.05	0.01	0.06	0.02	0.05	0.01	0.05	0.01	0.05	0.01	0.05	0.01	0.03	0.004

Cpx	PM25-02		PM25-04		PM25-05		PM25-06		PM25-08		PM25-09		PM25-10		PM25-12		PM25-13		PM25-15		PM25-16				PM25-17		PM25-21		PM25-28		PM25-34		PM25-42	
Major (n=)	20	2σ	20	2σ	33	2σ	20	2σ	22	2σ	20	2σ	22	2σ	24	2σ	22	2σ	34	2σ	21	2σ			22	2σ	25	2σ	29	2σ	27	2σ	20	2σ
SiO_2	51.43	0.33	51.18	0.16	51.55	0.57	52.46	0.40	50.86	0.27	51.59	0.36	51.43	0.32	52.59	0.85	51.51	0.55	52.27	0.53	50.65	0.42			51.46	0.53	51.76	0.41	51.70	0.43	52.56	0.52	51.51	0.49
TiO_2	0.19	0.21	0.50	0.29	0.59	0.09	0.51	0.23	0.35	0.18	0.63	0.23	0.41	0.25	0.63	0.35	0.22	0.24	0.64	0.12	0.65	0.31			0.54	0.36	0.72	0.33	0.68	0.26	0.59	0.27	0.35	0.24
Al_2O_3	4.29	0.22	5.64	0.13	7.20	0.29	5.67	0.25	4.87	0.19	6.57	0.26	4.40	0.34	6.92	0.39	4.94	0.39	7.26	0.35	5.83	0.22			6.77	0.27	6.85	0.24	6.86	0.20	6.42	0.26	4.91	0.21
Cr_2O_3	0.92	0.24	0.97	0.15	0.73	0.11	1.11	0.15	1.49	0.21	0.78	0.20	1.39	0.37	0.79	0.18	0.86	0.28	0.74	0.10	0.78	0.18			0.73	0.15	0.74	0.23	0.72	0.20	0.74	0.20	1.00	0.21
MgO	16.81	0.40	15.46	0.30	15.07	0.33	15.52	0.46	16.28	0.18	15.23	0.26	16.44	0.38	15.11	0.40	15.92	0.43	14.78	0.39	15.62	0.47			15.61	0.44	15.40	0.43	15.46	0.68	15.26	0.33	15.73	0.32
CaO	20.69	0.27	19.59	0.11	19.36	0.36	19.45	0.25	20.01	0.13	19.21	0.30	20.50	0.34	19.53	0.32	20.72	0.31	19.17	0.42	19.91	0.12			18.76	0.32	18.83	0.39	18.70	0.48	19.25	0.30	19.72	0.41
MnO	0.10	0.12	0.09	0.11	0.11	0.06	0.08	0.08	0.11	0.08	0.08	0.09	0.09	0.09	0.10	0.11	0.09	0.09	0.09	0.07	0.11	0.14			0.08	0.11	0.11	0.09	0.09	0.12	0.10	0.10	0.08	0.11
FeO_T	3.18	0.12	3.33	0.15	3.56	0.17	2.94	0.15	2.77	0.17	3.15	0.15	2.63	0.15	2.88	0.14	2.91	0.16	3.12	0.14	3.13	0.13			3.52	0.22	3.24	0.23	3.01	0.18	2.96	0.15	3.66	0.51
NiO	0.06	0.06	0.06	0.06	0.05	0.07	0.05	0.07	0.04	0.07	0.06	0.07	0.05	0.06	0.04	0.07	0.06	0.08	0.05	0.07	0.06	0.08			0.06	0.08	0.06	0.09	0.05	0.08	0.05	0.07	0.05	0.06
Na_2O	1.06	0.17	1.88	0.10	1.52	0.14	2.02	0.13	1.81	0.13	1.48	0.25	1.51	0.16	1.74	0.16	1.59	0.17	1.83	0.17	2.11	0.19			1.88	0.16	1.91	0.14	1.51	0.37	1.82	0.13	1.68	0.15
K_2O	0.01	0.02	0.01	0.04	0.01	0.02	0.01	0.02	0.01	0.02	0.01	0.02	0.01	0.02	0.01	0.03	0.01	0.02	0.01	0.03	0.01	0.02			0.01	0.02	0.01	0.02	0.02	0.02	0.00	0.01	0.01	0.03
Total	98.75	0.54	98.71	0.44	99.75	0.89	99.83	0.44	98.61	0.27	98.80	0.74	98.87	0.65	100.34	1.13	98.83	0.55	99.95	0.82	98.86	0.80			99.44	1.05	99.63	0.73	98.83	0.63	99.75	0.94	98.72	0.40
Ens	50.14	0.74	49.13	0.60	48.55	0.57	49.76	1.00	50.42	0.36	49.37	0.65	50.26	0.78	49.03	0.82	48.97	0.78	48.69	0.86	49.18	0.84			50.17	0.79	49.97	0.81	50.43	1.49	49.51	0.64	49.14	0.80
Fs	5.33	0.19	5.93	0.28	6.43	0.28	5.29	0.26	4.82	0.26	5.73	0.27	4.52	0.27	5.25	0.26	5.03	0.27	5.76	0.23	5.53	0.25			6.35	0.38	5.90	0.41	5.52	0.36	5.39	0.23	6.42	0.93
Wo	44.37	0.80	44.77	0.47	44.82	0.60	44.82	0.90	44.56	0.36	44.75	0.50	45.07	0.85	45.55	0.74	45.84	0.73	45.39	0.85	45.09	0.69			43.34	0.69	43.94	0.89	43.87	1.29	44.92	0.57	44.29	0.70
Mg#[a]	90.39	0.35	89.22	0.52	88.30	0.50	90.39	0.50	91.27	0.44	89.60	0.51	91.75	0.46	90.33	0.49	90.68	0.49	89.42	0.45	89.90	0.52			88.77	0.68	89.44	0.70	90.13	0.75	90.18	0.42	88.45	1.60
Cpx Trace (n=)	18	2σ	15	2σ	8	2σ	16	2σ	8	2σ	8	2σ	12	2σ	8	2σ	8	2σ	8	2σ	8	2σ	2^c	2σ^c	8	2σ	8	2σ	8	2σ	8	2σ	8	2σ
B	-		-		0.57	0.10	-		0.68	0.14	0.63	0.08	-		0.65	0.04	-		-		0.63	0.27	*0.71*	*0.09*	-		0.36	0.000	0.58	0.06	-		0.51	0.095
Cs	0.05	0.000	-		-		0.05	0.000	-		-		-		-		-		-		-		-	-	-		-		-		-		-	
Rb	0.16	0.02	0.23	0.08	-		0.23	0.13	-		-		0.37	0.11	-		-		-		-		-	-	-		-		-		-		-	
Ba	0.22	0.15	0.38	0.49	0.04	0.02	0.27	0.000	0.03	0.03	0.04	0.01	-		0.01	0.000	0.03	0.05	2.04	8.06	0.03	0.000	-	-	0.08	0.07	0.02	0.01	0.03	0.04	0.04	0.04	0.03	0.02
W	0.01	0.000	0.01	0.01	-		0.01	0.003	-		-		0.02	0.003	-		-		-		-		-	-	-		-		-		-		-	
Th	0.29	0.10	0.67	0.07	0.02	0.002	0.03	0.01	0.03	0.01	0.15	0.08	0.03	0.04	0.02	0.01	0.01	0.002	0.15	0.04	0.90	0.07	*0.05*	*0.05*	0.06	0.05	0.01	0.004	0.13	0.02	0.003	0.002	0.74	0.07
U	0.09	0.04	0.16	0.02	0.01	0.003	0.01	0.01	0.02	0.005	0.04	0.02	0.01	0.01	0.01	0.01	0.01	0.002	0.05	0.02	0.26	0.03	*0.01*	*0.01*	0.04	0.01	0.002	0.000	0.04	0.02	0.002	0.000	0.19	0.02
Nb	1.19	0.68	1.44	0.22	0.22	0.02	0.35	0.07	0.15	0.02	0.17	0.10	0.35	0.17	0.13	0.01	0.13	0.02	0.10	0.01	1.08	0.93	*0.06*	*0.02*	0.38	0.26	0.10	0.02	0.78	0.17	1.03	0.01	1.64	0.10
Ta	0.09	0.08	0.19	0.08	0.02	0.01	0.03	0.01	0.01	0.004	0.005	0.004	0.04	0.01	0.01	0.004	0.01	0.01	0.01	0.01	0.48	0.11	*0.02*	*0.01*	0.01	0.01	0.01	0.01	0.05	0.03	0.002	0.001	0.19	0.10
La	2.08	1.48	9.84	1.59	1.08	0.04	1.44	0.11	0.67	0.04	1.48	0.95	0.96	0.53	0.80	0.02	0.57	0.03	1.36	0.22	10.25	0.64	*0.28*	*0.36*	0.78	0.11	1.06	0.10	1.70	0.23	0.66	0.03	6.58	0.99
Ce	3.81	2.78	26.30	7.82	4.44	0.30	4.98	0.32	2.75	0.17	5.10	2.56	2.58	0.83	3.22	0.15	1.95	0.12	4.58	0.28	30.08	1.81	*0.88*	*1.08*	3.19	0.24	4.38	0.27	4.93	0.72	1.58	0.04	12.99	3.89
Pb	0.11	0.11	0.26	0.14	0.08	0.13	0.06	0.08	0.03	0.02	0.12	0.13	0.07	0.08	0.05	0.03	0.07	0.04	0.08	0.04	0.16	0.15	*0.07*	*0.000*	0.07	0.01	0.09	0.06	0.08	0.06	0.05	0.09	0.29	0.04
Pr	0.44	0.29	3.55	1.55	0.78	0.07	0.87	0.07	0.49	0.02	0.82	0.30	0.42	0.08	0.63	0.02	0.33	0.03	0.77	0.05	3.91	0.35	*0.12*	*0.15*	0.61	0.05	0.80	0.07	0.81	0.12	0.36	0.03	1.31	0.61
Sr	46.44	30.40	172.88	25.72	80.94	3.52	89.40	2.84	57.44	1.58	66.94	4.79	41.58	8.73	71.65	2.14	44.13	2.39	81.33	2.89	58.68	4.48	*1.52*	*1.93*	65.58	2.15	80.50	4.21	86.28	5.09	51.16	1.38	93.99	11.17
Nd	1.93	0.89	15.26	8.84	4.85	0.31	4.98	0.29	3.02	0.23	4.33	1.00	2.41	0.41	4.01	0.15	1.81	0.11	4.67	0.42	15.93	1.20	*0.47*	*0.52*	3.94	0.19	4.89	0.38	4.58	0.51	3.04	0.21	5.06	2.43
Sm	0.66	0.15	3.51	2.26	1.87	0.19	1.87	0.29	1.17	0.13	1.64	0.23	1.08	0.19	1.71	0.17	0.76	0.11	1.81	0.18	3.03	0.29	*0.13*	*0.13*	1.84	0.24	1.93	0.21	1.82	0.21	1.54	0.18	1.44	0.46
Zr	12.42	14.75	69.22	56.28	33.75	1.64	38.36	2.58	18.81	1.20	28.78	3.46	22.57	1.32	33.59	0.55	3.97	0.22	34.49	2.56	217.45	66.97	*12.88*	*7.29*	28.18	1.92	36.74	4.01	40.18	6.02	29.64	2.01	28.99	20.17
Hf	0.42	0.53	1.45	1.19	1.06	0.09	1.14	0.11	0.56	0.05	0.88	0.14	0.77	0.11	1.03	0.08	0.14	0.03	1.06	0.11	3.69	1.36	*0.16*	*0.10*	0.94	0.08	1.17	0.16	1.13	0.11	0.96	0.08	0.69	0.15
Eu	0.26	0.05	1.26	0.75	0.77	0.05	0.75	0.07	0.47	0.06	0.69	0.07	0.46	0.07	0.71	0.05	0.30	0.03	0.76	0.07	0.97	0.08	*0.04*	*0.04*	0.71	0.06	0.83	0.07	0.74	0.08	0.71	0.06	0.55	0.12
Sn	0.14	0.00	0.72	0.47	-		0.43	0.15	-		-		0.28	0.17	-		-		-		-		-	-	-		-		-		-		-	
Sb	0.04	0.000	-		-		0.03	0.000	-		-		0.03	0.01	-		-		-		-		-	-	-		-		-		-		-	
Gd	1.11	0.17	3.74	2.04	2.64	0.12	2.55	0.23	1.59	0.16	2.24	0.31	1.86	0.20	2.62	0.13	1.24	0.15	2.57	0.25	3.51	0.29	*0.14*	*0.09*	2.39	0.21	2.72	0.27	2.74	0.25	2.50	0.16	1.84	0.23
Tb	0.22	0.03	0.62	0.28	0.45	0.03	0.45	0.04	0.29	0.01	0.41	0.05	0.36	0.03	0.47	0.03	0.24	0.02	0.45	0.03	0.54	0.04	*0.03*	*0.02*	0.44	0.04	0.48	0.07	0.51	0.03	0.44	0.03	0.34	0.05
Dy	1.66	0.21	4.03	1.28	3.33	0.15	3.06	0.32	2.13	0.11	2.99	0.26	2.53	0.16	3.42	0.22	1.93	0.16	3.27	0.24	3.83	0.26	*0.27*	*0.15*	3.17	0.14	3.58	0.40	3.91	0.31	3.26	0.25	2.34	0.30
Li	-		-		6.07	2.70	-		6.49	2.01	10.26	2.92	-		4.51	1.20	19.32	8.25	8.86	4.42	20.22	5.94	*2.66*	*2.12*	9.17	1.34	10.42	2.44	6.55	1.27	9.54	3.29	17.44	4.62
Y	9.86	0.71	21.60	5.68	17.69	0.91	16.36	0.82	11.61	0.61	16.22	1.60	14.37	0.59	18.73	0.65	12.10	0.73	18.00	1.27	21.83	1.03	*1.92*	*0.87*	17.31	0.99	18.89	2.10	17.89	1.37	20.55	0.99	12.83	0.95
Ho	0.38	0.04	0.85	0.23	0.66	0.03	0.65	0.05	0.46	0.03	0.63	0.07	0.57	0.03	0.73	0.05	0.44	0.03	0.72	0.05	0.83	0.05	*0.07*	*0.03*	0.68	0.04	0.76	0.09	0.75	0.03	0.77	0.06	0.50	0.04
Er	1.14	0.14	2.40	0.68	1.99	0.12	1.80	0.15	1.34	0.07	1.84	0.24	1.58	0.13	2.08	0.10	1.34	0.10	2.08	0.19	2.53	0.24	*0.27*	*0.11*	2.00	0.11	2.22	0.30	2.12	0.21	2.25	0.20	1.49	0.10
Tm	0.17	0.02	0.33	0.08	0.29	0.02	0.25	0.03	0.19	0.02	0.27	0.03	0.21	0.02	0.28	0.02	0.20	0.02	0.28	0.03	0.38	0.04	*0.05*	*0.02*	0.29	0.04	0.30	0.04	0.31	0.02	0.31	0.04	0.20	0.02
Yb	1.11	0.13	2.17	0.33	1.96	0.26	1.65	0.16	1.23	0.13	1.78	0.22	1.35	0.15	1.90	0.10	1.43	0.08	1.91	0.12	2.51	0.21	*0.42*	*0.12*	1.95	0.20	2.02	0.21	1.93	0.20	2.01	0.17	1.36	0.14
Lu	0.16	0.02	0.31	0.07	0.26	0.02	0.23	0.03	0.16	0.02	0.25	0.04	0.19	0.03	0.27	0.02	0.21	0.02	0.26	0.04	0.36	0.04	*0.08*	*0.02*	0.28	0.02	0.27	0.04	0.28	0.03	0.29	0.03	0.18	0.01

Sp Major	PM25-02	2σ	PM25-04	2σ	PM25-05	2σ	PM25-06	2σ	PM25-08	2σ	PM25-09	2σ	PM25-10	2σ	PM25-12	2σ	PM25-13	2σ	PM25-15	2σ	PM25-16	2σ	PM25-17	2σ	PM25-21	2σ	PM25-28	2σ	PM25-34	2σ	PM25-42	2σ
(n=)	7		9		20		8		9		16		10		20		7		14		12		20		19		13		22		10	
SiO$_2$	0.02	0.05	0.08	0.15	0.02	0.04	0.02	0.02	0.02	0.04	0.02	0.06	0.02	0.04	0.02	0.08	0.00	0.01	0.02	0.05	0.01	0.04	0.05	0.09	0.03	0.05	0.02	0.04	0.02	0.08	0.02	0.04
TiO$_2$	0.16	0.21	0.13	0.18	0.16	0.09	0.31	0.26	0.18	0.22	0.12	0.18	0.12	0.15	0.14	0.17	0.09	0.18	0.18	0.18	0.13	0.23	0.21	0.22	0.17	0.17	0.12	0.22	0.13	0.24	0.16	0.16
Al$_2$O$_3$	48.03	0.85	55.11	1.08	56.63	0.43	52.82	0.75	48.75	0.70	56.38	0.47	45.99	0.73	56.78	0.53	54.59	0.65	56.66	0.42	56.82	0.61	55.61	0.48	56.60	0.63	56.52	0.37	56.71	0.40	49.30	0.96
Cr$_2$O$_3$	17.81	0.67	10.56	0.50	8.61	0.34	14.24	0.84	18.59	1.14	9.46	0.55	21.72	0.70	9.53	0.47	11.80	0.64	9.58	0.31	10.49	0.71	9.49	0.59	8.64	0.15	9.56	0.54	9.75	0.39	15.65	0.76
MgO	19.51	0.40	20.57	0.49	20.69	0.31	20.29	0.25	19.72	0.40	21.51	0.37	19.34	0.56	21.41	0.54	20.66	0.19	20.78	0.42	20.99	0.34	21.65	0.69	21.48	0.56	21.57	0.57	20.84	0.21	18.67	0.44
CaO	0.01	0.03	0.01	0.02	0.01	0.02	0.02	0.04	0.01	0.02	0.01	0.02	0.01	0.02	0.01	0.02	0.01	0.03	0.02	0.04	0.00	0.01	0.01	0.02	0.01	0.03	0.01	0.03	0.01	0.02	0.01	0.02
MnO	0.11	0.16	0.12	0.13	0.13	0.06	0.09	0.09	0.10	0.10	0.10	0.08	0.12	0.09	0.11	0.11	0.13	0.09	0.13	0.08	0.08	0.09	0.11	0.13	0.07	0.11	0.08	0.14	0.11	0.11	0.15	0.08
FeO$_T$	12.74	0.59	11.90	0.27	12.04	0.29	11.20	0.36	11.17	0.55	11.25	0.28	11.30	0.55	10.32	0.50	11.10	0.35	11.51	0.61	10.72	0.18	11.81	0.35	11.30	0.36	10.44	0.39	10.73	0.23	14.61	1.05
NiO	0.34	0.11	0.40	0.08	0.39	0.08	0.31	0.10	0.32	0.11	0.36	0.10	0.29	0.08	0.39	0.09	0.37	0.06	0.36	0.10	0.37	0.10	0.40	0.09	0.39	0.09	0.40	0.09	0.37	0.12	0.34	0.07
Na$_2$O	0.00	0.01	0.02	0.02	0.01	0.02	0.01	0.02	0.02	0.03	0.01	0.02	0.02	0.02	0.01	0.03	0.02	0.03	0.00	0.01	0.01	0.04	0.01	0.02	0.01	0.03	0.00	0.02	0.01	0.03	0.01	0.02
K$_2$O	0.00	0.01	0.01	0.02	0.01	0.02	0.00	0.01	0.00	0.01	0.00	0.01	0.01	0.01	0.01	0.02	0.01	0.02	0.00	0.01	0.01	0.02	0.01	0.02	0.01	0.02	0.01	0.01	0.01	0.02	0.01	0.02
Total	98.76	1.20	98.90	1.19	98.71	0.50	99.31	0.46	98.89	1.51	99.24	0.90	98.93	1.30	98.76	0.91	98.79	1.13	99.22	1.21	99.63	1.23	99.35	0.99	98.72	0.54	98.72	0.60	98.70	0.38	98.92	1.21
Cr#[b]	19.91	0.50	11.38	0.50	9.26	0.37	15.31	0.93	20.36	1.10	10.11	0.53	24.06	0.71	10.12	0.42	12.66	0.61	10.18	0.30	11.01	0.63	10.27	0.60	9.29	0.18	10.18	0.50	10.33	0.42	17.55	0.95
Mg#[a]	73.18	0.98	75.49	0.63	75.39	0.50	76.34	0.71	75.89	1.04	77.31	0.49	75.31	0.96	78.70	1.06	76.84	0.61	76.29	1.12	77.73	0.45	76.55	0.87	77.21	0.53	78.64	1.01	77.58	0.38	69.49	1.86

Table S5. Representative major (wt.%) and trace element (ppm) average compositions for the Coyhaique mantle xenoliths. n = number of analyses. Uncertainties (2σ). The total iron is reported as FeO$_T$. [a]Mg# = 100 × Mg/(Mg + Fe) atomic ratio. [b]Cr# = 100×(Cr/Cr+Al) atomic ratio.

[c]Clinopyroxene exsolutions in orthopyroxene. Ol: olivine. Opx: orthopyroxene. Cpx: clinopyroxene. Sp: spinel.

Sample		Rb	Sr	$^{87}Sr/^{86}Sr$	Sm	Nd	$^{143}Nd/^{144}Nd$	εNd
PM25-02	WR	0.130	6.811	0.702911(07)	15.58	48.63	0.513089(09)	8.80
	Cpx	-	-	0.70322(3)	0.92	3.51	0.513160(20)	10.19
PM25-04	WR	0.058	6.393	0.702924(04)	16.24	31.53	0.513036(11)	7.76
	Cpx	-	-	0.70281(3)	1.10	2.93	0.513372(25)	14.33
PM25-05*	WR	3.29	31.94	0.702531(13)	0.62	1.90	0.513181(14)	10.60
	Cpx	-	-	0.70403(5)	-	-	-	-
PM25-06	WR	0.198	4.979	0.703192(05)	14.21	26.84	0.512974(13)	6.55
	Cpx	-	-	0.70234(2)	1.05	2.86	0.513066(17)	8.35
PM25-08	WR	0.279	8.344	0.702347(08)	15.11	48.34	0.513140(06)	9.80
	Cpx	-	-	0.70308(2)	1.11	2.92	0.513124(19)	9.48
PM25-09*	WR	2.23	21.33	0.703052(11)	0.43	1.28	0.513073(17)	8.50
	Cpx	-	-	0.70200(5)	1.55	4.19	0.513451(24)	15.85
PM25-10	WR	0.102	7.221	0.702725(03)	6.18	20.35	0.513062(08)	8.27
	Cpx	-	-	0.70276(6)	1.05	2.48	0.513202(16)	11.01
PM25-12*	WR	1.25	15.57	0.703410(07)	0.58	1.71	0.513005(16)	7.10
	Cpx	-	-	0.70211(3)	1.31	3.16	0.513326(15	13.42
PM25-13	WR	0.328	9.897	0.702447(06)	17.84	40.12	0.513159(16)	10.17
	Cpx	-	-	0.70372(5)	-	-	-	-
PM25-15*	WR	3.09	20.81	0.702750(06)	0.42	1.10	0.513195(06)	10.90
	Cpx	-	-	-	-	-	-	-
PM25-16	WR	0.534	5.964	0.703198(04)	18.79	24.94	0.512940(11)	5.89
	Cpx	-	-	0.70330(4)	2.22	10.02	0.513022(13)	7.50
PM25-17*	WR	5.76	16.68	0.703359(13)	0.36	1.15	0.513022(15)	7.50
	Cpx	-	-	-	-	-	-	-
PM25-21*	WR	4.40	27.48	0.703392(12)	0.66	2.02	0.513040(12)	7.80
	Cpx	-	-	0.70239(2)	1.58	4.16	0.513145(18)	9.89
PM25-28*	WR	3.74	17.25	0.704175(09)	0.46	1.77	0.512862(09)	4.40
	Cpx	-	-	0.70240(2)	1.28	3.19	0.513135(17)	9.69
PM25-34*	WR	2.28	20.12	0.703791(04)	0.54	2.08	0.512934(16)	5.80
	Cpx	-	-	0.70200(2)	1.26	2.5264	0.513632(13)	19.39
PM25-42	WR	-	-	-	-	-	-	-
	Cpx	-	-	-	-	-	-	-

Table S6. Whole-rock (WR) and clinopyroxene (Cpx) Rb-Sr (WR), Sr-Sr (Cpx), and Sm-Nd (WR and Cpx) isotopic data for Coyhaique mantle xenoliths. Rb, Sr, Sm, and Nd eleme concentrations are in ppm. The numbers in the parentheses indicate the 2σ uncertainties in the last digits. *Samples published by Jalowitzki et al. (2017). WR: whole-rock. Cpx: clinopyroxene.

| | Partition coefficients ($D^{mineral/melt}$) (Ionov et al., 2002) | | | | Melting source | | | | | Melt mode (Johnson, 1998) |
| | | | | | Trace element content | | Modal composition (%) | | | |
	Kd ol	Kd opx	Kd cpx	Kd sp	[a]Primitive Mantle (Sun and McDonough, 1989)	[b]Coyhaique whole-rock average		[a]Primitive mantle (McDonough, 1990)	[b]Coyhaique modal average	
La	0.0001	0.0002	0.0540	0.0004	0.69	0.86	Ol	56	58	-0.06
Ce	0.0002	0.0004	0.0860	0.0005	1.78	2.04	Opx	22	26	0.28
Pr	0.0003	0.0006	0.1390	0.0007	0.28	0.30	Cpx	19	13	0.67
Nd	0.0004	0.0010	0.1870	0.0006	1.35	1.30	Sp	3	3	0.11
Sm	0.0004	0.0030	0.2910	0.0005	0.44	0.39	Total	100	100	
Eu	0.0006	0.0040	0.3500	0.0005	0.17	0.13				
Gd	0.0008	0.0128	0.4000	0.0004	0.60	0.52				
Tb	0.0010	0.0186	0.4290	0.0004	0.11	0.10				
Dy	0.0014	0.0261	0.4420	0.0004	0.74	0.66				
Ho	0.0018	0.0356	0.4390	0.0004	0.16	0.15				
Er	0.0024	0.0474	0.4360	0.0004	0.48	0.46				
Tm	0.0030	0.0617	0.4330	0.0005	0.07	0.07				
Yb	0.0036	0.0787	0.4300	0.0005	0.49	0.48				
Lu	0.0044	0.0986	0.4270	0.0005	0.07	0.07				

Table S7. Chemical and modal parameters used in partial melting models. See equations proposed by Shaw (2006) and Johnson (1990) in section 5.1. [a]Parameters used for whole-rock partial melting model. [b]Parameters used for clinopyroxene model. Ol: olivine. Opx: orthopyroxene. Cpx: clinopyroxene. Sp: spinel.

Reference

Ionov, D.A., 2002. Mechanisms and Sources of Mantle Metasomatism: Major and Trace Element Compositions of Peridotite Xenoliths from Spitsbergen in the Context of Numerical Modelling. J. Petrol. 43, 2219–2259. https://doi.org/10.1093/petrology/43.12.2219

Jalowitzki, T., Gervasoni, F., Conceição, R. V., Orihashi, Y., Bertotto, G.W., Sumino, H., Schilling, M.E., Nagao, K., Morata, D., Sylvester, P., 2017. Slab-derived components in the subcontinental lithospheric mantle beneath Chilean Patagonia: Geochemistry and Sr–Nd–Pb isotopes of mantle xenoliths and host basalt. Lithos 292–293, 179–197. https://doi.org/10.1016/j.lithos.2017.09.008

Jalowitzki, T., Sumino, H., Conceição, R. V., Orihashi, Y., Nagao, K., Bertotto, G.W., Balbinot, E., Schilling, M.E., Gervasoni, F., 2016. Noble gas composition of subcontinental lithospheric mantle: An extensively degassed reservoir beneath Southern Patagonia. Earth Planet. Sci. Lett. 450, 263–273. https://doi.org/10.1016/j.epsl.2016.06.034

Jochum, K.P., Weis, U., Stoll, B., Kuzmin, D., Yang, Q., Raczek, I., Jacob, D.E., Stracke, A., Birbaum, K., Frick, D.A., Günther, D., Enzweiler, J., 2011. Determination of reference values for NIST SRM 610-617 glasses following ISO guidelines. Geostand. Geoanalytical Res. 35, 397–429. https://doi.org/10.1111/j.1751-908X.2011.00120.x

Johnson, K.T.M., 1998. Experimental determination of partition coefficients for rare earth and high-field-strength elements between clinopyroxene, garnet, and basaltic melt at high pressures. Contrib. to Mineral. Petrol. 133, 60–68. https://doi.org/10.1007/s004100050437

Johnson, K.T.M., Dick, H.J.B., Shimizu, N., 1990. Melting in the oceanic upper mantle: An ion microprobe study of diopsides in abyssal peridotites. J. Geophys. Res. 95, 2661. https://doi.org/10.1029/JB095iB03p02661

Kennedy, B.M., Hiyagon, H., Reynolds, J.H., 1990. Crustal neon: a striking uniformity. Earth Planet. Sci. Lett. 98, 277–286. https://doi.org/10.1016/0012-821X(90)90030-2

McDonough, W.F., 1990. Constraints on the composition of the continental lithospheric mantle. Earth Planet. Sci. Lett. 101, 1–18. https://doi.org/10.1016/0012-821X(90)90119-I

McDonough, W.F., Sun, S. -s., 1995. The composition of the Earth. Chem. Geol. 120, 223–253. https://doi.org/10.1016/0009-2541(94)00140-4

Moreira, M., Allègre, C.J., 1998. Helium–neon systematics and the structure of the mantle. Chem. Geol. 147, 53–59. https://doi.org/10.1016/S0009-2541(97)00171-X

Moreira, M., Kunz, J., Allègre, C., 1998. Rare gas systematics in popping rock: Isotopic and elemental compositions in the upper mantle. Science (80-.). 279, 1178–1181. https://doi.org/10.1126/science.279.5354.1178

Sarda, P., Staudacher, T., Allègre, C.J., 1988. Neon isotopes in submarine basalts. Earth Planet. Sci. Lett. 91, 73–88. https://doi.org/10.1016/0012-821X(88)90152-5

Shaw, D.M., 2006. Trace Elements in Magmas: A Theoretical Treatment. Cambridge University Press.

Streckeisen, A., 1976. To each plutonic rock its proper name. Earth-Science Rev. 12, 1–33. https://doi.org/10.1016/0012-8252(76)90052-0

Sun, S. -s., McDonough, W.F., 1989. Chemical and isotopic systematics of oceanic basalts: implications for mantle composition and processes. Geol. Soc. London, Spec. Publ. 42, 313–345. https://doi.org/10.1144/GSL.SP.1989.042.01.19

Tucker, J.M., Mukhopadhyay, S., Schilling, J.G., 2012. The heavy noble gas composition of the depleted MORB mantle (DMM) and its implications for the preservation of heterogeneities in the mantle. Earth Planet. Sci. Lett. 355–356, 244–254. https://doi.org/10.1016/j.epsl.2012.08.025

Workman, R.K., Hart, S.R., 2005. Major and trace element composition of the depleted MORB mantle (DMM). Earth Planet. Sci. Lett. 231, 53–72. https://doi.org/10.1016/j.epsl.2004.12.005

5 CONSIDERAÇÕES FINAIS

O manto litosférico subcontinental (SLCM) abaixo de Coyhaique é composto por espinélio-lherzolitos anidros com textura protogranular, evidenciando baixa taxa de deformação e quantidade significante de inclusões fluidas observadas em todos os silicatos. As correlações negativas entre MgO e elementos basálticos (CaO, Al_2O_3, TiO_2, Na_2O) associadas a depleção de ETR (<1 em relação ao manto primitivo) observadas em rocha total e fases minerais atestam o caráter residual desses xenólitos. As razões isotópicas não-radiogênicas de Sr e radiogênicas de Nd tanto em rocha total quanto em separados de clinopiroxênio ($^{87}Sr/^{86}Sr$ = 0,702347–0,703198; $^{143}Nd/^{144}Nd$ = 0,512940–0,513632) corroboram para o caráter depletado dos lherzolitos de Coyhaique. Estimativas de pressão variam entre 1,06 e 1,90 GPa, representando uma profundidade entre 35 e 63 km (a maioria dos lherzolitos tem > 40 km), com temperaturas entre 886 e 1150 °C. Estimativas de fusão parcial obtidas através dos ETR-pesados (e.g., Yb e Lu) em rocha total e clinopiroxênio sugerem baixos graus de fusão parcial (1–15%). Metassomatismo críptico é caracterizado pela ausência de piroxênios secundários e de fases minerais hidratadas, associadas a elevadas razões ETR-leves/ETR-pesados em rocha total e em clinopiroxênios Tipo-2, assim como pelo enriquecimento de LILE e elementos calcófilos somados a assinatura típica de arcos (e.g., anomalias negativas de Nb, Ta e Ti) observada em rocha total. Adicionalmente, olivinas possuem concentrações similares a mais elevadas de Li comparado ao manto primitivo, enquanto os piroxênios são enriquecidos, o que corrobora com um metassomatismo críptico causado por *melts* e/ou fluídos liberados por materiais subductados (crosta oceânica e sedimentos). Essa hipótese é corroborada pela correlação positiva de Pb e U vs. La, e correlação negativa de Nb/Nb* e Ti/Ti* vs. La observadas em clinopiroxênios. Os espinélio-lherzolitos possuem razões $^3He/^4He$ extremamente radiogênicas (0,20–2,52 R_A), $^{21}Ne/^{22}Ne$ (0,0286–0,0308) nucleogênicas, e $^{40}Ar/^{36}Ar$ (325–551) semelhantes a composição atmosférica (296). Propomos que as razões (U-Th)/^3He radiogênicas dos lherzolitos de Coyhaique são consequência da reciclagem de sedimentos terrígenos e/ou crosta oceânica através da subducção. Portanto, os espinélio-lherzolitos de Coyhaique registram a reciclagem de material crustal e voláteis resultante da subducção associada a orogenia andina desde o Carbonífero.

6 REFERÊNCIAS BIBLIOGÁFICAS

Anderson, D.., 1989. Theory of the Earth. Blackwell Scientific Publications, Oxford.

Anderson, D.L., 2006. Speculations on the nature and cause of mantle heterogeneity. Tectonophysics 416, 7–22. https://doi.org/10.1016/j.tecto.2005.07.011

Aragón, E., D'Eramo, F., Castro, A., Pinotti, L., Brunelli, D., Rabbia, O., Rivalenti, G., Varela, R., Spakman, W., Demartis, M., Cavarozzi, C.E., Aguilera, Y.E., Mazzucchelli, M., Ribot, A., 2011. Tectono-magmatic response to major convergence changes in the North Patagonian suprasubduction system; the Paleogene subduction-transcurrent plate margin transition. Tectonophysics 509, 218–237. https://doi.org/10.1016/j.tecto.2011.06.012

Aragón, E., Pinotti, L., D'eramo, F., Castro, A., Rabbia, O., Coniglio, J., Demartis, M., Hernando, I., Cavarozzi, C.E., Aguilera, Y.E., 2013. The Farallon-Aluk ridge collision with South America: Implications for the geochemical changes of slab window magmas from fore- to back-arc. Geosci. Front. 4, 377–388. https://doi.org/10.1016/j.gsf.2012.12.004

Barfod, D.N., Ballentine, C.J., Halliday, A.N., Fitton, J.G., 1999. Noble gases in the Cameroon line and the He, Ne, and Ar isotopic compositions of high μ (HIMU) mantle. J. Geophys. Res. Solid Earth 104, 29509–29527. https://doi.org/10.1029/1999JB900280

Bertotto, G.W., Mazzucchelli, M., Zanetti, A., Vannucci, R., 2013. Petrology and geochemistry of the back-arc lithospheric mantle beneath eastern Payunia (La Pampa, Argentina): Evidence from Agua Poca peridotite xenoliths. Geochem. J. 47, 219–234. https://doi.org/10.2343/geochemj.2.0256

Bjerg, E.A., Ntaflos, T., Kurat, G., Dobosi, G., Labudía, C.H., 2005. The upper mantle beneath Patagonia, Argentina, documented by xenoliths from alkali basalts. J. South Am. Earth Sci. 18, 125–145. https://doi.org/10.1016/j.jsames.2004.09.002

Bjerg, E.A., Ntaflos, T., Thöni, M., Aliani, P., Labudia, C.H., 2009. Heterogeneous lithospheric mantle beneath Northern Patagonia: Evidence from Prahuaniyeu garnet- and spinel-peridotites. J. Petrol. 50, 1267–1298. https://doi.org/10.1093/petrology/egp021

Bodinier, J.-L., Godard, M., 2014. Orogenic, Ophiolitic, and Abyssal Peridotites, in: Treatise on Geochemistry. Elsevier, p. 103–167. https://doi.org/10.1016/B978-0-08-095975-7.00204-7

Boutonnet, E., Arnaud, N., Guivel, C., Lagabrielle, Y., Scalabrino, B., Espinoza, F., 2010. Subduction of the South Chile active spreading ridge: A 17 Ma to 3 Ma magmatic record in central Patagonia (western edge of Meseta del Lago Buenos Aires, Argentina). J. Volcanol. Geotherm. Res. 189, 319–339. https://doi.org/10.1016/j.jvolgeores.2009.11.022

Breitsprecher, K., Thorkelson, D.J., 2009. Neogene kinematic history of Nazca-Antarctic-Phoenix slab windows beneath Patagonia and the Antarctic Peninsula. Tectonophysics 464, 10–20. https://doi.org/10.1016/j.tecto.2008.02.013

Buikin, A., Trieloff, M., Hopp, J., Althaus, T., Korochantseva, E., Schwarz, W.H., Altherr, R., 2005. Noble gas isotopes suggest deep mantle plume source of late Cenozoic mafic alkaline volcanism in Europe. Earth Planet. Sci. Lett. 230, 143–162. https://doi.org/10.1016/j.epsl.2004.11.001

Burnard, P., Graham, D., Turner, G., 1997. Vesicle-specific noble gas analyses of "popping rock": Implications for primordial noble gases in earth. Science (80-.). 276, 568–571. https://doi.org/10.1126/science.276.5312.568

Cande, S.C., Leslie, R.B., 1986. Late Cenozoic tectonics of the Southern Chile Trench. J. Geophys. Res. 91, 471. https://doi.org/10.1029/JB091iB01p00471

Carlson, R., 2003. Volume Editor's Introduction, in: Carlson, R.W. (Org.), The Mantle and Core: Treatise on Geochemistry. Elsevier-Pergamon, Oxford.

Carlson, R.W., 1995. Isotopic inferences on the chemical structure of the mantle. J. Geodyn. 20, 365–386. https://doi.org/10.1016/0264-3707(95)00027-7

Conceição, R. V., Mallmann, G., Koester, E., Schilling, M., Bertotto, G.W., Rodriguez-Vargas, A., 2005. Andean subduction-related mantle xenoliths: Isotopic evidence of Sr-Nd decoupling during metasomatism. Lithos 82, 273–287. https://doi.org/10.1016/j.lithos.2004.09.022

D'Orazio, M., Innocenti, F., Piero, M., Haller, M., Orazio, M.D., Innocenti, F., Manetti, P., Miguel, P., 2004. Cenozoic back-arc magmatism of the southern extra-Andean Patagonia (44° 30'-52° S): A review of geochemical data and geodynamic interpretations. Rev. la Asoc. Geol. Argentina 59, 525–538.

Dantas, C., Grégoire, M., Koester, E., Conceição, R.V., Rieck, N., 2009. The lherzolite–websterite xenolith suite from Northern Patagonia (Argentina): Evidence of mantle–melt reaction processes. Lithos 107, 107–120. https://doi.org/10.1016/j.lithos.2008.06.012

Dawson, J.B., 1980. Kimberlites and Their Xenoliths, Soil Science, Minerals and Rocks. Springer Berlin Heidelberg, Berlin, Heidelberg. https://doi.org/10.1007/978-3-642-67742-7

Demant, A., Hervé, F., Pankhurst, R.J., Suárez, M., 1996. Geochemistry of Early Tertiary back-arc basalts from Aysén, southern Chile (44-46 S): geodynamic implications.

Dick, H.J.B., Bullen, T., 1984. Chromian spinel as a petrogenetic indicator in abyssal and alpine-type peridotites and spatially associated lavas. Contrib. to Mineral. Petrol. 86, 54–76. https://doi.org/10.1007/BF00373711

Diegor, W., Longerich, H., Abrajano, T., Horn, I., 2001. Applicability of a high pressure digestion technique to the analysis of sediment and soil samples by inductively coupled plasma-mass spectrometry. Anal. Chim. Acta 431, 195–207. https://doi.org/10.1016/S0003-2670(00)01339-8

Eagles, G., Gohl, K., Larter, R.D., 2009. Animated tectonic reconstruction of the Southern Pacific and alkaline volcanism at its convergent margins since Eocene times. Tectonophysics 464, 21–29. https://doi.org/10.1016/j.tecto.2007.10.005

Eagles, G., Scott, B.G.C., 2014. Plate convergence west of Patagonia and the Antarctic Peninsula since 61Ma. Glob. Planet. Change 123, 189–198. https://doi.org/10.1016/j.gloplacha.2014.08.002

Espinoza, F., Morata, D., Pelleter, E., Maury, R.C., Suárez, M., Lagabrielle, Y., Polvé, M., Bellon, H., Cotten, J., De la Cruz, R., Guivel, C., 2005. Petrogenesis of the Eocene and Mio-Pliocene alkaline basaltic magmatism in Meseta Chile Chico, southern Patagonia, Chile: Evidence for the participation of two slab windows. Lithos 82, 315–343. https://doi.org/10.1016/j.lithos.2004.09.024

Faccini, B., Bonadiman, C., Coltorti, M., Grégoire, M., Siena, F., 2013. Oceanic Material Recycled within the Sub-Patagonian Lithospheric Mantle (Cerro del Fraile, Argentina). J. Petrol. 54, 1211–1258. https://doi.org/10.1093/petrology/egt010

Farley, K.A., Neroda, E., 1998. Noble gases in the Earth's mantle. Annu. Rev. Earth Planet. Sci. 26, 189–218. https://doi.org/10.1146/annurev.earth.26.1.189

Frey, F.A., Green, D.H., 1974. The mineralogy, geochemistry and origin of Iherzolite inclusions in Victorian basanites. Geochim. Cosmochim. Acta 38, 1023–1059. https://doi.org/10.1016/0016-7037(74)90003-9

Gautheron, C., Moreira, M., 2002. Helium signature of the subcontinental lithospheric mantle. Earth Planet. Sci. Lett. 199, 39–47. https://doi.org/10.1016/S0012-821X(02)00563-0

Gautheron, C., Moreira, M., Allègre, C., 2005. He, Ne and Ar composition of the European lithospheric mantle. Chem. Geol. 217, 97–112. https://doi.org/10.1016/j.chemgeo.2004.12.009

Gervasoni, F., Conceição, R.V., Jalowitzki, T.L.R., Schilling, M.E., Orihashi, Y., Nakai, S., Sylvester, P., 2012. Heterogeneidades do Manto Litosférico Subcontinental ao extremo Sul da Placa Sul-Americana: influência da subducção atual e interações litosfera-astenosfera sob o Campo Vulcânico de Pali Aike. Pesqui. em Geociências 39, 269. https://doi.org/10.22456/1807-9806.37388

Gianni, G.M., Pesce, A., Soler, S.R., 2018. Transient plate contraction between two simultaneous slab windows: Insights from Paleogene tectonics of the Patagonian Andes. J. Geodyn. 121, 64–75. https://doi.org/10.1016/j.jog.2018.07.008

Gioia, S.M.C.L., Pimentel, M.M., 2000. The Sm-Nd isotopic method in the geochronology laboratory of the University of Brasília. An. Acad. Bras. Cienc. 72, 219–245. https://doi.org/10.1590/S0001-37652000000200009

Gorring, M.L., Kay, S.M., 2001. Mantle processes and sources of neogene slab window magmas from Southern Patagonia, Argentina. J. Petrol. 42, 1067–1094. https://doi.org/10.1093/petrology/42.6.1067

Gorring, M.L., Kay, S.M., 2000. Carbonatite metasomatized peridotite xenoliths from southern Patagonia: Implications for lithospheric processes and Neogene plateau magmatism. Contrib. to Mineral. Petrol. 140, 55–72. https://doi.org/10.1007/s004100000164

Graham, D.W., 2002. Noble Gas Isotope Geochemistry of Mid-Ocean Ridge and Ocean Island Basalts: Characterization of Mantle Source Reservoirs. Rev. Mineral. Geochemistry 47, 247–317. https://doi.org/10.2138/rmg.2002.47.8

Griffin, W., Powell, W., Pearson, N.J., O'Reilly, S., 2008. GLITTER: data reduction software for laser ablation ICP-MS. Short Course Ser. 40, 308–311.

Griffin, W.L., O'Reilly, S.Y., Afonso, J.C., Begg, G.C., 2009. The Composition and Evolution of Lithospheric Mantle: a Re-evaluation and its Tectonic Implications. J. Petrol. 50, 1185–1204. https://doi.org/10.1093/petrology/egn033

Gurney, J.J., Moore, R.O., Otter, M.L., Kirkley, M.B., Hops, J.J., McCandless, T.E., 1991. Southern African Kimberlites and their Xenoliths, in: Magmatism in Extensional Structural Settings. Springer Berlin Heidelberg, Berlin, Heidelberg, p. 495–536. https://doi.org/10.1007/978-3-642-73966-8_18

Haggerty, S.E., 1995. Upper mantle mineralogy. J. Geodyn. 20, 331–364. https://doi.org/10.1016/0264-3707(95)00016-3

Hanyu, T., Tatsumi, Y., Senda, R., Miyazaki, T., Chang, Q., Hirahara, Y., Takahashi, T., Kawabata, H., Suzuki, K., Kimura, J.-I., Nakai, S., 2011. Geochemical characteristics and origin of the HIMU reservoir: A possible mantle plume source in the lower mantle. Geochemistry, Geophys. Geosystems 12, n/a-n/a. https://doi.org/10.1029/2010GC003252

Hart, S.R., 1988. Heterogeneous mantle domains: signatures, genesis and mixing chronologies. Earth Planet. Sci. Lett. 90, 273–296. https://doi.org/10.1016/0012-821X(88)90131-8

Hart, S.R., 1984. A large-scale isotope anomaly in the Southern Hemisphere mantle. Nature 309, 753–757. https://doi.org/10.1038/309753a0

Hart, S.R., Hauri, E.H., Oschmann, L.A., Whitehead, J.A., 1992. Mantle Plumes and Entrainment: Isotopic Evidence. Science (80-.). 256, 517–520. https://doi.org/10.1126/science.256.5056.517

Hervé, F., Greene, F., Pankhurst, R.J., 1994. Metamorphosed fragments of oceanic crust in the upper Paleozoic Chonos accretionary complex, southern Chile. J. South Am. Earth Sci. 7, 263–270. https://doi.org/10.1016/0895-9811(94)90012-4

Hilton, D.R., Porcelli, D., 2014. Noble Gases as Tracers of Mantle Processes, in: Treatise on Geochemistry. Elsevier, p. 327–353. https://doi.org/10.1016/B978-0-08-095975-7.00206-0

Hilton, D.R., Porcelli, D., 2003. Noble Gases as Mantle Tracers, in: Treatise on Geochemistry. Elsevier, p. 277–318. https://doi.org/10.1016/B978-0-08-095975-7.00217-5

Hofmann, A.W., 2007. Sampling Mantle Heterogeneity through Oceanic Basalts: Isotopes and Trace Elements, in: White, W.M. (Org.), Treatise on Geochemistry. Elsevier, p. 1–44. https://doi.org/10.1016/B978-0-08-095975-7.00203-5

Hofmann, A.W., 1997. Mantle geochemistry: the message from oceanic volcanism. Nature 385, 219–229. https://doi.org/10.1038/385219a0

Honda, M., McDougall, I., Patterson, D.B., Doulgeris, A., Clague, D.A., 1991. Possible solar noble-gas component in Hawaiian basalts. Nature 349, 149–151. https://doi.org/10.1038/349149a0

Honda, M., Reynolds, J.H., Roedder, E., Epstein, S., 1987. Noble gases in diamonds: Occurrences of solarlike helium and neon. J. Geophys. Res. 92, 12507. https://doi.org/10.1029/JB092iB12p12507

Jackson, E.D., Wright, T.L., 1970. Xenoliths in the honolulu volcanic series, Hawaii. J. Petrol. 11, 405–433. https://doi.org/10.1093/petrology/11.2.405

Jackson, M.G., Dasgupta, R., 2008. Compositions of HIMU, EM1, and EM2 from global trends between radiogenic isotopes and major elements in ocean island basalts. Earth Planet. Sci. Lett. 276, 175–186. https://doi.org/10.1016/j.epsl.2008.09.023

Jacques, G., Hoernle, K., Gill, J., Hauff, F., Wehrmann, H., Garbe-Schönberg, D., van den Bogaard, P., Bindeman, I., Lara, L.E., 2013. Across-arc geochemical variations in the Southern Volcanic Zone, Chile (34.5-38.0°S): Constraints on mantle wedge and slab input compositions. Geochim. Cosmochim. Acta 123, 218–243. https://doi.org/10.1016/j.gca.2013.05.016

Jalowitzki, T., Gervasoni, F., Conceição, R. V., Orihashi, Y., Bertotto, G.W., Sumino, H., Schilling, M.E., Nagao, K., Morata, D., Sylvester, P., 2017. Slab-derived components in the subcontinental lithospheric mantle beneath Chilean Patagonia: Geochemistry and Sr–Nd–Pb isotopes of mantle xenoliths and host basalt. Lithos 292–293, 179–197. https://doi.org/10.1016/j.lithos.2017.09.008

Jalowitzki, T., Sumino, H., Conceição, R. V., Orihashi, Y., Nagao, K., Bertotto, G.W., Balbinot, E., Schilling, M.E., Gervasoni, F., 2016. Noble gas composition of subcontinental lithospheric mantle: An extensively

degassed reservoir beneath Southern Patagonia. Earth Planet. Sci. Lett. 450, 263–273. https://doi.org/10.1016/j.epsl.2016.06.034

Jalowitzki, T.L.R., Conceição, R.V., Orihashi, Y., Bertotto, G.W., Nakai, S., Schilling, M., 2010. Evolução geoquímica de peridotitos e piroxenitos do Manto Litosférico Subcontinental do vulcão Agua Poca, Terreno Cuyania, Argentina. Pesqui. em Geociências 37, 143–167. https://doi.org/10.22456/1807-9806.22656

Jenner, G.A., Longerich, H.P., Jackson, S.E., Fryer, B.J., 1990. ICP-MS - A powerful tool for high-precision trace-element analysis in Earth sciences: Evidence from analysis of selected U.S.G.S. reference samples. Chem. Geol. 83, 133–148. https://doi.org/10.1016/0009-2541(90)90145-W

Kobayashi, M., Sumino, H., Nagao, K., Ishimaru, S., Arai, S., Yoshikawa, M., Kawamoto, T., Kumagai, Y., Kobayashi, T., Burgess, R., Ballentine, C.J., 2017. Slab-derived halogens and noble gases illuminate closed system processes controlling volatile element transport into the mantle wedge. Earth Planet. Sci. Lett. 457, 106–116. https://doi.org/10.1016/j.epsl.2016.10.012

Laurora, A., Mazzucchelli, M., Rivalenti, G., Vannucci, R., Zanetti, A., Barbieri, M.A., Cingolani, C.A., 2001. Metasomatism and Melting in Carbonated Peridotite Xenoliths from the Mantle Wedge: The Gobernador Gregores Case (Southern Patagonia). J. Petrol. 42, 69–87. https://doi.org/10.1093/petrology/42.1.69

Leya, I., Wieler, R., 1999. Nucleogenic production of Ne isotopes in Earth's crust and upper mantle induced by alpha particles from the decay of U and Th. J. Geophys. Res. 104, 15439. https://doi.org/10.1029/1999JB900134

Lucassen, F., Wiedicke, M., Franz, G., 2010. Complete recycling of a magmatic arc: Evidence from chemical and isotopic composition of Quaternary trench sediments in Chile (36°-40°S). Int. J. Earth Sci. 99, 687–701. https://doi.org/10.1007/s00531-008-0410-4

Lupton, J.E., 1983. Terrestrial Inert Gases: Isotope Tracer Studies and Clues to Primordial Components in the Mantle. Annu. Rev. Earth Planet. Sci. 11, 371–414. https://doi.org/10.1146/annurev.ea.11.050183.002103

Matsumoto, T., Honda, M., McDougall, I., Yatsevich, I., O'Reilly, S.Y., 1997. Plume-like neon in a metasomatic apatite from the Australian lithospheric mantle. Nature 388, 162–164. https://doi.org/10.1038/40606

McDonough, W.F., 1990. Constraints on the composition of the continental lithospheric mantle. Earth Planet. Sci. Lett. 101, 1–18. https://doi.org/10.1016/0012-821X(90)90119-I

McDonough, W.F., Sun, S. -s., 1995. The composition of the Earth. Chem. Geol. 120, 223–253. https://doi.org/10.1016/0009-2541(94)00140-4

McKenzie, D., Bickle, M.J., 1988. The Volume and Composition of Melt Generated by Extension of the Lithosphere. J. Petrol. 29, 625–679. https://doi.org/10.1093/petrology/29.3.625

Melchiorre, M., Faccini, B., Grégoire, M., Benoit, M., Casetta, F., Coltorti, M., 2020. Melting and metasomatism/refertilisation processes in the Patagonian sub-continental lithospheric mantle: A review. Lithos 354–355, 1–16. https://doi.org/10.1016/j.lithos.2019.105324

Menzies, M.A., 1990. Archaean, proterozoic and phanerozoic lithospheres, in: Menzies, M.A. (Org.), Continental Mantle. Clarendon Press, Oxford, p. 67–86.

Morata, D., Oliva, C., de la Cruz, R., Suárez, M., 2005. The Bandurrias gabbro: Late Oligocene alkaline magmatism in the Patagonian Cordillera. J. South Am. Earth Sci. 18, 147–162. https://doi.org/10.1016/j.jsames.2004.09.001

Moreira, M., 2018. Neon Isotopes, in: White, W.M. (Org.), Encyclopedia of geochemistry : A Comprehensive Reference Source on the Chemistry of the Earth. Springer, Cham, Switzerland, p. 975–978.

Moreira, M., 1998. Rare Gas Systematics in Popping Rock: Isotopic and Elemental Compositions in the Upper Mantle. Science (80-.). 279, 1178–1181. https://doi.org/10.1126/science.279.5354.1178

Moreira, M., Allègre, C.J., 1998. Helium–neon systematics and the structure of the mantle. Chem. Geol. 147, 53–59. https://doi.org/10.1016/S0009-2541(97)00171-X

Moreira, M., Kunz, J., Allègre, C., 1998. Rare gas systematics in popping rock: Isotopic and elemental compositions in the upper mantle. Science (80-.). 279, 1178–1181. https://doi.org/10.1126/science.279.5354.1178

Mundl, A., Ntaflos, T., Ackerman, L., Bizimis, M., Bjerg, E.A., Hauzenberger, C.A., 2015. Mesoproterozoic and Paleoproterozoic subcontinental lithospheric mantle domains beneath southern Patagonia: Isotopic evidence for its connection to Africa and Antarctica. Geology 43, 39–42. https://doi.org/10.1130/G36344.1

Niedermann, S., Bach, W., 1998. Anomalously nucleogenic neon in North Chile Ridge basalt glasses suggesting a previously degassed mantle source. Earth Planet. Sci. Lett. 160, 447–462. https://doi.org/10.1016/S0012-821X(98)00103-4

Ntaflos, T., Bjerg, E.A., Labudia, C.H., Kurat, G., 2007. Depleted lithosphere from the mantle wedge beneath Tres Lagos, southern Patagonia, Argentina. Lithos 94, 46–65. https://doi.org/10.1016/j.lithos.2006.06.011

O'Hara, M.J., 1968. The bearing of phase equilibria studies in synthetic and natural systems on the origin and evolution of basic and ultrabasic rocks. Earth-Science Rev. 4, 69–133. https://doi.org/10.1016/0012-8252(68)90147-5

O'Reilly, S.Y., Griffin, W.L., Poudjom Djomani, Y.H., Morgan, P., 2001. Are Lithospheres Forever? Tracking Changes in Subcontinental Lithospheric Mantle Through Time. GSA Today 11, 4. https://doi.org/10.1130/1052-5173(2001)011<0004:ALFTCI>2.0.CO;2

Oliveros, V., Vásquez, P., Creixell, C., Lucassen, F., Ducea, M.N., Ciocca, I., González, J., Espinoza, M., Salazar, E., Coloma, F., Kasemann, S.A., 2020. Lithospheric evolution of the Pre- and Early Andean convergent margin, Chile. Gondwana Res. 80, 202–227. https://doi.org/10.1016/j.gr.2019.11.002

Osawa, T., 2004. A New Correction Technique for Mass Interferences by 40Ar++ and CO2++ during Isotope Analysis of a Small Amount of Ne. J. Mass Spectrom. Soc. Jpn. 52, 230–232. https://doi.org/10.5702/massspec.52.230

Ozima, M., Podosek, F.., 2002. Noble Gas Geochemistry, 2nd ed. Cambridge Univ. Press.

Ozima, M., Zashu, S., 1988. Solar-type Ne in Zaire cubic diamonds. Geochim. Cosmochim. Acta 52, 19–25. https://doi.org/10.1016/0016-7037(88)90052-X

Palme, H., O'Neill, H.S.C., 2014. Cosmochemical Estimates of Mantle Composition, in: Treatise on Geochemistry. Elsevier, p. 1–39. https://doi.org/10.1016/B978-0-08-095975-7.00201-1

Pankhurst, R.., Leat, P.., Sruoga, P., Rapela, C.., Márquez, M., Storey, B.., Riley, T.., 1998. The Chon Aike province of Patagonia and related rocks in West Antarctica: A silicic large igneous province. J. Volcanol. Geotherm. Res. 81, 113–136. https://doi.org/10.1016/S0377-0273(97)00070-X

Pankhurst, R.J., Riley, T.R., Fanning, C.M., Kelley, S.P., 2000. Episodic Silicic Volcanism in Patagonia and the Antarctic Peninsula: Chronology of Magmatism Associated with the Break-up of Gondwana. J. Petrol. 41, 605–625. https://doi.org/10.1093/petrology/41.5.605

Pankhurst, R.J., Weaver, S.D., Hervé, F., Larrondo, P., 1999. Mesozoic-Cenozoic evolution of the North Patagonian Batholith in Aysen, southern Chile. J. Geol. Soc. London. 156, 673–694. https://doi.org/10.1144/gsjgs.156.4.0673

Parada, M.A., Lahsen, A., Palacios, C., 2001. Ages and geochemistry of Mesozoic-Eocene back-arc volcanic rocks in the Aysén region of the Patagonian Andes, Chile. Rev. geológica Chile.

Parai, R., Mukhopadhyay, S., Lassiter, J.C., 2009. New constraints on the HIMU mantle from neon and helium isotopic compositions of basalts from the Cook-Austral Islands. Earth Planet. Sci. Lett. 277, 253–261. https://doi.org/10.1016/j.epsl.2008.10.014

Paton, C., Hellstrom, J., Paul, B., Woodhead, J., Hergt, J., 2011. Iolite: Freeware for the visualisation and processing of mass spectrometric data. J. Anal. At. Spectrom. 26, 2508. https://doi.org/10.1039/c1ja10172b

Pearson, D.G., Canil, D., Shirey, S.B., 2003. Mantle Samples Included in Volcanic Rocks: Xenoliths and Diamonds, in: Treatise on Geochemistry. Elsevier, p. 171–275. https://doi.org/10.1016/B0-08-043751-6/02005-3

Pearson, D.G., Nowell, G.M., 2002. The continental lithospheric mantle: characteristics and significance as a mantle reservoir. Philos. Trans. R. Soc. A Math. Phys. Eng. Sci. 360, 2383–2410. https://doi.org/10.1098/rsta.2002.1074

Ramos, V.A., Kay, S.M., 1992. Southern Patagonian plateau basalts and deformation: Backarc testimony of ridge collisions. Tectonophysics 205, 261–282. https://doi.org/10.1016/0040-1951(92)90430-E

Rivalenti, G., Mazzucchelli, M., Laurora, A., Ciuffi, S.I.A., Zanetti, A., Vannucci, R., Cingolani, C.A., 2004. The backarc mantle lithosphere in Patagonia, South America. J. South Am. Earth Sci. 17, 121–152. https://doi.org/10.1016/j.jsames.2004.05.009

Rivalenti, G., Mazzucchelli, M., Zanetti, A., Vannucci, R., Bollinger, C., Hémond, C., Bertotto, G.W., 2007. Xenoliths from Cerro de los Chenques (Patagonia): An example of slab-related metasomatism in the backarc lithospheric mantle. Lithos 99, 45–67. https://doi.org/10.1016/j.lithos.2007.05.012

Roduit, N., 2007. JMicroVision: un logiciel d'analyse d'images pétrographiques polyvalent. Terre Environ.

Sarda, P., Staudacher, T., Allègre, C.J., 1988. Neon isotopes in submarine basalts. Earth Planet. Sci. Lett. 91, 73–88. https://doi.org/10.1016/0012-821X(88)90152-5

Schilling, M., Conceição, R. V., Mallmann, G., Koester, E., Kawashita, K., Hervé, F., Morata, D., Motoki, A., 2005. Spinel-facies mantle xenoliths from Cerro Redondo, Argentine Patagonia: Petrographic, geochemical, and isotopic evidence of interaction between xenoliths and host basalt. Lithos 82, 485–502. https://doi.org/10.1016/j.lithos.2004.09.028

Schilling, M.E., Carlson, R.W., Conceição, R.V., Dantas, C., Bertotto, G.W., Koester, E., 2008. Re–Os isotope constraints on subcontinental lithospheric mantle evolution of southern South America. Earth Planet. Sci. Lett. 268, 89–101. https://doi.org/10.1016/j.epsl.2008.01.005

Schilling, M.E., Carlson, R.W., Tassara, A., Conceição, R.V., Bertotto, G.W., Vásquez, M., Muñoz, D., Jalowitzki, T., Gervasoni, F., Morata, D., 2017. The origin of Patagonia revealed by Re-Os systematics of mantle xenoliths. Precambrian Res. 294, 15–32. https://doi.org/10.1016/j.precamres.2017.03.008

Shaw, A.M., Hilton, D.R., Macpherson, C.G., Sinton, J.M., 2001. Nucleogenic neon in high 3He/4He lavas from the Manus back-arc basin: a new perspective on He–Ne decoupling. Earth Planet. Sci. Lett. 194, 53–66. https://doi.org/10.1016/S0012-821X(01)00539-8

Somoza, R., Ghidella, M.E., 2012. Late Cretaceous to recent plate motions in western South America revisited. Earth Planet. Sci. Lett. 331–332, 152–163. https://doi.org/10.1016/j.epsl.2012.03.003

Starkey, N.A., Stuart, F.M., Ellam, R.M., Fitton, J.G., Basu, S., Larsen, L.M., 2009. Helium isotopes in early Iceland plume picrites: Constraints on the composition of high 3He/4He mantle. Earth Planet. Sci. Lett. 277, 91–100. https://doi.org/10.1016/j.epsl.2008.10.007

Stern, C.R., 2004. Active Andean Volcanism. Andean Geol.

Stern, C.R., Kilian, R., Olker, B., Hauri, E.H., Kurtis Kyser, T., 1999. Evidence from mantle xenoliths for relatively thin (<100 km) continental lithosphere below the Phanerozoic crust of southernmost South America, in: Developments in Geotectonics. p. 217–235. https://doi.org/10.1016/S0419-0254(99)80013-5

Stracke, A., 2018. Mantle Geochemistry, in: White, W.M. (Org.), Encyclopedia of geochemistry : A Comprehensive Reference Source on the Chemistry of the Earth. Springer, Cham, Switzerland, p. 867–878.

Stracke, A., 2012. Earth's heterogeneous mantle: A product of convection-driven interaction between crust and mantle. Chem. Geol. 330–331, 274–299. https://doi.org/10.1016/j.chemgeo.2012.08.007

Stracke, A., Hofmann, A.W., Hart, S.R., 2005. FOZO, HIMU, and the rest of the mantle zoo. Geochemistry, Geophys. Geosystems 6. https://doi.org/10.1029/2004GC000824

Streckeisen, A., 1976. To each plutonic rock its proper name. Earth-Science Rev. 12, 1–33. https://doi.org/10.1016/0012-8252(76)90052-0

Stuart, F.M., Lass-Evans, S., Godfrey Fitton, J., Ellam, R.M., 2003. High 3He/4He ratios in picritic basalts from Baffin Island and the role of a mixed reservoir in mantle plumes. Nature 424, 57–59. https://doi.org/10.1038/nature01711

Sumino, H., Kaneoka, I., Matsufuji, K., Sobolev, A. V., 2006. Deep mantle origin of kimberlite magmas revealed by neon isotopes. Geophys. Res. Lett. 33, 2–7. https://doi.org/10.1029/2006GL027144

Sumino, H., Nagao, K., Notsu, K., 2001. Highly Sensitive and Precise Measurement of Helium Isotopes Using a Mass Spectrometer with Double Collector System. J. Mass Spectrom. Soc. Jpn. 49, 61–68. https://doi.org/10.5702/massspec.49.61

Sun, S. -s., McDonough, W.F., 1989. Chemical and isotopic systematics of oceanic basalts: implications for mantle composition and processes. Geol. Soc. London, Spec. Publ. 42, 313–345. https://doi.org/10.1144/GSL.SP.1989.042.01.19

Thorkelson, D.J., 1996. Subduction of diverging plates and the principles of slab window formation. Tectonophysics 255, 47–63. https://doi.org/10.1016/0040-1951(95)00106-9

Trieloff, M., Kunz, J., Clague, D.A., Harrison, D., Allègre, C.J., 2000. The nature of pristine noble gases in mantle plumes. Science (80-.). 288, 1036–1038. https://doi.org/10.1126/science.288.5468.1036

Tucker, J.M., Mukhopadhyay, S., Schilling, J.G., 2012. The heavy noble gas composition of the depleted MORB mantle (DMM) and its implications for the preservation of heterogeneities in the mantle. Earth Planet. Sci. Lett. 355–356, 244–254. https://doi.org/10.1016/j.epsl.2012.08.025

Weaver, B.L., 1991. The origin of ocean island basalt end-member compositions: trace element and isotopic constraints. Earth Planet. Sci. Lett. 104, 381–397. https://doi.org/10.1016/0012-821X(91)90217-6

Wetherill, G.W., 1954. Variations in the Isotopic Abundances of Neon and Argon Extracted from Radioactive Minerals. Phys. Rev. 96, 679–683. https://doi.org/10.1103/PhysRev.96.679

Willbold, M., Stracke, A., 2010. Formation of enriched mantle components by recycling of upper and lower continental crust. Chem. Geol. 276, 188–197. https://doi.org/10.1016/j.chemgeo.2010.06.005

Workman, R.K., Hart, S.R., 2005. Major and trace element composition of the depleted MORB mantle (DMM). Earth Planet. Sci. Lett. 231, 53–72. https://doi.org/10.1016/j.epsl.2004.12.005

Workman, R.K., Hart, S.R., Jackson, M., Regelous, M., Farley, K.A., Blusztajn, J., Kurz, M., Staudigel, H., 2004. Recycled metasomatized lithosphere as the origin of the Enriched Mantle II (EM2) end-member: Evidence from the Samoan Volcanic Chain. Geochemistry, Geophys. Geosystems 5, 1–44. https://doi.org/10.1029/2003GC000623

Yatsevich, I., Honda, M., 1997. Production of nucleogenic neon in the Earth from natural radioactive decay. J. Geophys. Res. Solid Earth 102, 10291–10298. https://doi.org/10.1029/97JB00395

Zaffarana, C., Tommasi, A., Vauchez, A., Grégoire, M., 2014. Microstructures and seismic properties of south Patagonian mantle xenoliths (Gobernador Gregores and Pali Aike). Tectonophysics 621, 175–197. https://doi.org/10.1016/j.tecto.2014.02.017

Zindler, A., Hart, S.R., 1986. Chemical Geodynamics. Annu. Rev. Earth Planet. Sci. 14, 493–571. https://doi.org/10.1146/annurev.earth.14.1.493

Zindler, A., Jagoutz, E., Goldstein, S., 1982. Nd, Sr and Pb isotopic systematics in a three-component mantle: a new perspective. Nature 298, 519–523. https://doi.org/10.1038/298519a0
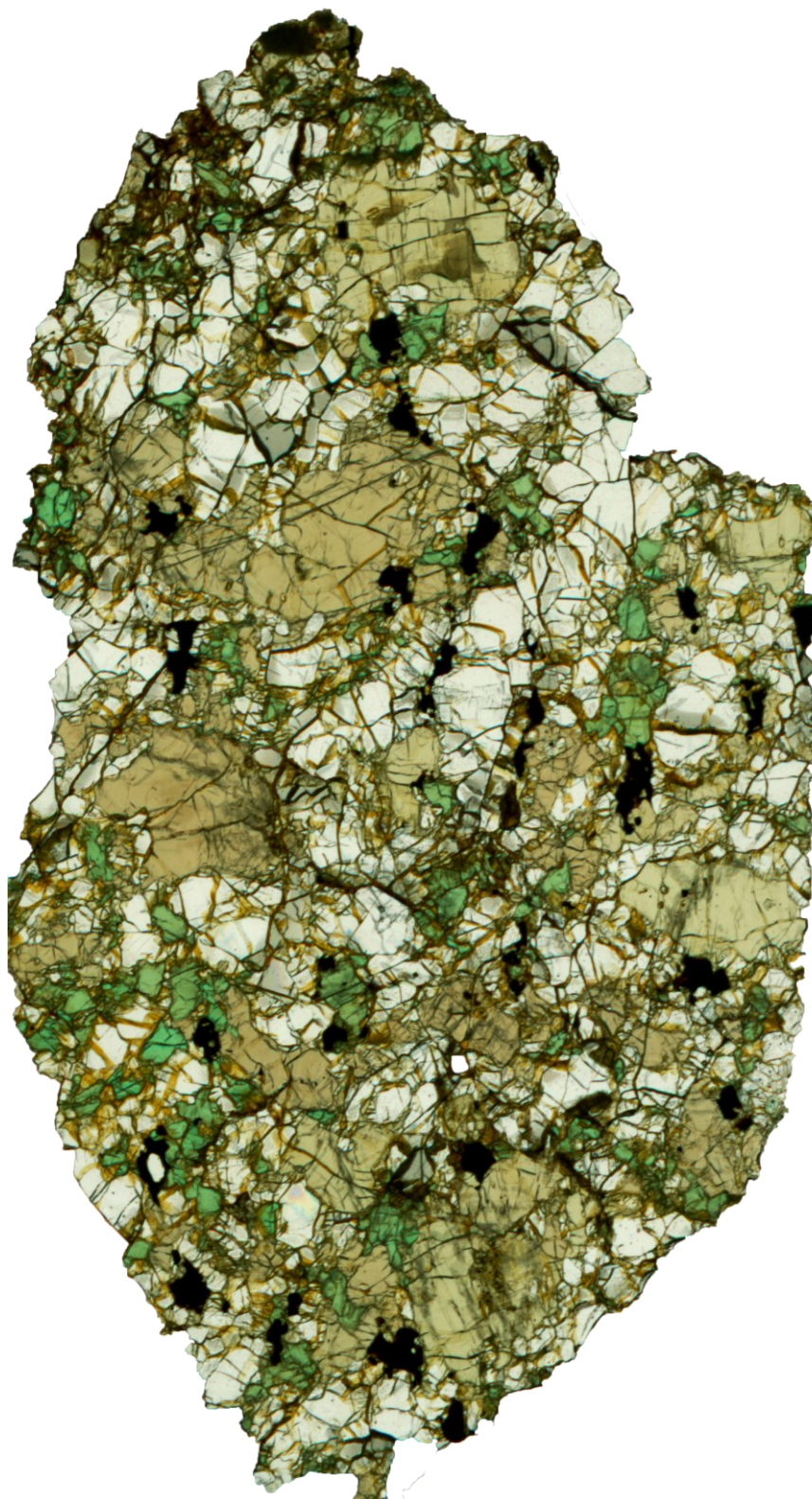
ANEXO I

Imagens representativas das sessões delgadas estudadas. As imagens foram obtidas escaneando-se as lâminas petrográficas, e as cores foram realçadas por meio de alteração do contraste para melhor visualização.
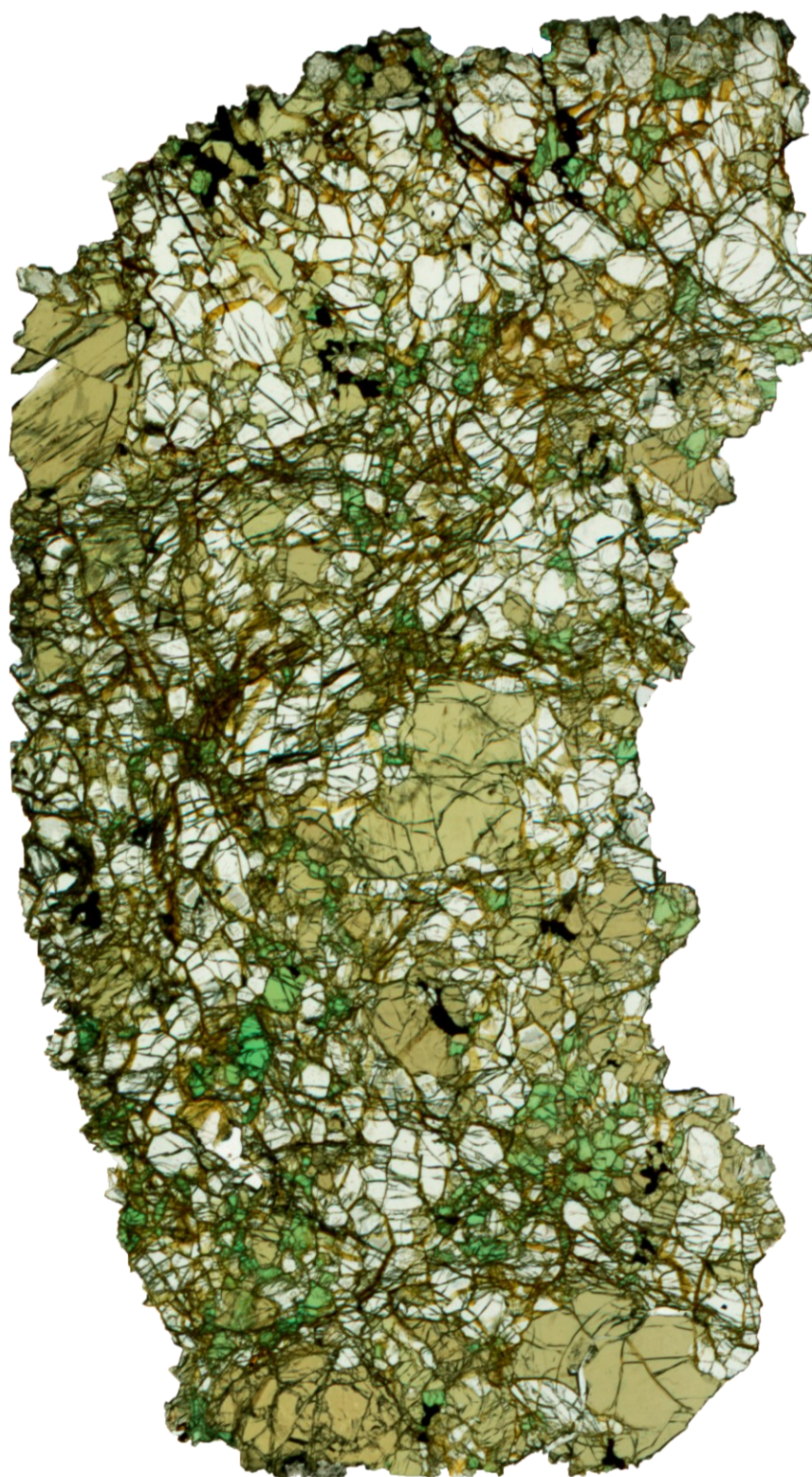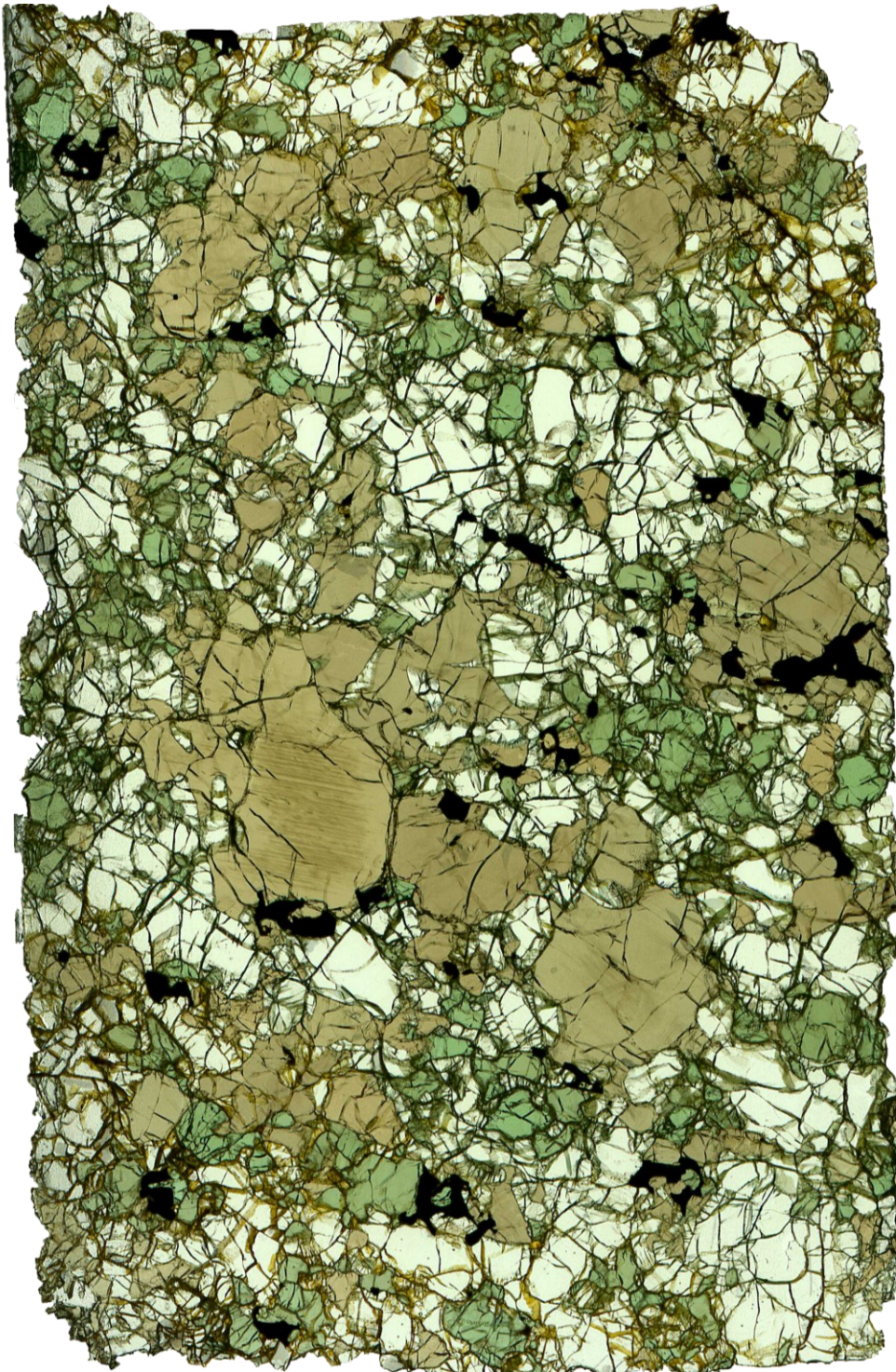
24 mm

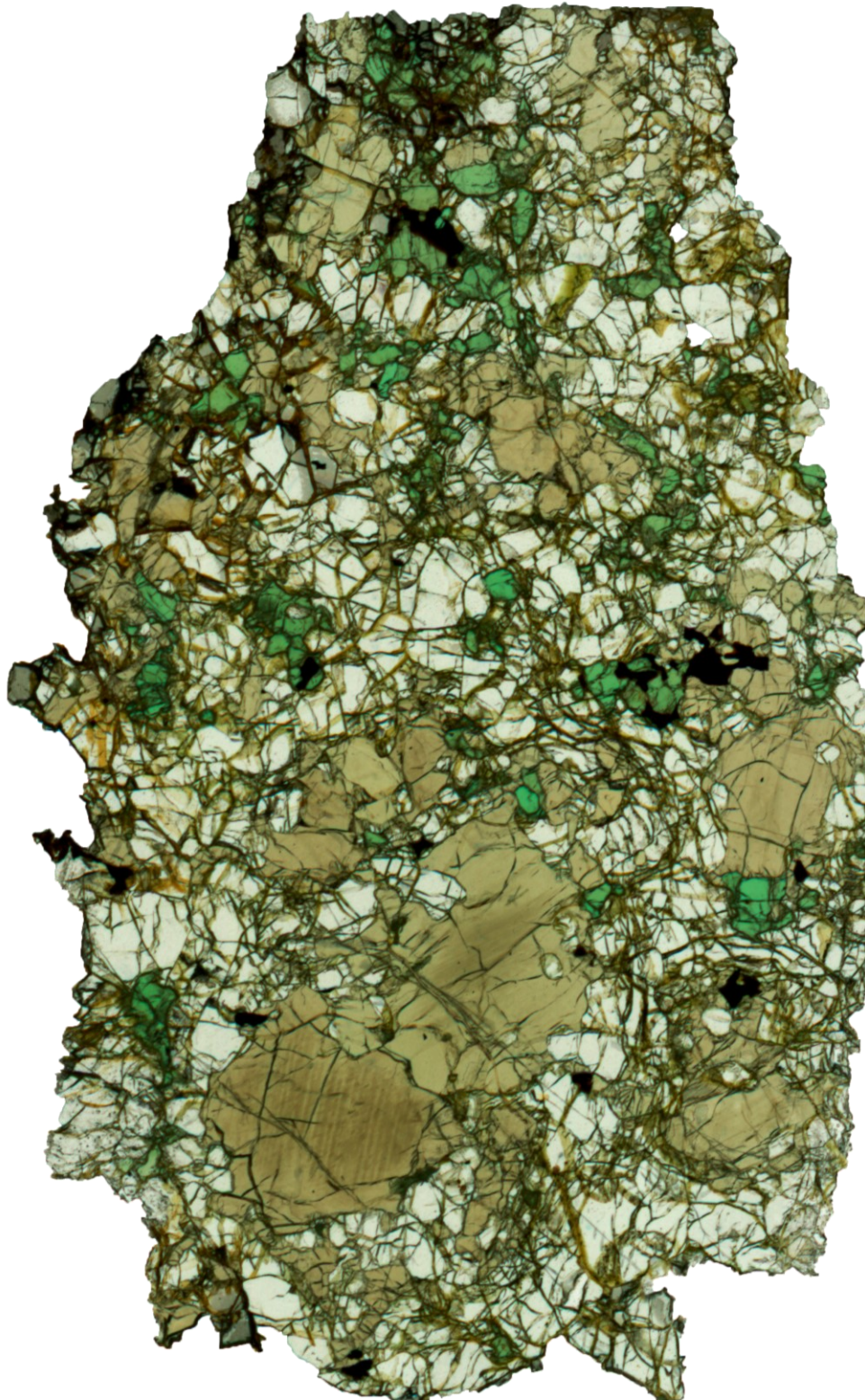Figura A1. Imagem escaneada da sessão delgada da amostra PM25-02.

24 mm

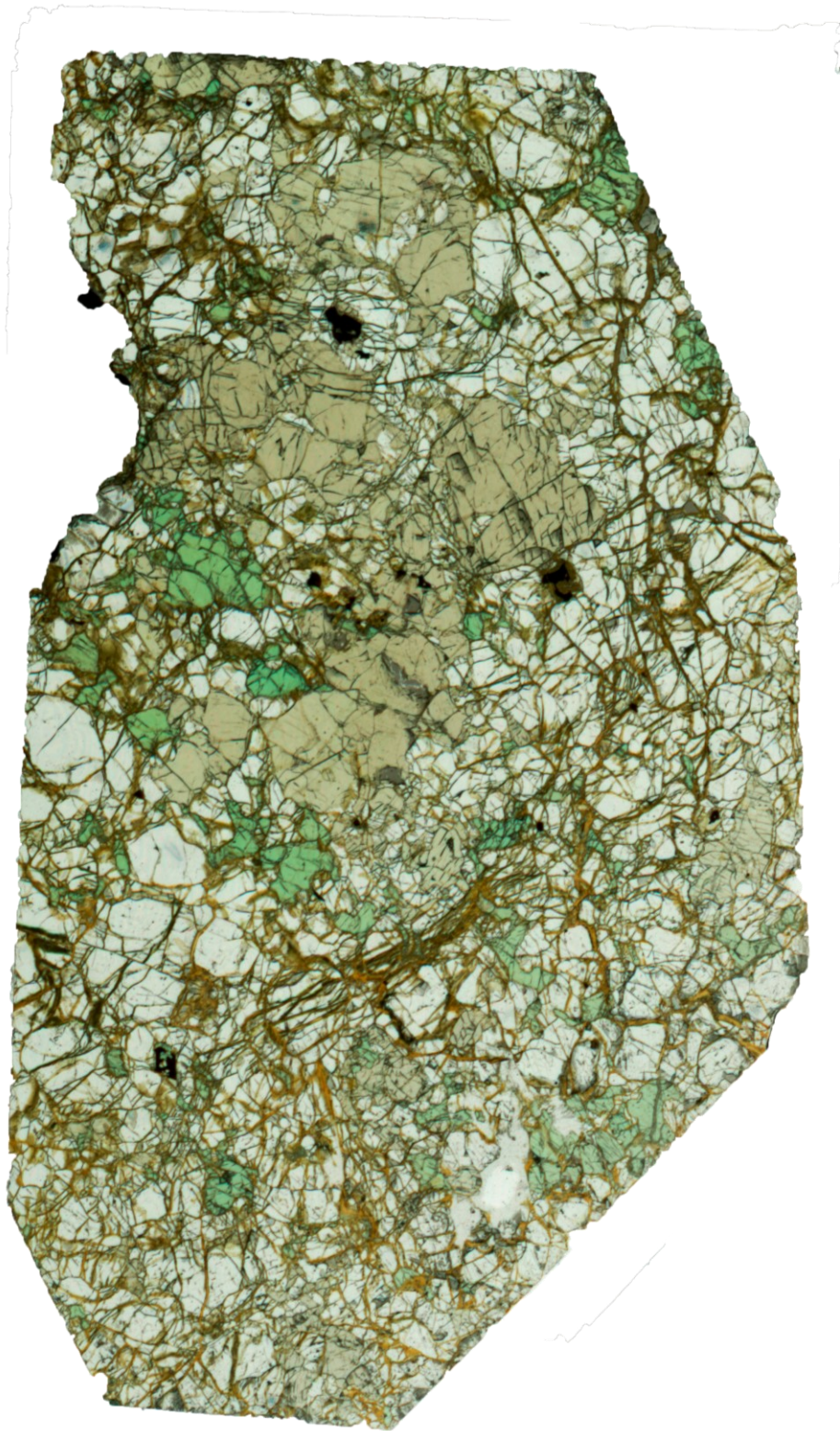Figura A2. Imagem escaneada da sessão delgada da amostra PM25-04.

24 mm

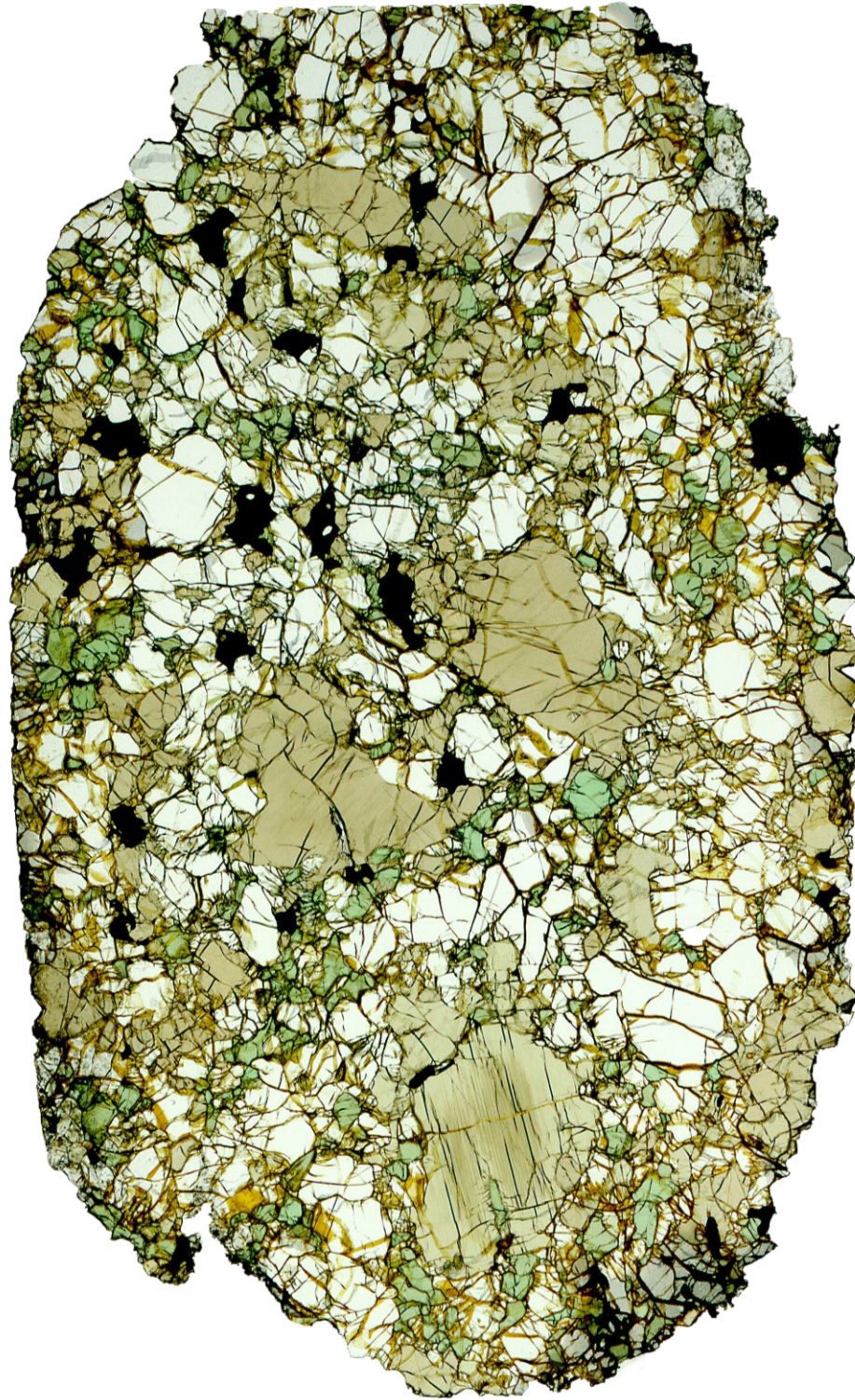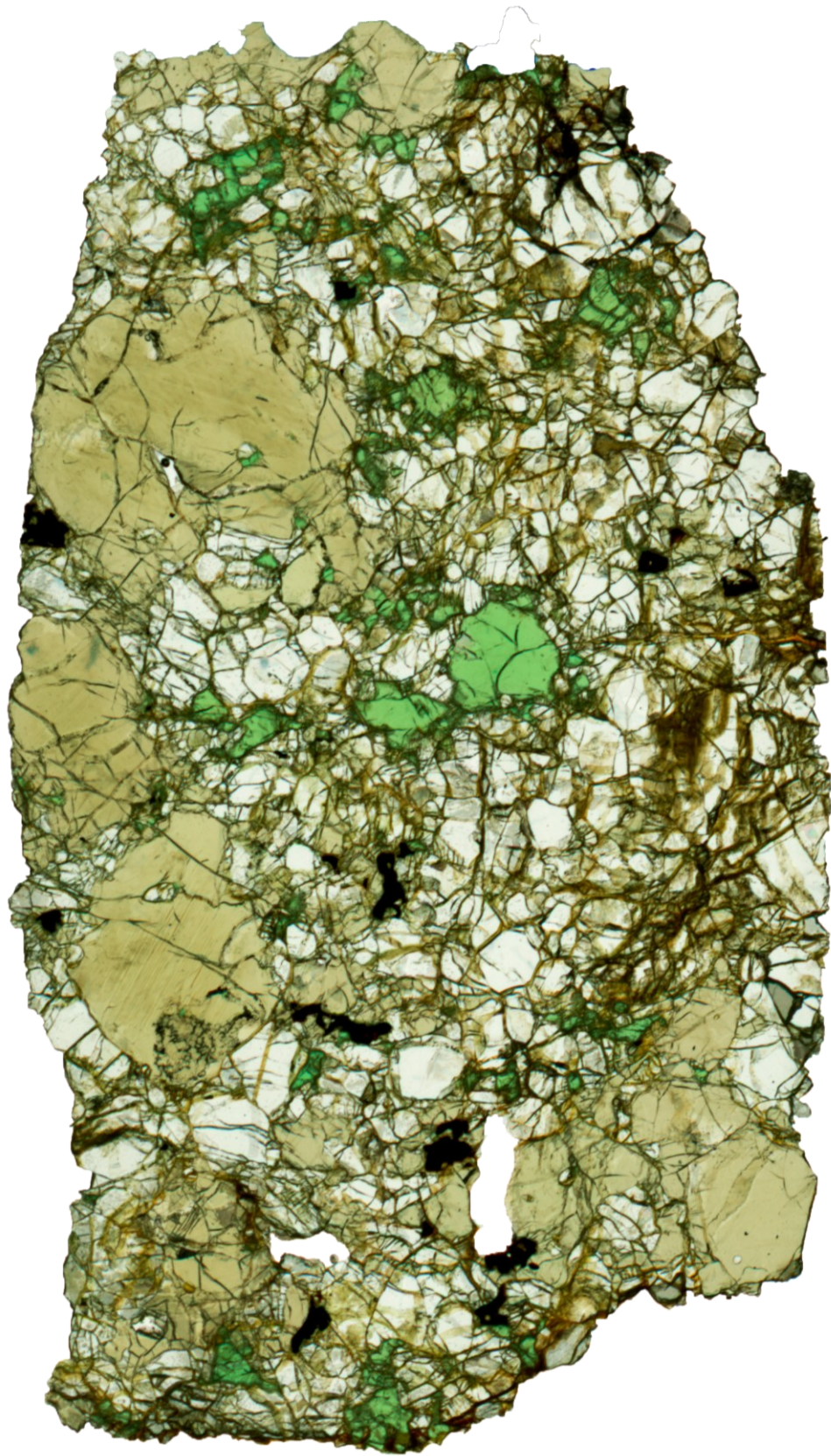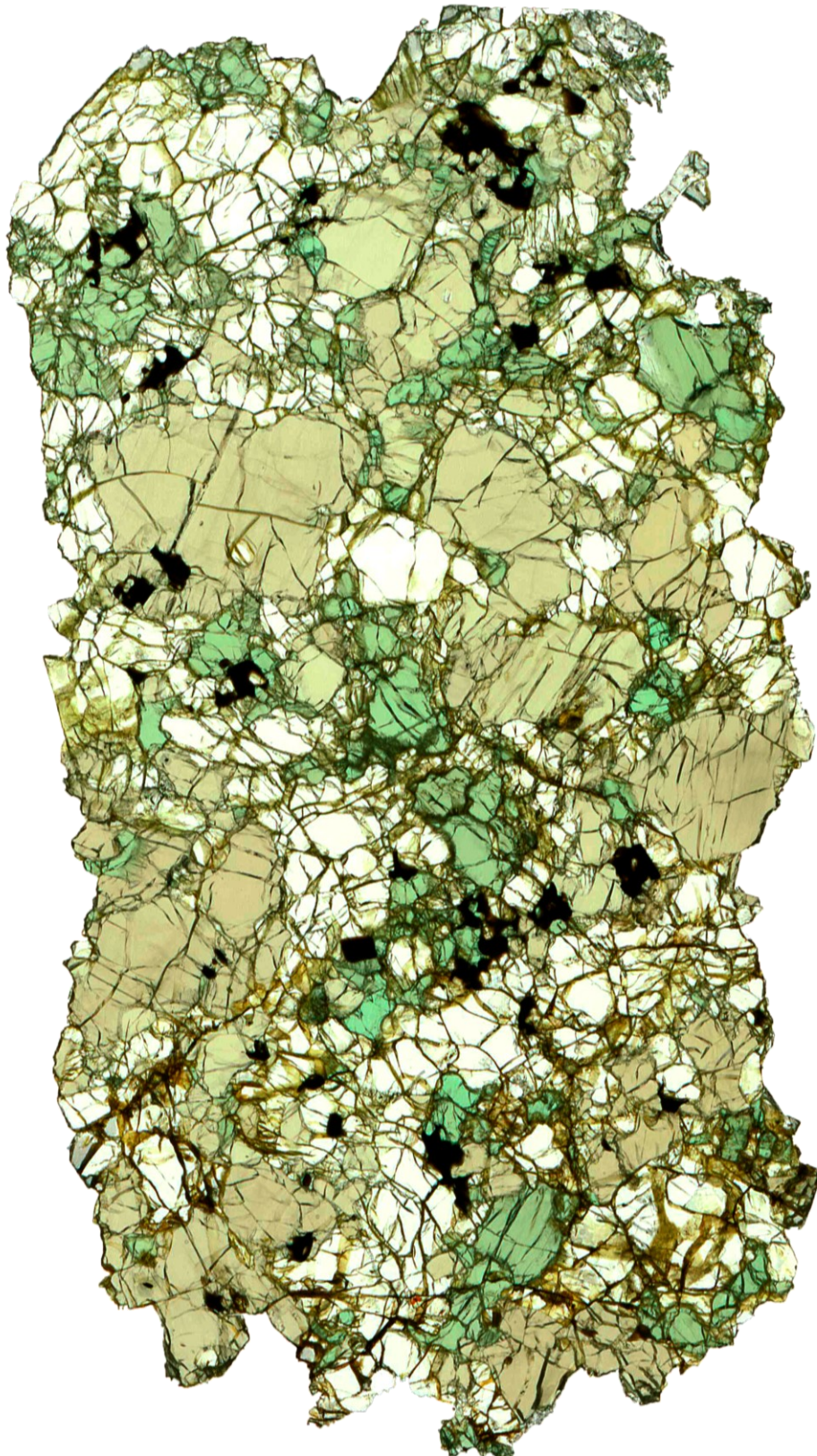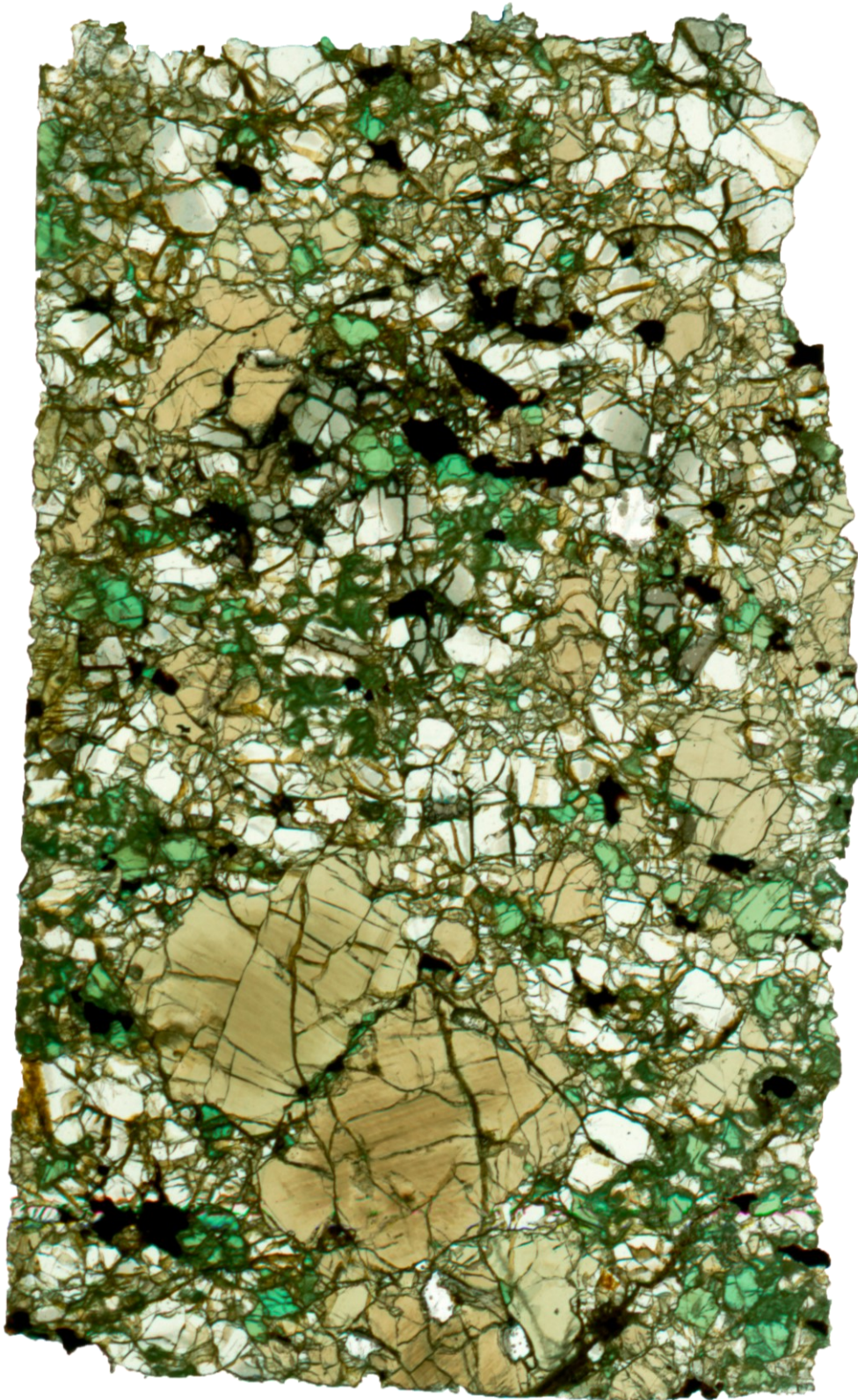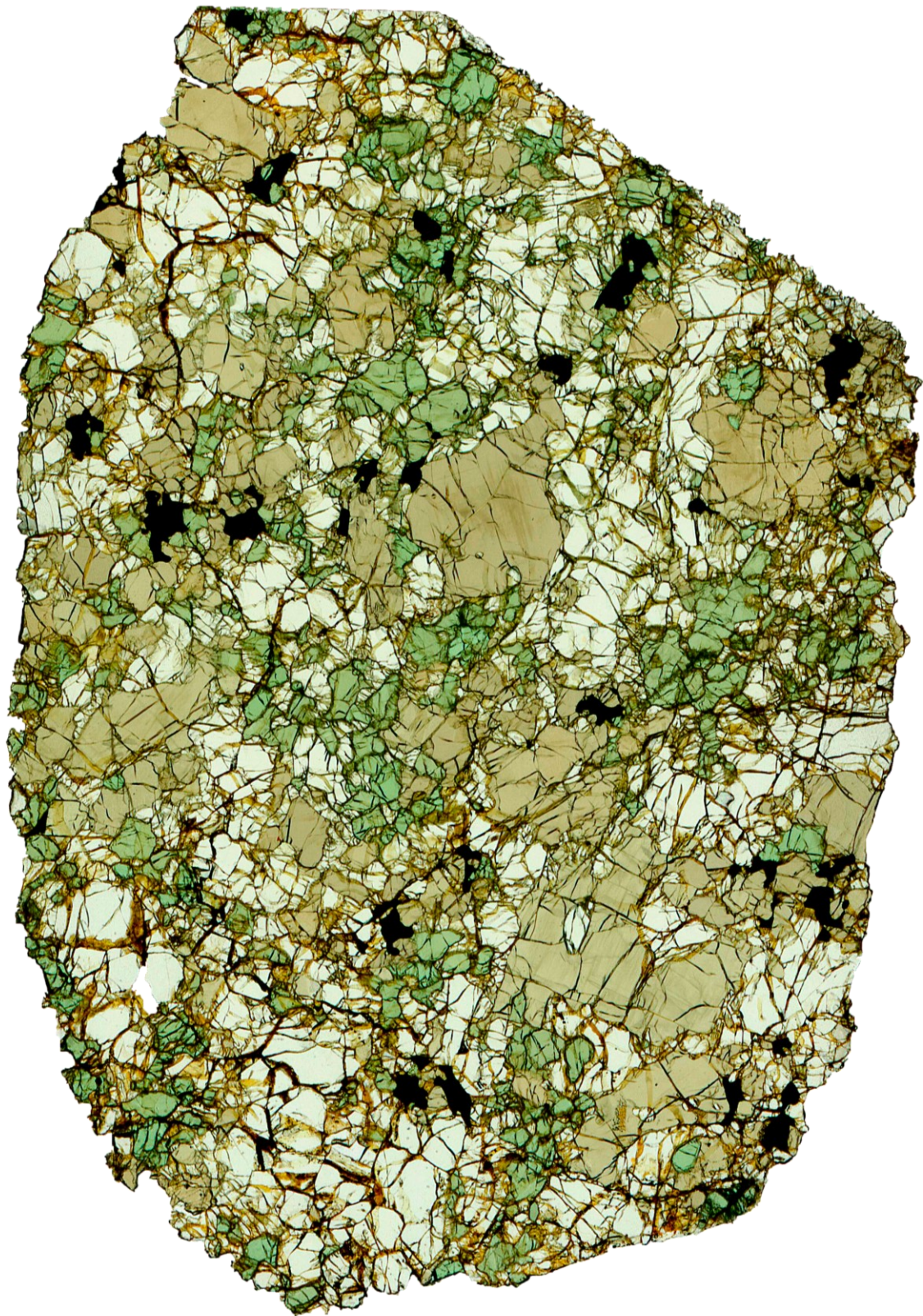Figura A3. Imagem escaneada da sessão delgada da amostra PM25-05.

24 mm

Figura A4. Imagem escaneada da sessão delgada da amostra PM25-06.

24 mm

Figura A5. Imagem escaneada da sessão delgada da amostra PM25-08.

24 mm

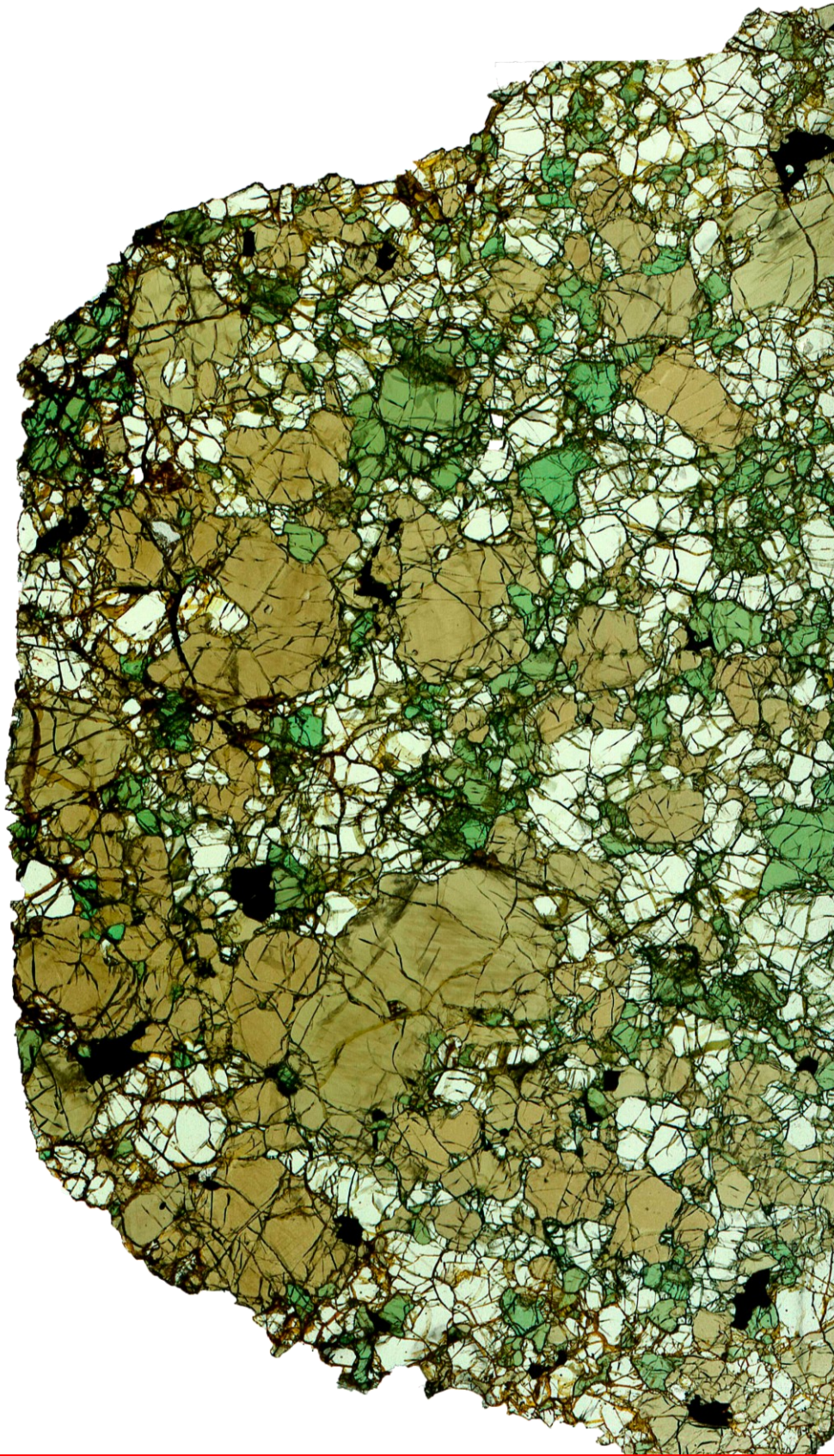Figura A6. Imagem escaneada da sessão delgada da amostra PM25-09.

24 mm

Figura A7. Imagem escaneada da sessão delgada da amostra PM25-10.

24 mm

Figura A8. Imagem escaneada da sessão delgada da amostra PM25-12.

24 mm

Figura A9. Imagem escaneada da sessão delgada da amostra PM25-13.

24 mm

Figura A10. Imagem escaneada da sessão delgada da amostra PM25-15.

24 mm

Figura A11. Imagem escaneada da sessão delgada da amostra PM25-16.

24 mm

Figura A12. Imagem escaneada da sessão delgada da amostra PM25-17.

24 mm

Figura A13. Imagem escaneada da sessão delgada da amostra PM25-21.

24 mm

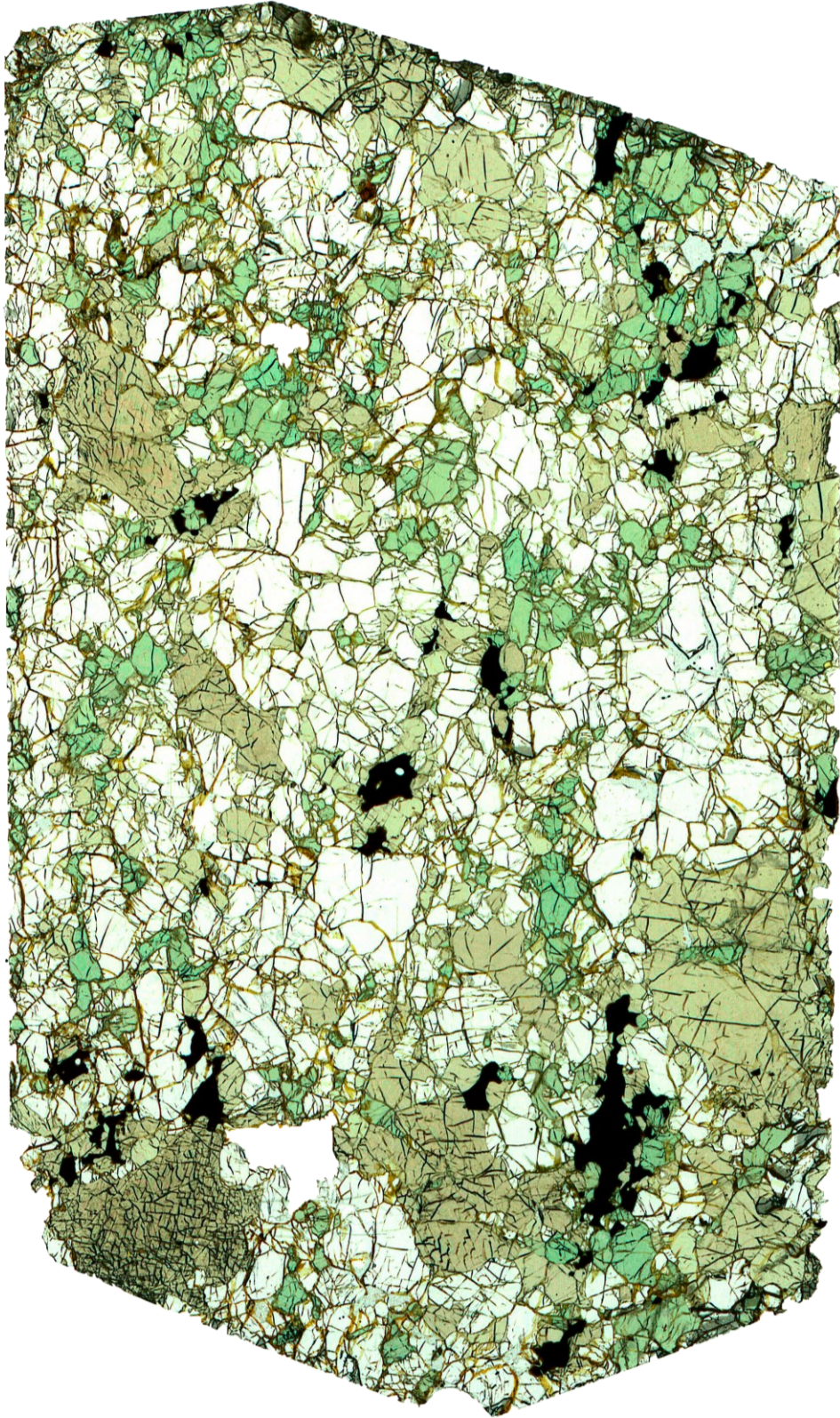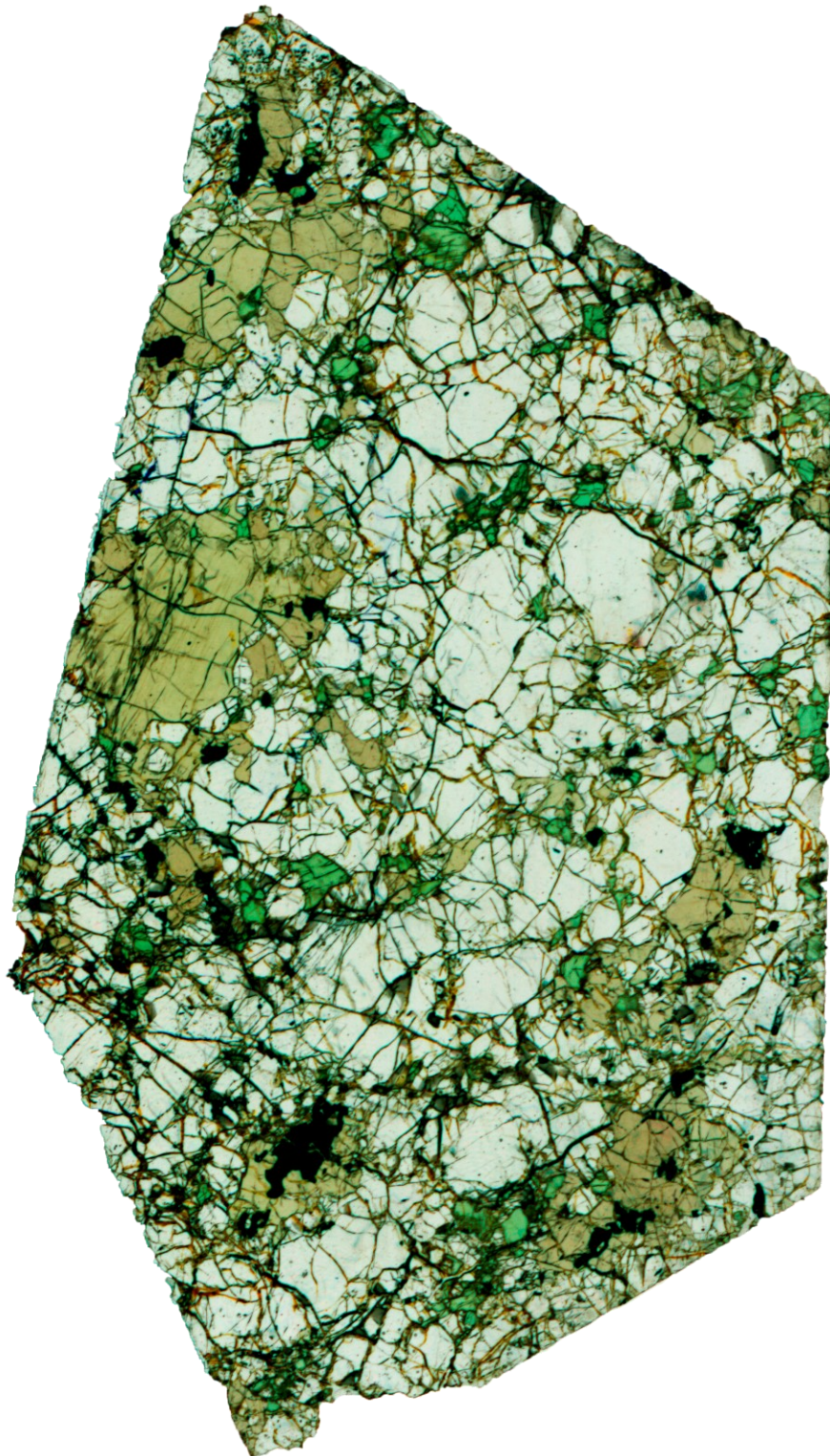Figura A14. Imagem escaneada da sessão delgada da amostra PM25-28.

24 mm

Figura A15. Imagem escaneada da sessão delgada da amostra PM25-34.

24 mm

Figura A16. Imagem escaneada da sessão delgada da amostra PM25-42.